Numerical Relativity in Higher Dimensional Spacetimes

William Gregory Cook

Supervisor: Dr U. Sperhake

Department of Applied Mathematics and Theoretical Physics
University of Cambridge

This dissertation is submitted for the degree of
Doctor of Philosophy

Trinity Hall   July 2018

To my parents and my brother

Declaration

This dissertation is the result of my own work and includes nothing which is the outcome of work done in collaboration except as declared in the Preface and specified in the text. It is not substantially the same as any that I have submitted, or, is being concurrently submitted for a degree or diploma or other qualification at the University of Cambridge or any other University or similar institution except as declared in the Preface and specified in the text. I further state that no substantial part of my dissertation has already been submitted, or, is being concurrently submitted for any such degree, diploma or other qualification at the University of Cambridge or any other University or similar institution except as declared in the Preface and specified in the text.

William Gregory Cook

July 2018

Acknowledgements

Abstract

The study of general relativity in higher dimensions has proven to be a fruitful avenue of research, revealing new applications of the theory, for instance in understanding strongly coupled quantum field theories through the holographic principle, and proposing an explanation of the hierarchy problem through TeV gravity scenarios. To understand the non-linear regime of higher dimensional general relativity, such as that involved in the merger of black holes, we use numerical relativity to solve the Einstein equations. In this thesis we develop and demonstrate several diagnostic tools and new initial data for use in numerical relativity simulations of higher dimensional spacetimes, and use these to investigate binary black hole systems. Firstly, we present a formalism for calculating the gravitational waves in a numerical simulation of a higher dimensional spacetime, and apply this formalism to the example of the head on merger of two equal mass black holes. In doing so, we simulate the merger of black holes in up to 10 spacetime dimensions for the first time, and investigate the dependence of the energy radiated away in gravitational waves on the number of dimensions. We also apply this formalism to the example of head on unequal mass black hole collisions, investigating the dependence of radiated energy and momentum on the number of dimensions and the mass ratio. This study complements and sheds further light on previous work on the merger of point particles with black holes in higher dimensions, and presents evidence for a link between the regime studied, and the *large D regime* of general relativity where D is the number of spacetime dimensions. We also present initial data that enables us to study black holes with initial momentum and angular momentum, putting in place the framework needed to study problems such as the scattering cross section of black holes in higher dimensions, and the nature of black hole orbits in higher dimensions. Finally, we present, and demonstrate the use of, an apparent horizon finder for higher dimensional spacetimes. This allows us to calculate a black hole's mass and spin, which characterise the black hole.

Table of contents

List of figures

List of tables

Chapter 1

Introduction

In 1915 Albert Einstein published his theory of general relativity (GR) [1–3], a theory that still stands as a pillar of modern theoretical physics today. GR has passed all of the experimental tests that it has so far been set [4]. These tests have however, until very recently, only probed the weak field regime of GR. With the first detection of gravitational waves (GWs) [5], for the first time we have the opportunity to test general relativity in the strong field, in the context of the mergers of ultra-compact objects, such as black holes (BHs). This exciting era promises to reveal answers to many questions about the universe, from astrophysical questions about the nature of the population of black holes we see [6], to testing general relativity for the presence of modifications only apparent in this strong field regime [7, 8]. Much of the study of general relativity has restricted attention to the 4 spacetime dimensions that we perceive, but, increasingly, attention has turned to the case of general relativity in more than 3 spatial dimensions. The study of higher-dimensional spacetimes dates back at least to the attempts by Kaluza [9] and Klein [10] to unify gravitation and electromagnetism. It has been in the search for a quantum theory of gravity however that the most motivation for the study of higher dimensional spacetimes has arisen. General relativity is a classical theory, that describes the gravitational interaction, whereas the other interactions in nature, electromagnetism and the strong and weak nuclear forces are described by quantum theories, as part of the Standard Model. The search for a quantum theory of gravity, that will describe gravity on the smallest length scales, is perhaps the biggest open question in theoretical physics today. Currently the leading contender for a quantum theory of gravity is string theory, a term that encapsulates a number of different theories that exist in more than 4 spacetime dimensions, which are thought of as different aspects of one larger theory, "M-theory" [11]. These theories are populated by

1 dimensional strings and higher dimensional extended objects called branes, and our four dimensional observed universe is viewed as embedded in this higher dimensional theory, or as the result of some compactification of the extra dimensions. In this chapter we will review some of the key motivations for extending the study of GR to higher dimensions, and introduce the field of numerical relativity, which we will use in this thesis to study higher dimensional GR.

1.1 Higher dimensional general relativity

The generalisation of general relativity to more than four spacetime dimensions has revealed a plethora of new phenomena not apparent in $4D$, as well as proposing solutions to fundamental questions in physics, and connections between seemingly disconnected fields. In higher dimensions results on black hole topology are different to $4D$ [12], leading to the discovery of such topologically non trivial solutions as the black ring [13] and black saturn [14]. The addition of more spatial dimensions also changes the nature of a spinning black hole, with the Myers-Perry black hole [15], the higher dimensional analogue of the Kerr black hole, having no upper bound on its spin in $D \geq 6$, and able to spin in multiple planes at the same time.

Higher-dimensional spacetimes have also been used as a purely mathematical construct, where the number D of spacetime dimensions is regarded as just one other parameter to be varied. Emparan and collaborators [16–19] have recently investigated this aspect of higher-dimensional spacetimes by focusing on the large-D limit. They showed that the physics of four-dimensional spacetimes can be recovered to good precision from a large-D expansion, and that the large-D limit offers precious physical insight into the nature of classical and quantum gravity in arbitrary dimensions.

1.1.1 TeV gravity scenarios

One of the most prominent open issues in modern physics is the question of the hierarchy problem. This asks the question, why is the characteristic energy scale of the theory of the electroweak interaction, $\mathcal{O}(1)$ TeV, 16 orders of magnitude lower than that of the gravitational interaction, also called the Planck scale, $\mathcal{O}(10^{16})$ TeV. Note we are, from here, setting $c = \hbar = 1$. There are a number of proposed explanations for this problem, including supersymmetry, in which this hierarchy arises naturally; invoking a multiverse, with our universe having the appropriately fine-tuned physical constants; or

requiring the existence of extra spatial dimensions. It is this final explanation that we will focus on, with more thorough reviews of the subject given in [20–22]. In a series of works, Arkani-Hamed, Dimopoulos and Dvali (ADD) [23, 24], along with Antoniadis [25, 26], proposed a theory of "Large Extra Dimensions". In 4 dimensions, the Planck scale, M_{pl}, is given by the value of Newton's constant, according to

$$M_{pl} := G_4^{-1/2} = \mathcal{O}(10^{16}) \text{ TeV,} \tag{1.1}$$

and similarly, in higher dimensions, a D dimensional Planck scale can be defined,

$$M_* := G_D^{-1/(D-2)}. \tag{1.2}$$

This higher dimensional Newton's constant, G_D, arises in the Einstein-Hilbert action for D dimensional general relativity,

$$S_D = \frac{1}{16\pi G_D} \int d^D x \sqrt{-g} \; R, \tag{1.3}$$

where g is the determinant of the spacetime metric, and R is the Ricci scalar. In their paper [23], ADD showed that, for a spacetime with $D - 4$ extra, compact, spatial dimensions with radius ρ, for gravitational experiments on a scale $r \gg \rho$, an effective $4D$ Planck scale would be observed,

$$M_{pl}^2 \sim M_*^{D-2}\rho^{D-4}. \tag{1.4}$$

By setting $M_* = M_{EW}$, the electroweak scale, the apparent hierarchy between these two scales can be explained as the result of our gravitational experiments not probing small enough distances. Since the true Planck scale is now $\mathcal{O}(1)$ TeV, this is sometimes referred to as "TeV gravity". The question of the hierarchy of these two scales is now transformed into a question of the geometry of the extra dimensions and why they have the volume that they do. A second question posed in this scenario is, why experiments involving the standard model have not seen evidence of these extra dimensions. The solution to this problem is given by string theory, in which the standard model can be

confined to live only on a 3+1 dimensional brane, embedded in a higher dimensional bulk spacetime. Examples of string theory models that can give rise to TeV gravity scenarios have been studied in [27–29], with [30] providing a review . A similar solution to the hierarchy problem was proposed by Randall and Sundrum, in [31, 32], involving warped extra dimensions.

If the Planck scale is now $\mathcal{O}(1)$ TeV, then experiments probing energies in excess of this can be expected to reveal new super-Planckian physics, an observational signature of a TeV gravity scenario. The obvious example of such an experiment is the Large Hadron Collider (LHC), which collides protons at energies of up to ~ 13 TeV. It was conjectured soon after the proposals of ADD and others that, in such a TeV gravity scenario, the end state of a collision at trans-Planckian energies would be a black hole [33–35]. From a gravitational perspective the colliding partons would appear to be gravitational point sources, i.e. black holes, or, in the limit of a boost to the speed of light and zero mass, Aichelberg-Sexl shockwaves [36], with such collisions studied in e.g. [37–40]. Then if the impact parameter of the collision was less than some critical impact parameter on the order of the Schwarzschild radius, the two objects would merge into a black hole. It was then expected that such a black hole would decay via Hawking radiation before eventually totally evaporating, though the quantum gravity mechanism by which this would occur is still unknown. Modelling of the observable signals of the process of black hole production and decay has been undertaken in a number of studies with some key results provided by [41–45], on features such as the cross section and decay products of black hole forming processes.

One question of value to the potential observation of black hole formation at the LHC is the amount of gravitational radiation expected to be radiated during the infall and merger of the two incoming objects. As the incoming partons appear to be gravitational point sources, we suggest that, from a gravitational point of view they can be modelled as black holes, the simplest gravitational source available in general relativity. Studies in $4D$ general relativity have also revealed that, in the limit as the boost velocity approaches the speed of light, the behaviour of colliding objects merging into black holes shows universal features and is insensitive to the structure of its constituent parts. This has been shown for spinning and non spinning back holes, as well as the collision of relativistic fluid balls [46–54]. This indicates that the approximation of highly boosted partons as black holes may be justified. We also assume that, for a black hole the mass of a parton, the Schwarzschild radius of the

black hole is sufficiently smaller than the size of the extra dimensions that we can treat the higher dimensional spacetime as asymptotically flat.

Tabletop experiments [55, 56] probing GR at small scales have ruled out extra dimensions with size greater than 44 μm, with the Randall-Sundrum model [31, 32] further constrained by astrophysical tests. These observe the lifespans of black holes present in X-ray binaries and the orbital evolution of the binary, in the strongest case constraining the size of extra dimensions to $\lesssim 3\mu m$ [57–60]. Atomic spectroscopy tests have also put bounds on the size of more than one extra dimension in [61]. At the time of writing, no evidence for black holes has yet been seen at the Large Hadron Collider, with quantum black hole production ruled out below 8.9 TeV by the ATLAS experiment, and below 9 TeV by the CMS experiment and semiclassical black holes ruled out below 9.5 TeV, also by the CMS experiment [62, 63].

1.1.2   The AdS/CFT correspondence

One of the leading motivations in the study of higher dimensional theories of gravity is due to the gauge/gravity correspondence. First proposed by Maldacena [64] and further developed in [65, 66] this correspondence is an example of the holographic principle, where information about a system in D dimensions is encoded into a system defined on its $D-1$ dimensional boundary. In the case of this correspondence, it is shown that there is a duality between a theory of gravity in D dimensional Anti-de-Sitter (AdS) space, that is a spacetime with a negative cosmological constant, and a conformal field theory (CFT) in $D-1$ dimensions defined on its boundary. This gives rise to the name of the AdS/CFT correspondence. This correspondence gives the hope that intractable calculations in strongly coupled CFTs can be translated into simpler calculations from the gravitational side. One application of interest is in modelling of heavy ion collisions, of the sort studied at the Relativistic Heavy Ion Collider or the LHC, in order to learn more about the quark-gluon plasma, by investigating the dual gravitational process in AdS space studied in e.g. [67–73].

1.2   Numerical relativity

The field of numerical relativity is concerned with solving the full non-linear Einstein equations in situations where an analytic approach is not feasible. The most obvious example of a simple problem in general relativity which is in general intractable in the

full non-linear, dynamical, regime analytically is the two body problem, the interaction of two black holes. Unlike in Newtonian physics, the two body problem is not stable in general relativity, and two orbiting black holes cannot remain indefinitely in orbit. They must either scatter to infinity, or, through the emission of gravitational radiation, inspiral and merge into a final remnant black hole. Since the 1960s efforts have been made to detect gravitational wave radiation in our universe, from not only black holes, but from the merger of neutron stars and from cosmological sources imprinted in the Cosmic Microwave Background (CMB) also. In 2015, this search finally proved successful, with ground based interferometry at the Advanced Laser Interferometer Gravitational-Wave Observatory (aLIGO)[74–76] experiment detecting a black hole-black hole merger for the first time [5]. Soon after, the Advanced Virgo [77–79] experiment joined LIGO, with the first coincident detection made in 2017 [80]. At the time of writing 5 black hole-black hole mergers, and one neutron star-neutron star merger have been detected between LIGO and Virgo [81–83, 80, 84]. In order to detect the gravitational wave signal of a black hole merger, the noisy data seen in the detector is compared to a template bank of waveforms calculated through an effective one body formalism [85] that combines analytic calculations with numerical data. To facilitate this, the wave signal can be split into three parts, each of which is analysed using a different method. The first part, the inspiral, is studied in the Post-Newtonian limit, which involves expressing general relativity as the sum of corrections to Newtonian gravity in the parameter v/c, where v is the characteristic speed of the system. A review of this method is given in [86]. The final part, the ringdown, is studied using black hole perturbation theory, where linear perturbations are studied on a fixed black hole background, reviewed in [87, 88]. The merger phase, in between these two, cannot be described in either the small v or linearised approximations however, and so we must use numerical relativity to predict the wave signal here.

The breakthrough in numerical relativity came in 2005, when Pretorius first simulated the merger of a binary black hole system and extracted gravitational waves [89], but the 15 years preceding had contained many advances that paved the way for this result. We will detail in greater depth many of these key developments in Chapter 2.

1.2.1 Black hole collisions

Before the success in simulating binary black hole inspirals, numerical relativity could still be used in axisymmetric scenarios, to study the energy radiated in an equal mass head on black hole collision from rest by Anninos and collaborators [90, 91]. These

studies found that in such collisions approximately $0.001M$, where M is the total ADM mass of the spacetime was radiated away in gravitational waves. Hawking previously used the area law, that the area of the event horizon cannot decrease in such a collision, to provide an upper bound on the energy that could be radiated in an equal mass collision between two non spinning black holes, finding a limit of $(1 - 2^{-1/2})M \approx 0.29M$ on the fraction of the total mass of the system that could be radiated away [92]. Clearly, the numerical results show that this upper bound far exceeds the values for collisions from rest. In the case of ultrarelativistic collisions, Penrose modelled highly boosted black holes as Aichelberg-Sexl shockwaves, and constructed a similar upper bound in unpublished work, also finding an upper limit of 29% on the radiated energy [93], for further detail see [94]. The study of such high energy boosted collisions was further studied by D'Eath and Payne in a series of papers using perturbative techniques [95–98]. Here an estimate for the expected fraction of the total energy radiated in GWs is given to be 16.4%. Subsequent numerical studies of high energy head on collisions [46] were performed, reaching boost velocities for the black holes of up to $0.94c$, which found a value of $14 \pm 3\%$ for the energy radiated in GWs, consistent both with Penrose's upper bound, and D'Eath and Payne's perturbative estimate. The study of high energy collisions continued in numerical relativity, with studies into highly boosted collisions of black holes with non-zero impact parameters finding up to $35 \pm 5\%$ of the total energy radiated in gravitational waves, with the remnant a nearly extremal Kerr black hole [48, 47]. Investigations into the highly boosted collisions of boson stars [50] and fluid balls [51, 52] have also been performed, with it being found that for sufficient boosts these mergers result in black hole formation, in line with Thorne's hoop conjecture [99]. Along with simulations of highly boosted spinning black holes [49], these studies also suggest the existence of universal behaviour at high boosts, that is, at high enough boosts the kinetic energy dominates over any internal structure of the objects being collided, and all these scenarios display the same behaviours independent of their internal structure. This has come to be known as the "matter-does-not-matter" conjecture.

1.2.2   Higher dimensional numerical relativity

Since the breakthrough of Pretorius, numerical relativity has been applied to higher dimensional asymptotically flat spacetimes to reveal a plethora of new results.

Critical spin parameters have been identified above which Myers-Perry BHs become unstable to bar mode perturbations in $D \geq 6$ dimensions and migrate to more slowly

spinning BHs via GW emission [100]. Similar numerical results for $D = 5$ dimensional BHs [101] have not been confirmed in perturbative studies [102] and may be subject to revision in future, more accurate numerical investigations [103]. The celebrated Gregory-Laflamme instability [104] has been shown to lead to the formation of naked singularities in finite asymptotic time in numerical simulations of black strings in $D = 5$ dimensions [105, 106]. Most recently, a similar behaviour has been identified in evolutions of thin black rings demonstrating the first violation of cosmic censorship for a generic type of asymptotically flat initial data [107]; see also [108] for a perturbative study. In addition, Myers-Perry black holes with large spin parameters, in the so called ultraspinning regime have been shown to be unstable, with the endpoint leading to a violation of weak cosmic censorship also [109]. Collisions of black holes and inspirals have been studied in up to 6 spacetime dimensions and their gravitational wave signals investigated [110–113]. It is particularly this class of simulations that we shall attempt to push further in this thesis.

The remainder of this thesis is organised as follows. In Chapter 2, we will present an introduction to numerical relativity, and highlight the key features needed to successfully evolve the Einstein equations on a computer. In Chapter 3 we will present the Einstein equations in a dimensionally reduced form that will permit their evolution in higher dimensions using the *modified Cartoon* formalism, and present the first numerical merger of black holes in $7D$. This was originally published as [114]. In Chapter 4 we will present a new method for extracting gravitational waves from higher dimensional numerical relativity simulations, analogous to the $4D$ Newman-Penrose Ψ_4 method. We demonstrate that it provides consistent results with previously employed methods for wave extraction in higher dimensions. This was originally published as [115]. In Chapter 5 we use the aforementioned wave extraction technique to calculate the energy and momentum radiated in head on collisions of black holes of varying mass ratio, and compare the results to existing data calculated in the point particle limit. We draw links between our results and results previously shown for quasinormal modes of higher dimensional black holes found both numerically and analytically in the large D limit. This was originally published as [116]. In Chapter 6 we describe the implementation of a higher dimensional analogue of Bowen-York initial data in our modified Cartoon based code, which will permit the evolution of boosted, inspiralling and spinning black holes, as well as the ADM integrals in higher dimensions. In Chapter 7 we present an apparent horizon finder for higher dimensional black holes, which will allow us to calculate the mass and spin of our simulated black holes before and after they merge.

We present tests of this horizon finder on a variety of initial data. In Chapter 8 we present a formula for extracting the angular momentum in gravitational waves using the formalism introduced in Chapter 4. We present our conclusions and outlook for future work in Chapter 9.

Chapter 2

Numerical Relativity

2.1 Notation

For reference purposes we define the general notation for coordinate systems and index ranges used in this thesis. In specific circumstances we may define new notation, this will be made clear at the time.

In most situations we will refer to two specific coordinate systems adapted to the spacetime we are studying. The first is a set of Cartesian coordinates

$$X^A = (t, \underbrace{x^1, \ldots, x^{d-1}}_{(d-1)\times}, z, \underbrace{w^{d+1}, \ldots, w^{D-1}}_{(D-d-1)\times}) = (t, x^{\hat{i}}, z, w^a) = (t, x^i, w^a), \qquad (2.1)$$

where middle Latin indices without (with) a caret range from $i = 1, \ldots, d$ ($\hat{i} = 1, \ldots, d-1$) and early Latin indices run from $a = d+1, \ldots, D-1$. Here D is the number of spacetime dimensions, and d will be the number of dimensions on our effective computational grid, a distinction which will become clear in our discussion of the modified Cartoon formalism in Chapter 3. The second is a system of spherical coordinates

$$Y^A = (t, r, \underbrace{\phi^2, \phi^3, \ldots, \phi^{D-1}}_{(D-2)\times}) = (t, r, \phi^\alpha), \qquad (2.2)$$

where Greek indices run from $\alpha = 2, \ldots, D-1$. We use middle, upper case Latin indices to denote all spatial coordinates of either of these systems, so that $X^I = (x^{\hat{i}}, z, w^a)$ and $Y^I = (r, \phi^\alpha)$ with $I = 1, \ldots, D-1$. In contexts where we refer to this spherical coordinate system, rotational symmetry will be assumed in all directions ϕ^a, $a = 4, \ldots, D-1$. In the special case $d = 3$, which will be the value that this

parameter always takes in our simulations, we use the notation $x^{\hat{i}} \equiv (x, y)$, so that Eq. (2.1) becomes

$$X^A = (t, x, y, z, w^4, \ldots, w^{D-1}) \,. \tag{2.3}$$

We orient the Cartesian coordinates (2.1) such that they are related to the spherical coordinates (2.2) by

$$(w^1 \equiv) \quad x^1 = r \cos \phi^2 \,,$$

$$(w^2 \equiv) \quad x^2 = r \sin \phi^2 \, \cos \phi^3 \,,$$

$$\vdots$$

$$(w^{d-1} \equiv) \quad x^{d-1} = r \sin \phi^2 \, \ldots \sin \phi^{d-1} \, \cos \phi^d \,,$$

$$(w^d \equiv) \quad z = r \sin \phi^2 \, \ldots \sin \phi^{d-1} \, \sin \phi^d \, \cos \phi^{d+1} \,,$$

$$w^{d+1} = r \sin \phi^2 \, \ldots \sin \phi^{d-1} \, \sin \phi^d \, \sin \phi^{d+1} \, \cos \phi^{d+2} \,,$$

$$\vdots$$

$$w^{D-3} = r \sin \phi^2 \, \ldots \sin \phi^{D-3} \, \cos \phi^{D-2} \,,$$

$$w^{D-2} = r \sin \phi^2 \, \ldots \sin \phi^{D-3} \, \sin \phi^{D-2} \, \cos \phi^{D-1} \,,$$

$$w^{D-1} = r \sin \phi^2 \, \ldots \sin \phi^{D-3} \, \sin \phi^{D-2} \, \sin \phi^{D-1} \,. \tag{2.4}$$

Here $\phi^{D-1} \in [0, 2\pi]$, and all other $\phi^\alpha \in [0, \pi]$, and we have formally extended the w coordinates to also include (in parentheses in the equation) $w^i = x^i$. Note that for the orientation chosen here, the x axis denotes the reference axis for the first polar angle rather than the z axis which more commonly plays this role for spherical coordinates in three spatial dimensions. Throughout our work, we use the conventions of Misner, Thorne and Wheeler [117] for the metric signature, Christoffel symbols and the Riemann tensor.

For orientation among the different sets of indices, we conclude this section with a glossary listing index variables and their ranges as employed throughout this work.

- Upper case early Latin indices A, B, C, $\ldots$ range over the full spacetime from 0 to $D-1$.

- Upper case middle Latin indices I, J, K, ... denote all spatial indices, inside and outside the effective d dimensional computational domain, running from 1 to $D - 1$.

- Lower case middle Latin indices i, j, k, ... denote indices in the spatial computational domain and run from 1 to d. For $d = 3$, we have $x^i = (x, y, z)$.

- Lower case middle Latin indices with a caret $\hat{i}$, $\hat{j}$, ... run from 1 to $d - 1$ and represent the x^i (without caret) excluding z. In $d = 3$, we write $x^{\hat{i}} = (x, y)$.

- Lower case early Latin indices a, b, c, ... denote spatial indices outside the computational domain, ranging from $d + 1$ to $D - 1$.

- Greek indices α, β, ... denote all angular directions and range from 2 to $D - 1$.

- Greek indices with a caret $\hat{\alpha}, \hat{\beta}$, ... denote the subset of angular coordinates in the computational domain, i.e. range from $2, \ldots, d$. As before, a caret thus indicates a truncation of the index range.

- Upper case early Latin indices with a caret $\hat{A}, \hat{B}, \hat{C} \ldots$ run from 0 to d, including the spatial indices inside the computational domain, and the timelike coordinate.

- Upper case early Latin indices with a bar, $\bar{A}, \bar{B}, \bar{C}, \ldots$ will denote only the t and r components of the spherical coordinate system.

- Put inside parentheses, indices cover the same range but merely denote labels rather than tensor indices.

- An index 0 denotes a contraction with the timelike normal to the foliation, rather than the time component, as detailed in Section 4.3.1.

- ∇_A denotes the covariant derivative in the full D dimensional spacetime, whereas D_I denotes the covariant derivative on a spatial hypersurface and is calculated from the spatial metric γ_{IJ}.

- We denote by R with appropriate indices the Riemann tensor (or Ricci tensor/scalar) of the full D dimensional spacetime, and by $\mathcal{R}$ the spatial Riemann tensor (or Ricci tensor/scalar) calculated from γ_{IJ}.

- The round metric on the sphere will be denoted by $\omega_{\alpha\beta}$. Its covariant derivative is denoted by $\mathcal{D}_\alpha$. Unless otherwise specified this will be the metric of the $D-2$ sphere.

- The line element on the n sphere will be denoted by $\mathrm{d}\Omega_n$.

2.2 The $(D-1)+1$ split

Einstein's theory of special relativity placed space and time on an equal footing, by invoking the idea of a $4D$ spacetime endowed with the Minkowski metric, with inertial frames related by Lorentzian, rather than Galilean transformations. General relativity added gravity into the theory, telling us that spacetime is a 4 dimensional manifold $\mathcal{M}$, endowed with a metric g_{AB} of Lorentzian signature. We will use the convention $(-,+,+,+)$ for this signature. This follows in higher dimensions also, with spacetime now described by a D dimensional manifold, with a metric with Lorentzian signature $(-,+,\cdots,+)$. In order to perform a computer simulation of the Einstein equations however, we must cast them in the form of an initial boundary value problem (IBVP), where initial data is prescribed on a spacelike $D-1$ dimensional hypersurface of the manifold, and then evolved forwards in time. This requires us to separate space and time apart from each other again, which we do by foliating the D dimensional spacetime with $D-1$ dimensional spacelike hypersurfaces. This separation of space and time was first performed in $4D$ by Arnowitt, Deser and Misner (ADM) [118] and reformulated by York [119, 120], and follows similarly in arbitrary D, as can be seen in, for instance [22, 121]. We reproduce this splitting here.

Let $(\mathcal{M}, g_{AB})$ be a D-dimensional spacetime with a Lorentzian metric, and associated covariant derivative ∇_A. Define a scalar function t such that the 1-form $\mathbf{d}t$ is timelike everywhere, which defines spatial hypersurfaces Σ_t on which t is constant. Spatial coordinates x^I cover Σ_t. We call the coordinates (t, x^I) adapted coordinates (to the foliation). We can then define a timelike unit normal vector field to the hypersurfaces,

$$\mathbf{n} := -\frac{\mathbf{d}t}{|\mathbf{d}t|} = -\alpha\mathbf{d}t, \tag{2.5}$$

where $\alpha(t, x^I)$ is the lapse function. By definition this is the 4-velocity of an observer moving normal to the hypersurfaces, so α relates the proper time of such an observer to the coordinate time elapsed,

$$\delta\tau = \alpha\delta t. \tag{2.6}$$

We also define the shift vector β^I which determines how the spatial coordinates x^I change for such a normally moving observer between hypersurfaces Σ_t and $\Sigma_{t+\delta t}$,

$$\beta^I := \left(\frac{\partial}{\partial t}\right)^I - \alpha n^I. \tag{2.7}$$

Thus for an observer starting at coordinates (x^I) on hypersurface Σ_t, moving along n^A from hypersurface Σ_t to $\Sigma_{t+\delta t}$, β^I is the vector that lies in hypersurface $\Sigma_{t+\delta t}$ that points from the location of the observer to the point on $\Sigma_{t+\delta t}$ with coordinates (x^I). In other words, β^I gives the difference between the worldline of a normal observer, and lines of constant coordinates. α and β^I provide D freely specifiable degrees of freedom, which correspond to the D degrees of freedom that we have to choose the coordinates on our spacetime, i.e. the gauge freedom of general relativity. We now define a projection operator,

$$\perp^A_B = \delta^A_B + n^A n_B, \tag{2.8}$$

which projects tensors onto the spatial hypersurface by contracting each component of the tensor with the projection operator. As an example, we project the vector n^A,

$$\perp^A_B n^B = \delta^A_B n^B + n^A n_B n^B = n^A - n^A = 0. \tag{2.9}$$

As expected, since n^A is normal to the hypersurface, its projection is 0. The projection of the spacetime metric g_{AB} is denoted by γ_{AB}, which we note is the same as the projection operator itself,

$$\gamma_{AB} = \perp^C_A \perp^D_B g_{CD} = g_{AB} + n_A n_B = \perp_{AB}. \tag{2.10}$$

We can also calculate projections orthogonal to the hypersurfaces, in the time direction, by contracting any given tensor with the normal vector n^A.

By performing all the possible projections of the spacetime metric, and using Eq. (2.7), we can write it in adapted coordinates as

$$ds^2 = g_{AB}dx^A dx^B = \left(-\alpha^2 + \beta_K\beta^K\right)dt^2 + 2\beta_I dt dx^I + \gamma_{IJ}dx^I dx^J, \qquad (2.11)$$

where purely spatial tensors have their indices raised and lowered by the spatial metric γ_{IJ}. The spatial metric γ_{IJ} has a metric compatible connection Γ^I_{JK}, given by the Christoffel symbols of this metric, from which a covariant derivative D_I can be defined.

We finally define the extrinsic curvature of the spatial hypersurface embedded in the full spacetime, K_{AB},

$$K_{AB} := - \perp^C_A \nabla_C n_B = -\frac{1}{2}\mathcal{L}_{\mathbf{n}}\gamma_{AB}. \qquad (2.12)$$

We note at this point that rewriting the Lie derivative of the induced metric γ_{AB} in terms of the extrinsic curvature will allow us to rewrite the second order in time differential equations we will find for γ_{AB} as a set of twice as many first order in time equations for γ_{AB} and K_{AB}.

Now we can take the Einstein equations and project them fully onto the spatial hypersurface, project them twice along the time direction, and project one index onto the hypersurface and one along the time direction to find the Einstein equations in $(D-1)+1$ split form. First we must perform all the possible projections of the Riemann tensor. Let $\mathcal{R}$ with the appropriate number of indices be the Ricci scalar/tensor or Riemann tensor associated to the spatial metric γ_{AB}, i.e. giving the intrinsic curvature of the spatial hypersurface. The Gauss and Codazzi equations give the fully spatial projection, and the projection of one index in the time direction, and the rest onto the spatial hypersurface, respectively [122],

$$\perp^A_E \perp^F_B \perp^G_C \perp^H_D R^E_{FGH} = \mathcal{R}^A_{BCD} + K^A_C K_{BD} - K^A_D K_{BC}, \qquad (2.13)$$

$$\perp^A_E n^F \perp^G_C \perp^H_D R^E_{FGH} = D_D K^A_C - D_C K^A_D. \qquad (2.14)$$

The final projection of the Riemann tensor is with 2 indices in the time direction and 2 onto the spatial hypersurface,

$$\perp_{AE}\perp_C^G n^F n^H R_{FGH}^E = -\mathcal{L}_{\mathbf{n}} K_{AC} + K_{AB}K_C^B + \frac{1}{\alpha}D_A D_C \alpha. \tag{2.15}$$

Performing appropriate contractions of these equations allows us to also express the D-dimensional Ricci tensor and Ricci scalar in terms of quantities defined on the spatial hypersurface. Let us now introduce the Einstein equations. In general these are given by

$$G_{AB} := R_{AB} - \frac{1}{2}Rg_{AB} + \Lambda g_{AB} = 8\pi G\, T_{AB}, \tag{2.16}$$

though in this thesis we will consider only cases with the cosmological constant $\Lambda = 0$ and the energy momentum tensor $T_{AB} = 0$. For completeness sake we shall retain them in this section. Henceforth, we shall also set the gravitational constant $G = 1$.

We define the projections of the energy-momentum tensor,

$$\rho = T_{AB}n^A n^B, \tag{2.17}$$
$$j_A = -\perp_A^C n^B T_{BC}, \tag{2.18}$$
$$S_{AB} = \perp_A^C \perp_B^D T_{CD}, \tag{2.19}$$
$$S = \gamma^{AB}S_{AB}. \tag{2.20}$$

The variables ρ, j_A and S_{AB} defined in this way represent the energy density, momentum density and spatial stress tensor as measured by an Eulerian observer, i.e. an observer moving with four velocity n^A. Projecting the Einstein equations twice in the timelike direction gives the Hamiltonian constraint,

$$\mathcal{H} := \mathcal{R} + K^2 - K^{IJ}K_{IJ} - 2\Lambda - 16\pi\rho = 0, \tag{2.21}$$

where $K = K_{IJ}\gamma^{IJ}$ is the trace of the extrinsic curvature. Projecting the Einstein equations once onto the timelike direction and once onto the spatial hypersurface gives the momentum constraint,

$$\mathcal{M}_I := D_I K - D_J K^J_{\ I} + 8\pi j_I = 0. \tag{2.22}$$

It can be shown, by projecting the Bianchi identities onto, and orthogonal to, the spacelike hypersurface, that if the constraint equations are initially satisfied, they will remain satisfied throughout the time evolution [122], though we note that numerical errors can still cause constraint violations. Attempts to minimise this effect can be found in [123, 124]. Therefore they will not have to be solved on every time slice to obtain data. Instead we only need to solve them once, on our initial time slice, to obtain initial data for our simulations.

Finally projecting the Einstein equations twice onto the spatial hypersurface gives an expression for $\mathcal{L}_{\mathbf{n}} K_{IJ}$ in terms of quantities defined on the spatial hypersurface. This allows us to write explicit PDEs in time for the induced metric γ_{IJ} and the extrinsic curvature K_{IJ}, using the definition of their Lie derivatives, which can, in principle be solved numerically,

$$
\begin{aligned}
\partial_t \gamma_{IJ} &= \beta^M \partial_M \gamma_{IJ} + \gamma_{MJ}\partial_I \beta^M + \gamma_{IM}\partial_J \beta^M - 2\alpha K_{IJ}, \tag{2.23}\\
\partial_t K_{IJ} &= \beta^M \partial_M K_{IJ} + K_{MJ}\partial_I \beta^M + K_{IM}\partial_J \beta^M - D_I D_J \alpha + \alpha \left(\mathcal{R}_{IJ} + K K_{IJ} - 2K_{IM}K^M_J \right)\\
&\quad + 8\pi\alpha \left(\frac{S-\rho}{D-2}\gamma_{IJ} - S_{IJ} \right) - \frac{2}{D-2}\alpha\Lambda\gamma_{IJ}.
\end{aligned}
$$

$$\tag{2.24}$$

2.3   Well-posedness of the evolution scheme

The ADM-York decomposition was found in the 1960s, yet it took until 2005 until the first simulation of a binary black hole merger was performed [89] . This was not only due to a lack of computational resources, there were many more theoretical steps that needed to be taken to obtain a set of equations that could be evolved on a computer to simulate a black hole inspiral. One of these problems was in finding a well-posed system of equations suitable for evolution on a computer. In the simpler example of linear PDEs, a system of PDEs is well-posed if the solution to the PDE, $u(t, x^i)$, can be bounded by the initial data $f(x^i)$ in the form,

$$||u(t)|| \leq Ke^{\alpha t}||f||, \tag{2.25}$$

where $||.||$ denotes the L_2 norm, and K, α are constants. The generalisation of this definition to non-linear PDEs can be found in [125]. For our purposes we focus on the fact that well-posedness ensures that the solution to a PDE is continuously dependent on the initial data given, clearly a vital feature for numerical evolution of the initial data. A necessary condition for finding a well-posed IBVP is to find a system of equations that are strongly hyperbolic [126, 127], a condition that imposes requirements on the principal part of the differential operator, the highest order derivatives in the equation. A simplified definition states that for a system of equations to be weakly hyperbolic, the principal part must have all of its eigenvalues real, and for strong hyperbolicity the principal part must be diagonalisable, as well as satisfying the conditions for weak hyperbolicity. If either of these conditions is not met it can be shown that the solution to the PDE will grow faster than any bound of the form given in Eq. (2.25). For more detailed reviews of this subject see [125, 128]. It has been shown that as presented above, in Eqs (2.23 - 2.24), the ADM equations in four dimensions have the property of weak, but not strong hyperbolicity for a fixed (densitised) gauge [129], making them unsuitable for numerical relativity. This motivated a search for strongly hyperbolic formulations of the Einstein equations that could be implemented numerically. Since the 1950s it was known that the Einstein equations were strongly hyperbolic when written in the harmonic gauge [130]. This led to the first successful simulation of a binary black hole merger, completed by Pretorius [89], using the Generalised Harmonic Gauge formalism. Key works on the use of this formalism in numerical relativity can be found in [131–133, 123]. In this formalism the generalised harmonic gauge is taken, where the coordinates are the solution to the equation $\Box x^A = H^A$ for arbitrary functions H^A [134, 135], which are then evolved as dynamical variables in the time evolution. This gauge choice allows the Einstein equations to be clearly rewritten such that the principal part of the equation is that of the scalar wave operator. This naturally presents the Einstein equations in strongly hyperbolic form.

An alternate method even more commonly used to put the Einstein equations into strongly hyperbolic form, is by reformulating the equations in a method first developed by Baumgarte and Shapiro [136] and Shibata and Nakamura [137], giving rise to what are known as the BSSN equations. In this formalism the induced metric γ_{IJ} is split into a conformal factor χ and a conformally rescaled metric $\tilde{\gamma}_{IJ}$, and the extrinsic curvature is split into its trace, K and conformally rescaled tracefree part $\tilde{A}_{IJ}$. The final step is to promote the conformally rescaled Christoffel symbols, contracted with the conformal metric, to become dynamical variables evolved in time, denoted by $\tilde{\Gamma}^I = \tilde{\gamma}^{JK}\Gamma^I_{JK}$. We

reproduce the full D dimensional BSSN equations in Section 3.3.1. These will be the equations that we evolve in performing the simulations in this thesis. It has been shown [138] that, with appropriate gauge conditions discussed below, this is a strongly hyperbolic system. It is through using this formalism that much of the key work on black hole simulations has been performed, with the first stable evolutions of black hole inspirals using this method coming shortly after the aforementioned result by Pretorius [139, 140].

Further developments have been made since the implementation of the BSSN scheme, notably the Z4 [141–143] scheme, in which the constraints are evolved as dynamical variables, satisfying evolution equations that damp constraint violations, and the CCZ4 scheme [144–147], a conformal decomposition of the Z4 scheme in the manner of the BSSN scheme.

2.4   Initial data

In order to initialise the induced metric γ_{IJ} and the extrinsic curvature K_{IJ}, we must solve the constraint equations, Eqs (2.21 - 2.22), on the initial timeslice. Here we recap how this is done for $4D$ spacetimes for initially stationary black holes, and black holes with initial momentum and spin. We also recap the construction of initially stationary black holes in higher dimensions. Later, in Chapter 6, we will introduce new data for higher dimensional black holes with non-zero momentum and angular momentum. For a full review of initial data in numerical relativity, see [148].

We begin with 12 components of the metric and extrinsic curvature to specify, 4 of which will be determined by the constraint equations. To identify which components we should solve for and which we should specify, we employ the York-Lichnerowicz [149–153] conformal decomposition. First we decompose the metric into a conformal factor and a conformal metric, and split the extrinsic curvature into trace and trace free parts. We will assume here that we are in vacuum, and thus $T_{AB} = 0$.

$$\gamma_{ij} = \psi^4 \bar{\gamma}_{ij}, \tag{2.26}$$

$$A^{ij} = K^{ij} - \frac{1}{3}\gamma^{ij}K. \tag{2.27}$$

The Hamiltonian and momentum constraints are now given by

$$8\bar{D}^i\bar{D}_i\psi - \bar{R}\psi + \psi^5(A_{ij}A^{ij} - \frac{2}{3}K^2) = 0, \qquad (2.28)$$

$$D_j A^{ij} - \frac{2}{3}D^i K = 0, \qquad (2.29)$$

where $\bar{D}$ and $\bar{R}$ are the covariant derivative and Ricci scalar respectively for the conformal metric $\bar{\gamma}_{ij}$.

For time symmetric initial data, such as initial data for any number of initially static Schwarzschild black holes, the extrinsic curvature is initially zero. In this case the momentum constraint is automatically satisfied, and the Hamiltonian constraint reduces to

$$8\bar{D}^i\bar{D}_i\psi - \bar{R}\psi = 0. \qquad (2.30)$$

Further, we can choose the conformal metric to be flat, reducing the Hamiltonian constraint to the flat space Laplace equation,

$$\delta_{ij}\partial^i\partial^j\psi = 0. \qquad (2.31)$$

We now must solve for ψ. The trivial solution $\psi = \text{const}$ gives Minkowski space, but $\psi = 1 + \frac{M}{2r}$ gives a metric of the form,

$$\gamma_{ij}dx^i dx^j = \left(1 + \frac{M}{2r}\right)^4 (dr^2 + r^2 d\Omega^2). \qquad (2.32)$$

This is the spatial part of the metric for a Schwarzschild black hole in isotropic coordinates, and so this represents a static black hole. We note that, in isotropic coordinates, the event horizon is located at $r = M/2$, and that the metric can be put back into more familiar Schwarzschild coordinates with the coordinate transformation $\tilde{r} = r(1 + M/(2r))^2$, where $\tilde{r}$ is the Schwarzschild radial coordinate. This coordinate change makes it clear that, at $r = 0$ we are in fact at $\tilde{r} = \infty$, and not at the black hole singularity. In fact $r < M/2$ corresponds to the other side of the Einstein-Rosen bridge, with the other asymptotically flat end of the Schwarzschild metric compactified into this region, and $r = M/2$ corresponding to the throat of the wormhole. Since nothing

can escape from the horizon, the region $r < M/2$ cannot communicate with the region $r > M/2$. As the point $r = 0$ is a singular point corresponding to the compactification of the other flat end, our spacetime is really a manifold with the point $r = 0$ taken out of it. Consequently, this point is often referred to as the black hole "puncture". As the Laplace equation is linear, we are able to superpose solutions for the conformal factor ψ to construct initial data for multiple black holes. This is known as "Brill-Lindquist data" [154] and is given by

$$\psi = 1 + \sum_{i=1}^{N} \frac{M_{(i)}}{2r_{(i)}}, \tag{2.33}$$

where $M_{(i)}, r_{(i)}$ are the bare masses and radial distances from the initial positions respectively of the N Schwarzschild black holes.

For black holes with initial momentum or angular momentum, the initial data is no longer time symmetric, so the extrinsic curvature cannot be set to zero. We return to Eqs (2.28, 2.29). We now assume again that the metric is conformally flat, and now assume that the extrinsic curvature is trace free. This reduces the constraint equations to

$$8\delta_{ij}\partial^i\partial^j\psi + \psi^5 A_{ij}A^{ij} = 0, \tag{2.34}$$
$$D_j A^{ij} = 0. \tag{2.35}$$

Bowen and York [155, 152] showed that an analytic solution for the momentum constraints could be found,

$$A_{ij} = \frac{3}{2\psi^2 r^2}(n_i P_j + n_j P_i + n_k P^k(n_i n_j - \delta_{ij})) - \frac{3}{\psi^2 r^3}(\epsilon_{ilk}n_j + \epsilon_{jlk}n_i)n^l S^k, \quad (2.36)$$

which we call Bowen-York initial data, where n^i is the outwards pointing unit radial vector. It can be shown using the definitions of linear and angular momentum at spatial infinity given below in Section 2.6.4 that P^i and S^i are the linear and angular momentum of the black hole. By the linearity of Eq. (2.35) we note that for multiple black hole solutions, we can superpose multiple copies of the extrinsic curvature given in Eq. (2.36). Finally, we must solve the Hamiltonian constraint for ψ. Since the

extrinsic curvature is non zero, Eq. (2.34) is now very difficult to solve, so we look to solve it numerically. To do this we assume that the conformal factor takes the form

$$\psi = 1 + \sum_{i=1}^{N} \frac{M_{(i)}}{2r_{(i)}} + u, \tag{2.37}$$

i.e. the Brill-Lindquist form with a correction u. We then numerically solve Eq. (2.34) for u. Within the code employed in this thesis, the elliptic PDE solver for u is provided by the TwoPunctures thorn [156, 157].

When generalising to higher dimensional spacetimes, the construction of initially static black holes proceeds in direct analogy to the Brill-Lindquist procedure in $4D$ [158]. We now perform the conformal decomposition for arbitrary D.

$$\gamma_{IJ} = \psi^{\frac{4}{D-3}} \bar{\gamma}_{IJ}, \qquad K_{IJ} = \psi^{-2} \bar{A}_{IJ} + \frac{1}{D-1} \gamma_{IJ} K. \tag{2.38}$$

As we are only searching for static black hole initial data, we can see that the momentum constraints are again trivially satisfied, so we focus on the Hamiltonian constraint, which becomes

$$\delta_{IJ} \partial^I \partial^J \psi + \frac{D-3}{4(D-2)} \psi^{-(3D-5)/(D-3)} \bar{A}^{IJ} \bar{A}_{IJ} = 0, \tag{2.39}$$

which, for extrinsic curvature equal to 0, becomes the flat space Laplace equation again, but in $D-1$ dimensions

$$\delta_{IJ} \partial^I \partial^J \psi = 0. \tag{2.40}$$

This is now solved by

$$\psi = 1 + \frac{\mu_{(i)}}{4r_{(i)}^{D-3}}, \tag{2.41}$$

where μ is the mass parameter of the black hole. This is related to the ADM mass M of the spacetime, and the horizon radius R_h, by

$$\mu = \frac{16\pi M}{(D-2)\mathcal{A}_{D-2}}, \qquad \mu = R_{\mathrm{h}}^{D-3}, \qquad \mathcal{A}_{D-2} = \frac{2\pi^{(D-1)/2}}{\Gamma\left(\frac{D-1}{2}\right)}. \qquad (2.42)$$

Comparison with the Schwarzschild-Tangherlini metric [159], [1] in isotropic coordinates, reveals that again, we have constructed the metric corresponding to two asymptotically flat ends connected by an Einstein-Rosen bridge [160]. We will discuss the Schwarzschild-Tangherlini solution in isotropic coordinates further in Section 7.3.1. Again, we can superpose data of this form for multiple black holes, so that the higher dimensional generalisation of Brill-Lindquist initial data for N black holes is given by

$$K_{IJ} = 0, \quad \gamma_{IJ} = \psi^{4/(D-3)}\delta_{IJ}, \quad \psi = 1 + \sum_{(i)=1}^{N} \frac{\mu_{(i)}}{4\left[\sum_{K=1}^{D-1}(X^K - X_{(i)}^K)^2\right]^{(D-3)/2}}. \quad (2.43)$$

2.5 Gauge conditions

While the gauge functions α, β^I can be freely specified, due to the diffeomorphism invariance of general relativity, in reality only a limited class of choices for these functions will lead to a stable numerical evolution. One key problem that has to be avoided through gauge choice is the appearance of a singularity on the grid. While singularities are a common occurrence when studying black holes, both coordinate and physical, a singularity in a numerical simulation will lead to non-assigned numbers which will cause the simulation to crash [161]. This can be avoided by choosing a lapse function that becomes smaller closer to a singularity, so that coordinate time passes more slowly the closer one approaches the singularity [162]. Such singularity avoiding lapses were extensively studied by Bona and Masso [163, 164]. On its own, such a singularity avoiding lapse can cause the phenomenon of *grid stretching*, as time passes slowly close to the singularity but more rapidly elsewhere on the hypersurface, leading to distorted hypersurfaces with large gradients. This can be counterbalanced with an appropriately chosen shift vector [165]. The most popular gauge conditions employed alongside the BSSN equations and puncture data are the "1+log" slicing and "Γ-driver" conditions:

---

[1]This is the higher dimensional counterpart to the Schwarzschild metric.

$$\partial_t \alpha = \beta^M \partial_M \alpha - c_1 \alpha K, \tag{2.44}$$

$$\partial_t \beta^I = \beta^M \partial_M \beta^I + \frac{3}{4} B^I, \tag{2.45}$$

$$\partial_t B^I = \beta^M \partial_M B^I + \partial_t \tilde{\Gamma}^I - \eta B^I. \tag{2.46}$$

Here η and c_1 are free parameters which we determine empirically for each simulation [2], and $\tilde{\Gamma}^I$ is the BSSN variable formed from the Christoffel symbol of the conformally rescaled metric. We will fully introduce this variable in Eq. (3.11). Often the conditions for the shift vector, Eqs (2.45 - 2.46) are replaced with a first order in time set of equations [166],

$$\partial_t \beta^I = \beta^M \partial_M \beta^I + \frac{3}{4} \tilde{\Gamma}^I - \eta \beta^I. \tag{2.47}$$

Altogether this choice of gauge, along with the use of puncture data, is known as the moving puncture approach [165, 140, 139, 166]. While they were developed for $4D$ spacetimes, these conditions extend in the obvious fashion to higher dimensional spacetimes and continue to perform successfully in most cases. In Section 5.2.2 we will discuss adjustments made to the equation for the lapse in order to achieve stable simulations in higher dimensions for collisions of black holes of unequal masses.

2.6   Diagnostic tools

The above sections in this chapter provide the machinery to successfully evolve black holes in a higher dimensional spacetime. In order to discover new physical results from these simulations however, we need to develop diagnostic tools to extract meaningful physical quantities from the simulated spacetime. A large section of this thesis will focus on the construction of a method to extract information about gravitational waves from such a simulated spacetime in higher dimensions, so here we recap the state of the art of wave extraction in 4 dimensions, and in higher dimensions prior to the work discussed in this thesis.

---

[2]We note that in the search for stable numerical evolutions, sometimes these free parameters are replaced with functions of the coordinates on the spatial slice

There are a number of methods that have been developed to extract gravitational waves from numerical relativity simulations in $4D$, from using the quadrupole formula, to calculating the Landau-Lifshitz pseudotensor [167, 168], to Cauchy characteristic extraction (CCE), where a second characteristic evolution takes data found by solving the Cauchy problem in a finite domain and propagates it to $\mathscr{I}^+$ [169–171]. For a full review of the history of various wave extraction techniques, see [172]. The 2 most popular methods are using gauge invariant perturbations, developed by Regge, Wheeler [173], Zerilli [174] and Moncrief [175] (RWZM), and calculating the Newman-Penrose scalar Ψ_4 [176–178]. Several comparisons of the accuracy of these techniques have been made, which are listed in [172], one of which compares these 2 methods with CCE in the context of stellar core collapse [179]. This study found that, despite calculating gravitational waves at a finite time and radius rather than at $\mathscr{I}^+$, Ψ_4 and the RWZM method both find results within 10% of the values found by CCE. Given the comparative ease of implementing these techniques over CCE, these two methods have become by far the most widely used. It was also noted in this study that the RWZM formalism was more vulnerable to the effects of spurious high frequency noise which distorted the calculated wave signals, as compared to Ψ_4.

2.6.1   Wave extraction using Ψ_4

Let us recap the Ψ_4 wave extraction formalism. In their seminal work [176], Newman and Penrose (NP) recast the Einstein equations into a spin coefficient formalism. In this formalism a null (complex) tetrad is defined at each point in spacetime, such that, projected onto this tetrad the metric is flat. Within this formalism we shall focus on the treatment of the Weyl tensor, C_{ABCD} since this is the object in general relativity that encodes information about the vacuum curvature of the spacetime, including gravitational waves. In the NP formalism the Weyl tensor is projected onto the tetrad in all possible ways, which leads to the 10 degrees of freedom in the Weyl tensor being encoded in 5 complex scalar functions denoted $\Psi_0, \ldots, \Psi_4$, which we will call Weyl scalars. It was shown that these Weyl scalars obey a peeling property, i.e. that they obey the asymptotic behaviour,

$$\Psi_i \sim \frac{1}{r^{5-i}}. \tag{2.48}$$

Therefore, if we are interested in outgoing gravitational waves, calculated at a large radius, Ψ_4 will be the scalar containing this information at leading order [180–183]. Let us now explicitly define the tetrad and Ψ_4. There is no unique choice of tetrad in the Newman-Penrose formalism, however the most commonly used in numerical relativity is the Kinnersley tetrad [184]. This is chosen due to its appearance in the Teukolsky formalism of black hole perturbation theory [185], allowing connections to be easily made between quantities calculated in numerics and in this formalism. In this tetrad Ψ_1, Ψ_3 can be set to 0, with Ψ_0 containing at leading order the ingoing gravitational radiation, Ψ_4 the outgoing gravitational radiation, and Ψ_2 the Coulomb part of the gravitational field. The search for the appropriate construction of this tetrad in numerical relativity simulations is an ongoing and deep field of research, with key issues reviewed in [186], however a common choice of tetrad is one that approaches the Kinnersley tetrad as the spacetime approaches a Petrov type D spacetime (for our purposes, this will mean as the spacetime approaches either a Schwarzschild or Kerr spacetime). Such a tetrad (known as quasi-Kinnersley [187–191]) can be constructed from the normal vector, n^A, to the hypersurface, and the radial and angular unit vectors of the coordinates on the hypersurface, $(\hat{r}^A, \hat{\theta}^A, \hat{\phi}^A)$. The tetrad consists of 4 vectors $(\ell^A, k^A, m^A, \bar{m}^A)$ where m is complex.

$$\ell^A = n^A + \hat{r}^A, \tag{2.49}$$

$$k^A = n^A - \hat{r}^A, \tag{2.50}$$

$$m^A = \hat{\theta}^A + i\hat{\phi}^A, \tag{2.51}$$

$$\bar{m}^A = \hat{\theta}^A - i\hat{\phi}^A. \tag{2.52}$$

Ψ_4 is then the projection given by

$$\Psi_4 = C_{ABCD}k^A\bar{m}^B k^C\bar{m}^D. \tag{2.53}$$

As we will use this formalism for extracting waves in vacuum, we can at this point replace the Weyl tensor with the Riemann tensor since, in vacuum, the Ricci scalar and tensor are 0. We note here that, in $4D$, a decomposition of the Weyl tensor is available, into its so called electric and magnetic parts [135],

$$E_{AB} = \perp_A^C \perp_B^E C_{CDEF} n^D n^F, \tag{2.54}$$

$$B_{AB} = \perp_A^C \perp_B^E \star C_{CDEF} n^D n^F, \tag{2.55}$$

where $\star$ denotes the Hodge dual. In practice it is through this decomposition that the calculation proceeds in $4D$, though since we do not use it in higher dimensions we shall not comment further on it. For the use of this method in implementing this wave extraction formalism in $4D$ see Appendix C of [192]. Whether using this decomposition or the full Riemann tensor, we know from the Gauss and Codazzi relations that we can rewrite everything in Eq. (2.53) in terms of quantities defined on the spatial hypersurface, and thus it can be calculated in our simulation. The final step is to relate this object to gravitational waves. Explicitly performing the contraction in Eq. (2.53), and replacing the Weyl tensor with the Riemann tensor we can write Ψ_4 as [193]

$$\begin{aligned} \Psi_4 \quad &= -\tfrac{1}{4}(R_{t\theta t\theta} - 2iR_{t\theta t\phi} - 2R_{t\theta r\theta} + 2iR_{t\phi r\theta} - R_{t\phi t\phi} \\ &\quad + R_{r\theta r\theta} + 2iR_{t\theta r\phi} + 2R_{t\phi r\phi} - 2iR_{r\phi r\theta} - R_{r\phi r\phi}). \end{aligned} \tag{2.56}$$

We then compare this to the linearised Einstein equations, writing the metric as $g_{AB} = \eta_{AB} + h_{AB}$, with $|h_{AB}| \ll 1$, to find a wave equation for the gravitational wave, and find that the Riemann tensor takes the form

$$R_{ABCD} = \frac{1}{2}(\partial_A \partial_D h_{BC} + \partial_B \partial_C h_{AD} - \partial_B \partial_D h_{AC} - \partial_A \partial_C h_{BD}). \tag{2.57}$$

Since we know in the transverse traceless gauge the metric of a radially propagating wave takes the form

$$h_{\theta\theta} = -h_{\phi\phi} = h_+, \tag{2.58}$$

$$h_{\theta\phi} = h_{\phi\theta} = h_\times, \tag{2.59}$$

we can substitute Eq. (2.57) into Eq. (2.56), noting that the only non zero components will be those for which the angular indices appear in the metric, and not in the derivatives. For an outgoing wave at large r we have that

$$h_{AB}(t, r, \theta, \phi) = \frac{h_{AB}(t - r, \theta, \phi)}{r}, \tag{2.60}$$

and so we can replace ∂_r with $-\partial_t$. Eventually we obtain

$$\Psi_4 = \ddot{h}_+ - i\ddot{h}_\times. \tag{2.61}$$

Now we have the information required to calculate gravitational wave strains, and thus the energy, momentum and angular momentum radiated in gravitational waves. Explicit calculations of these quantities can be found in [194].

2.6.2   Wave extraction using gauge invariant perturbations

We now give a brief overview of the RWZM formalism, saving a more thorough discussion for the introduction of its higher dimensional analogue which will follow. For further details see [172, 195, 196, 121]. The RWZM formalism is based on the decomposition of perturbations around a background metric into multipoles over a family of tensor harmonics. These metric perturbations will, however, be gauge dependent quantities, so the key step in this method is to find combinations of the different metric perturbations that provide what is called a gauge invariant *master function*.

First, we write the spacetime metric as a background metric, $g^{(0)}$ (say Schwarzschild) with some perturbation on top, h,

$$g_{AB} = g^{(0)}_{AB} + h_{AB}. \tag{2.62}$$

We now expand h_{AB} into its multipolar contributions for even parity perturbations,

$$
\begin{aligned}
h^{lm,\ \text{even}}_{\bar{A}\bar{B}} &= H^{lm}_{\bar{A}\bar{B}} Y^{lm}, & (2.63)\\
h^{lm,\ \text{even}}_{\bar{A}\beta} &= H^{lm}_{\bar{A}} Y^{lm}_\beta, & (2.64)\\
h^{lm,\ \text{even}}_{\alpha\beta} &= r^2(K^{lm}\omega_{\alpha\beta}Y^{lm} + G^{lm}Z^{lm}_{\alpha\beta}), & (2.65)
\end{aligned}
$$

and odd parity perturbations,

$$
\begin{aligned}
h^{lm,\ \text{odd}}_{\bar{A}\bar{B}} &= 0 & (2.66)\\
h^{lm,\ \text{even}}_{\bar{A}\beta} &= h^{lm}_{\bar{A}} X^{lm}_\beta, & (2.67)\\
h^{lm,\ \text{even}}_{\alpha\beta} &= r^2(h^{lm}X^{lm}_{\alpha\beta}). & (2.68)
\end{aligned}
$$

Here Y^{lm} are the standard spherical harmonics, with the other basis functions defined by

$$Y_\alpha^{lm} = \mathcal{D}_\alpha Y^{lm}, \tag{2.69}$$

$$Z_{\alpha\beta}^{lm} = \mathcal{D}_\alpha \mathcal{D}_\beta Y^{lm} + \frac{1}{2}l(l+1)\omega_{\alpha\beta}Y^{lm}, \tag{2.70}$$

$$X_\alpha^{lm} = -\epsilon_\alpha^\beta \mathcal{D}_\beta Y^{lm}, \tag{2.71}$$

$$X_{\alpha\beta}^{lm} = \mathcal{D}_{(a} X_{\beta)}^{lm}, \tag{2.72}$$

where $\epsilon_{\alpha\beta}$ is the antisymmetric tensor on the 2 sphere. By defining an appropriate inner product for the basis functions Y, X, Z, and using the orthogonality relations it gives, we can extract any of the perturbation functions of (t, r) from our simulation $(H_{\bar{A}\bar{B}}, H_{\bar{A}}, K, G, h_{\bar{A}}, h)$ by taking the metric g_{AB}, subtracting off the background metric, and taking the inner product with the appropriate basis function. For perturbations of odd parity Regge and Wheeler [173] derived a wave equation describing the propagation of gravitational waves in the associated perturbations, while Zerilli [197, 174] did the same for even parity. Moncrief then found gauge invariant combinations of these perturbations to construct a gauge invariant master function [175], from which information about gravitational waves could be extracted.

2.6.3 Kodama-Ishibashi formalism

The perturbative formalism of RWZM has already been generalised to higher dimensions by Kodama and Ishibashi (KI) [198–200]. This has been implemented to extract gravitational waves previously by Witek et al. [110]. In our work we will also implement this form of wave extraction as a check of our formalism developed in Chapter 4, and we will show how these formalisms complement each other in Chapter 5. We note however that so far this wave extraction formalism has only been implemented for axisymmetric spacetimes, meaning that the only non zero projections of the metric perturbations will be those projected onto scalar harmonics (functions that solve the higher dimensional scalar Laplace equation), and not vector or tensor harmonics. Explicitly, these scalar harmonics, $\mathbb{S}$, are solutions of

$$\omega^{\alpha\beta}\mathcal{D}_\beta \mathcal{D}_\alpha \mathbb{S}^l(\phi^\gamma) = -k^2 \mathbb{S}^l(\phi^\gamma), \tag{2.73}$$

where we recall that $\omega_{\alpha\beta}$ is the metric on the $D-2$ sphere, and $\mathcal{D}_\alpha$ is the associated covariant derivative. From these functions we can construct a vector and $(0,2)$ tensor,

$$\mathbb{S}^l_\alpha = -\frac{1}{k}\partial_\alpha \mathbb{S}^l, \tag{2.74}$$

$$\mathbb{S}^l_{\alpha\beta} = \frac{1}{k^2}\mathcal{D}_\beta \mathcal{D}_\alpha \mathbb{S}^l + \frac{1}{D-2}\omega_{\alpha\beta}\mathbb{S}^l, \tag{2.75}$$

where $k^2 = l(l+D-3)$. We note that due to the assumption of axisymmetry the spherical harmonics are only dependent on 1 angular parameter, l, rather than $D-2$ in the generic case. The solutions to Eq. (2.73) are explicitly given by the Gegenbauer polynomials [201, 202]. We assume that the background metric is that of the Tangherlini black hole, and, as in the $4D$ case, we decompose the metric perturbations onto these spherical harmonics. The number of angular indices in the perturbation determines which harmonic we project onto, with the projections given by

$$h_{\bar{A}\bar{B}} = f_{\bar{A}\bar{B},l}\mathbb{S}^l, \tag{2.76}$$

$$h_{\bar{A}\beta} = r f_{\bar{A},l}\mathbb{S}^l_\beta, \tag{2.77}$$

$$h_{\alpha\beta} = 2r^2(H_{L,l}\omega_{\alpha\beta}\mathbb{S}^l + H_{T,l}\mathbb{S}^l_{\alpha\beta}), \tag{2.78}$$

with summation over the angular l indices implicit. If we were to generalise to non-axisymmetry, we would also have vector harmonic $\mathbb{V}^\alpha$ and tensor harmonic $\mathbb{T}_{\alpha\beta}$ copies of Eqs (2.77)-(2.78), given by the solutions to the equations

$$\omega^{\alpha\beta}\mathcal{D}_\beta \mathcal{D}_\alpha \mathbb{V}^{\delta,l_\rho}(\phi^\gamma) = -k^2 \mathbb{V}^{\delta,l_\rho}(\phi^\gamma), \tag{2.79}$$

$$\omega^{\alpha\beta}\mathcal{D}_\beta \mathcal{D}_\alpha \mathbb{T}^{l_\rho}_{\delta\sigma}(\phi^\gamma) = -k^2 \mathbb{T}^{l_\rho}_{\delta\sigma}(\phi^\gamma). \tag{2.80}$$

We note there is a subscript on the angular parameter l in the above equations, as there are generically $D-2$ parameters here in the absence of symmetry.

Returning to the axisymmetric case, we have 4 gauge dependent perturbation functions of (t,r), $\{f_{\bar{A}\bar{B},l}, f_{\bar{A},l}, H_{T,l}, H_{L,l}\}$. As in $4D$, gauge invariant combinations of

these can be found [199],

$$
F_l = H_{L,l} + \frac{1}{D-2}H_{T,l} + \frac{1}{r}X_{\bar{A},l}\nabla^{\bar{A}}r, \tag{2.81}
$$

$$
F_{\bar{A}\bar{B},l} = f_{\bar{A}\bar{B},l} + \nabla_{\bar{B}}X_{\bar{A},l} + \nabla_{\bar{A}}X_{\bar{B},l}, \tag{2.82}
$$

$$
X_{\bar{A},l} = \frac{r}{k}(f_{\bar{A},l} + \frac{r}{k}\nabla_{\bar{A}}H_{T,l}), \tag{2.83}
$$

from which we can define a master function,

$$
\partial_t\Phi_l = (D-2)r^{(D-4)/2}\frac{F_{t,l}^r + 2r\partial_t F_l}{k^2 - D + 2 + \frac{(D-2)(D-1)r_S^{D-3}}{2r^{D-3}}}. \tag{2.84}
$$

It has been shown [201] that, using the time derivative of this master function, we can calculate the energy and momentum radiated in gravitational waves,

$$
\frac{dE_l}{dt} = \frac{1}{32\pi}\frac{D-3}{D-2}k^2(k^2 - D + 2)(\Phi_{,t}^l)^2. \tag{2.85}
$$

As in the $4D$ case, by exploiting the orthogonality conditions of the functions solving Eq. (2.73), we can take the inner product of our numerically evolved metric with these scalar spherical harmonics to extract $f_{\bar{A}\bar{B},l}, f_{\bar{A},l}, H_{T,l}, H_{L,l}$ and so construct Φ. Further details can be found in [111, 201] as well as the papers referenced above. Our implementation of this method in our code closely follows that detailed in the appendices of [110].

2.6.4 ADM integrals

As well as using gravitational wave extraction to determine the change in the Bondi mass and momentum of the spacetime, we also wish to calculate integrals over the whole spatial slice to find the conserved ADM quantities [118]. Between these values, the radiated quantities in gravitational waves, and the values of the mass and spin of the black hole calculated from an apparent horizon finder we can independently account for the entire contents of a black hole spacetime. In this section we will introduce the quantities used in $4D$ numerical relativity.

To define the ADM quantities we will first restrict ourselves to asymptotically flat slices, defined as slices Σ_t with 3 metric γ_{ij}, that admit a Riemannian 3 metric f_{ij} such that [203]

1. f_{ij} is flat outside of a compact domain of Σ_t

2. There exists a coordinate system (x, y, z) in which $f_{ij} = \text{diag}(1, 1, 1)$ and $r = \sqrt{x^2 + y^2 + z^2}$ can take arbitrarily large values

3. In the limit $r \to \infty$,

$$\gamma_{ij} = f_{ij} + \mathcal{O}(r^{-1}), \tag{2.86}$$

$$\frac{\partial \gamma_{ij}}{\partial x^k} = \mathcal{O}(r^{-2}), \tag{2.87}$$

$$K_{ij} = \mathcal{O}(r^{-2}), \tag{2.88}$$

$$\frac{\partial K_{ij}}{\partial x^k} = \mathcal{O}(r^{-3}). \tag{2.89}$$

With these assumptions made, we can write the Hamiltonian of GR as

$$16\pi H = -\int_{\Sigma_t} (\alpha \mathcal{H} - 2\beta^i \mathcal{M}_i)\sqrt{\gamma}d^3x - 2\int_{S^2}(\alpha(k - k_0) - \beta_i(K^{ij} - K\gamma^{ij})n_j)d\Omega, \tag{2.90}$$

[122, 204]. Here k is the trace of the extrinsic curvature of the boundary S^2 embedded in the spatial slice Σ_t with induced metric γ_{ij}, and k_0 is the extrinsic curvature of the S^2 embedded in Σ_t with the flat metric f_{ij}. $\mathcal{H}$ and $\mathcal{M}_i$ are the Hamiltonian and momentum constraints defined in Eqs (2.21, 2.22). For solutions of the Einstein equations, this first integral is equal to zero, and it is the second integral that provides us with the conserved quantities that we call the ADM mass and momentum. In coordinates corresponding to an observer moving forwards in coordinate time, we can set $\alpha = 1$, $\beta_i = 0$, and in coordinates corresponding to an observer undergoing a spatial translation we can set $\alpha = 0, \beta_i = 1$ for a fixed i corresponding to each of the three spatial translations. This identifies the first quantity in parentheses with the ADM mass, and the second quantity with the momentum.

This leads to the definition of the ADM mass of a 3D spatial hypersurface as

$$M_{ADM} = \frac{1}{16\pi} \lim_{r \to \infty} \int_{S^2} (\delta^{ik}\partial_k h_{ij} - \partial_j h) \, d\Omega^j, \tag{2.91}$$

where h_{ij} is the perturbation of the metric on top of a flat Minkowski background, and $h = \delta^{ij}h_{ij}$. Similarly the ADM momentum is defined as

$$P_i = \frac{1}{8\pi} \lim_{r \to \infty} \int_{S^2} (K_{ij} - \delta_{ij} K) \, d\Omega^j. \tag{2.92}$$

In coordinates where the decay conditions of Eqs (2.86 - 2.89) are not met this calculation does not provide meaningful information. For instance, in Painlevé-Gullstrand coordinates, the Schwarzschild line element is

$$ds^2 = -\left(1 - \frac{2M}{r}\right) dt^2 + 2\sqrt{\frac{2M}{r}} dt dr + dr^2 + r^2 d\Omega^2. \tag{2.93}$$

Due to the factor of $r^{-1/2}$ in the shift vector, the extrinsic curvature does not obey the decay rate of Eq. (2.88), instead having the asymptotic behaviour

$$K_{ij} = \mathcal{O}(r^{-3/2}). \tag{2.94}$$

Equations (2.88, 2.89) are not satisfied, and the calculation of the ADM mass gives zero instead of M [193].

In four dimensions there is however, no well defined expression for an "ADM-like" concept of angular momentum. The ADM mass and momentum, which are defined at spatial infinity are preserved by the transformation of the symmetry group of the above decay conditions, Eqs (2.86 - 2.89). This group consists of Lorentz transformations and angle-dependent supertranslations. The natural definition of a conserved angular momentum from the Hamiltonian is

$$J^i = \frac{\epsilon_{ijk}}{8\pi} \lim_{r \to \infty} \int_{S^2} x^j (K^{kl} - \delta^{kl} K) \, d\Omega_l, \tag{2.95}$$

but firstly the decay conditions above do not guarantee that this integral is finite, and secondly, this vector does not transform covariantly under supertranslations. A commonly used remedy was proposed by York [119], who suggested restrictions on the gauges that could be chosen, within which the angular momentum vector did transform appropriately. These gauge choices were the quasi-isotropic gauge condition and asymptotic maximal gauge condition, respectively,

$$\frac{\partial \tilde{\gamma}_{ij}}{\partial x^j} = \mathcal{O}(r^{-3}), \tag{2.96}$$

$$K = \mathcal{O}(r^{-3}), \tag{2.97}$$

where $\tilde{\gamma}_{ij}$ is the conformally rescaled 3-metric, such that its determinant is one. We note also the work of Ashtekar in further elaborating on this supertranslation ambiguity in the context of the 3+1 splitting, describing the necessary conditions to remove the ambiguity in terms of conditions on the magnetic part of the Weyl tensor [205–207]. Finally we note that the gauge conditions used in the moving puncture approach in our simulations does satisfy the conditions in Eqs (2.96)-(2.97).

2.7 Dimensional reduction by isometry

So far the generalisation from $4D$ numerical relativity to higher dimensions of the evolution equations, gauge conditions and initial data construction has proceeded in a straightforward manner. The largest roadblock to successful evolution of a higher dimensional spacetime on a computer however is one of resources, often called the *curse of dimensionality*. Take a 3 dimensional grid of the type calculated at each time step in the code, with $\mathcal{O}(100)$ points across each of the 3 dimensions. If one were to naïvely generalise this code, the computational resources required would increase by a factor of 100 for each added dimension. If we wish to probe values of D much larger than 4, we cannot afford for the problem to scale like this. We therefore require a method of dimensional reduction, to allow us to simulate an effective grid of lower dimension than the $D-1$ dimensional surface we use in our physical problem [3]. In the following chapter of this thesis, (Chapter 3) we discuss at length the "modified Cartoon" method of dimensional reduction which we employ in all of the simulations performed in this thesis, and describe its implementation in our code. Here we give a brief overview of an alternate method of dimensional reduction used in other works on higher dimensional numerical relativity that preceded this work. We call this method "dimensional reduction by isometry", based on work by Geroch and others [209–211], and notably employed in [212, 110, 213]. In this method we assume that we work with a spacetime with an $SO(D-3)$ symmetry (though this can be applied to any $SO(n)$ symmetry), which will allow us to write the spatial part of the metric as an arbitrary $3D$ metric, which we will numerically evolve, added to the metric on the $D-4$ sphere, multiplied by a function of the $3D$ coordinates, which we also evolve. This added function can then be moved to the right hand side of the Einstein equations,

---

[3]That said, we note that interesting results have recently been published on the use of discontinuous Galerkin methods on "sparse" grids that allow a higher dimensional system that has *not* been dimensionally reduced to be simulated in full with low computational cost [208]

and treated as a matter term, reducing the problem of D dimensional vacuum general relativity to 4 dimensional general relativity in the presence of a matter field. We briefly introduce this method below, following analysis in [214–216, 22].

Any metric can be written in the form,

$$\mathrm{d}s^2 = g_{AB}\mathrm{d}x^A\mathrm{d}x^B = \left(g_{\hat{A}\hat{B}} + g_{ab}B_{\hat{A}}^a B_{\hat{B}}^b\right)\mathrm{d}x^{\hat{A}}\mathrm{d}x^{\hat{B}} + 2B_{\hat{A}}^a g_{ab}\mathrm{d}x^{\hat{A}}\mathrm{d}x^b + g_{ab}\mathrm{d}x^a\mathrm{d}x^b,$$
(2.98)

splitting the coordinates into the angular coordinates on a $D-4$ sphere, and the coordinates on the remaining $4D$ space. For a spacetime with $SO(D-3)$ symmetry, there exist $(D-3)(D-4)/2$ Killing vectors $\xi_{(p)}$, labelled by p, with the Killing equation giving us that,

$$\mathcal{L}_{\xi_{(p)}}g_{\hat{A}\hat{B}} = 0, \tag{2.99}$$

$$\mathcal{L}_{\xi_{(p)}}B_{\hat{A}}^a = 0, \tag{2.100}$$

$$\mathcal{L}_{\xi_{(p)}}g_{ab} = 0. \tag{2.101}$$

Equation (2.99) tells us that the metric components on the $4D$ space only depend on the coordinates on that space, $g_{\hat{A}\hat{B}} = g_{\hat{A}\hat{B}}\left(x^{\hat{C}}\right)$. Equation (2.100) tells us that all of the Killing vectors commute with $B_{\hat{A}}^a$. This means that $B_{\hat{A}}^a = 0$ since there is no non-trivial vector field on the sphere that commutes with all the Killing vectors. Note, this is not true for an $SO(2)$ symmetry. Hence we would have to treat $SO(D-3)$ symmetry differently in $D=5$. This caveat is also true in the modified Cartoon method discussed in Section 3.4, and we leave discussion of this problem until then. Equation (2.101) tells us that g_{ab} admits the maximal number of Killing vector fields, so is the metric of the maximally symmetric space at each point $\left(x^{\hat{A}}\right)$, the $D-4$ sphere. So

$$g_{ab} = \lambda\left(x^{\hat{A}}\right)\omega_{ab}^{(D-4)}, \tag{2.102}$$

where $\omega_{ab}^{(D-4)}$ is the round metric on the $D-4$ sphere. Hence the full spacetime metric can be written as

$$\mathrm{d}s^2 = g_{AB}\mathrm{d}x^A\mathrm{d}x^B = g_{\hat{A}\hat{B}}\left(x^{\hat{C}}\right)\mathrm{d}x^{\hat{A}}\mathrm{d}x^{\hat{B}} + \lambda\left(x^{\hat{C}}\right)\mathrm{d}\Omega_{D-4}.$$

(2.103)

Substituting this metric into the D dimensional Einstein equations provides the equations for $4D$ gravity, non-minimally coupled to a scalar field λ,

$$\hat{R}_{\hat{A}\hat{B}} = \frac{D-4}{2\lambda}\left(\hat{\nabla}_{\hat{A}}\partial_{\hat{B}}\lambda - \frac{1}{2\lambda}\partial_{\hat{A}}\lambda\partial_{\hat{B}}\lambda\right),$$

(2.104)

$$\hat{\nabla}^{\hat{A}}\partial_{\hat{A}}\lambda = 2(D-5) - \frac{D-6}{2\lambda}\partial_{\hat{A}}\lambda\partial^{\hat{A}}\lambda,$$

(2.105)

where $\hat{R}_{\hat{A}\hat{B}}$ and $\hat{\nabla}_{\hat{A}}$ are the Ricci tensor and covariant derivative respectively with respect to the $4D$ metric $g_{\hat{A}\hat{B}}$. Now we have a system of equations that appear to be indistinguishable from the case of $4D$ gravity with matter, which we can solve using existing numerical relativity techniques.

2.8 Mesh refinement

To fully model a physical problem such as the inspiral of 2 black holes, we must be able to resolve a number of different length scales in our simulation. On one end, we must be able to resolve the Schwarzschild radius of the black hole, which is of size $\mathcal{O}(M)$, and on the other end, we must be able to resolve gravitational waves at a distance far from the black hole, at $\mathcal{O}(100M)$. The resolution required near the black hole is much higher than the resolution required far from the black hole, where we extract gravitational waves, so to save computational resources, we employ mesh refinement. The first example of the necessity of mesh refinement was in Choptuik's famous study of critical phenomena in gravitational collapse, which required the resolution of smaller and smaller length scales as the black hole produced from collapse approached a naked singularity [217]. There are many ways to implement mesh refinement, in this thesis we employ the scheme implemented by the CARPET thorn [218, 219] within CACTUS [220]. This involves placing a high resolution grid on top of the black hole, which lies nested within a hierarchy of grids of decreasing resolution. These grids can be of fixed position, or centred on the black hole, in which case they follow the location of the black hole puncture, and, in the case of a binary black hole spacetime, can merge with

the grids centred on the other black hole when they approach each other. The different grids communicate with each other through the Berger-Oliger algorithm [221, 218].

2.9   Boundary conditions

In this thesis we seek to model asymptotically flat spacetimes. In practice we must evolve a finite sized grid in our simulation, so we have the option of either compactifying our coordinates to fit the full spatial slice into a finite sized grid, or to only evolve a finite sized patch of the spatial slice, with appropriate boundary conditions. In evolutions employing the BSSN formalism the second of these two options is the most widely used. The search for appropriate boundary conditions that both preserve the well-posedness of the BSSN equations, and do not introduce violations to the constraint equations is still ongoing and is a problem that has not been fully solved. In practice, we apply boundary conditions that give the physical requirements that we desire, that there should be no radiation incoming from the boundary, and ensure that the boundary is sufficiently far away from the regions of the spacetime we are interested in, such as the region in which we extract gravitational waves, that they remain causally disconnected for the length of the simulation [222]. To impose these boundary conditions, we assume that all functions f on our grid decay with the following behaviour,

$$f = f_0 + \frac{u(t-r)}{r^n}, \tag{2.106}$$

with n some integer and u is a retarded time coordinate. Then at the outer boundary f obeys the condition

$$\partial_t f + n\frac{f - f_0}{r} + \frac{x^I}{r}\partial_I f = 0. \tag{2.107}$$

These are known as Sommerfeld boundary conditions. We note that, in order to evaluate these derivatives at the boundary, we must implement one-sided "advection" derivatives.

Chapter 3

Dimensional Reduction with the Modified Cartoon Formalism

This chapter, as well as Appendix A, is based on [114] authored in collaboration with Pau Figueras, Markus Kunesch, Saran Tunyasuvunakool and Ulrich Sperhake. In particular the generalisation of the dimensional reduction technique to $d > 3$ was performed by the author, as well as independent verification of all other results. The study of the case of $SO(2)$ symmetry was performed by M. Kunesch.

3.1 Introduction

Numerical simulations of BH spacetimes in higher dimensions are a challenging task. First and foremost this is simply a consequence of the required computational resources. Simulations in $D = 4$ require of the order of $\mathcal{O}(10^2)$ cores and $\mathcal{O}(10^2)$ Gb of memory. Each extra spatial dimension introduces an additional factor of $\mathcal{O}(10^2)$ grid points and correspondingly more memory and floating point operations. Even with modern high-performance computing systems, this sets practical limits on the feasibility of accurately evolving higher-dimensional spacetimes. At the same time, many of the outstanding questions in numerical relativity can be addressed by imposing symmetry assumptions on the spacetimes in question such as planar symmetry in modelling asymptotically AdS spacetimes [69], cylindrical symmetry for black strings [105] or different types of rotational symmetries [107]. This can be achieved in practice by either (i) using a specific form of the line element that directly imposes the symmetry in question (see e.g. [69]), (ii) starting with a generic line element and applying dimensional reduction through isometry (see [209, 212, 214] and Section 2.7) or (iii)

implementing the symmetry through a so-called *Cartoon method* [223]. Here we are concerned with the latter approach and, more specifically, with a modification thereof originally introduced in [133] (see also [100, 224, 225]) which we will henceforth refer to as the *modified Cartoon method.*

This chapter is structured as follows. In Section 3.2, we introduce the notation used throughout our work, and illustrate the modified Cartoon implementation of the symmetries for a specific example. In Section 3.3 we introduce the Baumgarte-Shapiro-Shibata-Nakamura [137, 136] (BSSN) evolution system we use for the Einstein equations, and derive their specific form in $SO(D-d)$ symmetry when rotational symmetry is present in ≥ 2 planes which corresponds to $d < D - 2$. The axisymmetric case $d = D - 2$ imposes less restrictive conditions on the vanishing of tensor density components and their derivatives, and the particulars of its numerical implementation are briefly discussed in Section 3.4. As an example, we present in Section 3.5 numerical simulations of a BH head-on collision in $D = 7$ dimensions employing $SO(4)$ symmetry. We summarise our findings in Section 3.6 and include in Appendix A a list of important relations for the components of tensors and derived quantities as well as the regularisation necessary at the origin in the quasi-radial direction.

3.2 $SO(D-d)$ **symmetry in the modified Cartoon method**

3.2.1   **Coordinates**

It is instructive to illustrate the method by considering first a simpler scenario: axisymmetry in three spatial dimensions. Let (x, z, w) denote Cartesian coordinates and assume rotational symmetry about the x axis[1] i.e., there exists a rotational Killing field in the z, w plane. Evidently, the geometry of such a three-dimensional manifold can be constructed straightforwardly provided all tensors (e.g. the metric) are known on the semi infinite plane $w = 0$, $z \geq 0$, $x \in \mathbb{R}$. We note the simplification in the computational task: the w coordinate has dropped out and the quasi-radius z takes on only non-negative values, reducing an originally three-dimensional computational domain to a calculation on half of $\mathbb{R}^2$. This is the case considered in the original papers [223, 133].

---

[1]It is more common to label the coordinates (x, y, z) and use symmetry about the z axis, but our choice of labels emphasises more clearly the analogy to the higher-dimensional case.

The most common applications, for instance the inspiral, or head-on collision of spinning or non-spinning black holes, will likely consider higher-dimensional spacetimes with $SO(D-3)$ symmetry, but here we present the general application to a D dimensional spacetime with $SO(D-d)$ symmetry, where $d \in \mathbb{N}$, $1 \leq d \leq D-2$. Let us then consider a D dimensional spacetime consisting of a manifold $\mathcal{M}$ and a metric g_{AB} satisfying the D dimensional Einstein equations which are given by Eq. (2.16).

We now assume the spacetime to obey $SO(D-d)$ symmetry and introduce the Cartesian coordinates of Eq. (2.1), which we recall are

$$X^A = (t, \underbrace{x^1, x^2, \ldots x^{d-1}}_{(d-1)\times}, z, \underbrace{w^{d+1}, w^{d+2}, \ldots, w^{D-1}}_{(D-d-1)\times}) =: (t, x^{\hat{i}}, z, w^a), \qquad (3.1)$$

where $\hat{i} = 1, \ldots d-1$, $a = d+1, \ldots, D-1$. $SO(D-d)$ symmetry implies the existence of rotational Killing vectors in each plane spanned by two of the coordinates (z, w^a). In complete analogy with the axisymmetric scenario discussed above, it is now sufficient to provide data on the d-dimensional semi-infinite hyperplane $w^a = 0$, $x^{\hat{i}} \in \mathbb{R}$, $z \geq 0$. The components of a tensor at any point in the spacetime can then be obtained by appropriately rotating data from the hyperplane onto the point in question. This is illustrated in Fig. 3.1 where we show an example application consisting of a collision of two BHs. Note that the BHs can have non-zero spin components in the $x^{\hat{i}}$ directions and that the collision may be of grazing nature, that is, with a non-zero impact parameter, in the corresponding subspace.

In modelling spacetimes with such symmetries, it is therefore entirely sufficient to compute data on the hyperplane which largely solves the problem of increased computational cost mentioned in Section 2.7, as we now evolve a d dimensional grid, rather than one of $D-1$ dimensions. There remains, however, the difficulty that the Einstein equations, irrespective of the specific formulation one chooses, contain derivatives of tensor components in the w^a directions which cannot be evaluated numerically in the usual fashion, as for example using finite differences or spectral methods. Furthermore, the number of tensor components present in the Einstein equations still increases rapidly with the dimension parameter D resulting in a substantial increase of memory requirements and floating point operations. Both of these difficulties are overcome by exploiting the conditions imposed on the tensor components and their derivatives by the $SO(D-d)$ symmetry. It is these conditions which we address next. It turns out to be convenient in this discussion to distinguish between (1) the case $d = D-2$ corresponding to $SO(2)$ isometry, and (2) all remaining cases $d < D-2$. We will
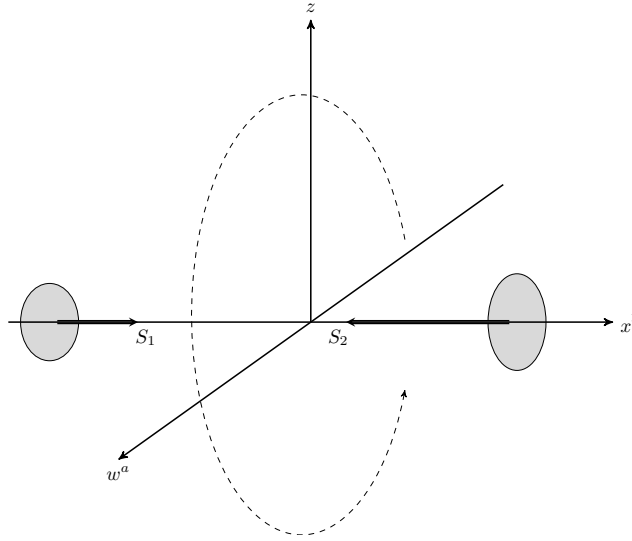
Fig. 3.1 Graphical illustration of a BH collision inside a plane spanned by the $x^{\hat{i}}$ directions. The BHs may rotate with a spin direction inside that plane. Note that in general there are multiple coordinates $x^{\hat{i}}$ and the collisions need not be headon but may instead be of grazing nature inside the subspace $(x^{\hat{i}})$. The dashed line illustrates the rotational symmetry in any of the (z, w^a) planes. Additional rotational symmetries in the (w^a, w^b) planes can be present but cannot be illustrated in the figure. Note that the computational domain is given by the hyperplane $w^a = 0, z \geq 0, x^{\hat{i}} \in \mathbb{R}$ and that each point in this domain represents a $D - d - 1$ sphere of radius z.

briefly discuss the case $d = D - 2$, though we note that for the physical scenarios studied in this thesis, it will not be needed. For a more thorough study of this case see Section 4 and Appendix C of [114], with an application of the modified Cartoon method in this particular symmetry class given in [107]. We focus on the generic case first, $d < D - 2$.

3.2.2   Tensor components in $SO(D-d)$ symmetry for $d < D-2$

The key ingredient we use in reducing the number of independent tensor components and relating their derivatives are the rotational Killing vectors and the use of coordinates adapted to the integral curves of these Killing vectors. The method is best introduced by considering a concrete example. Let $\boldsymbol{\xi}$ denote the Killing vector field corresponding to the rotational symmetry in the (z, w) plane, where $w \equiv w^a$ for some fixed number $a \in \{d+1, \ldots, D-1\}$. We introduce a new coordinate system that replaces (z, w)

with cylindrical coordinates and leaves all other coordinates unchanged,

$$\bar{X}^A = (t,\, x^{\hat{i}},\, \rho,\, w^{d+1},\, \dots,\, w^{a-1},\, \varphi,\, w^{a+1},\, \dots,\, w^{D-1})\,, \tag{3.2}$$

$$\rho = \sqrt{z^2 + w^2}\,, \qquad\qquad z = \rho\cos\varphi\,, \tag{3.3}$$

$$\varphi = \arctan\frac{w}{z}\,, \qquad\qquad w = \rho\sin\varphi\,. \tag{3.4}$$

In these coordinates, the Killing field is $\boldsymbol{\xi} = \boldsymbol{\partial}_\varphi$ and the vanishing of the Lie derivative $\mathcal{L}_{\boldsymbol{\xi}} g_{AB} = 0$ implies $\partial_\varphi g_{AB} = 0$. Note that quantities constructed from the spacetime metric directly inherit this property. This applies, in particular, to the ADM variables defined in Eqs (2.10),(2.12) and the BSSN variables widely used in numerical relativity, which we will shortly define. For $d < D - 2$, one can furthermore show that the φ component of a vector field and those components of a tensor field T_{AB}, where exactly one index is φ, vanish. Here the case $d = D - 2$ represents an exception; an axisymmetric, toroidal magnetic field, for example, satisfies $SO(2)$ symmetry, but has a non-vanishing φ component. We note that this is the same special case that arose in the method of dimensional reduction by isometry described in Section 2.7, with the non-vanishing of $B_{\hat{A}}^a$ in the case of $SO(2)$ symmetry in Eq. (2.100).

The concrete example we now discuss in more detail concerns a symmetric tensor density T_{AB} of weight $\mathcal{W}$ and, in particular, the mixed components T_{iw}, where the index i stands for any one of the $(x^{\hat{i}}, z)$ coordinates and w stands for one of the w^a. We first consider the components $T_{\hat{i}w}$ for some fixed value of $\hat{i}$. Transforming the component $\bar{T}_{\hat{i}\varphi}$ to Cartesian coordinates, one gets

$$\bar{T}_{\hat{i}\varphi} = \mathcal{D}^{\mathcal{W}} \frac{\partial X^A}{\partial \bar{X}^{\hat{i}}} \frac{\partial X^B}{\partial \varphi} T_{AB} = \mathcal{D}^{\mathcal{W}} \left(-w\, T_{\hat{i}z} + z\, T_{\hat{i}w} \right)\,, \tag{3.5}$$

where here $\mathcal{D}$ is the Jacobian $\det(\partial X^A / \partial \bar{X}^B) = \rho$. Using that $\bar{T}_{\hat{i}\varphi} = 0$ by symmetry, this equation implies

$$T_{\hat{i}w} = \frac{w}{z}\, T_{\hat{i}z}\,. \tag{3.6}$$

Similarly, transforming $\bar{T}_{\rho\varphi}$ to Cartesian coordinates and using that $\bar{T}_{\rho\varphi} = 0$ by symmetry, one straightforwardly gets

$$T_{zw} = \frac{zw}{z^2 - w^2}(T_{zz} - T_{ww})\,. \tag{3.7}$$

Recalling that the computational domain is the hyperplane $w^a = 0$, $x^{\hat{i}} \in \mathbb{R}$, $z \geq 0$, we conclude from Eqs (3.6) and (3.7) that on the computational domain $T_{iw} = 0$. This

argument holds for any specific choice of the coordinate w, so that we conclude

$$T_{ia} = 0 \,. \tag{3.8}$$

To compute the derivatives with respect to w on the $w = 0$ hyperplane, one can proceed as follows. For the tensor components in the example above, one can simply use (3.6) and (3.7) to calculate $\partial_w T_{ia}$ and then set $w = 0$. Alternatively, writing the Killing field $\boldsymbol{\xi}$ as

$$\boldsymbol{\xi} = z\,\boldsymbol{\partial_w} - w\,\boldsymbol{\partial_z} \,, \tag{3.9}$$

and imposing the vanishing of the Lie derivative $\mathcal{L}_{\boldsymbol{\xi}} T_{ia} = 0$ on the $w = 0$ hyperplane, one gets

$$\partial_w T_{iw} = \frac{T_{iz} - \delta_{iz} T_{ww}}{z} \,. \tag{3.10}$$

Repeating this process for all components of scalar, vector and rank 2 tensor densities as well as their first and second derivatives, we get the relations summarised in Appendix A.1.

We have shown the calculation here explicitly for the case of tensor densities. It can be shown that the vectorial expressions thus obtained also apply to the contracted Christoffel symbol $\Gamma^A \equiv g^{MN}\Gamma^A_{MN}$ constructed from the metric, even though it is not a vector density.

3.3 Dimensional reduction of the BSSN equations

In this section, we will apply the symmetry relations obtained above to the specific case of the BSSN formulation of the Einstein equations in D spacetime dimensions. We emphasise, however, that the procedure spelled out here for the BSSN system can be applied in similar form to any of the alternative popular formulations used in numerical relativity.

3.3.1 The D dimensional BSSN equations

The starting point for the BSSN formulation are the ADM equations, Eqs (2.21)-(2.24) arising from the $(D-1)+1$ split, performed in Section 2.2 . The BSSN system, as introduced in Section 2.3, is obtained from the ADM equations by applying a conformal transformation to the spatial metric, a trace split of the extrinsic curvature and promotion of the contracted spatial Christoffel symbols to the status of evolution

variables. The BSSN variables are defined as

$$\chi = \gamma^{-1/(D-1)}\,, \qquad\qquad K = \gamma^{MN}K_{MN},$$

$$\tilde{\gamma}_{IJ} = \chi\gamma_{IJ} \qquad \Leftrightarrow \quad \tilde{\gamma}^{IJ} = \frac{1}{\chi}\gamma^{IJ},$$

$$\tilde{A}_{IJ} = \chi\left(K_{IJ} - \frac{1}{D-1}\gamma_{IJ}K\right) \quad \Leftrightarrow \quad K_{IJ} = \frac{1}{\chi}\left(\tilde{A}_{IJ} + \frac{1}{D-1}\tilde{\gamma}_{IJ}K\right),$$

$$\tilde{\Gamma}^I = \tilde{\gamma}^{MN}\tilde{\Gamma}^I_{MN}\,, \tag{3.11}$$

where $\gamma = \det\gamma_{IJ}$, and $\tilde{\Gamma}^I_{MN}$ are the Christoffel symbols associated with the conformal metric $\tilde{\gamma}_{IJ}$. We formulate here the conformal factor in terms of the variable χ, following [140]. Alternative versions of the equations using variables $W \equiv \sqrt{\chi}$ or $\phi \equiv -(\ln\chi)/4$ can be found in [226, 165]. Note that the definition of the BSSN variables in (3.11) implies two algebraic and one differential constraints given by

$$\tilde{\gamma} = 1, \qquad \tilde{\gamma}^{MN}\tilde{A}_{MN} = 0, \qquad \mathcal{G}^I \equiv \tilde{\Gamma}^I - \tilde{\gamma}^{MN}\tilde{\Gamma}^I_{MN} = 0\,. \tag{3.12}$$

The D dimensional BSSN equations are then given by the Hamiltonian and momentum constraints

$$\mathcal{H} \;\equiv\; \mathcal{R} + \frac{D-2}{D-1}K^2 - \tilde{A}^{MN}\tilde{A}_{MN} - 16\pi\rho - 2\Lambda = 0\,, \tag{3.13}$$

$$\mathcal{M}_I \;\equiv\; \tilde{\gamma}^{MN}\tilde{D}_M\tilde{A}_{NI} - \frac{D-2}{D-1}\partial_I K - \frac{D-1}{2}\tilde{A}^M{}_I\frac{\partial_M\chi}{\chi} - 8\pi j_I = 0\,, \tag{3.14}$$

and the evolution system

$$\partial_t \chi = \beta^M \partial_M \chi + \frac{2}{D-1} \chi (\alpha K - \partial_M \beta^M) , \tag{3.15}$$

$$\partial_t \tilde{\gamma}_{IJ} = \beta^M \partial_M \tilde{\gamma}_{IJ} + 2\tilde{\gamma}_{M(I} \partial_{J)} \beta^M - \frac{2}{D-1} \tilde{\gamma}_{IJ} \partial_M \beta^M - 2\alpha \tilde{A}_{IJ} , \tag{3.16}$$

$$\partial_t K = \beta^M \partial_M K - \chi \tilde{\gamma}^{MN} D_M D_N \alpha + \alpha \tilde{A}^{MN} \tilde{A}_{MN} + \frac{1}{D-1} \alpha K^2$$
$$+ \frac{8\pi}{D-2} \alpha [S + (D-3)\rho] - \frac{2}{D-2} \alpha \Lambda , \tag{3.17}$$

$$\partial_t \tilde{A}_{IJ} = \beta^M \partial_M \tilde{A}_{IJ} + 2\tilde{A}_{M(I} \partial_{J)} \beta^M - \frac{2}{D-1} \tilde{A}_{IJ} \partial_M \beta^M + \alpha K \tilde{A}_{IJ} - 2\alpha \tilde{A}_{IM} \tilde{A}^M{}_J$$
$$+ \chi \left(\alpha \mathcal{R}_{IJ} - D_I D_J \alpha - 8\pi \alpha S_{IJ} \right)^{\mathrm{TF}} , \tag{3.18}$$

$$\partial_t \tilde{\Gamma}^I = \beta^M \partial_M \tilde{\Gamma}^I + \frac{2}{D-1} \tilde{\Gamma}^I \partial_M \beta^M - \tilde{\Gamma}^M \partial_M \beta^I + \tilde{\gamma}^{MN} \partial_M \partial_N \beta^I + \frac{D-3}{D-1} \tilde{\gamma}^{IM} \partial_M \partial_N \beta^N$$
$$- \tilde{A}^{IM} \left[(D-1)\alpha \frac{\partial_M \chi}{\chi} + 2\partial_M \alpha \right] + 2\alpha \tilde{\Gamma}^I_{MN} \tilde{A}^{MN} - 2\frac{D-2}{D-1} \alpha \tilde{\gamma}^{IM} \partial_M K$$
$$- 16\pi \frac{\alpha}{\chi} j^I - \sigma \mathcal{G}^I \partial_M \beta^M . \tag{3.19}$$

Here, the superscript "TF" denotes the trace-free part and we have added a constraint damping term $\sigma \mathcal{G}^I$ in the last line, following the suggestion by [124], which enables long term stable evolutions. The above equations are complemented by the following auxiliary relations,

$$\Gamma^I_{JK} = \tilde{\Gamma}^I_{JK} - \frac{1}{2\chi} \left(\delta^I{}_K \partial_J \chi + \delta^I{}_J \partial_K \chi - \tilde{\gamma}_{JK} \tilde{\gamma}^{IM} \partial_M \chi \right) , \tag{3.20}$$

$$\mathcal{R}_{IJ} = \tilde{\mathcal{R}}_{IJ} + \mathcal{R}^\chi_{IJ} , \tag{3.21}$$

$$\mathcal{R}^\chi_{IJ} = \frac{\tilde{\gamma}_{IJ}}{2\chi} \left[\tilde{\gamma}^{MN} \tilde{D}_M \tilde{D}_N \chi - \frac{D-1}{2\chi} \tilde{\gamma}^{MN} \partial_M \chi \, \partial_N \chi \right]$$
$$+ \frac{D-3}{2\chi} \left(\tilde{D}_I \tilde{D}_J \chi - \frac{1}{2\chi} \partial_I \chi \, \partial_J \chi \right) , \tag{3.22}$$

$$\tilde{\mathcal{R}}_{IJ} = -\frac{1}{2} \tilde{\gamma}^{MN} \partial_M \partial_N \tilde{\gamma}_{IJ} + \tilde{\gamma}_{M(I} \partial_{J)} \tilde{\Gamma}^M + \tilde{\Gamma}^M \tilde{\Gamma}_{(IJ)M}$$
$$+ \tilde{\gamma}^{MN} \left[2\tilde{\Gamma}^K_{M(I} \tilde{\Gamma}_{J)KN} + \tilde{\Gamma}^K_{IM} \tilde{\Gamma}_{KJN} \right] , \tag{3.23}$$

$$D_I D_J \alpha = \tilde{D}_I \tilde{D}_J \alpha + \frac{1}{\chi} \partial_{(I} \chi \, \partial_{J)} \alpha - \frac{1}{2\chi} \tilde{\gamma}_{IJ} \tilde{\gamma}^{MN} \partial_M \chi \, \partial_N \alpha . \tag{3.24}$$

The BSSN equations in this form are general and facilitate the numerical construction of D dimensional spacetimes. Next, we will describe in detail how the equations can be

reduced to an effective system in d spatial dimensions for spacetimes obeying rotational symmetry with $d < D - 2$.

3.3.2 The BSSN equations with $SO(D-d)$ symmetry for $d < D - 2$

We now apply the relations summarised in Appendix A.1 to the definition of the BSSN variables (3.11) and the D dimensional BSSN equations (3.13)-(3.19). Recalling that early and middle Latin indices run over $a, b, \ldots = d + 1, \ldots, D - 1$ and $i, j, \ldots = 1, \ldots d$, respectively, and introducing $\eta \equiv D - d - 1$, the variables are given in terms of their ADM counterparts by

$$\chi = \gamma^{-1/(D-1)}, \quad \gamma = \det \gamma_{IJ} = \gamma_{ww}^{\eta} \det \gamma_{ij}, \qquad K = \gamma^{MN} K_{MN} = \gamma^{mn} K_{mn} + \eta \gamma^{ww} K_{ww},$$

$$\tilde{\gamma}_{ij} = \chi \gamma_{ij}, \quad \tilde{\gamma}_{ww} = \chi \gamma_{ww} \qquad \Leftrightarrow \quad \tilde{\gamma}^{ij} = \frac{1}{\chi} \gamma^{ij}, \quad \tilde{\gamma}^{ww} = \frac{1}{\chi} \gamma^{ww},$$

$$\tilde{A}_{ij} = \chi \left(K_{ij} - \frac{1}{D-1} \gamma_{ij} K \right) \qquad \Leftrightarrow \quad K_{ij} = \frac{1}{\chi} \left(\tilde{A}_{ij} + \frac{1}{D-1} \tilde{\gamma}_{ij} K \right),$$

$$\tilde{A}_{ww} = \chi \left(K_{ww} - \frac{1}{D-1} \gamma_{ww} K \right) \qquad \Leftrightarrow \quad K_{ww} = \frac{1}{\chi} \left(\tilde{A}_{ww} + \frac{1}{D-1} \tilde{\gamma}_{ww} K \right),$$

$$\tilde{\Gamma}^i = \tilde{\gamma}^{MN} \tilde{\Gamma}^i_{MN} = \tilde{\gamma}^{mn} \tilde{\Gamma}^i_{mn} + \eta \tilde{\gamma}^{ww} \tilde{\Gamma}^i_{ww}, \tag{3.25}$$

where

$$\tilde{\Gamma}^i_{ww} = -\frac{1}{2} \tilde{\gamma}^{im} \partial_m \tilde{\gamma}_{ww} + \frac{\delta^i{}_z - \tilde{\gamma}^{zi} \tilde{\gamma}_{ww}}{z}. \tag{3.26}$$

We first note that the spatial metric with $SO(D-d)$ symmetry has the form

$$\tilde{\gamma}_{IJ} = \left(\begin{array}{cccc|cccc} \tilde{\gamma}_{x^1 x^1} & \cdots & \tilde{\gamma}_{x^1 x^{d-1}} & \tilde{\gamma}_{xz} & 0 & 0 & \cdots & 0 \\ \vdots & \ddots & \vdots & \vdots & \vdots & \vdots & \cdots & \vdots \\ \tilde{\gamma}_{x^{d-1} x^1} & \cdots & \tilde{\gamma}_{x^{d-1} x^{d-1}} & \tilde{\gamma}_{x^{d-1} z} & 0 & 0 & \cdots & 0 \\ \tilde{\gamma}_{zx^1} & \cdots & \tilde{\gamma}_{zx^{d-1}} & \tilde{\gamma}_{zz} & 0 & 0 & \cdots & 0 \\ \hline 0 & \cdots & 0 & 0 & \tilde{\gamma}_{ww} & 0 & \cdots & 0 \\ 0 & \cdots & 0 & 0 & 0 & \tilde{\gamma}_{ww} & \cdots & 0 \\ \vdots & \cdots & \vdots & \vdots & \vdots & \vdots & \ddots & \vdots \\ 0 & \cdots & 0 & 0 & 0 & 0 & \cdots & \tilde{\gamma}_{ww} \end{array} \right), \tag{3.27}$$

which simplifies the calculation of the inverse metric $\tilde{\gamma}^{AB}$; see Appendix A.2.

The constraint equations (3.13), (3.14) become

$$
\begin{aligned}
\mathcal{H} &= \chi\tilde{\gamma}^{mn}\mathcal{R}_{mn} - \tilde{A}^{mn}\tilde{A}_{mn} + \frac{D-2}{D-1}K^2 + \eta\left(\chi\tilde{\gamma}^{ww}\mathcal{R}_{ww} - \frac{\tilde{A}_{ww}^2}{\tilde{\gamma}_{ww}^2}\right) \\
&\quad -16\pi\rho - 2\Lambda = 0\,, \qquad\qquad\qquad\qquad\qquad\qquad\qquad (3.28) \\
\mathcal{M}_i &= \tilde{\gamma}^{mn}\partial_m\tilde{A}_{ni} - \tilde{\Gamma}^m\tilde{A}_{mi} - \tilde{\gamma}^{ml}\tilde{\Gamma}^n_{im}\tilde{A}_{nl} - \frac{D-2}{D-1}\partial_i K - \frac{D-1}{2\chi}\tilde{A}^m{}_i\partial_m\chi \\
&\quad +\eta\tilde{\gamma}^{ww}\left(\frac{\tilde{A}_{iz} - \delta_{iz}\tilde{A}_{ww}}{z} - \tilde{\Gamma}^m_{ww}\tilde{A}_{mi} - \frac{1}{2}\tilde{\gamma}^{ww}\tilde{A}_{ww}\partial_i\tilde{\gamma}_{ww}\right) - 8\pi j_i = 0\,. (3.29)
\end{aligned}
$$

and the BSSN evolution equations (3.15)-(3.19) are now written as

$$
\partial_t\chi = \beta^m\partial_m\chi + \frac{2}{D-1}\chi\left(\alpha K - \partial_m\beta^m - \eta\frac{\beta^z}{z}\right)\,, \qquad\qquad (3.30)
$$

$$
\partial_t\tilde{\gamma}_{ij} = \beta^m\partial_m\tilde{\gamma}_{ij} + 2\tilde{\gamma}_{m(i}\partial_{j)}\beta^m - \frac{2}{D-1}\tilde{\gamma}_{ij}\left(\partial_m\beta^m + \eta\frac{\beta^z}{z}\right) - 2\alpha\tilde{A}_{ij}\,, \qquad (3.31)
$$

$$
\partial_t\tilde{\gamma}_{ww} = \beta^m\partial_m\tilde{\gamma}_{ww} - \frac{2}{D-1}\tilde{\gamma}_{ww}\left(\partial_m\beta^m - d\frac{\beta^z}{z}\right) - 2\alpha\tilde{A}_{ww}\,, \qquad\qquad (3.32)
$$

$$
\begin{aligned}
\partial_t K &= \beta^m\partial_m K - \chi\tilde{\gamma}^{mn}D_m D_n\alpha + \alpha\tilde{A}^{mn}\tilde{A}_{mn} + \frac{1}{D-1}\alpha K^2 \\
&\quad +\eta\tilde{\gamma}^{ww}\left(\alpha\frac{\tilde{A}_{ww}^2}{\tilde{\gamma}_{ww}} - \chi D_w D_w\alpha\right) + \frac{2}{D-2}\alpha\{4\pi[S + (D-3)\rho] - \Lambda\}\,, (3.33)
\end{aligned}
$$

$$
\begin{aligned}
\partial_t\tilde{A}_{ij} &= \beta^m\partial_m\tilde{A}_{ij} + 2\tilde{A}_{m(i}\partial_{j)}\beta^m - \frac{2}{D-1}\tilde{A}_{ij}\left(\partial_m\beta^m + \eta\frac{\beta^z}{z}\right) + \alpha K\tilde{A}_{ij} \\
&\quad -2\alpha\tilde{\gamma}^{mn}\tilde{A}_{im}\tilde{A}_{jn} + \chi\left[\alpha(\mathcal{R}_{ij} - 8\pi S_{ij}) - D_i D_j\alpha\right]^{\mathrm{TF}}\,, \qquad (3.34)
\end{aligned}
$$

$$
\begin{aligned}
\partial_t\tilde{A}_{ww} &= \beta^m\partial_m\tilde{A}_{ww} - \frac{2}{D-1}\tilde{A}_{ww}\left(\partial_m\beta^m - d\frac{\beta^z}{z}\right) + \alpha\tilde{A}_{ww}(K - 2\tilde{\gamma}^{ww}\tilde{A}_{ww}) \\
&\quad +\chi\left[\alpha(\mathcal{R}_{ww} - 8\pi S_{ww}) - D_w D_w\alpha\right]^{\mathrm{TF}}\,, \qquad\qquad\qquad (3.35)
\end{aligned}
$$

$$
\begin{aligned}
\partial_t\tilde{\Gamma}^i &= \beta^m\partial_m\tilde{\Gamma}^i + \frac{2}{D-1}\tilde{\Gamma}^i\left(\partial_m\beta^m + \eta\frac{\beta^z}{z}\right) + \tilde{\gamma}^{mn}\partial_m\partial_n\beta^i + \frac{D-3}{D-1}\tilde{\gamma}^{im}\partial_m\partial_n\beta^n \\
&\quad -\tilde{\Gamma}^m\partial_m\beta^i + \eta\tilde{\gamma}^{ww}\left(\frac{\partial_z\beta^i}{z} - \delta^i{}_z\frac{\beta^z}{z^2}\right) + \frac{D-3}{D-1}\eta\left(\tilde{\gamma}^{im}\frac{\partial_m\beta^z}{z} - \tilde{\gamma}^{iz}\frac{\beta^z}{z^2}\right) \\
&\quad -\tilde{A}^{im}\left[(D-1)\alpha\frac{\partial_m\chi}{\chi} + 2\partial_m\alpha\right] + 2\alpha\left(\tilde{\Gamma}^i_{mn}\tilde{A}^{mn} + \eta\tilde{\Gamma}^i_{ww}\tilde{A}^{ww}\right) - 16\pi\frac{\alpha}{\chi}j_i \\
&\quad -2\frac{D-2}{D-1}\alpha\tilde{\gamma}^{im}\partial_m K - \sigma\left[\left(\partial_m\beta^m + \eta\frac{\beta^z}{z}\right)\left(\tilde{\Gamma}^i - \tilde{\gamma}^{mn}\tilde{\Gamma}^i_{mn} - \eta\tilde{\gamma}^{ww}\tilde{\Gamma}^i_{ww}\right)\right]\,.
\end{aligned}
$$
$$
(3.36)
$$

These equations contain a number of auxiliary expressions which are given in terms of the fundamental BSSN variables by Eq. (3.26) as well as

$$D_i D_j \alpha = \partial_i \partial_j \alpha - \tilde{\Gamma}^m_{ji} \partial_m \alpha + \frac{1}{2\chi}(\partial_i \chi \partial_j \alpha + \partial_j \chi \partial_i \alpha) - \frac{\tilde{\gamma}_{ij}}{2\chi}\tilde{\gamma}^{mn}\partial_m \chi \partial_n \alpha \tag{3.37}$$

$$[D_i D_j \alpha]^{\text{TF}} = D_i D_j \alpha - \frac{1}{D-1}\tilde{\gamma}_{ij}\left(\tilde{\gamma}^{mn}D_m D_n \alpha + \eta \tilde{\gamma}^{ww}D_w D_w \alpha\right), \tag{3.38}$$

$$D_w D_w \alpha = \left(\frac{1}{2}\tilde{\gamma}^{mn}\partial_n \tilde{\gamma}_{ww} + \frac{\tilde{\gamma}^{zm}}{z}\tilde{\gamma}_{ww}\right)\partial_m \alpha - \frac{1}{2\chi}\tilde{\gamma}_{ww}\tilde{\gamma}^{mn}\partial_m \chi \, \partial_n \alpha, \tag{3.39}$$

$$[D_w D_w \alpha]^{\text{TF}} = \frac{1}{D-1}\left(d \times D_w D_w \alpha - \tilde{\gamma}_{ww}\tilde{\gamma}^{mn}D_m D_n \alpha\right), \tag{3.40}$$

$$\mathcal{R}_{ij} = \mathcal{R}^\chi_{ij} + \tilde{\mathcal{R}}_{ij}, \tag{3.41}$$

$$\mathcal{R}_{ww} = \mathcal{R}^\chi_{ww} + \tilde{\mathcal{R}}_{ww}, \tag{3.42}$$

$$\mathcal{R}^\chi_{ij} = \frac{1}{2\chi}\tilde{\gamma}_{ij}\left[\tilde{\gamma}^{mn}\tilde{D}_m \tilde{D}_n \chi + \eta\left(\frac{1}{2}\tilde{\gamma}^{ww}\tilde{\gamma}^{mn}\partial_n \tilde{\gamma}_{ww} + \frac{\tilde{\gamma}^{mz}}{z}\right)\partial_m \chi \right.$$
$$\left. -\frac{D-1}{2\chi}\tilde{\gamma}^{mn}\partial_m \chi \, \partial_n \chi\right] + \frac{D-3}{2\chi}\left(\tilde{D}_i \tilde{D}_j \chi - \frac{1}{2\chi}\partial_i \chi \, \partial_j \chi\right), \tag{3.43}$$

$$\mathcal{R}^\chi_{ww} = \frac{\tilde{\gamma}_{ww}}{2\chi}\left[\tilde{\gamma}^{mn}\tilde{D}_m \tilde{D}_n \chi + (2D - d - 4)\left(\frac{1}{2}\tilde{\gamma}^{ww}\tilde{\gamma}^{mn}\partial_n \tilde{\gamma}_{ww} + \frac{\tilde{\gamma}^{mz}}{z}\right)\partial_m \chi \right.$$
$$\left. -\frac{D-1}{2\chi}\tilde{\gamma}^{mn}\partial_m \chi \, \partial_n \chi\right], \tag{3.44}$$

$$\tilde{\mathcal{R}}_{ij} = \eta \tilde{\gamma}^{ww}\left[-\frac{1}{2}\frac{\partial_z \tilde{\gamma}_{ij}}{z} + \frac{\delta_{z(i}\tilde{\gamma}_{j)z} - \delta_{iz}\delta_{jz}\tilde{\gamma}_{ww}}{z^2} + \frac{\tilde{\gamma}^{ww}\tilde{\gamma}_{z(j} - \delta_{z(j}}{z}\partial_{i)}\tilde{\gamma}_{ww} \right.$$
$$\left. -\frac{1}{4}\tilde{\gamma}^{ww}\partial_i \tilde{\gamma}_{ww}\, \partial_j \tilde{\gamma}_{ww}\right] - \frac{1}{2}\tilde{\gamma}^{mn}\partial_m \partial_n \tilde{\gamma}_{ij} + \tilde{\gamma}_{m(i}\partial_{j)}\tilde{\Gamma}^m$$
$$+\tilde{\Gamma}^m \tilde{\Gamma}_{(ij)m} + \tilde{\gamma}^{mn}\left[2\tilde{\Gamma}^k_{m(i}\tilde{\Gamma}_{j)kn} + \tilde{\Gamma}^k_{im}\tilde{\Gamma}_{kjn}\right], \tag{3.45}$$

$$\tilde{\mathcal{R}}_{ww} = -\frac{1}{2}\tilde{\gamma}^{mn}\partial_m \partial_n \tilde{\gamma}_{ww} + \frac{1}{2}\tilde{\gamma}^{ww}\tilde{\gamma}^{mn}\partial_m \tilde{\gamma}_{ww}\, \partial_n \tilde{\gamma}_{ww} - \frac{\eta}{2}\tilde{\gamma}^{ww}\frac{\partial_z \tilde{\gamma}_{ww}}{z} + \tilde{\gamma}_{ww}\frac{\tilde{\Gamma}^z}{z}$$
$$+\frac{1}{2}\tilde{\Gamma}^m \partial_m \tilde{\gamma}_{ww} + \frac{\tilde{\gamma}^{zz}\tilde{\gamma}_{ww} - 1}{z^2}, \tag{3.46}$$

$$[\mathcal{R}_{ij}]^{\text{TF}} = \mathcal{R}_{ij} - \frac{1}{D-1}\tilde{\gamma}_{ij}\tilde{\gamma}^{mn}\mathcal{R}_{mn} - \frac{\eta}{D-1}\tilde{\gamma}_{ij}\tilde{\gamma}^{ww}\mathcal{R}_{ww}, \tag{3.47}$$

$$[\mathcal{R}_{ww}]^{\text{TF}} = \frac{1}{D-1}\left(d \times \mathcal{R}_{ww} - \tilde{\gamma}_{ww}\tilde{\gamma}^{mn}\mathcal{R}_{mn}\right). \tag{3.48}$$

The BSSN equations in this form can readily be implemented in an existing "d+1" BSSN code with the addition of merely two new field variables, $\tilde{\gamma}_{ww}$ and $\tilde{A}_{ww}$. While the BSSN equations acquire additional terms, the computational domain remains d

dimensional. Furthermore, the entire set of Eqs. (3.28)-(3.48) contains exclusively derivatives in the x^i directions and in time, which can be evaluated without need of additional grid points, known as ghost zones, in the extra dimensions, which would be introduced solely for the purpose of evaluating finite difference stencils. Before it was noted that all terms of the type ∂_{w^a} could be rewritten as combinations of terms of the form ∂_{x^i} it was through the use of ghost zones in the additional dimensions that this technique was implemented. This allowed the use of finite difference stencils to evaluate derivatives in these extra dimensions without evolving the full spatial slice. This was the original Cartoon method of which this method is a modification [223, 168].

There only remains one further subtlety arising from the explicit division by z in several of the terms present. Some (though not all) numerical codes require evaluation of these expressions at $z = 0$ which makes regularization of these terms mandatory. As we show explicitly in Appendix A.2, this can be achieved for all terms, yielding expressions that are exact in the limit $z \to 0$. The results we discuss in Section 3.5 make use of these regularized terms on the plane $z = 0$ demonstrating that this procedure provides stable and accurate evolutions.

We conclude this section with a brief remark of the matter terms present in (3.28)-(3.48) in the form of the projections ρ, j^i, S_{ij} and $S = \chi(\tilde{\gamma}^{ij}S_{ij} + \eta\tilde{\gamma}^{ww}S_{ww})$ of the energy-momentum tensor. The specific form of these terms will depend on the physical system under consideration and will need to be evaluated separately for each case as will the precise form of the matter evolution equations resulting from the conservation law $\nabla_A T^{AB} = 0$. Many applications of higher-dimensional numerical relativity concern BHs and the example application discussed in Section 3.5 will be an asymptotically flat vacuum spacetime where the matter terms and the cosmological constant are zero.

3.4 $SO(2)$ symmetry

As referenced in our discussion of dimensional reduction by isometry in Section 2.7, the case of $SO(2)$ symmetry behaves differently to all of the other symmetry classes we investigate. As there is only one rotational Killing vector in such an axisymmetric spacetime, any scalar function multiplied by this vector commutes with all of the Killing vectors, and so Eq. (2.100) no longer implies that tensors with exactly one ϕ index are identically zero. This is also true for the ϕ component of vectors. In this symmetry class we cannot generically set any tensor or vector components to zero. We can however, still evolve a $d = D - 2$ dimensional grid rather than the full $D - 1$

dimensional grid. In practice the full D dimensional BSSN equations are evolved on a $D-2$ dimensional grid, and then the modified Cartoon method is used to rewrite derivatives with respect to w in terms of derivatives with respect to x^i. This formalism has notably been applied in [133, 107]. Therefore for the case of $SO(2)$ symmetry, we can still avoid the curse of dimensionality, though we must evolve more grid functions than in more symmetric cases. For explicit details of the modified Cartoon derivative terms in $SO(2)$ symmetry, see Appendix C of [114].

3.5 Application to a black-hole collision

In this section we present, as a specific example for the efficacy of the formalism, results from the numerical simulation of a head-on collision of two non-spinning BHs in $D = 7$ dimensions starting from rest. We use higher dimensional Brill-Lindquist data of the type described in Section 2.4 in the LEAN code [192, 227], which is based on CACTUS [220, 228] and uses CARPET [219, 218] for mesh refinement. The specific case presented here has been obtained using $SO(4)$ symmetry, i.e. $D = 7$, $d = 3$, for a collision along the x axis of two equal-mass BHs initially separated by 7.58 R_h, where R_h is the horizon radius associated with a single BH with $\mu = \mu_1 = \mu_2$. The computational domain consists of a set of seven refinement levels, the innermost two centred on the BHs and the five outer ones on the origin. We employ standard moving puncture gauge conditions introduced in Eqs (2.44-2.46) in the first order in time formulation, with parameter values given below,

$$\partial_t \alpha = \beta^m \partial_m \alpha - 3\alpha K \,, \tag{3.49}$$

$$\partial_t \beta^i = \beta^m \partial_m \beta^i + \frac{3}{4}\tilde{\Gamma}^i - \frac{1}{2^{1/4} R_h}\beta^i \,, \tag{3.50}$$

having initialised lapse and shift to their Minkowski values $\alpha = 1$, $\beta^i = 0$. Note that we use here $\beta^a = 0$ in accordance with Eq. (A.3). Two simulations have been performed in octant symmetry with a grid spacing $\Delta x = R_h/52$ and $\Delta x = R_h/104$, respectively, on the innermost level, that increases by a factor of two on each consecutive level further out.

Figure 3.2 shows the trajectories of the two BHs evolving in time from the initial separation through merger into a single hole centred on the origin, obtained from the high resolution simulation with $\Delta x = R_h/104$. In order to check the consistency of our numerical formalism, we have also analysed the constraint equations for this
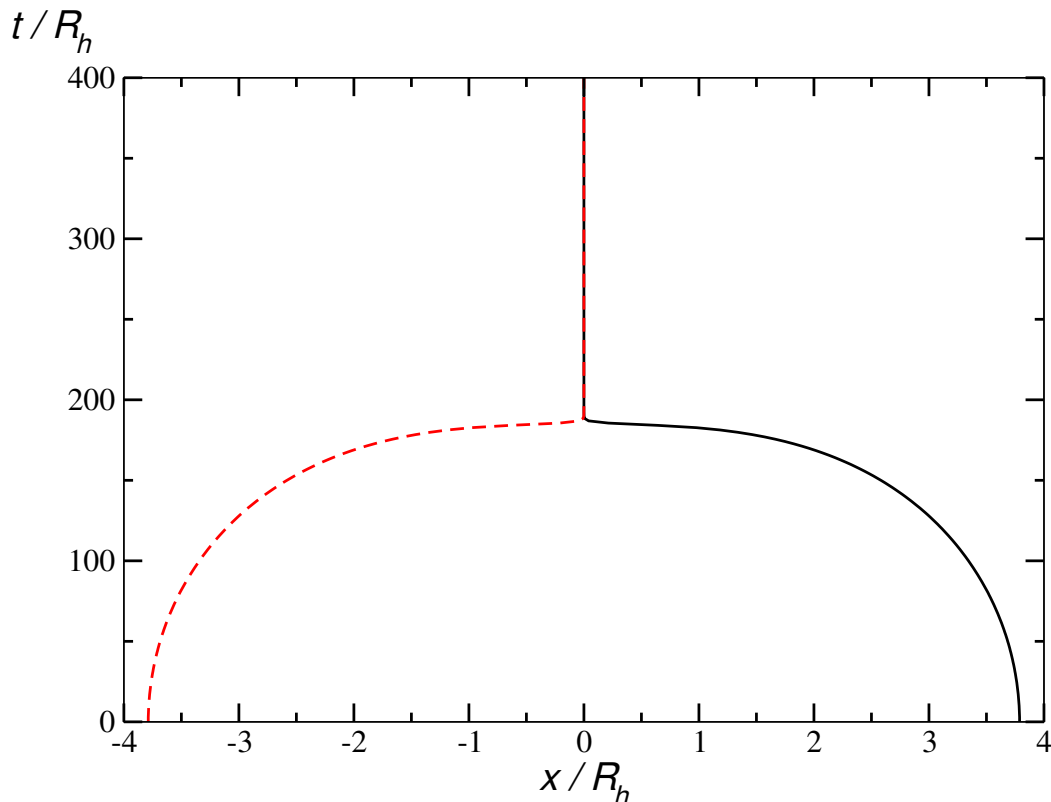
Fig. 3.2 BH trajectories for an equal-mass head-on collision of two non-spinning holes initially at rest in $D = 7$ dimensions. The collision takes place along the x axis.

configuration. A snapshot of the Hamiltonian constraint, Eq. (3.13), along the collision axis at evolution time $t = 80\ R_h$ is shown in Fig. 3.3. In this figure, the result obtained for the high resolution run has been amplified by a factor of four expected for second-order convergence. The overlap of the two curves demonstrates convergence at second order, compatible with the numerical scheme that employs second and fourth-order accurate discretisation and interpolation techniques. We have performed the same analysis for the Hamiltonian and momentum constraints at several points in time and observe the same second-order convergence of both constraints throughout infall and merger. Note that only one BH is present on the computational domain (at about $x = 2.5$ in the figure) because of the octant symmetry. The other BH is represented in this simulation through the symmetric boundary conditions imposed at $x = 0$.
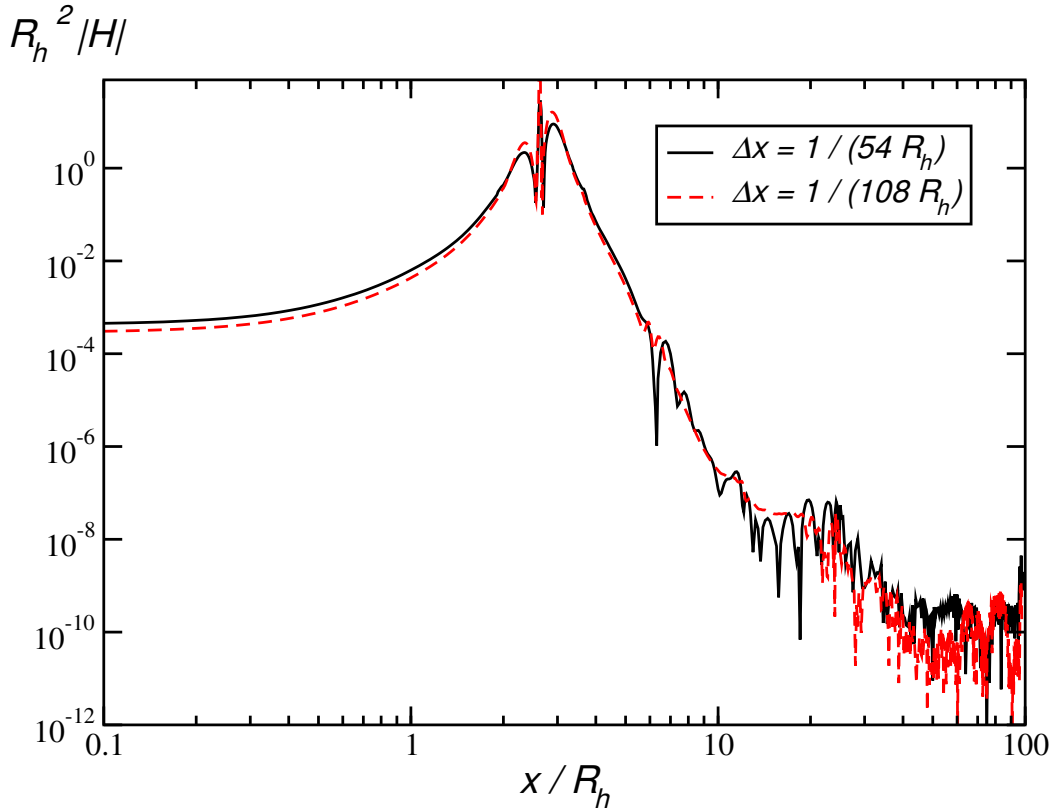
Fig. 3.3 The Hamiltonian constraint along the collision axis obtained for a BH head-on collision starting from rest using resolution parameters $\Delta x = R_h/52$ (solid, black curve) and $\Delta x = R_h/104$ (dashed, red curve). The latter has been amplified by a factor of four corresponding to second-order convergence.

3.6 Conclusions

In the presence of rotational symmetry, the Einstein equations simplify considerably and the generation of numerical solutions to these equations can be implemented with significant improvements in computational cost and the required amount of computer memory. The Cartoon method proposed in [223] was the first technique designed with the particular goal of efficiently modelling axisymmetric spacetimes in 3+1 numerical relativity. A modification, often dubbed the modified Cartoon method [133] used relations between tensor components in place of spatial interpolation operations, which not only eliminates the need of introducing a few extra grid points in the symmetry directions, but also allows for a particularly convenient generalisation to an arbitrary number of spacetime dimensions and number of rotational symmetries [100, 224, 225].

In this work, we have presented in detail the complete set of equations as obtained for the BSSN formulation of the Einstein equations in D spacetime dimensions with

$SO(D-d)$ isometry where $d \in \{1, 2, \ldots, D-2\}$. Furthermore, we note the presence of extra terms for the case $d = D-2$, where the symmetry condition allows for a wider class of components of tensor densities to remain non-zero. Finally, we have compiled a list of terms involving division by the quasi-radial coordinate (the z direction in our case) and illustrate how all irregularities at the origin $z = 0$ can be cured through equivalence with manifestly regular expressions. Even though we used the BSSN formulation for our discussion, the recipes detailed here can be applied straightforwardly to other popular formulations of the Einstein equations such as the generalised harmonic gauge [131, 133] or the conformal $Z4$ [144, 146] systems.

As an example, we have presented results from a head-on collision from rest of two equal-mass, non-spinning BHs in $D = 7$ spacetime dimensions. Following a rather slow acceleration phase, due to the rapid diminishing of the gravitational force with distance, the two BHs merge and we observe second-order convergence of the constraints. This confirms in yet another type of application the remarkable robustness observed for the modified Cartoon method in applications to spinning BHs [100] or high-energy collisions in $D = 5$ [112]. This seemingly superior robustness as compared with the method of reduction by isometry developed in [212] is, at present, empirical but merits further investigation at the analytic level.

Chapter 4

Higher Dimensional Gravitational Wave Extraction Using Weyl Scalars

This chapter, as well as Appendix B, is based on [115], authored in collaboration with Ulrich Sperhake. The formalism in this chapter was developed by the author and the calculations were verified by U. Sperhake. The numerical wave extraction code used to calculate the results shown in this chapter was developed by the author and independently verified by U. Sperhake.

4.1 Introduction

Gravitational waves entered the limelight with the recent detection of GW150914 [5] which not only constitutes the first observation of a black-hole binary system, but also marks a true milestone in gravitational physics. This breakthrough has opened a qualitatively new path for measuring BH parameters [229, 230], testing Einstein's theory of general relativity [7] and probing extreme astrophysical objects and their formation history [6], and substantially broadens the scope of multi-messenger astronomy [231]. GW modelling, however, finds important applications beyond the revolutionary field of GW astronomy. Many fundamental questions in general relativity in $D = 4$ and $D > 4$ spacetime dimensions concern the stability of strong-gravity sources (see [173, 197, 232, 107, 100, 108, 233, 234] and references therein) in the context of cosmic censorship violation, the solutions' significance as physical objects or expanding our understanding of the strong-field regime of general relativity. As we

have discussed in Section 1.1.1, GW emission represents a channel for mass-energy loss in ultra-relativistic collisions that are studied in the context of the so-called TeV gravity scenarios that may explain the hierarchy problem in physics; for further reviews see e.g. [235, 236].

The calculation of GW signals in the theoretical modelling of $D = 4$ dimensional sources in the framework of general relativity has been increasingly well understood following seminal work by Pirani, Bondi, Sachs and others in the 1950s and 1960s; see e.g. [237–240, 176, 180, 181] and [241] for a review. Applications are now routinely found in numerical and (semi-)analytic calculations [242–246, 194, 189, 247, 179, 248] even though care needs to be taken when applied to numerical simulations on finite domains [186].

The numerical study of solutions to Einstein's equations has proven incredibly useful for understanding the behaviour of black holes and other compact objects. Most recently, the application of numerical relativity in the generation of gravitational waveform templates for GW data analysis [249, 248, 250–254] contributed to the above mentioned detection of GW150914.

The wave extraction techniques presently used in numerical simulations of astrophysical GW sources can be classified as follows: perturbative methods based on the formalism developed by Regge, Wheeler, Zerilli and Moncrief [173, 197, 175]; application of the quadrupole formula [255] in matter simulations [256, 257]; a method using the Landau-Lifshitz pseudo-tensor [167, 258] ; Cauchy characteristic extraction [170, 169, 171]; and, probably the most popular technique, using the Weyl scalars from the Newman-Penrose formalism [176, 89, 139, 140, 192, 259–261].

The calculation of GWs in higher dimensional relativity requires generalisation of these techniques to $D > 4$. The extraction of the GW energy flux from the Landau-Lifshitz pseudotensor has been generalised straightforwardly to higher dimensions in [262, 168]. An extension of the Regge-Wheeler-Zerilli-Moncrief formalism for perturbations of spherically symmetric background spacetimes is available in the form of the Kodama and Ishibashi formalism [198, 263] and forms the basis of the wave extraction techniques developed in [110, 264], discussed in Section 2.6.3. Even though both of these methods are in practice applied at finite extraction radius, their predictions have been found to agree within a $\sim 1\,\%$ error tolerance when applied to BH head-on collisions starting from rest in $D = 5$ [113]. Recent years have also seen considerable progress in the understanding of the peeling properties of the Weyl tensor; see [265, 266] and references therein.

In particular, Godazgar & Reall [265] have performed a decomposition of the Weyl tensor in higher dimensions, and derived a generalisation of the Newman-Penrose formalism for wave extraction to $D > 4$. This analysis provides us with a quantity analogous to the Weyl scalar Ψ_4, from which we can calculate the energy radiated in gravitational waves in a similar fashion to the method in $D = 4$. The one qualitative difference between the $D = 4$ and $D > 4$ cases comes in the availability of a mode decomposition of the gravitational wave. In the case $D = 4$ we can project the Weyl scalar onto spin weighted spherical harmonics, due to the decoupling of the equations of motion as shown by Teukolsky [267, 185]. In higher dimensions however, a set of conditions identified as sufficient for decoupling are not satisfied in black hole spacetimes [268], and so at present we are unable to project out the angular dependence of the gravitational wave energy. The numerical implementation of this formalism and probing the accuracy for a concrete example application is the subject of this chapter.

For the simulations presented in this chapter, in which this wave extraction formalism is implemented, we evolve the D dimensional BSSN equations in effective $3 + 1$ form, using the modified Cartoon formalism as detailed in Chapter 3. The relevant expressions for the GW computation, however, will be expressed in terms of the Arnowitt-Deser-Misner [118] variables, and the formalism as presented here can be straightforwardly applied in other common evolution systems used in numerical relativity.

The chapter is structured as follows. In Section 4.2 we recapitulate the key results of [265] which sets up the formalism. In Section 4.3 we put the formalism into a form compatible with the modified Cartoon dimensional reduction of our simulations. In Section 4.4 we describe the numerical set up used in our simulations, analyse the energy radiated in BH collisions in $D = 6$ and compare the predictions with literature results based on alternative wave extraction techniques.

4.2   Theoretical formalism

Our wave extraction from numerical BH simulations in $D > 4$ dimensions is based on the formalism developed by Godazgar & Reall [265, 269, 270]. In this section, we summarise the key findings and expressions from their work.

The derivation [265] is based on the definition of asymptotic flatness using Bondi coordinates [181] $(u, \mathfrak{r}, \phi^\alpha)$ where u is retarded time, $\mathfrak{r}$ the radius and ϕ^α are $D - 2$ angular coordinates covering the unit $D - 2$ sphere. A spacetime is asymptotically flat at future null infinity [270] if the metric outside a cylindrical world tube of finite

radius can be written in terms of functions $\mathcal{A}(u, \mathfrak{r}, \phi^\alpha)$, $\mathcal{B}(u, \mathfrak{r}, \phi^\alpha)$, $\mathcal{C}(u, \mathfrak{r}, \phi^\alpha)$ as

$$ds^2 = -\mathcal{A}e^{\mathcal{B}}du^2 - 2e^{\mathcal{B}}du\,d\mathfrak{r} + \mathfrak{r}^2 h_{\alpha\beta}(d\phi^\alpha + \mathcal{C}^\alpha du)(d\phi^\beta + \mathcal{C}^\beta du)\,, \qquad (4.1)$$

with $\det h_{\alpha\beta} = \det \omega_{\alpha\beta}$ where $\omega_{\alpha\beta}$ is the unit metric on the $D-2$ sphere. For an asymptotically flat spacetime $h_{\alpha\beta}$ can be expanded as [270]

$$h_{\alpha\beta} = \omega_{\alpha\beta}(\phi^\gamma) + \sum_{s \geq 0} \frac{h_{\alpha\beta}^{(s+1)}(u, \phi^\gamma)}{\mathfrak{r}^{D/2+s-1}}\,, \qquad (4.2)$$

and the Bondi news function is obtained from this expansion as the leading-order correction $h_{\alpha\beta}^{(1)}$.

In analogy with the $D = 4$ case, a null frame of vectors is constructed which is asymptotically given by [1]

$$l = -\frac{\partial}{\partial \mathfrak{r}}, \quad k = \frac{\partial}{\partial u} - \frac{1}{2}\frac{\partial}{\partial \mathfrak{r}}, \quad m_{(\alpha)} = \frac{\partial}{\partial \phi^\alpha}\,. \qquad (4.3)$$

Note that all the tetrad vectors are real in contrast to the $D = 4$ dimensional case where the two vectors $m_{(2)}$ and $m_{(3)}$ are often written as two complex null vectors. Next, the components of the Weyl tensor are projected onto the frame (4.3) and the leading order term in the radial coordinate is extracted. Following [265], we denote this quantity by Ω' and its components are given by

$$\Omega'_{(\alpha)(\beta)} \equiv C_{ABCD}k^A m_{(\alpha)}^B k^C m_{(\beta)}^D = -\frac{1}{2}\frac{\hat{e}_{(\alpha)}^\mu \hat{e}_{(\beta)}^\nu \ddot{h}_{\mu\nu}^{(1)}}{\mathfrak{r}^{D/2-1}} + \mathcal{O}(\mathfrak{r}^{-D/2})\,. \qquad (4.4)$$

Here $\hat{e}_{(\alpha)}^\beta$ denote a set of vectors forming an orthonormal basis for the unit metric $\omega_{\alpha\beta}$ on the $D-2$ sphere. In practice, this basis is constructed using Gram-Schmidt orthonormalisation starting with the radial unit vector.

As with the Newman-Penrose scalar Ψ_4 in the four dimensional case, we note that this is the contraction of the Weyl tensor with the ingoing null vector twice and two spatial vectors. Whereas in $D = 4$ the two polarisations of the gravitational waves are

---

[1]As in Section 2.6.1, we have freedom in our choice of frame. Again, we choose to construct the higher dimensional quasi-Kinnersley frame [184, 188] in order to naturally compare our formalism with the $D = 4$ case. The error arising from the use of an asymptotic form of the tetrad at finite extraction radii is mitigated by extracting at various radii and extrapolating to infinity [248] and we pursue this approach, too, in this work.

encoded in the real and imaginary parts of Ψ_4, here $\Omega'_{(\alpha)(\beta)}$ is purely real, with the α, β labels providing the different polarisations. By counting the independent components of the symmetric, tracefree $(D-2) \times (D-2)$ matrix $\Omega'_{(\alpha)(\beta)}$, we obtain $D(D-3)/2$ degrees of freedom, which agrees with the number of polarisation states of the graviton in D dimensions. Equivalently, this is the number of components that determine the D dimensional metric, $D(D+1)/2$, minus D degrees of freedom due to diffeomorphism invariance, and a further D degrees of freedom from the Bianchi identities.

The final ingredient for extracting the energy radiated in GWs is the rate of change of the Bondi mass given by [270]

$$\dot{M}(u) = \frac{1}{32\pi} \int_{S^{D-2}} \dot{h}^{(1)}_{\alpha\beta} \dot{h}^{(1)\alpha\beta} d\Omega \,. \tag{4.5}$$

By substituting in for $\dot{h}^{(1)}_{\alpha\beta}$ from the definition of $\Omega'_{(\alpha)(\beta)}$ we obtain an expression for the mass loss.

$$\dot{M}(u) = -\lim_{\mathbf{r}\to\infty} \frac{\mathbf{r}^{D-2}}{8\pi} \int_{S^{D-2}} \left(\int_{-\infty}^{u} \Omega'_{(\alpha)(\beta)}(\tilde{u}, \mathbf{r}, \phi^\gamma) d\tilde{u} \right)^2 d\Omega \,, \tag{4.6}$$

where the notation $(\ldots)^2$ implies summation over the (α), (β) labels inside the parentheses, and $d\Omega$ denotes the area element of the $D-2$ sphere. In practice, we will apply Eq. (4.6) at constant radius $\mathbf{r}$, therefore replace retarded time u with "normal" time t and start the integration at $t=0$ rather than $-\infty$, assuming that GWs generated prior to the start of the simulation can be neglected.

4.3 Modified Cartoon implementation

The formalism summarised in the previous section is valid in generic D dimensional spacetimes with or without symmetries. We now assume that the spacetime under consideration obeys $SO(D-d)$ isometry with $1 \le d \le D-3$, and will derive the expressions required for applying the GW extraction formalism of Sec. 4.2 to numerical simulations employing the modified Cartoon method.

Throughout this derivation, we will make use of the expressions for scalars, vectors and tensors in spacetimes with $SO(D-d)$ symmetry and the regularisation of their components at $z=0$ as listed in Appendix A. The key result of these relations for our purposes is that the ADM variables α, β^I, γ_{IJ}, K_{IJ} for a spacetime with $SO(D-d)$ isometry can be expressed completely in terms of their d dimensional components β^i,

γ_{ij} and K_{ij} as well as two additional functions γ_{ww} and K_{ww} according to

$$\beta^I = (\beta^i, 0),$$

$$\gamma_{IJ} = \begin{pmatrix} \gamma_{ij} & 0 \\ 0 & \delta_{ab}\gamma_{ww} \end{pmatrix},$$

$$K_{IJ} = \begin{pmatrix} K_{ij} & 0 \\ 0 & \delta_{ab}K_{ww} \end{pmatrix}, \tag{4.7}$$

while the scalar α remains unchanged.

From the viewpoint of numerical applications, the key relations of the procedure reviewed in Sec. 4.2 are Eqs. (4.4) and (4.6). The first provides $\Omega'_{(\alpha)(\beta)}$ in terms of the Weyl tensor and the normal frame, and the second tells us how to calculate the mass loss from $\Omega'_{(\alpha)(\beta)}$. The latter is a straightforward integration conveniently applied as a post processing operation, so that we can focus here on the former equation. For this purpose, we first note that in practice wave extraction is performed in the wave zone far away from the sources. Even if the sources are made up of non-trivial energy matter fields, the GW signal is calculated in vacuum where the Weyl and Riemann tensors are the same. Our task at hand is then twofold: (i) calculate the Riemann tensor from the ADM variables and (ii) to construct a null frame. These two tasks are the subject of the remainder of this section.

4.3.1 The Riemann tensor

The $(D-1)+1$ splitting of the Riemann tensor

To calculate the Riemann tensor, we will start with its projections onto the spatial hypersurfaces, which we recall are given by the Gauss-Codazzi relations used in the standard ADM splitting of the Einstein Equations, which we recap here,

$$\perp R_{ABCD} = \mathcal{R}_{ABCD} + K_{AC}K_{BD} - K_{AD}K_{CB}, \tag{4.8}$$

$$\perp R_{A0CD} \equiv \perp(R_{ABCD}n^B) = -D_C K_{AD} + D_D K_{AC}, \tag{4.9}$$

$$\perp R_{A0C0} \equiv \perp(R_{ABCD}n^B n^D) = \perp R_{AC} + \mathcal{R}_{AC} + K K_{AC} - K_{AE}K^E{}_C$$

$$= \mathcal{R}_{AC} + K K_{AC} - K_{AE}K^E{}_C, \tag{4.10}$$

where in the last line we used the fact that in vacuum R_{AC} and, hence, its projection vanishes (note, however, that in general $\mathcal{R}_{AC} \neq 0$ even in vacuum). Furthermore

$D_C K_{AD} = \partial_C K_{AD} - \Gamma^B_{CA} K_{BD} - \Gamma^B_{CD} K_{AB}$ is the covariant derivative of the extrinsic curvature defined on the spatial hypersurface, with Christoffel symbols calculated from the induced metric γ_{AB}. Equations (4.8)-(4.10) tell us how to reconstruct the full D dimensional Riemann tensor from $D - 1$ dimensional quantities defined on the spatial hypersurfaces which foliate our spacetime.

From this point on, we will use coordinates adapted to the $(D - 1) + 1$ split. In such coordinates, we can replace in Eqs. (4.8)-(4.10) the spacetime indices A, B, ... on the left and right-hand side by spatial indices I, J, ... while the time components of the spacetime Riemann tensor are taken into account through the contractions with the unit timelike normal n^A and which we denote with the suffix 0 in (4.9), (4.10). Note that more than two contractions of the Riemann tensor with the timelike unit normal n^A vanish by symmetry of the Riemann tensor.

The Riemann tensor in $SO(D - 3)$ symmetry

The expressions given in the previous subsection for the components of the Riemann tensor are valid for general spacetimes with or without symmetries. In this section, we will work out the form of the components of the Riemann tensor in spacetimes with $SO(D - d)$ isometry for $1 \le d \le D - 3$.

For this purpose we recall the Cartesian coordinate system $X^I = (x^{\hat{i}}, z, w^a)$ of Eq. (2.1), adapted to a spacetime that is symmetric under rotations in any plane spanned by two of the (z, w^a). We discuss in turn how the terms appearing on the right-hand sides of Eqs. (4.8)-(4.10) simplify under this symmetry. We begin with the components of the spatial Riemann tensor, given in terms of the spatial metric and Christoffel symbols by

$$
\begin{aligned}
\mathcal{R}_{IJKL} =& \frac{1}{2} \left(\partial_L \partial_I \gamma_{JK} + \partial_K \partial_J \gamma_{IL} - \partial_K \partial_I \gamma_{JL} - \partial_L \partial_J \gamma_{IK} \right) \\
& - \gamma_{MN} \Gamma^N_{IK} \Gamma^M_{JL} + \gamma_{MN} \Gamma^N_{IL} \Gamma^M_{JK} .
\end{aligned}
\tag{4.11}
$$

The rotational symmetry imposes conditions on the derivatives of the metric, the Christoffel symbols and the components of the Riemann tensor that are obtained in complete analogy to the derivation in Section 3.2.2 and Appendix A. We thus calculate all components of the Riemann tensor, where its indices can vary over the coordinates

inside and outside the computational domain, and obtain

$$\mathcal{R}_{ijkl} = \frac{1}{2}\left(\partial_l\partial_i\gamma_{jk} + \partial_k\partial_j\gamma_{il} - \partial_k\partial_i\gamma_{jl} - \partial_l\partial_j\gamma_{ik}\right) - \gamma_{mn}\Gamma^n_{ik}\Gamma^m_{jl} + \gamma_{mn}\Gamma^n_{il}\Gamma^m_{jk}, \quad (4.12)$$

$$\mathcal{R}_{ajkl} = 0, \quad (4.13)$$

$$\mathcal{R}_{iajb} = \delta_{ab}\mathcal{R}_{iwjw}, \quad (4.14)$$

$$\mathcal{R}_{iwjw} \equiv \frac{\partial_{(i}\gamma_{j)z} - \delta_{z(j}\partial_{i)}\gamma_{ww}}{z} - \delta_{z(i}\frac{\gamma_{j)z} - \delta_{j)z}\gamma_{ww}}{z^2} - \frac{1}{2}\partial_j\partial_i\gamma_{ww} - \gamma_{mn}\Gamma^n_{ij}\Gamma^m_{ww}$$
$$- \frac{1}{2}\frac{\partial_z\gamma_{ij}}{z} + \frac{\delta_{z(i}\gamma_{j)z} - \delta_{iz}\delta_{jz}\gamma_{ww}}{z^2} + \frac{1}{4}\gamma^{ww}\partial_i\gamma_{ww}\partial_j\gamma_{ww}, \quad (4.15)$$

$$\Gamma^m_{ww} \equiv -\frac{1}{2}\gamma^{ml}\partial_l\gamma_{ww} + \frac{\delta^m_z - \gamma^{mz}\gamma_{ww}}{z}, \quad (4.16)$$

$$\mathcal{R}_{abcl} = 0, \quad (4.17)$$

$$\mathcal{R}_{abcd} = (\delta_{ac}\delta_{bd} - \delta_{bc}\delta_{ad})\mathcal{R}_{wuwu}, \quad (4.18)$$

$$\mathcal{R}_{wuwu} \equiv -\frac{1}{4}\gamma^{mn}\partial_m\gamma_{ww}\partial_n\gamma_{ww} - \gamma_{ww}\frac{\gamma^{zm}}{z}\partial_m\gamma_{ww} + \frac{\gamma_{ww} - \gamma^{zz}\gamma_{ww}^2}{z^2}. \quad (4.19)$$

For the right-hand side of Eq. (4.10), we also need the spatial Ricci tensor which is obtained from contraction of the Riemann tensor over the first and third index. In $SO(D-d)$ symmetry, its non-vanishing components are

$$\mathcal{R}_{ij} = \gamma^{mn}\mathcal{R}_{minj} + (D - d - 1)\gamma^{ww}\mathcal{R}_{iwjw}, \quad (4.20)$$

$$\mathcal{R}_{ab} = \delta_{ab}\mathcal{R}_{ww}, \quad (4.21)$$

$$\mathcal{R}_{ww} \equiv \gamma^{mn}\mathcal{R}_{mwnw} + (D - d - 2)\gamma^{ww}\mathcal{R}_{wuwu}. \quad (4.22)$$

Note that the last expression, $\gamma^{ww}\mathcal{R}_{wuwu}$, does *not* involve a summation over w, but merely stands for the product of γ^{ww} with the expression (4.19).

The components of the extrinsic curvature are given by Eq. (4.7). Its derivative is directly obtained from Eqs (A.1 - A.12) in Appendix A and can be written as

$$D_iK_{jk} = \partial_iK_{jk} - \Gamma^l_{ij}K_{kl} - \Gamma^l_{ik}K_{lj}, \quad (4.23)$$

$$D_iK_{ab} = \delta_{ab}(\partial_iK_{ww} - K_{ww}\gamma^{ww}\partial_i\gamma_{ww}), \quad (4.24)$$

$$D_aK_{bj} = \delta_{ab}\left(\frac{K_{jz} - \delta_{jz}K_{ww}}{z} - \frac{1}{2}K_{ww}\gamma^{ww}\partial_j\gamma_{ww} - K_{ij}\Gamma^i_{ww}\right). \quad (4.25)$$

Next, we plug the expressions assembled in Eqs. (4.11)-(4.25) into the Gauss-Codazzi equations (4.8)-(4.10) where, we recall, early Latin indices A, B, ... are now replaced by I, J, ... following our switch to adapted coordinates. Splitting the index range I

into (i, a) for components inside and outside the computational domain, and recalling that an index 0 denotes contraction with $\boldsymbol{n}$, we can write the resulting components of the spacetime Riemann tensor as

$$R_{ijkl} = \mathcal{R}_{ijkl} + K_{ik}K_{jl} - K_{il}K_{jk}, \tag{4.26}$$

$$R_{ibkd} = \delta_{bd}R_{iwkw}, \tag{4.27}$$

$$R_{iwkw} \equiv \mathcal{R}_{iwkw} + K_{ik}K_{ww}, \tag{4.28}$$

$$R_{abcd} = (\delta_{ac}\delta_{bd} - \delta_{bc}\delta_{ad})(\mathcal{R}_{wuwu} + K_{ww}^2), \tag{4.29}$$

$$R_{ajkl} = R_{abcl} = 0, \tag{4.30}$$

$$R_{i0kl} = D_l K_{ik} - D_k K_{il}, \tag{4.31}$$

$$R_{a0ck} = \delta_{ac}R_{w0wk}, \tag{4.32}$$

$$R_{w0wk} \equiv \partial_k K_{ww} - \frac{1}{2}\gamma^{ww}K_{ww}\partial_k\gamma_{ww} - \frac{K_{kz} - \delta_{kz}K_{ww}}{z} + \Gamma_{ww}^m K_{mk}, \tag{4.33}$$

$$R_{a0cd} = R_{i0kd} = R_{a0kl} = 0, \tag{4.34}$$

$$R_{i0j0} = \mathcal{R}_{ij} + KK_{ij} - K_{im}K_j^m, \tag{4.35}$$

$$K = \gamma^{mn}K_{mn} + (D - d - 1)\gamma^{ww}K_{ww}, \tag{4.36}$$

$$R_{a0b0} = \delta_{ab}R_{w0w0}, \tag{4.37}$$

$$R_{w0w0} \equiv \mathcal{R}_{ww} + (K - \gamma^{ww}K_{ww})K_{ww}, \tag{4.38}$$

$$R_{a0i0} = 0. \tag{4.39}$$

With these expressions, we are able to calculate all components of the spacetime Riemann tensor directly from the ADM variables γ_{ij}, γ_{ww}, K_{ij} and K_{ww} and their spatial derivatives. There remains, however, one subtlety arising from the presence of terms containing explicit division by z. Numerical codes employing vertex centred grids need to evaluate these terms at $z = 0$. As described in detail in Appendix B.1, all the above terms involving division by z are indeed regular and can be rewritten in a form where this is manifest with no divisions by zero.

4.3.2 The null frame

The null frame we need for the projections of the Weyl tensor consists of D unit vectors as given in Eq. (4.3): (i) the ingoing null vector k^A, (ii) the outgoing null vector l^A which, however, does not explicitly appear in the scalars (4.4) for the outgoing

gravitational radiation, and (iii) the $(D-2)$ vectors $m^A_{(\alpha)}$ pointing in the angular directions on the sphere.

We begin this construction with the $D-2$ unit basis vectors on the $D-2$ sphere, $m^A_{(\alpha)}$, and recall for this purpose Eq. (2.4) that relates our spherical coordinates (r, ϕ^α) to the Cartesian $(x^{\hat{i}}, z, w^a)$. The set of spatial vectors, although not yet in orthonormalised form, then consists of a radial vector denoted by $\tilde{m}_{(1)}$ and $D-2$ angular vectors $\tilde{m}_{(\alpha)}$ whose components in Cartesian coordinates $X^I = (x^{\hat{i}}, z, w^a)$ on the computational domain $w^a = 0$ are obtained through the chain rule

$$\tilde{m}_{(1)} = \frac{\partial}{\partial r} = \frac{\partial X^I}{\partial r} \frac{\partial}{\partial X^I} \quad \Rightarrow \quad \tilde{m}^I_{(1)} = \frac{1}{r}(x^1, \, \ldots, \, x^{d-1}, \, z, \, 0, \, \ldots, \, 0)\,, \tag{4.40}$$

$$\tilde{m}_{(\alpha)} = \frac{\partial}{\partial \phi^\alpha} = \frac{\partial X^I}{\partial \phi^\alpha} \frac{\partial}{\partial X^I}\,, \tag{4.41}$$

We can ignore time components here, because our coordinates are adapted to the space-time split, so that all spatial vectors have vanishing time components and this feature is preserved under the eventual Gram-Schmidt orthonormalisation. Plugging Eq. (2.4) into (4.41), we obtain for $\tilde{m}_{(\alpha)}$ (after rescaling by $r \times \sin \phi^2 \times \ldots \times \sin \phi^\alpha$)

$$\underbrace{\begin{pmatrix} -\sum\limits_{s=2}^{D-1}(w^s)^2 \\ w^1 w^2 \\ \vdots \\ \vdots \\ \vdots \\ w^1 w^{D-1} \end{pmatrix}}_{=\tilde{m}^I_{(2)}}, \ldots, \underbrace{\begin{pmatrix} 0 \\ \vdots \\ 0 \end{pmatrix} \Big\} (\alpha-2)\times \\ -\sum\limits_{s=\alpha}^{D-1}(w^s)^2 \\ w^{\alpha-1} w^\alpha \\ \vdots \\ w^{\alpha-1} w^{D-2} \\ w^{\alpha-1} w^{D-1} \end{pmatrix}}_{=\tilde{m}^I_{(\alpha)}}, \ldots, \underbrace{\begin{pmatrix} 0 \\ \vdots \\ \vdots \\ \vdots \\ \vdots \\ 0 \\ -(w^{D-2})^2 - (w^{D-1})^2 \\ w^{D-3} w^{D-2} \\ w^{D-3} w^{D-1} \end{pmatrix}}_{=\tilde{m}^I_{(D-2)}}, \underbrace{\begin{pmatrix} 0 \\ \vdots \\ \vdots \\ \vdots \\ \vdots \\ 0 \\ 0 \\ -(w^{D-1})^2 \\ w^{D-2} w^{D-1} \end{pmatrix}}_{=\tilde{m}^I_{(D-1)}}. \tag{4.42}$$

In $D = 4$ dimensions, these vectors, together with $\tilde{m}_{(1)}$ of Eq. (4.40) would form the starting point for Gram-Schmidt orthonormalisation; see e.g. Appendix C in [192]. In $D \geq 5$ dimensional spacetimes with $SO(D-d)$ symmetry, however, we face an additional difficulty: on the computational domain $w^a = 0$, all components of the vectors $\tilde{m}_{(d+1)}, \ldots, \tilde{m}_{(D-1)}$ vanish and their normalisation would result in divisions of zero by zero. This difficulty is overcome by rewriting the Cartesian components of the

vectors in terms of spherical coordinates and then exploiting the freedom we have in suitably orienting the frame. The details of this procedure are given in Appendix B.2 where we derive a manifestly regular set of spatial vectors given by

$$\tilde{m}^A_{(1)} = (0 \mid x^1, \ldots, x^d \mid 0, \ldots, 0)\,, \tag{4.43}$$

$$\tilde{m}^A_{(2)} = (0 \mid -\rho_2^2, \ x^1 x^2, \ x^1 x^3, \ \ldots, \ x^1 x^d \mid 0, \ \ldots, \ 0)\,, \tag{4.44}$$

$$\cdots\cdots$$

$$\tilde{m}^A_{(\hat{\alpha})} = (0, \mid \underbrace{0, \ \ldots, \ 0}_{(\hat{\alpha}-2)\times}, \ -\rho_{\hat{\alpha}}^2, \ x^{\hat{\alpha}-1}x^{\hat{\alpha}}, \ \ldots, \ x^{\hat{\alpha}-1}x^d \mid 0, \ \ldots, \ 0)\,, \tag{4.45}$$

$$\cdots\cdots$$

$$\tilde{m}^A_{(d)} = (0, \mid \underbrace{0, \ \ldots, \ 0}_{(d-2)\times}, \ -x^d, \ x^{d-1} \mid 0, \ \ldots, \ 0)\,, \tag{4.46}$$

$$\tilde{m}^A_{(d+1)} = (0 \mid \underbrace{0, \ \ldots, \ 0}_{d\times} \mid 1, \ 0, \ \ldots, \ 0)\,, \tag{4.47}$$

$$\cdots\cdots$$

$$\tilde{m}^A_{(D-1)} = (0 \mid \underbrace{0, \ \ldots, \ 0}_{d\times} \mid 0, \ \ldots, \ 0, \ 1)\,, \tag{4.48}$$

where $\rho_I = \sum_{s=I}^{D-1}(w^s)^2$, we have restored, for completeness, the time component and the vertical bars highlight the three component sectors: time, spatial on-domain, and spatial off-domain. Equations (4.47)-(4.48) can, of course, be conveniently written in short-hand notation as $\tilde{m}^A_{(a)} = \delta^A{}_a$. For the special case $d = 3$, the vectors are given by

$$\tilde{m}^A_{(1)} = (0 \mid x, \ y, \ z \mid 0, \ldots, \ 0)\,, \tag{4.49}$$

$$\tilde{m}^A_{(2)} = (0 \mid -y^2 - z^2, \ xy, \ xz \mid 0, \ldots, \ 0)\,, \tag{4.50}$$

$$\tilde{m}^A_{(3)} = (0 \mid 0, \ -z, \ y \mid 0, \ \ldots, \ 0)\,, \tag{4.51}$$

$$\tilde{m}^A_{(4)} = (0 \mid 0, \ 0, \ 0 \mid 1, \ 0, \ \ldots, \ 0)\,, \tag{4.52}$$

$$\cdots\cdots \tag{4.53}$$

$$\tilde{m}^A_{(D-1)} = (0 \mid 0, \ 0, \ 0 \mid 0, \ \ldots, \ 0, \ 1)\,, \tag{4.54}$$

The next step is to orthonormalise these vectors. Clearly the vectors $m^A_{(a)}$ with components in the w^a dimensions are normalised by:

$$m^A_{(a)} = \frac{1}{\sqrt{\gamma_{ww}}} \delta^A{}_a \tag{4.55}$$

For the remaining d vectors given by Eqs. (4.43)-(4.46) or, for $d = 3$, the spatial triad consisting of the three vectors (4.49)-(4.51), we use standard Gram-Schmidt orthonormalisation. Note that under this procedure the components outside the computational domain of these vectors remain zero and can therefore be ignored.

The final element of the null frame we need is the ingoing null vector, which we call k^A. Given in [265] as $\partial/\partial u - \frac{1}{2}\partial/\partial \mathbf{r}$ asymptotically, we transform out of Bondi coordinates, sending $(u, \mathbf{r}) \to (t, r)$ and furthermore use the freedom of rescaling this null vector by applying a constant factor of[2] $\sqrt{2}$

$$k^A = \frac{1}{\sqrt{2}}\left(n^A - m^A_{(1)}\right) \tag{4.56}$$

Expressing the timelike unit normal field n^A in terms of our gauge variables α, β^I we find

$$k^A = \frac{1}{\sqrt{2}}\left(\frac{1}{\alpha}, -\frac{\beta^I}{\alpha} - m^I_{(1)}\right), \tag{4.57}$$

where $\beta^I = (\beta^i, 0, \ldots, 0)$, $m^I_{(1)} = (m^i_{(1)}, 0, \ldots, 0)$. This result provides the ingoing null vector for any choice of d and is the version implemented in the code.

4.3.3 The projections of the Weyl tensor

Finally, we calculate the projections of the Weyl tensor that encode the outgoing gravitational radiation

$$\Omega'_{(\alpha)(\beta)} = R_{ABCD}k^A m^B_{(\alpha)}k^C m^D_{(\beta)}, \tag{4.58}$$

[cf. Eq. (4.4)] where k^A is given by Eq. (4.57) and the normal frame vectors $m_{(2)}, \ldots, m_{(D-1)}$ are those obtained from Gram-Schmidt orthonormalising the right-hand sides of Eqs. (4.43)-(4.48).

We first note that $\Omega'_{(\alpha)(\beta)}$ is symmetric in $\alpha \leftrightarrow \beta$, so contractions solely with $m_{(2)}, \ldots, m_{(d)}$ will result in $d(d-1)/2$ components $\Omega'_{(\hat{\alpha})(\hat{\beta})}$. For the special case $d = 3$, we obtain the three components $\Omega'_{(2)(2)}, \Omega'_{(2)(3)}, \Omega'_{(3)(3)}$. The null vector k has vanishing w components and from Eqs. (4.26)-(4.39) we see that all components of the Riemann tensor where an odd number of indices is in the range $a, b, \ldots$ are zero. The only non-vanishing terms involving the Riemann tensor with off-domain indices $a, b, \ldots$, therefore, have either four such indices or two and contain a Kronecker delta δ_{ab}; cf. Eqs. (4.27), (4.29), (4.32), (4.37). As a consequence, the mixed components

---

[2]The convention we adopt here is more common (though not unanimous) in numerical relativity.

$\Omega'_{(\hat{\alpha})(a)} = 0$ and the purely off-domain components $\Omega'_{(a)(b)} \propto \delta_{ab}$. The list of all non-vanishing components $\Omega'_{(\alpha)(\beta)}$ is then given by

$$\Omega'_{(\hat{\alpha})(\hat{\beta})} = \frac{1}{4} \left[R_{0k0l} m^k_{(\hat{\alpha})} m^l_{(\hat{\beta})} - R_{mk0l} m^m_{(1)} m^k_{(\hat{\alpha})} m^l_{(\hat{\beta})} - R_{0kml} m^k_{(\hat{\alpha})} m^m_{(1)} m^l_{(\hat{\beta})} \right.$$
$$\left. + R_{mknl} m^m_{(1)} m^k_{(\hat{\alpha})} m^n_{(1)} m^l_{(\hat{\beta})} \right] , \tag{4.59}$$

$$\Omega'_{(a)(b)} = \delta_{ab} \, \Omega'_{(w)(w)} , \tag{4.60}$$

$$\Omega'_{(w)(w)} = \frac{1}{4\gamma_{ww}} \left[R_{w0w0} - R_{w0wk} m^k_{(1)} - R_{w0wl} m^l_{(1)} + R_{wkwl} m^k_{(1)} m^l_{(1)} \right] , \tag{4.61}$$

where $\hat{\alpha}, \hat{\beta} = 2, \ldots, d$ and all components of the Riemann tensor on the right-hand sides are listed in the set of Eqs. (4.26)-(4.39). In particular, the components R_{w0w0}, R_{w0wk} and R_{wkwl}, which contain indices in the off-domain directions, are obtained from Eqs. (4.38), (4.33) and (4.28), respectively and thus derived directly from quantities computed in the simulation (the γ_{ij}, K_{ij}, γ_{ww} and K_{ww} that appear on the right-hand sides of these equations or enter in the calculation of the spatial Riemann tensor). It should be noted here that $\Omega'_{(\alpha)(\beta)}$ is trace free, and so $\Omega'_{(w)(w)}$ can be calculated from the diagonal terms $\Omega'_{(2)(2)}, \ldots \Omega'_{(d)(d)}$. In a numerical simulation, the components of $\Omega'_{(\alpha)(\beta)}$ are calculated as functions of time and then can be integrated according to Eq. (4.6) to extract the amount of energy radiated in gravitational waves.

4.3.4 $SO(2)$ **symmetry**

In the axisymmetric case $d = D - 2$ there exists only one w direction (off domain). As discussed in Section 4 of [114], and briefly above in Section 3.4, we keep all tensor components as we would in the absence of symmetry, and the modified Cartoon method and, thus, the rotational symmetry, only enters in the calculation of spatial derivatives in the w direction. For $SO(2)$ symmetry, the extraction of gravitational waves therefore proceeds as follows.

- All components of the ADM metric and extrinsic curvature are extracted on the $D - 2$ dimensional computational domain.

- The spatial Riemann tensor and its contractions are directly evaluated using Eq. (4.11) with the relations of Appendix C in [114] for off-domain derivatives.

- The necessary components of the spacetime Riemann tensor and its projections onto the timelike unit normal are evaluated through Eqs. (4.8)-(4.10).

- The null frame is constructed as detailed in Sec. 4.3.2, simply setting $d = D - 2$.

- All the projections of the Weyl tensor onto the null frame vectors are obtained from Eq. (4.59), but now covering the entire range of spatial indices

$$\Omega'_{(\alpha)(\beta)} = \frac{1}{4} \left[R_{0K0L} m^K_{(\alpha)} m^l_{(\beta)} - R_{MK0L} m^M_{(1)} m^K_{(\alpha)} m^L_{(\beta)} - R_{0KML} m^K_{(\alpha)} m^M_{(1)} m^L_{(\beta)} \right.$$
$$\left. + R_{MKNL} m^M_{(1)} m^K_{(\alpha)} m^N_{(1)} m^L_{(\beta)} \right] . \tag{4.62}$$

Note that with the existence of more components of the Riemann tensor, more projections of the Weyl tensor now exist, specifically cross-terms such as $\Omega'_{(2)(w)}$. This can be seen straightforwardly by using $SO(2)$ modified Cartoon terms from appendix C of [114] and the expressions for the full and spatial Riemann tensor given in Eqs. (4.8) and (4.11). For example, we can see that a component such as R_{wijk} is non-zero. This will contribute to terms of the form $\Omega'_{(\hat{\alpha})(w)}$. As already emphasised in [114], the key gain in employing the modified Cartoon method for simulating axisymmetric spacetimes does *not* lie in the elimination of tensor components, but in the dimensional reduction of the computational domain.

4.4   Numerical simulations

In the remainder of this work, we will implement the specific version of the wave extraction for $d = 3$ and $D = 6$ and simulate head-on collisions of equal-mass, non-spinning BHs starting from rest. We will calibrate the numerical uncertainties arising from the numerical discretisation of the equations (fourth order in space and time and second order at the outer and refinement boundaries), the use of large but finite extraction radii and also consider the dependency of the results on the initial separation of the BHs. This type of collisions has already been studied by Witek *et al.* [113] who calculate the GW energy using the Kodama-Ishibashi formalism, which enables us to compare our findings with their values.

4.4.1   Code infrastructure and numerical set-up

We perform evolutions using the LEAN code [192, 227] which is based on CACTUS [220, 228] and uses CARPET [219, 218] for mesh refinement. The Einstein equations are implemented in the BSSN formulation with the modified Cartoon method employed to reduce computational cost. For the explicit equations under the $SO(D-3)$ symmetry that we use, see Section 3.3.2 with parameter $d = 3$. Without loss of generality, we perform collisions along the x-axis, such that the centre-of mass is located at the origin of the grid, and impose octant symmetry.

   We specify the gauge in terms of the "1+log" and "Γ driver" conditions for the lapse function and shift vector, as given by Eqs (2.44 - 2.46) with parameter values given by

$$\partial_t \alpha = \beta^m \partial_m \alpha - 2\alpha K \,, \tag{4.63}$$

$$\partial_t \beta^i = \beta^m \partial_m \beta^i + \frac{1}{4}\tilde{\Gamma}^i - \frac{1}{2^{1/3}R_h}\beta^i \,, \tag{4.64}$$

with initial values $\alpha = 1$, $\beta^i = 0$.

   The BH initial data is calculated using the higher dimensional generalisation of Brill-Lindquist data [154, 271] described in Section 2.4 As mentioned above, we place the BHs on the x axis in the centre-of-mass frame, so that in the equal-mass case, we have $X_{\mathcal{N}}^1 = \pm x_0$ in Eq. (2.43). Our initial configuration is therefore completely specified by the initial separation which we measure in units of the horizon radius R_h of a single BH. The BH mass and the radius R_h are related through the mass parameter μ given by Eq. (2.42).

   The computational domain used for these simulations consists of a set of eight nested refinement levels which we characterise in terms of the following parameters: (i) the resolution h on the innermost level which gets coarser by a factor of two on each consecutive outer level, (ii) the size L of the domain which describes the distance of the outermost edge from the origin, and (iii) the resolution H on the refinement level where the gravitational waves are extracted.

   For each simulation, we calculate the $\Omega'_{(\alpha)(\beta)}$ on our three dimensional computational grid and project them onto a two dimensional array representing a spherical grid at fixed coordinate radius. The data thus obtained on the extraction sphere are inserted into Eq. (4.6). The $\Omega'_{(\alpha)(\beta)}$ are scalars and so in our angular coordinate system do not

depend on $\phi^4, \ldots, \phi^{D-1}$, so the integral over the sphere in (4.6) can be simplified:

$$\dot{M}(u) = - \lim_{r \to \infty} \frac{r^{D-2}}{8\pi} \mathcal{A}_{D-4} \int_0^\pi \int_0^\pi I[\Omega'^2] \, \sin^{D-3}(\phi^2) \, \sin^{D-4}(\phi^3) \, d\phi^3 d\phi^2 \,, \qquad (4.65)$$

where $I[\Omega'^2] \equiv \left(\int_{-\infty}^u \Omega'_{(\alpha)(\beta)} d\tilde{u} \right)^2$. A final integration over time of the variable $\dot{M}$ then gives the total radiated energy.

4.4.2   Numerical results

We begin our numerical study with an estimate of the uncertainty in our GW estimates arising from the discretisation of the equations. For this purpose, we have evolved two BHs initially located at at $x = \pm x_0 = \pm 4.0 \, R_h$ using a computational grid of size $L = 181 \, R_h$ and three resolutions $h_1 = R_h/50.8$, $h_2 = R_h/63.5$ and $h_3 = R_h/76.2$ which corresponds to $H_1 = R_h/2.12$, $H_2 = R_h/2.65$ and $H_3 = R_h/3.17$ in the extraction zone.

We measure the radiated energy in units of the total ADM mass of the spacetime, which for Brill-Lindquist data is given by Eq. (2.42) with $\mu \equiv \mu_1 + \mu_2$, the mass parameters of the initial BHs. The radiated energy as a function of time is shown in the upper panel of Fig. 4.1. The radiation is almost exclusively concentrated within a window of $\Delta t \approx 20 \, R_h$ around merger. During the infall and the post-merger period, in contrast, E_{rad} remains nearly constant. In comparison with collisions in $D = 4$ dimensions, we find the burst of spurious (colloquially referred to as "junk") radiation significantly weaker, presumably because the Brill-Lindquist data in higher D more closely represent two black holes in isolation due to the higher fall-off rate of the gravitational interaction. By comparing the high-resolution result with that obtained for the coarser grids, we can test the order of convergence. To leading order, the numerical result f_h for some variable obtained at finite resolution h is related to the continuum limit solution f by $f = f_h + \mathcal{O}(h^n)$, where n denotes the order of convergence. By evaluating the quotient

$$Q_n = \frac{f_{h_1} - f_{h_2}}{f_{h_2} - f_{h_3}} = \frac{(h_1/h_2)^n - 1}{1 - (h_3/h_2)^n} \,, \qquad (4.66)$$

we can then plot the two differences $f_{h_1} - f_{h_2}$ and $f_{h_2} - f_{h_3}$ and test whether their ratio is consistent with a given value n. The results for our study are shown in the lower panel of Fig. 4.1 which demonstrates that our numerical results converge at fourth order. The discretisation error of the total radiated energy is then obtained as
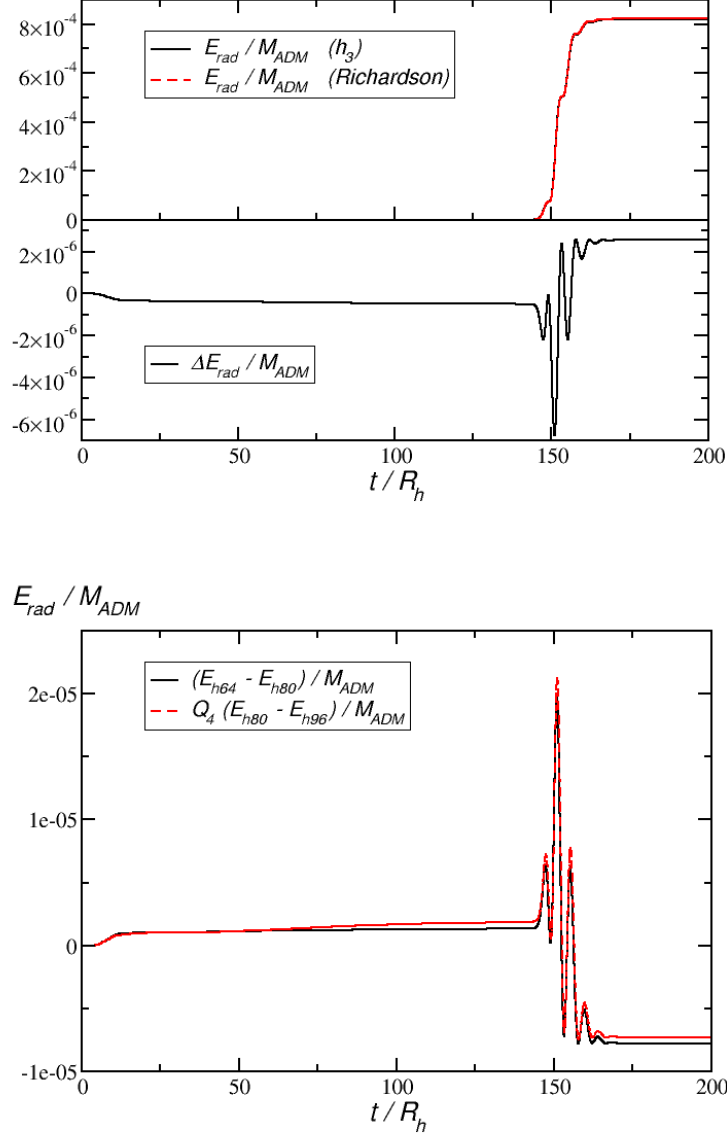
Fig. 4.1 Upper panel: Radiated energy as a function of time obtained for the highest resolution $h_3 = R_h/76.2$ (solid curve) and Richardson extrapolated to infinite resolution assuming fourth-order convergence (dashed curve). The curves are nearly on top of each other and we plot in the lower half of the panel their difference to show the level of agreement. Lower panel: Convergence plot for the radiated energy $E_{\rm rad}$ extracted at $r_{\rm ex} = 50.4 \, R_h$ from an equal-mass collision of two non-spinning BHs in $D = 6$ starting from a separation $8 \, R_h$. The results shown have been obtained using resolutions $h_1 = R_h/50.8$, $h_2 = R_h/63.5$ and $h_3 = R_h/76.2$. The difference in radiated energy between the medium and high-resolution simulations has been rescaled by a factor $Q_4 = 2.784$ expected for fourth-order convergence.

the difference between the finite resolution result and that predicted by Richardson extrapolation (see upper panel in the figure). We obtain for the high-resolution case a total radiated energy $E_{\rm rad} = 8.19 \times 10^{-4} \, M_{\rm ADM}$ with a discretisation error of $\sim 0.4 \, \%$, but note that the error in the cumulative energy peaks at a larger value of a few $\%$ during the sharp increase of $E_{\rm rad}(t)$ marking the merger phase.

A second source of error arises from the extraction at finite radius. Following standard practice (see e.g. [248]), we estimate this uncertainty by extracting the GW energy at a set of seven or eight finite radii in the range 40 R_h to 110 R_h and extrapolating these values assuming a functional dependency

$$E_{\rm rad}(r) = E_{\rm rad}(\infty) + \frac{a}{r} + \mathcal{O}\left(\frac{1}{r^2}\right) , \tag{4.67}$$

where a is a coefficient obtained through the fitting of the numerical data. By applying this procedure, we estimate the uncertainty due to the extraction radius at 0.2 $\%$ at $R_{\rm ex} = 110 \, {\rm R_h}$ and 0.4 $\%$ at $R_{\rm ex} = 60 \, R_h$.

An independent check of our results is available in comparing the radiated energy with the predictions of the perturbative extraction method [110] based on the Kodama-Ishibashi formalism. For this purpose, we have calculated using $h_3 = R_h/76.2$ the gravitational-wave energy radiated in the quadrupole mode as predicted by the Kodama-Ishibashi formalism. Contributions from higher-order multipoles are negligible for this comparison; for odd l they vanish completely by symmetry and for even l up to $l = 8$ they are well below the numerical uncertainty budget. This quadrupole energy is compared with the result obtained from the Weyl tensor in Fig. 4.2. The difference for the total radiated energy is about 0.3 $\%$, though a larger temporary discrepancy for $E_{\rm rad}$ as a function of time is encountered during the steep increase at merger, up to a few $\%$. This discrepancy is within the error budget of the two extraction methods.

Finally, we have measured the dependency of the total radiated energy on the initial separation of the BHs. In addition to the simulations discussed so far, we have performed high-resolution simulations placing the BHs at $x_0 = \pm 7.8 \, R_h$ and $x_0 = \pm 12.8 \, R_h$. We have found very small variations at a level of 0.1 $\%$ in the radiated energy for these cases, well below the combined error budget obtained above. Compared with collisions in $D = 4$ dimensions (see e.g. Table II in [192]), $E_{\rm rad}$ shows significantly weaker variation with initial separation in $D = 6$. We attribute this to the more rapid fall-off of the force of gravity in higher dimensions leading to a prolonged but dynamically slow infall phase which generates barely any GWs.
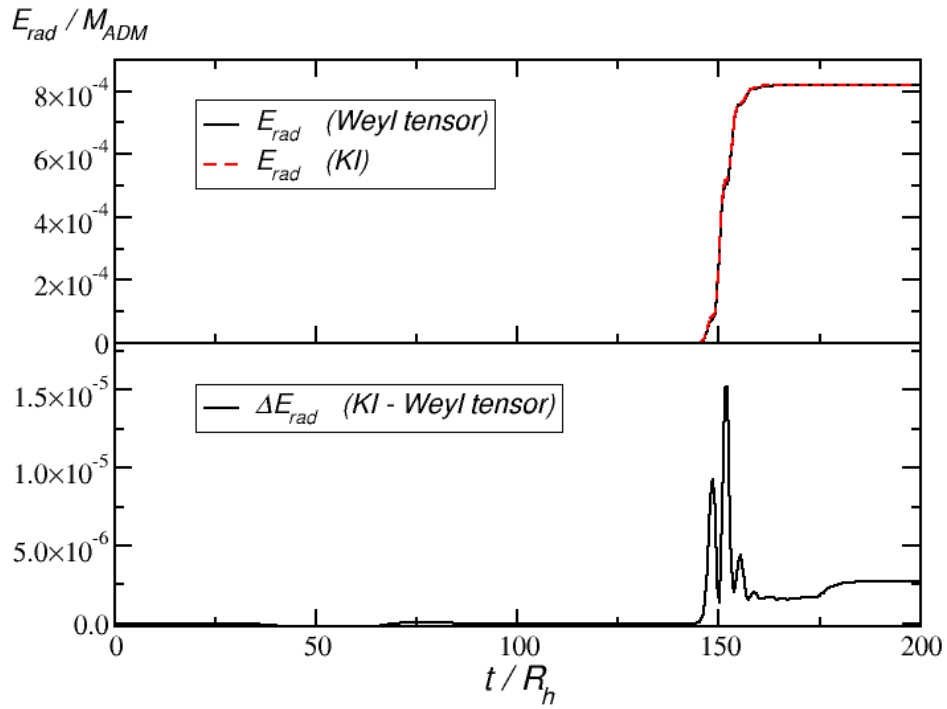
Fig. 4.2 Gravitational wave energy $E_{\rm rad}$ as a function of time using $h_3 = R_h/76.2$ and extracted at $r_{\rm ex} = 50.4\ R_h$ for the $D = 6$ equal-mass head-on collision. The prediction by the new formalism is compared with that of the Kodama-Ishibashi formalism for the quadrupole mode (the higher-order multipoles provide negligible contributions in this case). The bottom panel shows the differences between the two curves.

In summary, we find the total energy radiated in gravitational waves in a head-on collision of two equal-mass, non-spinning BHs to be

$$E_{\text{rad}} = (8.19 \pm 0.05) \times 10^{-4} \ M_{\text{ADM}} \,, \tag{4.68}$$

in excellent agreement with the value $(8.1 \pm 0.4) \times 10^{-4}$ reported in the independent study by [113] using dimensional reduction by isometry and the Kodama-Ishibashi formalism.

4.5 Conclusions

The extraction of gravitational waves from numerical simulations is one of the most important diagnostic tools in studying the strong-field dynamics of compact objects in four as well as higher dimensional spacetimes. In this work we have formulated the Weyl tensor based wave extraction technique of Godazgar & Reall [265] – a higher dimensional generalisation of the Newman-Penrose scalars – in a form suitable for numerical simulations of $D > 4$ dimensional spacetimes with $SO(D-d)$, $1 \leq d \leq D-2$, symmetry employing the modified Cartoon method. The only prerequisite for implementing our formalism is the availability of the ADM variables on each spatial hypersurface of the effective computational domain. These are constructed straightforwardly from all commonly used numerical evolution systems such as BSSN, generalised harmonic or conformal Z4.

The recipe for extracting the GW signal then consists of the following steps.

(1) Computation of the on and off-domain components of the spatial Riemann tensor (which equals the Weyl tensor in the vacuum extraction region) and the derivative of the extrinsic curvature according to Eqs. (4.12)-(4.25).

(2) Reconstruction of the components of the spacetime Riemann tensor as well as its contractions with the unit timelike normal from the quantities of the previous step according to Eqs. (4.26)-(4.39).

(3) Construction of the null-frame vectors through Gram-Schmidt orthonormalising the expressions of Eqs. (4.43)-(4.48) and then using (4.57) for the ingoing null vector.

(4) Calculation of the projections $\Omega'_{(\alpha)(\beta)}$ of the Weyl tensor onto the null frame vectors using Eqs. (4.59)-(4.61).

(5) Calculation of the energy flux in GWs through Eq. (4.6) and integration in time of the flux to obtain the total radiated energy.

The most common case of modelling higher dimensional spacetimes with rotational symmetries is the case of $d = 3$ effective spatial dimensions which allows for straightforward generalisation of existing codes (typically developed for 3+1 spacetimes) and also accommodates sufficiently complex dynamics to cover most of the important applications of higher dimensional numerical relativity. We have, for this purpose, explicitly given the specific expressions of some of our relations for $d = 3$ where these are not trivially derived from their general counterparts.

For testing the efficacy and accuracy of this method, we have applied the wave extraction to the study of equal-mass, non-spinning head-on collisions of BHs starting from rest in $D = 6$ using $d = 3$. We find these collisions to radiate a fraction $(8.19 \pm 0.05) \times 10^{-4}$ of the ADM mass in GWs, in excellent agreement with a previous study [113] employing a perturbative extraction technique based on the Kodama-Ishibashi formalism. We find this energy to be essentially independent of the initial separation which we have varied from 8.0 to 15.6 and 25.6 times the horizon radius of a single BH. We attribute this result to the higher fall-off rate of the gravitational attraction in higher dimensions and the correspondingly slow dynamics during the infall stage.

We finally note that the Weyl tensor based wave extraction ideally complements the perturbative extraction technique of the Kodama-Ishibashi formalism. The latter provides the energy contained in individual (l, m) radiation multipoles but inevitably requires cutoff at some finite l. In contrast, the $\Omega'_{(\alpha)(\beta)}$ facilitate calculation of the total radiation, but without multipolar decomposition. It is by putting both extraction techniques together, that we obtain a comprehensive description of the entire wave signal. Future applications include the stability of highly spinning BHs and their transition from unstable to stable configurations, the wave emission in evolutions of black rings and an extended study of higher dimensional BH collisions over a wider range of dimensionality D, initial boosts and with non-zero impact parameter. These studies require particularly high resolution to accurately model the rapid fall-off of gravity, especially for $D \gg 4$, and are therefore beyond the scope of the present study. However, the foundation for analysing in detail the GW energy emission in these and many more scenarios is now available in as convenient a form as in the more traditional 3+1 explorations of numerical relativity.

Chapter 5

Head-on Black Hole Collisions

This chapter is based on [116], authored in collaboration with Ulrich Sperhake, Emanuele Berti and Vitor Cardoso. Almost all of the numerical simulations of black hole mergers were performed by the author, with the wave extraction code developed in [115] with U. Sperhake, described in Chapter 4. The fitting of the data was performed by E. Berti and V. Cardoso.

5.1 Introduction

The purpose of this chapter is to extend previous results on the low-energy collision of BHs to higher dimensions. This effort was started a few years ago [111, 113], but a combination of gauge issues and difficulties in the regularization of variables in the dimensional reduction method used, the dimensional reduction by isometry of Section 2.7, generated numerical instabilities, restricting all binary BH simulations to $D \leq 6$ spacetime dimensions. Building on earlier work [133, 168] on the so-called *modified Cartoon method*, our previously presented simulations in Chapters 3, 4 have not shown these instabilities. Also, in contrast to earlier works on this subject, we have at our disposal the new wave extraction tool developed in Chapter 4.

Using these methods, we present new results for the collision of unequal-mass BH binaries in $D = 4, 5, \ldots, 10$ dimensions, and compare these with perturbative predictions. We expect our results to also allow for making contact with the large-D regime studied by Emparan and collaborators.

5.1.1 General relativity in the large D limit

Let us briefly introduce the aspects of the large D regime that we will make reference to in this chapter. In a sequence of papers Emparan and collaborators have taken the number of dimensions D as a free parameter in the theory of GR, and investigated the effects of sending it to infinity [16–19, 272, 273]. For the purpose of this chapter we will focus on their results on the behaviour of the quasinormal modes of a black hole in the large D limit. We focus particularly on the results of [272], and the numerical results of [102]. In the large D limit, it was shown in [16] that there are two important length scales associated to a black hole spacetime. As expected the horizon radius R_h provides one, but due to the large gradients present around the horizon, a shorter length scale R_h/D also becomes apparent. Clearly in the large D limit, there is a hierarchy between these scales. Qualitatively we can understand the large gradients by looking at the fall off of the gravitational potential, which decays proportional to $\sim (R_h/r)^{D-3}$, which clearly becomes a sharper fall off as D increases. As a result, it can be shown that in the large D limit, the radial gradient of the gravitational potential at the horizon is $\sim D/R_h$ [16]. Consequently in the large D limit a Schwarzschild black hole spacetime simply looks like flat Minkowski space, until one approaches within $r - R_h \lesssim R_h/D$ of the black hole horizon, where these large gradients become apparent. In [272] the quasinormal modes of black holes in the large D limit were studied, with two separate families being identified, called "non-decoupling" and "decoupling" modes. These families are separated by their frequencies, which scale respectively with the two length scales, D/R_h and $1/R_h$. In order to find these quasinormal modes, we must solve the equation for the Kodama-Ishibashi master function, Φ [198],

$$\left(\frac{d^2}{dr_*^2} + \omega^2 - V \right) \Phi = 0, \tag{5.1}$$

where r_* is a radial coordinate, ω is the frequency of the wave, and V is a radial potential function. As can be seen in Figures 1-3 of [272], in the large D limit, the radial potential V has a barrier outside the horizon which scales with D^2/R_h^2. Waves whose frequencies scale with $1/R_h$ cannot tunnel through this barrier, and so to satisfy the boundary conditions of quasinormal modes, they must lie within the region between the potential barrier and the horizon. These modes are therefore named decoupling modes. The non-decoupling modes however, with frequencies that scale with D/R_h can penetrate this barrier, and extend out to asymptotic infinity.

In [102] the Kodama-Ishibashi master function was solved for and the quasinormal modes calculated numerically (with the two families of modes called saturating (decoupling) which do not scale with D, and non-saturating (non-decoupling), which do scale with D). The values found agreed closely with those calculated using the analytic predictions in the large D limit as discussed in [272].

5.2   Modelling framework

The physical scenario we consider in this work consists of two D dimensional, nonspinning BHs with masses M_1 and $M_2 \leq M_1$ initially at rest, which then collide head-on under their gravitational attraction and merge into a single BH. The gravitational radiation released during the encounter of the two BHs, and its total energy and momentum in particular, is the key diagnostic quantity we wish to extract from our calculations. For this purpose, we employ two techniques: (i) a perturbative point-particle (PP) approximation, and (ii) numerical relativity simulations assuming $SO(D-3)$ isometry. In this section we review these two methods in turn.

5.2.1   Point-particle calculations

The first attempt at understanding this process considers a somewhat restricted parameter space: one of the BHs is much more massive than the other, i.e. $q \equiv M_2/M_1 \ll 1$ or

$$\eta \equiv \frac{M_1 M_2}{(M_1 + M_2)^2} = \frac{q}{(1+q)^2} \ll 1 \,, \tag{5.2}$$

where η is the symmetric mass ratio. The smaller, lighter BH is then approximated as a structureless PP, moving on a geodesic of the background spacetime described by the massive BH, while generating a stress-energy tensor which perturbs it. This scheme is also sometimes known as the PP approximation. In such a framework, the resulting equations to solve are just linearised versions of the Einstein equations, expanded around a BH-background spacetime [173, 174, 274, 198, 201, 275]. When the massive BH is nonspinning, the equations reduce to a single second order ordinary differential equation for the Kodama-Ishibashi master function sourced by the smaller BH (the PP). The source term of this wave like equation, as provided by the energy-momentum tensor of the PP can be found in [275], based on the calculation for a massless particle in [201]. In this scheme, to leading order, the total energy $E_{\rm rad} \propto q^2$ as shown by

D	4	5	6	7	8
$\frac{E_{\mathrm{rad}}}{q^2 M}$	0.0104	0.0165	0.0202	0.0231	0.0292

Table 5.1 Energy radiated in GWs when a small BH of mass qM_1, $q \ll 1$ falls from rest at infinity into a D-dimensional BH of mass M_1.

post-Newtonian calculations [262, 276, 201]. The exact coefficient was computed in [274, 201, 275] for particles falling radially into the BH.

Table 5.1 summarises those results for different spacetime dimensions. Note that the proportionality coefficient increases with spacetime dimension at large D. An extrapolation of these results suggests that the perturbative PP calculation should cease to be valid at sufficiently large D, since the radiation ultimately becomes too large and the geodesic approximation breaks down: cf. the discussion around Fig. 1 of [275]. Thus, even within the PP approximation, we identify the need to solve the full, nonlinear Einstein equations at large D.

5.2.2 Numerical framework

To solve the fully non-linear problem of colliding two black holes, we use our numerical relativity code to solve the full Einstein equations. Specifically, as in Chapter 4, we use the LEAN code [192, 227], originally developed for BH simulations in $D = 4$ dimensions and upgraded to general D spacetime dimension with $SO(D-3)$ isometry in [212, 114]. We use the Baumgarte-Shapiro-Shibata-Nakamura [137, 136] formulation of the Einstein equations, combined with the moving puncture [139, 140] gauge and Berger-Oliger mesh refinement provided by CARPET [218, 219] as part of the CACTUS computational toolkit [228, 220]. In order to calculate the GW signal, we compute the higher-dimensional Weyl scalars, as detailed in the previous chapter. For comparison and to determine the contributions of the individual multipoles, we also extract waveforms calculated with the perturbative Kodama-Ishibashi approach [198, 263] as detailed in [110] and Section 2.6.3.

When simulating the more extreme cases, that is cases for the largest values of D and the smallest values of q, we find it necessary to implement two changes to achieve accurate and stable evolutions. First, we evolve the lapse function α according to

$$\partial_t \alpha = \beta^i \partial_i \alpha - c_1 \alpha K^{c_2} \,, \tag{5.3}$$

where β^i is the shift vector and K the trace of the extrinsic curvature; the slicing condition typically used in moving puncture simulations is recovered for $c_1 = 2$, $c_2 = 1$ – cf. Eq. (2.44) in Section 2.5 – but here we vary these parameter in the ranges $2 \leq c_1 \leq 10$ and $1 \leq c_2 \leq 1.5$. The exact values vary from configuration to configuration and have been determined empirically. We identify this modification empirically, with the justification that we expect a slower evolution of the lapse in regions of large extrinsic curvature, near to the black hole, to be helpful for numerical stability due to the formations of the larger gradients as we increase D. As far as we are aware, no thorough study has been made of gauge conditions in higher dimensional BSSN evolutions, and this would be an interesting area to explore in the future. The second modification is an approximately linear reduction of the Courant factor $\Delta t / \Delta x$ as a function of D from 0.5 in $D = 4$ to 0.03 in $D = 10$. We shall see in Fig. 5.2 and its discussion in Sec. 5.3.2 that the merger becomes an increasingly instantaneous event with an ever sharper burst in radiation as we increase D. We believe the necessity of reducing the Courant factor to arise from this increasing demand for time resolution around merger. All of these difficulties can be encapsulated in the dimension dependent nature of the fall off of the gravitational field. As D increases, the size of the gradients created near the black holes increase, thus requiring more resolution in both the spatial and time domains in these situations.

5.3   Results

In our results below, we measure energy in units of the ADM mass M of the spacetime under consideration, and we measure length and time in units of the Schwarzschild radius R_h associated with this ADM mass according to Eq. (2.42). We note that due to this equation mass and length do not have the same physical dimensions, unless $D = 4$.

5.3.1   Numerical uncertainties

Our numerical relativity results for the GW energy released in head-on collisions of BHs are affected by the following uncertainties:

Discretisation error. We estimate the error due to finite grid resolution by studying a head-on collision of two BHs in $D = 8$ dimensions with mass ratio $q = 1/20$. We use a computational grid composed of 8 nested refinement levels, 2 inner boxes initially
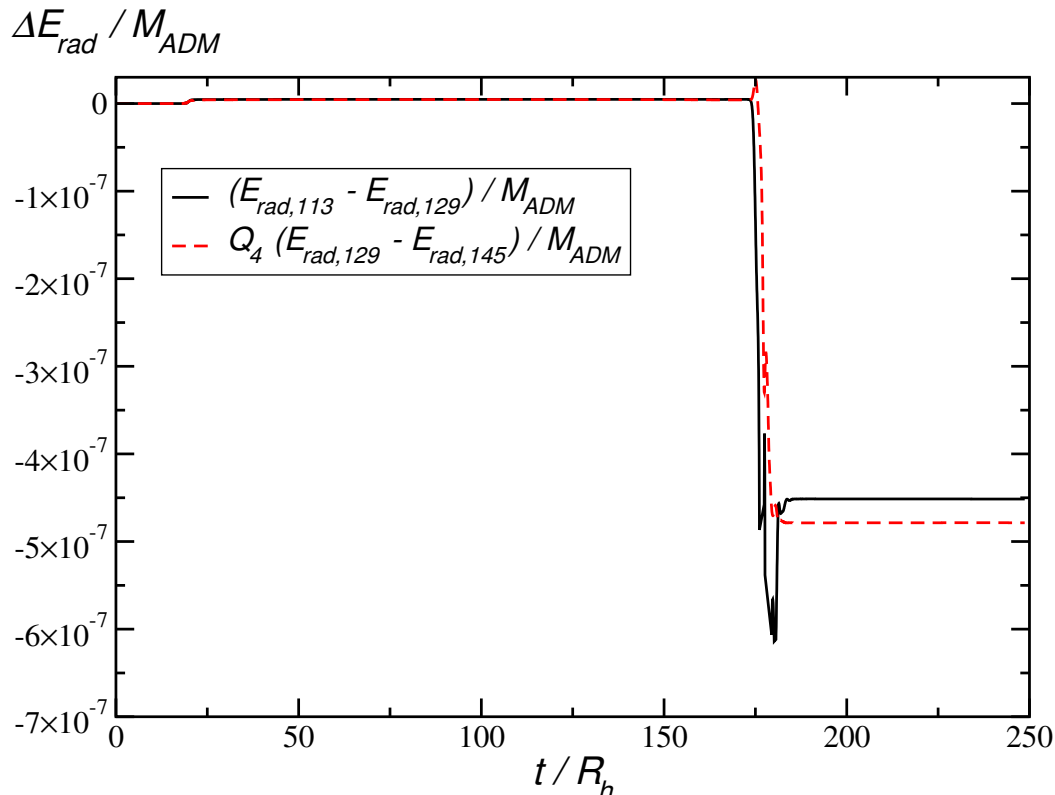
Fig. 5.1 Convergence plot for the radiated energy $E_{\rm rad}$ extracted from a $q = 1/20$ head-on collision in $D = 8$ at $40\,R_h$ as a function of time for grid spacing $h_1 = R_h/113$, $h_2 = R_h/129$ and $h_3 = R_h/145$. The difference between the high and medium resolution simulations has been scaled by a factor $Q_4 = 1.88$ expected for fourth-order convergence and agrees well with the difference of the coarse and medium resolution energies.

centred on the individual holes, and 6 outer levels centred on the origin. The grid spacing around the BHs is $h_1 = R_h/113$, $h_2 = R_h/129$ and $h_3 = R_h/145$, respectively, in our three simulations for checking convergence, and increases by a factor 2 on each consecutive outer level. The radiated energy as a function of time is extracted at $40\,R_h$, where the grid resolution is $H_i = 32\,h_i$ for the three runs $i = 1, 2, 3$. The difference between the high and medium resolution runs is compared with that between the medium and coarse resolution runs in Fig. 5.1. Multiplying the former by a factor $Q_4 = 1.88$ (as expected for the fourth-order discretisation of the code) yields good agreement between the two curves, and using the according Richardson-extrapolated result gives an error estimate of $3\,\%$ for the medium resolution simulation, which is closest to our set of production runs in terms of resolution around the smaller BH and in the wave extraction zone.

We have analysed several other configurations (including the collision in $D = 10$ dimensions) and find the discretisation error to mildly increase with mass ratio and dimensionality D, from about $1\,\%$ for $q = 1$, $D = 5,\,6$ to about $4\,\%$ for $q = 1$, $D = 10$ and about $5\,\%$ for $q \ll 1$, $D = 8$.

Finite extraction radius. The computational domain used in our simulations is of finite extent, about $200\,R_h$ for the runs analysed here, so that we cannot extract the GW signal at infinity. Instead we use finite radii and estimate the uncertainty incurred through this process by fitting the total radiated energy using a polynomial in $1/r_{\mathrm{ex}}$,

$$E_{\mathrm{rad}}(r_{\mathrm{ex}}) = E_{\mathrm{rad}} + \frac{a}{r_{\mathrm{ex}}} + \mathcal{O}\left(\frac{1}{r_{\mathrm{ex}}^2}\right) , \qquad (5.4)$$

where a is a parameter determined through fitting and E_{rad} is the estimate for the radiated energy extracted at infinity. We then take the extrapolated value at infinity as our result, and its difference from the largest numerical extraction radius as the uncertainty estimate. Applying this procedure yields a fractional error ranging from about $0.4\,\%$ for all equal-mass collisions to about $4\,\%$ for configurations with $q \ll 1$.

Spurious waves. Initial data of the type used here typically contain a small amount of unphysical GWs colloquially referred to as "junk radiation". The amount of unphysical radiation depends on the initial separation of the BHs (vanishing in the limit of infinite distance) and on the number of dimensions. As in Chapter 4, we find the amount of spurious radiation to be orders of magnitude below the errors due to discretisation and extraction radius. We attribute this to the rapid falloff of gravity in higher dimensions, so that the constituent BHs of the Brill-Lindquist data are almost in isolation even for relatively small coordinate separations. We have noticed, however, that spurious radiation is more prominent in the Kodama-Ishibashi modes as compared with the results based on the Weyl scalars. We cannot account for the precise causes for the seemingly superior behaviour of the Weyl scalars, but we note that similar findings have been reported for the $D = 4$ case in [179].

Initial separation. The head-on collisions performed here start from finite initial separation of the BHs, while the idealised scenario considers two BHs falling in from infinity. By varying the initial separation for several collisions in $D = 5$ and $D = 6$ we estimated the difference in E_{rad} due to the initial separation and, as for the junk radiation above, we found that the differences are well below the numerical error budget.
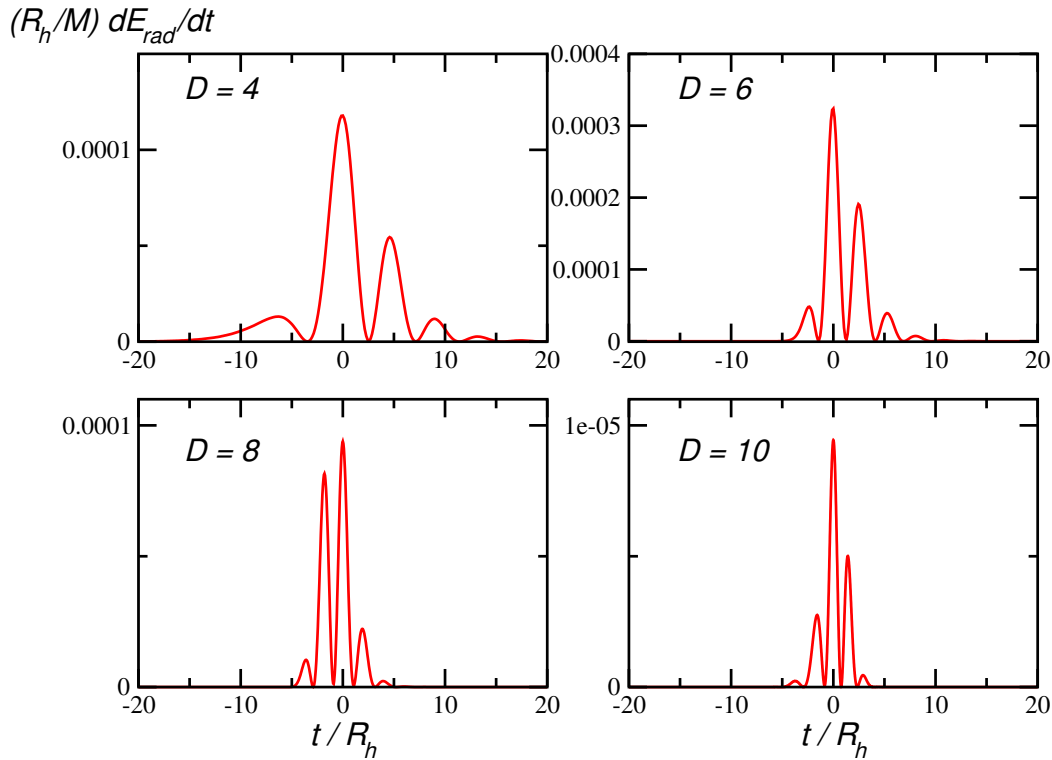
Fig. 5.2 Normalised energy flux $(R_h/M)\dot{E}_{\rm rad}$ as a function of time for equal-mass collisions, with $t = 0$ defined by the maximum in $\dot{E}_{\rm rad}$. As D increases, the burst of radiation becomes increasingly concentrated in time. Note also here that there are several nodes in each panel where the flux of energy goes to zero. For a head on collision the Ω'_{23} projection of the Weyl tensor is equal to zero due to axisymmetry, and so does not contribute, leading to this feature. This is analogous to the $D = 4$ case, where, in axisymmetry, the $h_\times$ polarisation is zero.

Again, we attribute this observation to the rapid falloff of the gravitational attraction for large D, leading to a prolonged but nearly stationary infall phase followed by an almost instantaneous merger that generates nearly all of the radiation.

In summary, our error is dominated by discretisation and use of finite extraction radii. It ranges from about $1.5\,\%$ for comparable mass collisions in low D to about $9\,\%$ for $q \ll 1$ in $D = 8$. For the gravitational recoil, we find similar significance of the individual error contributions, but overall larger uncertainties by about a factor 4. We attribute these larger uncertainties to the fact that the recoil arises from asymmetries in GW emission, and in this sense it is a weaker, differential effect.
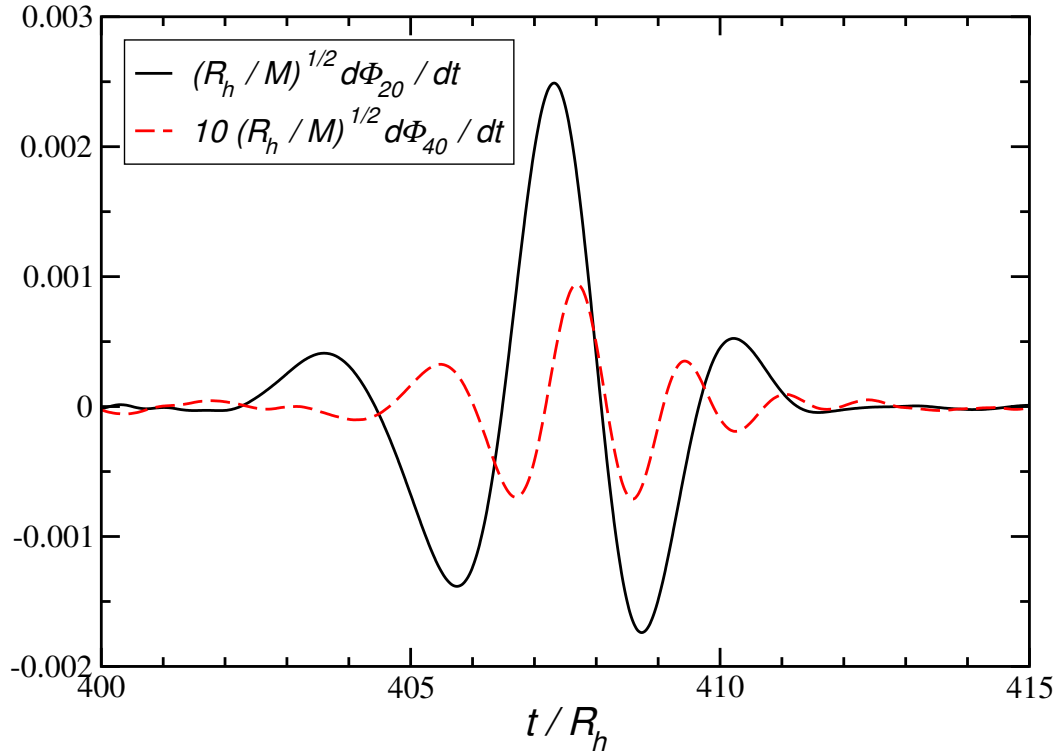
Fig. 5.3 The $l = 2$ (solid black line) and $l = 4$ (dashed red line) waveforms from the collision of two equal-mass BHs in $D = 10$.

5.3.2   Equal-mass collisions

The collision of two equal-mass BHs has already been studied in $D = 4$, 5 [111], and $D = 6$ [113] spacetime dimensions. We have verified those results, extending them to $D = 7$, 8 , 9 , 10. For illustration, in Fig. 5.2 we plot a normalised energy flux $(R_h/M)\dot{E}$ for collisions in $D = 4$, 6, 8 and 10 spacetime dimensions. As D increases, the burst of radiation becomes increasingly concentrated in time. This concentration suggests that the burst may approach a distribution of infinitesimal width in the large-D limit; it would be interesting to see if this is borne out in the large-D limit formalism of [16–19].

For further illustration, in Fig. 5.3 we plot the Kodama-Ishibashi waveform $\dot{\Phi}_{l0}$ [198, 263, 110, 113] for $D = 10$; the qualitative features of the signal are the same for all other D. The waveform consists of a precursor part with small amplitude when the two BHs are widely separated, followed by a smooth merger phase connecting to ringdown. A perturbative calculation, using direct integration techniques on the Kodama-Ishibashi master equation, yields the following two modes for gravitational-type scalar perturbations: $\omega R_h = 1.2346 - 0.9329i$ and $\omega R_h = 2.4564 - 0.9879i$. These are the decoupling (or saturating) and nondecoupling (or nonsaturating) modes in
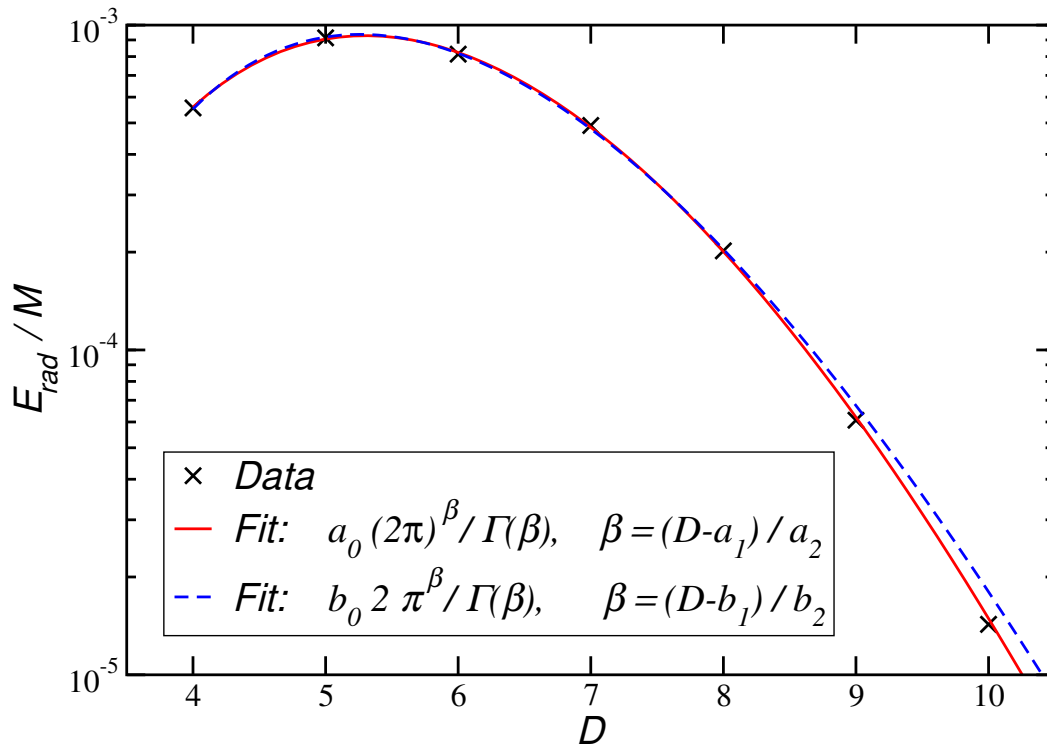
Fig. 5.4 Fractional energy $E_{\rm rad}/M$ radiated in GWs during collisions of equal-mass, nonspinning BHs starting from rest, in D spacetime dimensions. Crosses are numerical data points and the solid red line is the fit Eq. (5.5). The blue dashed line shows a fit obtained for the expression $b_0 \, 2\pi^\beta/\Gamma(\beta)$ which resembles even more closely the functional form of the surface area $A_{D-2} = 2\pi^{(D-1)/2}/\Gamma[(D-1)/2]$ of the $D-2$ sphere, but does not match the data points as well.

the language of [272, 273] ([102]). We find agreement to the level of $\ll \sim 0.1\%$ or better with [102] and very good agreement with the analytical, large-D estimates of [272]. A one-mode fit of numerical waveforms yields very poor agreement with any of the frequencies above. However, a two-mode fit yields the following two frequencies: $\omega R_h = 2.48 - 0.94i$, $1.22 - 0.91i$. Given the errors in numerical simulations, this is a reasonable level of agreement with linearised predictions, and it indicates that both modes are excited to comparable amplitudes for this particular simulation. We note here also that the amplitudes of the two families of perturbations, the real parts of the frequencies, are not widely separated at the values of D we are simulating. As can be seen in Figures 2 and 4 of [102] for the decoupling and non-decoupling modes respectively, a clear separation of the two scales becomes more apparent at higher values of D, with a factor of 10 difference in the real part of the frequency after $D \approx 30$.

When plotted as a function of the number D of dimensions (Fig. 5.4), the fraction of center-of-mass energy radiated in GWs by equal-mass head-on collisions reaches a maximum $E_{\mathrm{rad}}/M \sim 9.1 \times 10^{-4}$ for $D = 5$. Beyond this value, we find the total radiation output to rapidly decrease as a function of D. This suppression is consistent with the fact that the spacetime is nearly flat outside the horizon: in fact, the gravitational potential $(R_h/r)^{D-3}$ vanishes exponentially with D [16]. Another intuitive explanation for this rapid decay is that, as D increases, the energy is radiated almost instantaneously (cf. Fig. 5.2): spacetime is flat except extremely near the horizons, and bremsstrahlung radiation is suppressed. These features have also been seen in zero-frequency limit calculations [262]. Thus, at large D, radiation is emitted in a burst precisely when the BHs collide, but this is also the instant where one would expect common horizon formation, and consequent absorption of a sizeable fraction of this energy. This is, of course, a very loose description, unable to give us a quantitative estimate. The results in Fig. 5.4 are (perhaps surprisingly) well described by the following simple analytic expression,

$$\frac{E_{\mathrm{rad}}^{q=1}}{M} = a_0 \frac{(2\pi)^\beta}{\Gamma[\beta]}\,, \quad \beta = \frac{D - a_1}{a_2}\,, \tag{5.5}$$

where $a_0 = 1.7288 \times 10^{-6}$, $a_1 = 1.5771$, $a_2 = 0.5497$. This fit reproduces our numerical results to within $\sim 1\%$ for all $D = 4, \ldots, 10$. It is tempting to relate this expression to

the area $A_{D-2} = \frac{2\pi^{(D-1)/2}}{\Gamma(\frac{D-1}{2})}$ of a $(D-2)$-dimensional unit sphere, but we do not see an evident connection as the numerical factors do not match exactly[1].

The results for the radiated energy are in stark contrast to the predictions one would get by applying the PP results of Table 5.1 to the equal-mass case $q = 1$, where, instead of a strong suppression of $E_{\rm rad}$ at large D, we see a mild increase in the radiative efficiency. While the PP approximation is by construction not expected to capture the equal-mass limit with high precision, it is valuable to understand the origin of this qualitative discrepancy.

A potential explanation for this difference lies in the features of general relativity in the large D limit as introduced in Section 5.1.1, specifically the existence of two separate length scales. For equal-mass collisions the excitation of the modes with length scale R_h/D (and the radiation output) are strongly suppressed at large D [16]. However, dynamical processes are very sensitive to the dominant scale in higher dimensions, and it has been shown that small variations in parameters can, for instance, lead to large variations in energy emitted in gravitational waves [262, 16]. In the next section, we explore in more detail unequal-mass collisions and indeed find that these collisions can trigger the excitation of smaller-scale modes even at the low energies considered in our simulations.

5.3.3 Unequal-mass collisions and the point-particle limit

The stark contrast between the PP results summarised in Table 5.1 and the numerical relativity calculations of the previous section strongly points towards a qualitatively different behaviour of the radiated energy as a function of D for comparable-mass binaries (where $E_{\rm rad}$ rapidly drops beyond $D = 6$) as compared with the high mass-ratio regime (where $E_{\rm rad}$ mildly increases with D). The question we are now facing is: does the difference in the behaviour arise from the dominance of different physical mechanisms in the respective regions of the parameter space, and where does the crossover from one regime to the other occur? To shed light on this issue, we have performed collisions of unequal-mass, nonspinning BHs focusing on the range $q = 1, \ldots, 1/100$ and $D = 4, \ldots, 8$. The GW energy and linear momentum radiated in these collisions are summarised in Figs. 5.5-5.8.

---

[1]The expression $b_0\, 2\pi^\beta/\Gamma(\beta)$ resembles even more closely that of the surface area A_{D-2}, but yields a less accurate fit to the data points (cf. Fig. 5.4). It also does not establish a satisfactory relation between A_{D-2} and the numerical parameters appearing in the fit for β, now given by $\beta = (D - 2.4772)/0.7671$.
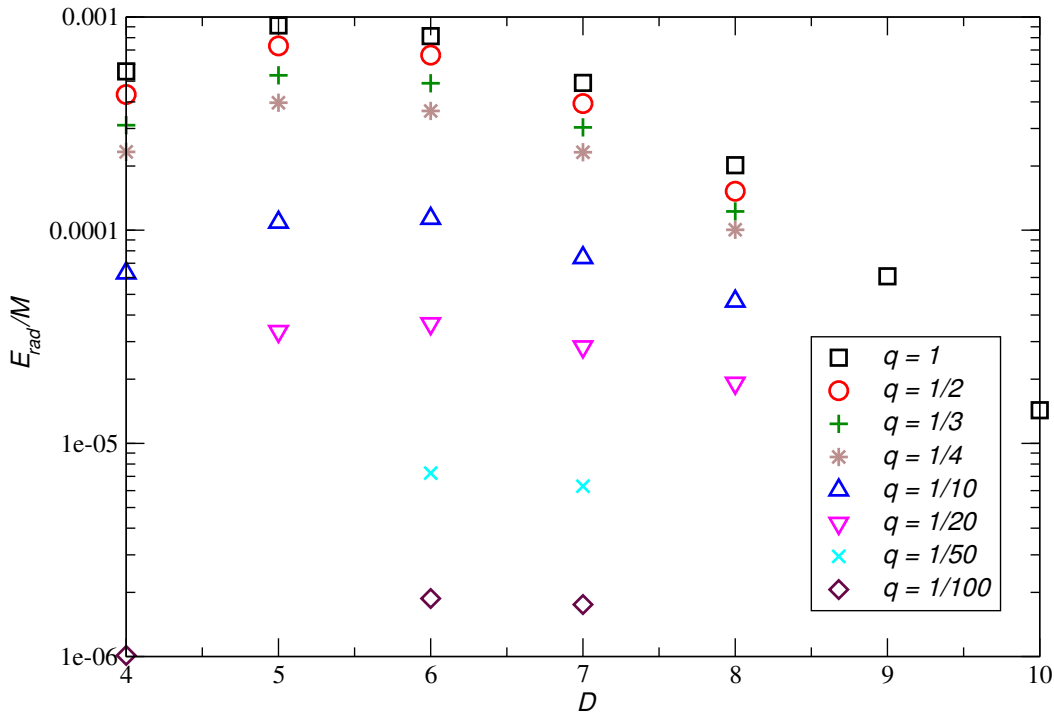
Fig. 5.5 Fractional energy $E_{\mathrm{rad}}/M_{\mathrm{ADM}}$ radiated in GWs in collisions of nonspinning BHs starting from rest with mass ratio q in D spacetime dimensions.

By analysing the waveforms for the most extreme mass ratios we find good agreement between the ringdown stage and estimates from linearised perturbations. However, our results indicate that only the high-frequency modes (the "non decoupling" modes) are excited. Since these modes probe the small scales presumably excited by the smaller BH [17, 19], it is reassuring to find high-frequency excitations.

Figure 5.5 shows the fractional center-of-mass energy released as GWs when two BHs collide, and Fig. 5.6 shows the same data normalised by (the square of) the kinematic, symmetric mass ratio parameter η. Note that η is directly connected to the reduced mass of the system and is known to yield a very good rescaling of all quantities in four-dimensional spacetimes (see for instance [277–279]). For low D (in particular for $D = 4, 5$) the total radiated energy $E_{\mathrm{rad}}/(M\eta^2)$ is weakly dependent on η. At small mass ratios q, or equivalently at small η, our results smoothly approach the PP limit of Table 5.1 (shown in Fig. 5.6 as filled data points at $\eta = 0$).

For $q \lesssim 1$ and sufficiently large D, the radiated energy decreases monotonically with D (Fig. 5.5). This behaviour would clearly contradict the PP results if it held for arbitrarily small mass ratio. In fact, at small mass ratios the behaviour of the radiated energy changes. The maximum of the radiated energy as a function of D
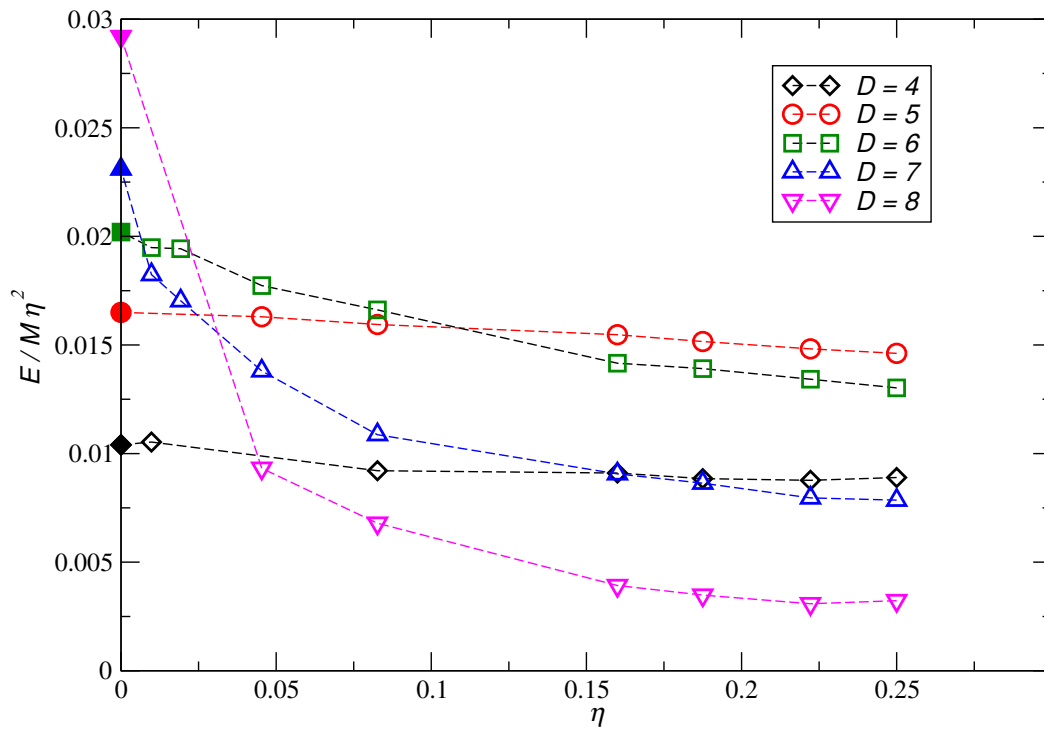
Fig. 5.6 The same data as in Fig. 5.5, but rescaled by η^2 (i.e. we plot $E_{\mathrm{rad}}/(M\eta^2)$) in order to facilitate the comparison with PP calculations of the radiated energy, which are shown as filled symbols at $\eta = 0$.

D	4	5	6	7	8
$-10^2 b_1$	0.54	0.95	2.82	3.63	3.58
b_2	0.72	1.18	0.83	0.44	0.19

Table 5.2 Fitting coefficients of Eq. (5.7), describing the η dependence of the total radiated energy.

shifts from $D = 5$ to $D = 6$ between $q = 1/4$ and $q = 1/10$. Results for even smaller q indicate a further shift towards $D = 7$, and possibly yet higher D as we approach the PP limit. It was noted in [275] that the monotonic increase in radiated energy in the PP limit would violate Hawking's area law, which in D dimensions gives that the fraction of radiated energy is bounded above by $1 - 2^{-1/(D-2)}$. Clearly, this bound decreases as D increases. This violation of the area law was taken as an indication of the breakdown of the PP approximation. It is reassuring to see here therefore that for fixed q the radiated energy eventually decreases for sufficiently large D in line with the area law. Furthermore, we see from Fig. 5.6 that $E_{\rm rad}/(M\eta^2)$ shows a steep increase for very small η and large D. This behaviour supports our interpretation that new scales are being probed. If this is indeed the correct interpretation, and if the new scale is of order R_h/D, one can estimate the mass ratio at which these new scales are excited. By using Eq. (2.42), and recalling that $M_2/M_1 = q$, we get the scaling $(r_2/R_h)^{D-3} = q$, with r_2 the scale of the small BH and R_h the scale of the large BH in terms of coordinate quantities. If we equate the "small scale" R_h/D to the size r_2 of the second colliding object we find the threshold mass ratio

$$q \sim D^{3-D} \,. \tag{5.6}$$

It seems sensible to understand the mass ratio dependence by *fixing* the PP limit to be that of Table 5.1. In other words, we fit our results to the expression

$$\frac{E_{\rm rad}}{M\eta^2} = b_0 + b_1 \eta^{b_2} \,, \tag{5.7}$$

where b_0 are the PP values listed in Table 5.1. The exponents b_2 obtained by fitting our data are listed in Table 5.2. These numbers are consistent with the behaviour shown in Figs 5.5, 5.6: the dependence of the total radiated energy on η is more complex for large D. In particular, at large D the expansion of $E_{\rm rad}$ in powers of η converges more slowly, and the convergence of the PP results (a leading-order expansion in mass ratio)

v_{kick} [km/s]
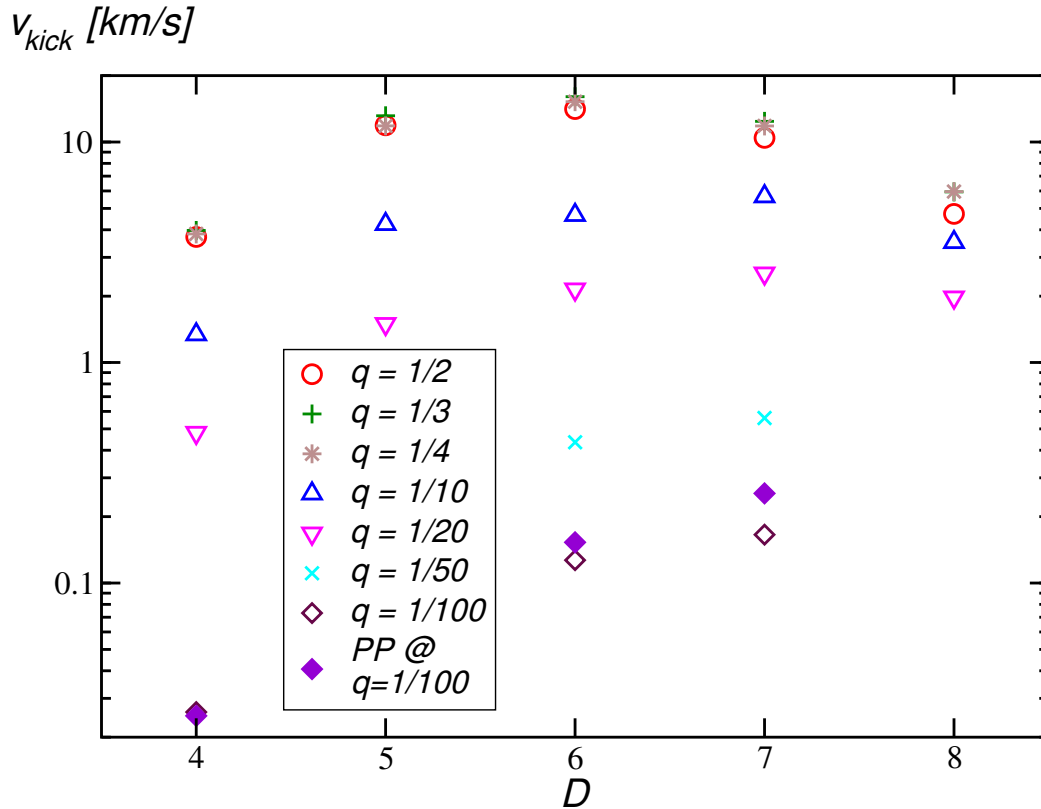
Fig. 5.7 Recoil due to asymmetric emission of GWs in the collision of nonspinning BHs starting from rest with mass ratio q in D spacetime dimensions. Note that the agreement with PP predictions in the small-q limit is very good for $D = 4$, and degrades for higher D.

is poor in the small-η regime. It would be interesting to find an analytical prediction for the coefficient b_2.

5.3.4   Kicks

For unequal mass head on BH mergers we expect the emission of linear momentum in gravitational waves as well as energy. To conserve total momentum, this will cause the remnant black hole to recoil with a certain velocity, known as a "kick". Using the Weyl scalars calculated from our simulations, we find the radiated linear momentum similarly to the radiated energy, by calculating

$$\dot{P}^I(u) = - \lim_{\mathbf{r} \to \infty} \frac{\mathbf{r}^{D-2}}{8\pi} \int_{S^{D-2}} n^I \left(\int_{-\infty}^{u} \Omega'_{(\alpha)(\beta)}(\tilde{u}, \mathbf{r}, \phi^\gamma) d\tilde{u} \right)^2 d\Omega \,, \tag{5.8}$$
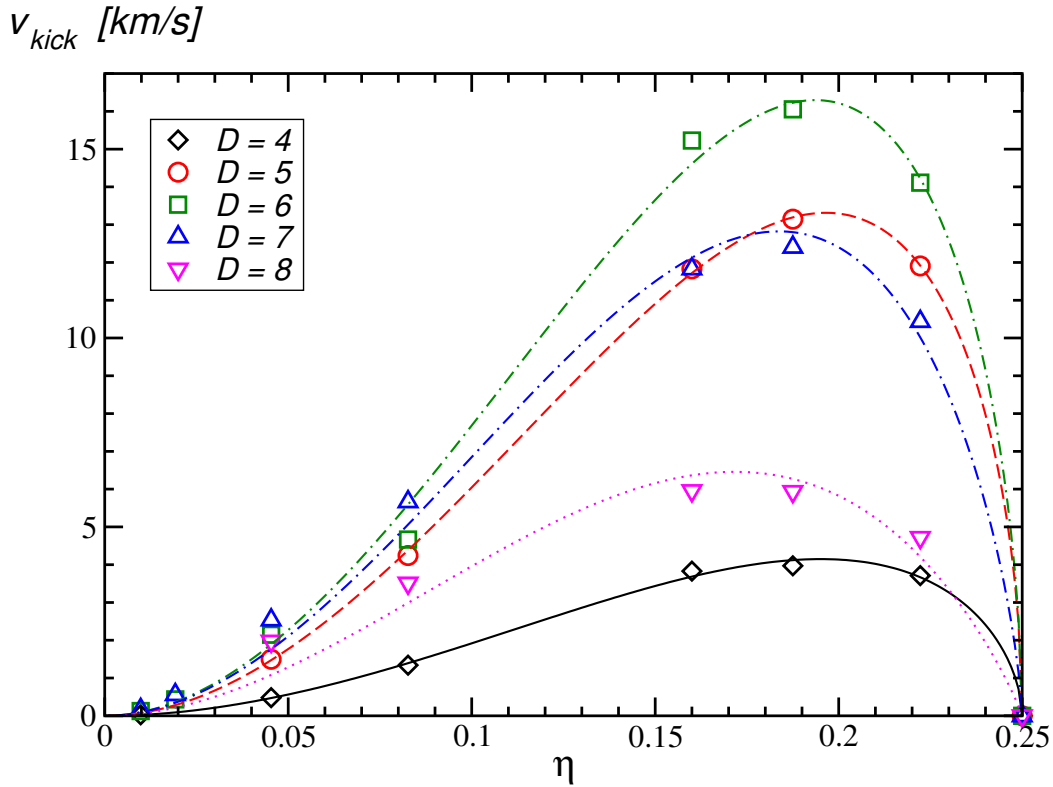
Fig. 5.8 As Fig. 5.7 but here symbols denote the kick for fixed D as a function of the symmetric mass ratio η. The lines are the simple two-parameter fit of Eq. (5.10).

where n^I is the normal radial unit vector, as detailed in [270]. To calculate the velocity of the remnant black hole we normalise this momentum by the mass of the remnant black hole, and report the value in km/s by reintroducing the value of the speed of light c, previously set to 1.

In Fig. 5.7, we show the gravitational recoil (or "kick") velocity of the post-merger BH as a function of D for fixed values of the mass ratios q, calculated from the Weyl scalars with Eq. (8.4). As in the case of the radiated energy (Fig. 5.5), we observe a shift in the maximum kick towards higher D as the mass ratio decreases. In particular, the maximum shifts from $D = 6$ to $D = 7$ as we change q from $1/4$ to $1/10$. In Fig. 5.8 we show the same results, but now plotting the kick for fixed D as a function of the symmetric mass ratio η.

The data in Figs. 5.7 and 5.8 are in good agreement with PP recoil calculations [280, 281, 275]: for example, in $D = 4$ the PP calculation yields $P_{\mathrm{rad}}/M = 8.33 \times 10^{-4} q^2$, or $v_{\mathrm{kick}} = 250 q^2$ km/s. This is in percent-level agreement with the $D = 4$, $\eta = 0.01$ simulation, for which we get $v_{\mathrm{kick}} = 0.026$ km/s (for such small mass ratios, of course,

$q \simeq \eta = 0.01$). As D increases, the PP prediction becomes less accurate: the relative error is 4% in $D = 4$, 21% in $D = 6$ and 54% in $D = 7$. This is consistent with the trend observed for the radiated energy and with physical expectations: according to Eq. (2.42), for a fixed q the less massive black hole appears less and less like a PP. It is also possible that some of this disagreement comes from the larger errors in the high-D, small-mass ratio simulations.

Following previous work on unequal mass collisions in $D = 4$ dimensions [282] we first tried to fit the data using the following mass ratio dependence (see e.g. the classic work by Fitchett & Detweiler [283]):

$$v_{\text{kick}}^{(1)} = v_D \eta^2 \sqrt{1 - 4\eta}, \tag{5.9}$$

where the superscript (1) means that this is a one-parameter fit. According to this simple formula, the maximum recoil occurs when $\eta = 0.2$ ($q \simeq 0.38$) for all D. Note that for $\eta = 0.2$ we get $v_{\text{kick,max}}^{(1)} \simeq 0.018 v_D$, so the parameter v_D is related to the maximum kick by a simple proportionality relation.

However, our previous considerations suggest that the mass ratio dependence of the radiated energy and of the recoil velocity should vary with D. As a simple way to investigate this D dependence we used a two-parameter fitting function:

$$v_{\text{kick}}^{(2)} = \tilde{v}_D \eta^2 (1 - 4\eta)^{c_D}. \tag{5.10}$$

Assuming this dependence, the maximum kick $v_{\text{kick,max}}^{(2)}$ will correspond to a D-dependent $\eta_{\max}$ that can be obtained by fitting the data.

The fitting coefficients and maximum kicks obtained with these two expressions are listed in Table 5.3. Note that the D dependence of $\eta_{\max}$ is very mild for all but the largest D simulations. More accurate simulations may be needed to resolve the issue of the D-dependence of $\eta_{\max}$ and of the maximum kick velocity. However, the following conclusion is quite independent of the assumed functional dependence: the maximum kick is ~ 16.3 km/s, and it is achieved for $D = 6$ and $\eta_{\max} \simeq 0.2$. We note that in all of our simulations the kick is in the direction of origin of the less massive black hole. This is in agreement with the argument of [284], which says that the smaller black hole, as it is travelling faster during the infall, will beam its gravitational radiation along its direction of travel more than the more massive black hole. This will lead to more radiation emitted in the direction of travel of the smaller BH, so the remnant will be kicked towards the direction of origin of the smaller BH.

D	4	5	6	7	8
v_D [km/s]	232.9	746.9	915.2	714.8	349.0
$v_{\mathrm{kick,max}}^{(1)}$ [km/s]	4.166	13.361	16.372	12.787	6.244
$\tilde{v}_D$ [km/s]	255.8	798.4	1034	989.9	630.7
c_D	0.5629	0.5445	0.5821	0.7214	0.9110
η_{max}	0.1951	0.1965	0.1936	0.1837	0.1718
$v_{\mathrm{kick,max}}^{(2)}$ [km/s]	4.148	13.314	16.297	12.822	6.457

Table 5.3 Fitting coefficients of Eqs. (5.9) and (5.10), describing the η dependence of the kick velocity.

5.4 Conclusions

We have numerically simulated head-on collisions of black holes in $D = 4, \ldots, 10$ dimensions, extracted the GW signal and computed the energy and linear momentum radiated in the collisions. Starting with the equal-mass case, we find values for the radiated energy in agreement with previously published results for $D = 5$ and $D = 6$ dimensions. The radiated energy, measured in units of the ADM mass M, is maximal in $D = 5$, where $E_{\mathrm{rad}}/M = 9.1 \times 10^{-4}$. For larger D we observe a strong reduction in the radiated energy: the fit $E_{\mathrm{rad}}/M = (2\pi)^\beta/\Gamma(\beta)$, $\beta = (D - 1.5771)/(0.5497)$ models our results to within 1% for all D simulated. This functional dependence closely resembles that of the surface area $\mathcal{A}_{D-2} = 2\pi^{(D-1)/2}/\Gamma[(D-1)/2]$, but the discrepancy in the numerical parameters in the argument suggests a more complicated relation between the two quantities.

The numerical results for the equal-mass case differ strikingly from those obtained in the PP approximation, which predicts a mild increase of $E_{\mathrm{rad}}/(q^2 M)$ with D when a small BH of mass qM_1, $q \ll 1$ falls into a BH of mass M_1. We reconcile these seemingly different predictions by numerically simulating a wider set of BH collisions with mass ratios ranging from $q = 1$ to $q = 1/100$ in up to $D = 8$ dimensions. In Fig. 5.6 we observe that the (symmetric mass ratio-normalised) energy $E_{\mathrm{rad}}/(M\eta^2)$ increases in the PP limit $q \to 0$. This increase becomes particularly steep for $D = 7$ and $D = 8$, and the numerical data extrapolated to $q = 0$ are in good agreement with the PP predictions.

These findings can be understood by invoking the presence of multiple length scales in the large-D limit, as identified in [16]. Additionally to the length scale R_h of the Schwarzschild horizon, the large-D limit reveals a shorter scale R_h/D for the spatial variation of potential terms in the equations governing BH perturbations. It

is natural then to assume that these shorter length scales will be excited with much higher efficiency by a small object falling into a BH, while they are largely insensitive to the collision of two objects of size R_h. The parameter regime in between these two extremes, on the other hand, is characterised by excitations of comparable magnitude on both length scales.

Our intuitive interpretation is strengthened by the analysis of the quasinormal mode frequencies: for $q = 1$ (and large D) the ringdown exhibits comparable contributions from two frequencies, corresponding to the "decoupling" and "nondecoupling" modes in the language of [102], while the ringdown is dominated by the nondecoupling modes for $q \ll 1$. For large D, the emission of gravitational waves therefore appears to be sensitive to the properties of the two BHs. It is interesting to contrast this observation with the corresponding *insensitivity* of the collision dynamics in high-energy collisions in $D = 4$ [49, 54]. This contrast naturally raises the question which effect dominates in high-energy, large-D collisions: sensitivity to structure due to large D or universality due to high energy?

With regard to the large-D limit, we notice a further connection in the shape of the energy flux as a function of time. In units of the Schwarzschild horizon associated with the ADM mass of the spacetime, the flux becomes increasingly peaked in higher D and it appears to approach the shape of an infinitesimally wide distribution, which is what one would intuitively expect in the large-D limit, where the spacetime exterior to a BH approaches Minkowski.

Finally, we analyse the gravitational recoil resulting from the asymmetric emission of GWs in unequal-mass collisions. We find the data to be well fitted by Fitchett's [283] formula commonly applied to the four-dimensional case, but we also observe a mild indication that the mass ratio maximising the recoil varies with D at large D. The maximum kick due to gravitational recoil ($v_{\text{kick,max}} \sim 16.3$ km/s) is achieved for $D = 6$, and for a symmetric mass ratio $\eta = \eta_{\text{max}} \simeq 0.2$ ($q \simeq 0.4$). When regarding both energy or linear momentum as a function of D at fixed mass ratio q, we observe a shift in the maximum towards higher D as we move from the equal-mass case $q = 1$ to the PP limit $q \ll 1$. This observation further confirms one of our main conclusions: the PP limit provides exquisitely accurate predictions for small mass ratios, but it must be taken with a grain of salt when extrapolated to the comparable-mass regime in higher dimensions.

Chapter 6

Initial Data in Higher Dimensions

The work in this chapter is unpublished, and was performed in collaboration with Ulrich Sperhake.

6.1 Introduction

The higher dimensional Brill-Lindquist data introduced in Section 2.4 has allowed us to simulate head on collisions from rest of higher dimensional black holes in Chapters 3 - 5. If, however, we wish to simulate scenarios in which the black holes have initial momenta, such as BH inspirals, grazing BH collisions, or high energy BH collisions, we must implement new initial data, for example the higher dimensional analogue to $4D$ Bowen-York initial data. This will be the focus of this chapter. In Section 6.2 we introduce the analogue of the Bowen-York data for black holes with initial momentum, first found in [285] and implemented in the reduction by isometry scheme of dimensional reduction in [271]. We then explicitly show its implementation in the modified Cartoon formalism for the first time. In Section 6.3 we do the same for black holes with initial angular momentum, taking initial data again from [285] and implementing it for the first time in the modified Cartoon formalism. Finally in Section 6.4 we introduce the higher dimensional analogues of the ADM integrals of Section 2.6.4, which will allow us to calculate the mass, momentum and angular momentum content of a spatial slice.

6.2 Initial data for black holes with momentum

We have already shown, in Section 2.4, the generalisation of the Brill-Lindquist initial data for initially static black holes to higher dimensions. In this chapter we will begin by introducing the generalisation of the Bowen-York initial data to higher dimensions, and implementing it in our modified Cartoon formalism. This is based on the ansatz for the extrinsic curvature provided by [285], and the implementation of the Bowen-York like data for head on boosted collisions in a reduction by isometry scheme in [271].

In order to construct the initial data, we must again solve the D constraint equations, one Hamiltonian constraint, and $D - 1$ momentum constraints, which we reproduce here,

$$
\begin{aligned}
\mathcal{H} &= \mathcal{R} + K^2 - K^{IJ}K_{IJ} = 0, & (6.1) \\
\mathcal{M}^I &= D_J(K^{IJ} - \gamma^{IJ}K) = 0. & (6.2)
\end{aligned}
$$

Following the York-Lichnerowicz split detailed in Section 2.4, we decompose the metric and extrinsic curvature, [149–152]

$$
\gamma_{IJ} = \psi^{\frac{4}{D-3}}\bar{\gamma}_{IJ}, \qquad K_{IJ} = \psi^{-2}\bar{A}_{IJ} + \frac{1}{D-1}\gamma_{IJ}K, \tag{6.3}
$$

where ψ is a conformal factor, and $K = \gamma^{IJ}K_{IJ}$ is the trace of the extrinsic curvature. In contrast to the $4D$ case, we will here work in terms of the conformally rescaled trace free extrinsic curvature $\bar{A}_{IJ}$. We assume that the metric is conformally flat, $\bar{\gamma}_{IJ} = \delta_{IJ}$, and that the maximal slicing condition, $K = 0$, is satisfied, which gives the Hamiltonian and momentum constraints in the form

$$
\partial_I \bar{A}^{IJ} = 0, \tag{6.4}
$$

$$
\delta_{IJ}\partial^I\partial^J\psi + \frac{D-3}{4(D-2)}\psi^{-(3D-5)/(D-3)}\bar{A}^{IJ}\bar{A}_{IJ} = 0. \tag{6.5}
$$

Note that the indices on conformally rescaled quantities, such as $\bar{A}^{IJ}$ are raised with the conformal metric $\bar{\gamma}^{IJ}$. Following the calculation of Bowen and York, Yoshino et al. [285], found the ansatz for $\bar{A}_{IJ}$ for a single black hole with linear momentum,

$$
\bar{A}^{IJ} = \frac{4\pi(D-1)}{(D-2)\mathcal{A}_{D-2}}\frac{1}{r^{D-2}} \\
\left[n^I P^J + n^J P^I - n_M P^M \bar{\gamma}^{IJ} + (D-3)n^I n^J P^M n_M\right],
\tag{6.6}
$$

where P^I corresponds to the ADM momentum of the black hole and n^I is the normal radial vector in Cartesian coordinates given by

$$n^I \equiv \frac{x^I - x_0^I}{r}, \qquad r^2 = \delta_{MN}(x - x_0)^M (x - x_0)^N, \tag{6.7}$$

where x_0^I denotes the position of the BH. This ansatz is chosen such that it solves Eq. (6.4), and reproduces the ADM linear momentum of the black hole spacetime (see Section 6.4 for discussion of the higher dimensional ADM quantities). We are then left with the task of solving Eq. (6.5), an elliptic PDE for ψ. As in $4D$ for Bowen-York data, we decompose ψ into a Brill-Lindquist component ψ_{BL} [154], which on its own gives initial data for a static black hole, giving the spacetime approximately the correct ADM mass, and a correction $u\left(x^I\right)$. For a single black hole centred at the origin, this is given by

$$\psi = \psi_{BL} + u = 1 + \frac{\mu}{4r^{D-3}} + u, \tag{6.8}$$

where μ is the Schwarzschild-Tangherlini mass parameter, and r is the radial distance from the black hole. If we wish to solve for, for instance, two black holes, clearly Eq. (6.4) is linear in $\bar{A}^{IJ}$, so we can superpose two copies of the extrinsic curvature,

$$\bar{A}^{IJ} = \bar{A}_{(1)}^{IJ}\left(P_{(1)}^K, n_{(1)}^L\right) + \bar{A}_{(2)}^{IJ}\left(P_{(2)}^K, n_{(2)}^L\right), \tag{6.9}$$

where $P_{(i)}^K$ and $n_{(i)}^L$ are the linear momentum, and radial vector respectively, corresponding to the ith black hole. We then let ψ take the same form as above, with the Brill-Lindquist term modified to include a contribution from the second black hole,

$$\psi = 1 + \frac{\mu_{(1)}}{4r_{(1)}^{D-3}} + \frac{\mu_{(2)}}{4r_{(2)}^{D-3}} + u, \tag{6.10}$$

where $\mu_{(i)}$ and $r_{(i)}$ are respectively the mass parameter of, and radial distance from, the ith black hole. Now we must solve Eq. (6.5) for u, which we achieve using a spectral elliptic PDE solver detailed in [156, 271], implemented in the CACTUS thorn TwoPunctures.

The final step is to identify how $\bar{A}^{IJ}$ simplifies within the $SO(D-3)$ symmetry we impose on our spacetime in implementing the modified Cartoon formalism. Without loss of generality let us consider the case of a single black hole with initial momentum

and position

$$P^I = (P_x, \ P_y, \ 0, \ 0, \ \ldots, \ 0) \,, \qquad x_0^I = (x_0, \ 0, \ 0, \ 0, \ \ldots, \ 0) \,. \tag{6.11}$$

This will give the initial conditions for a collision in the $x - y$ plane, which is the only plane in which BH collisions can occur, due to the assumption of $SO(D-3)$ symmetry. Let us define for convenience

$$\bar{a}^{IJ} = n^I P^J + n^J P^I - n_M P^M \bar{\gamma}^{IJ} + (D-3)n^I n^J P^M n_M \,, \tag{6.12}$$

so that

$$\bar{A}^{IJ} = \frac{4\pi(D-1)}{(D-2)\mathcal{A}_{D-2} r^{D-2}} \bar{a}^{IJ} \,. \tag{6.13}$$

In the modified Cartoon approach, we have $w_4 = \ldots = w_{D-1} = 0$, so that the radial vector has non-vanishing components only in the x, y and z directions. Furthermore, we use Cartesian coordinates, so that the expressions we insert into Eq. (6.12) are given by Eq. (6.11) as well as

$$n^I = \left(\frac{x - x_0}{r}, \ \frac{y}{r}, \ \frac{z}{r}, \ 0, \ \ldots, \ 0 \right) , \tag{6.14}$$

$$\bar{\gamma}_{IJ} = \delta_{IJ} \,. \tag{6.15}$$

We can now calculate the individual terms in Eq. (6.12), firstly for terms inside the computational domain,

$$
n^i P^j = \begin{pmatrix} P_x \frac{x-x_0}{r} & P_y \frac{x-x_0}{r} & 0 \\ P_x \frac{y}{r} & P_y \frac{y}{r} & 0 \\ P_x \frac{z}{r} & P_y \frac{z}{r} & 0 \end{pmatrix}, \qquad n^j P^i = \begin{pmatrix} P_x \frac{x-x_0}{r} & P_x \frac{y}{r} & P_x \frac{z}{r} \\ P_y \frac{x-x_0}{r} & P_y \frac{y}{r} & P_y \frac{z}{r} \\ 0 & 0 & 0 \end{pmatrix},
$$

$$
n_M P^M \bar{\gamma}^{ij} = \begin{pmatrix} P_x \frac{x-x_0}{r} + P_y \frac{y}{r} & 0 & 0 \\ 0 & P_x \frac{x-x_0}{r} + P_y \frac{y}{r} & 0 \\ 0 & 0 & P_x \frac{x-x_0}{r} + P_y \frac{y}{r} \end{pmatrix},
$$

$$
(D-3)n^i n^j n_M P^M = (D-3)\left(P_x \frac{x-x_0}{r} + P_y \frac{y}{r} \right) \begin{pmatrix} \frac{(x-x_0)^2}{r^2} & \frac{(x-x_0)y}{r^2} & \frac{(x-x_0)z}{r^2} \\ \frac{(x-x_0)y}{r^2} & \frac{y^2}{r^2} & \frac{yz}{r^2} \\ \frac{(x-x_0)z}{r^2} & \frac{yz}{r^2} & \frac{z^2}{r^2} \end{pmatrix}.
\tag{6.16}
$$

We thus obtain the components

$$
\bar{a}^{11} = P_y \frac{y}{r^3}\left(-y^2 - z^2 + (D-4)(x-x_0)^2 \right) + P_x \frac{x-x_0}{r^3}\left(y^2 + z^2 + (D-2)(x-x_0)^2 \right),
$$
$$
\bar{a}^{12} = P_y \frac{x-x_0}{r^3}\left((D-2)y^2 + z^2 + (x-x_0)^2 \right) + P_x \frac{y}{r^3}\left(y^2 + z^2 + (D-2)(x-x_0)^2 \right),
$$
$$
\bar{a}^{13} = (D-3)P_y \frac{yz}{r^3}(x-x_0) + P_x \frac{z}{r^3}\left(y^2 + z^2 + (D-2)(x-x_0)^2 \right),
\tag{6.17}
$$
$$
\bar{a}^{22} = P_y \frac{y}{r^3}\left((D-2)y^2 + z^2 + (x-x_0)^2 \right) + P_x \frac{x-x_0}{r^3}\left((D-4)y^2 - z^2 - (x-x_0)^2 \right),
$$
$$
\bar{a}^{23} = P_y \frac{z}{r^3}\left((D-2)y^2 + z^2 + (x-x_0)^2 \right) + (D-3)P_x \frac{yz}{r^3}(x-x_0),
$$
$$
\bar{a}^{33} = \left(P_y \frac{y}{r^3} + P_x \frac{x-x_0}{r^3} \right)\left(-y^2 + (D-4)z^2 - (x-x_0)^2 \right).
$$

Finally we calculate the off-domain components,

$$
\bar{a}^{ab} = \left(-P_x \frac{x-x_0}{r} - P_y \frac{y}{r} \right)\delta^{ab} = \bar{a}^{ww}\delta^{ab} \quad \Rightarrow \quad \bar{a}^{ww} = -P_x \frac{x-x_0}{r} - P_y \frac{y}{r},
\tag{6.18}
$$

and we note that $\bar{a}^{IJ}$ is trace free as expected. We can now fully implement the initial data in the modified Cartoon formalism.

6.3 Initial data for spinning black holes

Following Appendix A of [285], as well as Section 5.5.2 of [286], we can extend this Bowen-York like construction of initial data to include spinning black holes, as can be done in $4D$. For simplicity, we will restrict our attention to singly spinning BHs in the $x - y$ plane. In 3 spatial dimensions angular momentum can be encoded into a vector which is orthogonal to the plane in which the object in question is spinning. In higher dimensions however there is no longer a unique direction orthogonal to a given $2D$ plane, so it is no longer helpful to talk about an angular momentum vector. Instead, our black hole spins will be encoded in an antisymmetric $(D - 1 \times D - 1)$ angular momentum tensor J_{IJ} [232, 287], defined by

$$J_{IJ} = \frac{1}{8\pi} \lim_{r \to \infty} \int_{S^{D-2}} \left(x_I K_{JK} - x_J K_{IK} \right) d\Omega^K. \tag{6.19}$$

For our singly spinning black hole this will take the form

$$J_{IJ} \;\; = \;\; \begin{pmatrix} 0 & -J_1 & 0 & \dots & 0 \\ J_1 & 0 & 0 & \dots & 0 \\ 0 & 0 & 0 & \dots & 0 \\ \vdots & \vdots & \vdots & \ddots & \vdots \\ 0 & 0 & 0 & \dots & 0 \end{pmatrix}. \tag{6.20}$$

A multiply spinning BH will have more 2×2 antisymmetric blocks along the diagonal, spanning the columns and rows corresponding to the planes in which the spins occur, for an appropriately chosen coordinate system. We will see in Section 6.4 that this J_{IJ} matches with the angular momentum we can define at spatial infinity in the limit $r \to \infty$. Following [287] we can connect the parameter J_1 to the spin parameter a found in the singly-spinning Myers-Perry metric by the relation

$$J_1 = \frac{\mathcal{A}_{D-2}\mu a}{8\pi}, \tag{6.21}$$

where μ is the mass parameter, and the singly-spinning Myers-Perry metric is given by

$$
\begin{aligned}
ds^2 &= -dt^2 + \frac{\mu}{r^{D-5}\Sigma}(dt - a\sin^2\theta\, d\tilde{\phi})^2 + \frac{\Sigma}{\Delta}dr^2 + \Sigma d\theta^2 \\
&\quad + (r^2 + a^2)\sin^2\theta\, d\tilde{\phi}^2 + r^2\cos^2\theta\, d\Omega^2_{D-4}, \\
\Sigma &= r^2 + a^2\cos^2\theta, \\
\Delta &= r^2 + a^2 - \frac{\mu}{r^{D-5}}.
\end{aligned}
\tag{6.22}
$$

The ansatz of Yoshino et al [285] for Eq. (6.4) is now given by

$$
\bar{A}_{IJ} = -\frac{4\pi(D-1)}{\mathcal{A}_{D-2}r^{D-1}}(J_{IK}n^K n_J + J_{JK}n^K n_I),
\tag{6.23}
$$

which reproduces the asymptotic angular momentum of a spinning black hole. For a singly spinning BH in the $x - y$ plane, the only terms that contribute are

$$
\bar{A}_{11} = -\bar{A}_{22} = -\frac{4\pi(D-1)}{\mathcal{A}_{D-2}r^{D-1}}\left(2J_1\frac{xy}{r^2}\right),
\tag{6.24}
$$

$$
\bar{A}_{12} = \bar{A}_{21} = -\frac{4\pi(D-1)}{\mathcal{A}_{D-2}r^{D-1}}J_1\left(\frac{y^2 - x^2}{r^2}\right).
\tag{6.25}
$$

Again, since Eq. (6.4) is linear, for 2 (or more) spinning black holes, we can superpose terms of this form, with 2 potentially different spin parameters $J^{(+)}, J^{(-)}$, with the radial distance now taken from the respective black holes initial positions. Explicitly then, the initial data for N black holes with generic spin and momentum in the $x - y$ plane has its trace free conformally rescaled extrinsic curvature given by

$$
\bar{A}_{IJ} = \sum_{(i)=1}^{N}\bar{A}_{IJ}^{((i),mom)}\left(x_0^{(i)}, P_x^{(i)}, P_y^{(i)}\right) + \bar{A}_{IJ}^{((i),spin)}\left(x_0^{(i)}, J_1^{(i)}\right),
\tag{6.26}
$$

and conformal factor

$$
\psi = 1 + u + \sum_{(i)=1}^{N}\frac{\mu_{(i)}}{4r_{(i)}^{D-3}},
\tag{6.27}
$$

where u is the solution to

$$\delta_{IJ}\partial^I\partial^J u + \frac{D-3}{4(D-2)}\psi^{-(3D-5)/(D-3)}\bar{A}^{IJ}\bar{A}_{IJ} = 0. \tag{6.28}$$

6.4   ADM integrals in higher dimensions

As a further diagnostic tool, which will allow us to verify that our numerically constructed initial data does indeed have the physical properties of linear or angular momentum that we desire, we construct the higher dimensional analogues of the ADM integrals defined in Section 2.6.4. These are again conserved quantities defined at spatial infinity on the $D-1$ dimensional spatial slice using the Hamiltonian formalism. It was shown in [288] that, by considering the symmetries of asymptotically flat spatial infinity in higher dimensions, the generalisations of the ADM integrals we define below are the conserved charges associated to these symmetries.

To have asymptotic flatness at spatial infinity we enforce the dimension dependent analogue of the earlier gauge conditions [286], given in Eqs (2.86 - 2.89), with f a Riemannian flat metric on the $D-1$ spatial slice Σ_t satisfying conditions 1 and 2 in Section 2.6.4, with the induced metric and extrinsic curvature satisfying

$$\gamma_{ij} \;\; = \;\; f_{ij} + \mathcal{O}(r^{3-D}), \tag{6.29}$$

$$\frac{\partial\gamma_{ij}}{\partial x^k} \;\; = \;\; \mathcal{O}(r^{2-D}), \tag{6.30}$$

$$K_{ij} \;\; = \;\; \mathcal{O}(r^{2-D}), \tag{6.31}$$

$$\frac{\partial K_{ij}}{\partial x^k} \;\; = \;\; \mathcal{O}(r^{1-D}). \tag{6.32}$$

The expressions for ADM mass and linear momentum take the same form as in $4D$, but we now allow the indices to vary over the full $D-1$ spatial coordinates, and separate them into (i, a) index ranges, so that we can implement them in our modified Cartoon formalism. First we find the ADM mass,

$$
\begin{aligned}
M &= \frac{1}{16\pi} \int_{S^{D-2}} (\partial^I h_{IJ} - \partial_J h) \, d\Omega^J \\
&= \frac{1}{16\pi} \int_{S^{D-2}} (\partial^i h_{ij} + \partial^a h_{aj} - \partial_j h) \, d\Omega^j \\
&= \frac{1}{16\pi} \int_{S^{D-2}} \left(\partial^i \gamma_{ij} + (D-4) \left(\frac{\gamma_{jz} - \delta_{jz}\gamma_{ww}}{z} \right) - \partial_j h \right) d\Omega^j \\
&= \frac{1}{16\pi} \int_{S^{D-2}} \left(\partial^i \gamma_{ij} + (D-4) \left(\frac{\gamma_{jz} - \delta_{jz}\gamma_{ww}}{z} \right) - \delta^{ik}\partial_j\gamma_{ik} - (D-4)\partial_j\gamma_{ww} \right) d\Omega^j .
\end{aligned}
$$

(6.33)

The linear momentum is defined to be

$$
P_i = \frac{1}{8\pi} \int_{S^{D-2}} (K_{ij} - \delta_{ij}K) \, d\Omega^j , \tag{6.34}
$$

$$
P_a = \frac{1}{8\pi} \int_{S^{D-2}} (K_{ww} - K) \, d\Omega_a = 0 . \tag{6.35}
$$

The P_a components are identically 0 as any vector $V_a = 0$ in the modified Cartoon formalism is 0, as described in Appendix A.1. For angular momentum we again impose the quasi-isotropic gauge, and asymptotic maximal gauge condition,

$$
\frac{\partial \tilde{\gamma}_{ij}}{\partial x^j} = \mathcal{O}(r^{1-D}) , \tag{6.36}
$$

$$
K = \mathcal{O}(r^{1-D}) , \tag{6.37}
$$

and following e.g. [122] we define the total angular momentum to be

$$
J_{(p)} = \frac{1}{8\pi} \lim_{r \to \infty} \int_{S^{D-2}} (K_{JK} - K\delta_{JK})\varphi^J_{(p)} d\Omega^K , \tag{6.38}
$$

where $\varphi_{(p)}$ is the rotational Killing vector associated to the rotational symmetry in question. Since we will only be concerned with rotations in the $x - y$ plane, we can pick this to be

$$
\varphi^I = x \left(\frac{\partial}{\partial y} \right)^I - y \left(\frac{\partial}{\partial x} \right)^I . \tag{6.39}
$$

We note that the calculation of this Killing vector is the same as the calculation of the Killing vector in Chapter 8, detailed in Appendix C.1, though we here present it in Cartesian, rather than spherical coordinates. Restricted to our computational domain, the angular momentum reduces to

$$J_{(p)} = \frac{1}{8\pi} \lim_{r \to \infty} \int_{S^{D-2}} (K_{jk} - K\delta_{jk})\varphi^j_{(p)} d\Omega^k. \tag{6.40}$$

In the limit as $r \to \infty$ the radial unit vector within the area element $d\Omega^k$ will become orthogonal to the Killing vector φ^j. Therefore we can ignore this final term proportional to K and see that this angular momentum is the same as the angular momentum tensor we defined in Section 6.3 contracted with the appropriate Killing vector.

6.5 Evaluating the integrals

Let us now make explicit the evaluation of these integrals in the modified Cartoon formalism. All of the integrals have as their area element $d\Omega_j$, which, we recall, is the full $D - 2$ dimensional area element, multiplied by a vector that only has components in the computational domain, rather than being the area of e.g. the 2 sphere. Let $n^j = x^j/r$, the unit vector now centred at the origin, rather than at a black hole. The mass, momentum and angular momentum of the spacetime are then given by

$$
\begin{aligned}
M &= \frac{1}{16\pi} \int_{S^{D-2}} (\partial^i \gamma_{ij} + (D-4)\left(\frac{\gamma_{jz} - \delta_{jz}\gamma_{ww}}{z}\right) - \delta^{ik}\partial_j \gamma_{ik} - (D-4)\partial_j \gamma_{ww})\, d\Omega^j \\
&= \frac{r^{D-2}}{16\pi} \mathcal{A}_{D-4} \int_0^\pi \int_0^\pi (\partial^i \gamma_{ij} + (D-4)\left(\frac{\gamma_{jz} - \delta_{jz}\gamma_{ww}}{z}\right) - \delta^{ik}\partial_j \gamma_{ik} - (D-4)\partial_j \gamma_{ww}) \\
&\quad n^j \sin^{D-4}(\phi_3) \sin^{D-3}(\phi_2) d\phi_3 d\phi_2,
\end{aligned}
\tag{6.41}
$$

$$
\begin{aligned}
P_i &= \frac{1}{8\pi} \int_{S^{D-2}} (K_{ij} - \delta_{ij}K)\, d\Omega^j \\
&= \frac{r^{D-2}}{8\pi} \mathcal{A}_{D-4} \int_0^\pi \int_0^\pi (K_{ij} - \delta_{ij}K)n^j \sin^{D-4}(\phi_3) \sin^{D-3}(\phi_2)\, d\phi_3 d\phi_2,
\end{aligned}
\tag{6.42}
$$

$$
\begin{aligned}
J_{(p)} &= \frac{1}{8\pi} \int_{S^{D-2}} (K_{jk} - K\delta_{jk})\varphi^j_{(p)} d\Omega^k \\
&= \frac{r^{D-2}}{8\pi} \mathcal{A}_{D-4} \int_0^\pi \int_0^\pi (K_{jk} - K\delta_{jk})\varphi^j_{(p)} n^k \sin^{D-4}(\phi_3) \sin^{D-3}(\phi_2)\, d\phi_3 d\phi_2.
\end{aligned}
\tag{6.43}
$$

Clearly the expression for the energy in Eq. (6.41) has a term that appears to diverge at $z = 0$. This is however dealt with by one of the regularisation terms we have already calculated, given in Eq. (A.27),

$$\frac{\gamma_{jz} - \delta_{jz}\gamma_{ww}}{z} = \partial_z\gamma_{\hat{j}z},\tag{6.44}$$

where $\hat{j} \in \{x, y\}$, with the left hand side equal to 0 if $j = z$.

6.6 Conclusions

In this chapter we have introduced initial data for boosted and spinning black holes. This will allow us to investigate a new set of more physically relevant black hole interactions, such as black hole inspirals, and high energy black hole collisions. We have also introduced higher dimensional ADM integrals, which will allow us to calculate the total energy-momentum and angular momentum of a spatial slice. Using the wave extraction formalism of Chapter 4, we can also calculate the energy and momentum contained in gravitational waves in the spacetime. To be able to independently verify the values calculated through wave extraction and the ADM integrals using an energy balance argument, we need to be able to calculate the mass and spin of the black hole itself. Therefore the final missing diagnostic tool is a horizon finder, which we shall introduce in the following chapter.

Chapter 7

An Apparent Horizon Finder in Higher Dimensions

The work in this chapter is unpublished. It was performed in collaboration with Ulrich Sperhake and Diandian Wang. The horizon finding code was written by D. Wang and the author, and the results were generated by U. Sperhake and the author.

7.1 Introduction

A key goal for numerical relativity in any given setting, such as higher dimensions, is to have a full set of diagnostic tools for that setting. One such tool, the main focus of this chapter, is the ability to find the horizon of a black hole. Once we can find the horizon of a black hole, we can then find a measure of its spin and mass, independent of, for instance, wave extraction calculations. The event horizon of a black hole is a gauge independent object, but one that requires knowledge of future null infinity to compute, see [289, 290]. This is impractical to consider in many time evolution codes, so instead, we restrict our attention to the apparent horizon (AH) of the black hole. This is a slicing dependent object, that always lies on or within the event horizon of the black hole, defined as the outermost marginally trapped surface in the spacetime. Developing efficient, accurate horizon finding has been an important area of research within numerical relativity, especially in 4 spacetime dimensions, with key references including [291–294], for a review see [295]. Here we follow the work of Alcubierre et al. [291], and adapt an algorithm used for $4D$ horizon finding to higher dimensions. In this chapter we shall detail the algorithm used to find apparent horizons, and how it has been adapted to higher dimensional GR, we shall describe its numerical

implementation, and we shall demonstrate its diagnostic uses on several types of initial black hole data and time evolutions of black hole binaries. In order to do this, we will use the binary black hole data described in Chapter 6 to enable us to compute numerically, for the first time, the apparent horizon of a rotating BH dynamically formed in higher dimensions in a binary coalescence.

This chapter is organized as follows. In Section 7.2 we review the theory behind finding apparent horizons, and formulate the problem of horizon finding in the modified Cartoon formalism. We then derive expressions for the mass and spin of a black hole in terms of quantities we can extract from the apparent horizon. In Section 7.3 we present the results of testing this horizon finder on three types of initial data. Firstly we use analytic data for a single Schwarzschild-Tangherlini black hole and a single, singly spinning, Myers-Perry black hole. We then use numerically constructed data of the type detailed in Chapter 6 to simulate inspirals of non-spinning black holes to dynamically form a spinning black hole.

7.2 Horizon finding algorithm

7.2.1 Horizon finding in higher dimensions

The apparent horizon of a black hole is defined as the outermost marginally trapped surface in the spacetime. Equivalently, this is the surface on which the expansion of outgoing normal null geodesics is equal to 0. In order to find the apparent horizon on a spacelike hypersurface Σ_t we calculate the expansion $\Theta = \nabla_A k^A$ of a congruence of null geodesics with tangent vector k^A moving in the outward normal direction to a surface S, with outward unit normal vector s^A. The calculation of the expansion of this congruence in higher dimensions proceeds identically to the calculation in $4D$, and we present it here for completeness, following the derivation of Gundlach [292]. Consider a D dimensional spacetime $(\mathcal{M}, g_{AB})$, with covariant derivative ∇_A. We foliate this spacetime with $D-1$ dimensional spacelike hypersurfaces Σ_t with timelike normal n^A. We recall that the induced metric on these hypersurfaces is given by

$$\gamma_{AB} = g_{AB} + n_A n_B, \tag{7.1}$$

with extrinsic curvature

$$K_{AB} = -\gamma^C{}_A \nabla_C n_B = -D_A n_B, \tag{7.2}$$

where D_A is the covariant derivative associated to γ_{AB}. Now let S be a closed, $D-2$ dimensional, spacelike hypersurface of Σ, with unit outward spacelike normal s^A, which is also normal to n^A. γ_{AB} induces a metric q_{AB} on S,

$$q_{AB} = \gamma_{AB} - s_A s_B. \tag{7.3}$$

Now let us consider the future pointing, null geodesic congruence, whose projection onto Σ is orthogonal to S and n^A. k^A satisfies the following equations:

$$k^A \nabla_A k^B = 0\,, \qquad k^A k_A = 0\,, \qquad q_{AB} k^A|_S = 0. \tag{7.4}$$

In consequence of these conditions, we find that, up to a constant factor, here set to 1 without loss of generality,

$$k^A|_S = s^A + n^A\,. \tag{7.5}$$

Now we can express the expansion Θ in terms of $(D-1)+1$ quantities,

$$
\begin{aligned}
\Theta &= g^{AB}\nabla_A k_B = (\gamma^{AB} - n^A n^B)\nabla_A k_B \\
&= \gamma^{AB}\nabla_A(s_B + n_B) - (k^A - s^A)(k^B - s^B)\nabla_A k_B \\
&= \gamma^{AB}\nabla_A s_B + \gamma^{AB}\nabla_A n_B - s^A s^B \nabla_A n_B\,.
\end{aligned} \tag{7.6}
$$

In a coordinate basis adapted to the space-time split, we can write this equation in terms of spatial components,

$$\Theta = D_I s^I + s^I s^J K_{IJ} - K\,. \tag{7.7}$$

The outermost surface upon which $\Theta = 0$ everywhere will be our apparent horizon. It will prove convenient to parametrise this surface with a function $F(x^I)$, such that our surface is given by the solution to the equation $F(x^I) = 0$, so that we can write,

$$s^I = \frac{D^I F}{|DF|}\,, \qquad |DF| := \sqrt{D_J F\, D^J F}\,, \tag{7.8}$$

and Eq. (7.7) can be reframed as a partial differential equation to be solved for the scalar F.

In order to evaluate Eq. (7.7) in the modified Cartoon formalism, we must distinguish between directions inside and those pointing off the $3D$ computational domain. We can then use the rotational symmetry in the extra dimensions to simplify tensors as

described in Chapter 3, and furthermore rewrite derivatives in the extra dimensions in terms of derivatives in our computational domain, using the formulae in Appendix A. The only terms in Eq. (7.7) that will require such treatment of extra dimensional components are $D_I s^I$ and the trace of the extrinsic curvature. The latter is directly obtained as $K = K^I{}_J = K^i{}_i + (D - 4)\gamma^{ww}K_{ww}$ while we write the former as

$$D_I s^I = D_i s^i + D_a s^a \tag{7.9}$$
$$= \frac{D_i D^i F}{|DF|} - \frac{(D^i F)(D_j F)D_i D^j F}{|DF|^3} + (D - 4)\frac{\partial^z F}{|DF|z} + \frac{D - 4}{2}\gamma^{ww}\partial_k\gamma_{ww}\frac{\partial^k F}{|DF|}.$$

In summary the equation we will look to solve for F is

$$0 = \Theta = \frac{D_i D^i F}{|DF|} - \frac{(D^i F)(D_j F)D_i D^j F}{|DF|^3} + (D - 4)\frac{\partial^z F}{|DF|z}$$
$$+ \frac{1}{2}(D - 4)\gamma^{ww}\partial_k\gamma_{ww}\frac{\partial^k F}{|DF|} + \frac{K_{ij}\partial^i F\partial^j F}{|DF|^2} - K. \tag{7.10}$$

We note also that at $z = 0$ the term $\partial^z F/z$ appears ill-defined. According to the regularisation procedures laid out in Appendix A, in the limit of small z we can substitute

$$\lim_{z \to 0} \frac{\partial^z F}{z} = \lim_{z \to 0} \partial_z\partial^z F. \tag{7.11}$$

7.2.2 Minimisation algorithm

In order to numerically solve Eq. (7.10), we have extended the minimisation algorithm provided inside the Cactus Computational Toolkit [228, 220] and described in [291, 296] to the case of D dimensions with $SO(D - 3)$ isometry. The first step consists in parametrising the function F, restricted to the $3D$ computational domain, as

$$F(r, \phi^2, \phi^3) = r - h(\phi^2, \phi^3). \tag{7.12}$$

We can then expand h in terms of real spherical harmonics $Y_{lm}(\phi^2, \phi^3)$,

$$h(\phi^2, \phi^3) = \sum_l \sum_m \sqrt{4\pi}a_{lm}Y_{lm}(\phi^2, \phi^3). \tag{7.13}$$

The iterative search for a solution starts with a spherical trial function for h, from which we calculate F, and so Θ, by Eqs. (7.12), (7.10). Next, Θ is interpolated onto the points at which $r = h(\phi^2, \phi^3)$, and used to calculate the surface integral of Θ^2 over

this $2D$ surface. Powell's minimisation algorithm [297] then leads to the values a_{lm} for which this integral is minimised. Once a function F giving a minimum for Θ^2 is found, we must determine whether this is a local or global minimum. Following [291], this is achieved by recalculating the candidate function F with higher spatial resolution, and more terms in the spherical harmonic expansion (7.13). If the value of the integral of Θ^2 continues to decrease to zero, rather than reaching some non-zero limiting value, it is interpreted as a global minimum and the corresponding F defines the apparent horizon. The horizon surface then allows us to calculate further diagnostic quantities as described in the next section.

7.2.3   Black hole diagnostics

Once we have found the apparent horizon we wish to extract physical diagnostics of black holes from them. When we consider stationary black holes, such as those produced by exact initial data (e.g. Secs. 7.3.1 and 7.3.2), we know that the world tube of the apparent horizon coincides exactly with the event horizon, see [298] for the proof in $D = 4$, and [299] for a discussion of the generalisation of this, and related proofs, to higher dimensions. For black holes produced as the result of mergers in our simulations (e.g. Sec. 7.3.3) we assume that the spacetime will, after a long enough period of time, be perturbatively close to a stationary BH, and that in this case the apparent horizon will closely approximate the spatial cross section of an event horizon. We therefore base our calculation of BH mass and spin on the assumption that the spacetime describes a stationary BH.

Non-spinning black holes

For illustration, we first consider non-rotating BHs in D spacetime dimensions. These are described by the Tangherlini metric [159] given in Schwarzschild coordinates by

$$ds^2 = -\left(1 - \frac{\mu}{\tilde{r}^{D-3}}\right)dt^2 + \left(1 - \frac{\mu}{\tilde{r}^{D-3}}\right)^{-1}d\tilde{r} + \tilde{r}^2 d\Omega_{D-2}^2, \tag{7.14}$$

where

$$\mu = \frac{16\pi M_{ADM}}{(D-2)\mathcal{A}_{D-2}}, \tag{7.15}$$

is the mass parameter. $d\Omega_n$ is the line element on the unit n-sphere, parametrised by n angular coordinates, $(\phi^2, \ldots \phi^{D-1})$, $\mathcal{A}_n$ is the surface area of the unit n-sphere, and M_{ADM} is the ADM mass associated to the spacetime containing only the black hole

with mass parameter μ. By considering Eq. (7.14) we can see that the event horizon of the black hole is given by the surface $\tilde{r}_S^{D-3} = \mu$. We find the area of this surface to be

$$A_{\text{hor}} = \int_{\mathcal{H}} \sqrt{q} d\phi^2 \ldots d\phi^{D-1} = \tilde{r}_S^{D-2} \mathcal{A}_{D-2}, \tag{7.16}$$

where $q = \det q_{IJ}$, $\mathcal{H}$ is the horizon surface, and A_{hor} is the area of the apparent horizon, as this is a stationary black hole. Combining this expression with Eq. (7.15), we find

$$M_{ADM} = \frac{D-2}{16\pi} \mathcal{A}_{D-2}^{1/(D-2)} A_{\text{hor}}^{(D-3)/(D-2)}. \tag{7.17}$$

Spinning black holes

The Myers-Perry metric for a singly spinning black hole is given by [15]

$$
\begin{aligned}
ds^2 &= -dt^2 + \frac{\mu}{r^{D-5}\Sigma}(dt - a\sin^2\theta \, d\tilde{\phi})^2 + \frac{\Sigma}{\Delta}dr^2 + \Sigma d\theta^2 \\
&\quad + (r^2 + a^2)\sin^2\theta \, d\tilde{\phi}^2 + r^2\cos^2\theta \, d\Omega_{D-4}^2, \\
\Sigma &= r^2 + a^2\cos^2\theta, \\
\Delta &= r^2 + a^2 - \frac{\mu}{r^{D-5}},
\end{aligned}
\tag{7.18}
$$

where μ is the mass parameter, and a is the spin parameter. Note of course that, unlike in $4D$, where the Kerr black hole is the unique uncharged rotating black hole solution, in higher dimensions other solutions with the same mass and spin, such as black rings [13], or black saturns [14] can exist. In this discussion we assume that the end state of the black hole merger is a Myers-Perry black hole. Let $\phi^4, \ldots \phi^{D-1}$ be the angular coordinates on the $D-4$ sphere in the metric. The ranges of the angular coordinates are $\theta \in [0, \pi/2]$, $\tilde{\phi} \in [0, 2\pi]$, $\phi^{D-1} \in [0, 2\pi]$, with all other angles lying in the interval $[0, \pi]$. The location of the horizon is given by the largest root of $\Delta = 0$,

$$\frac{\mu}{r_+^{D-5}} = r_+^2 + a^2, \tag{7.19}$$

and, following a brief calculation, the horizon area is, similarly to Eq. (7.16), given by

$$A_{\text{hor}} = \int_{\mathcal{H}} \sqrt{q} \, d\theta \, d\tilde{\phi} \, d\phi^4 \ldots d\phi^{D-1} = r_+^{D-4}(r_+^2 + a^2)\mathcal{A}_{D-2} = r_+\mu\mathcal{A}_{D-2}. \tag{7.20}$$

To calculate the spin we will need the equatorial circumference

$$\ell_e = \int_0^{2\pi} \sqrt{g_{\tilde\phi\tilde\phi}} d\tilde\phi = 2\pi \frac{r_+^2 + a^2}{r_+} = 2\pi \frac{\mu}{r_+^{D-4}}\,,$$

giving us

$$r_+^{D-3} = \frac{2\pi}{\mathcal{A}_{D-2}} \frac{A_{\mathrm{hor}}}{\ell_e}\,, \qquad \mu = \frac{A_{\mathrm{hor}}}{r_+ \mathcal{A}_{D-2}}\,, \qquad a = \sqrt{\frac{\mu}{r_+^{D-5}} - r_+^2}\,. \qquad (7.21)$$

Note that Eq. (7.15) holds also for stationary, spinning BHs. Substituting μ in that expression in terms of $\mathcal{A}_{D-2}$ and A_{hor} and finally setting $\ell_e = 2\pi r_S$, $r_+ = r_S$ for the non-spinning limit, one indeed recovers Eq. (7.17). We conclude this diagnostic section by noting that the total angular momentum associated to the spacetime for the single-spin Myers-Perry metric (7.18) is given by [232]

$$J = \frac{2a}{D-2} M_{ADM}. \qquad (7.22)$$

7.3   Results

Our numerical simulations have been performed with the LEAN code [192, 227] originally developed for black-hole simulations in $D = 4$ dimensions and upgraded to general D spatial dimension with $SO(D-3)$ isometry in [212, 114, 115], using the modified Cartoon formalism detailed in Chapter 3.

We test the horizon finder in three different scenarios. The first two will involve analytic initial data for spacetimes containing a single black hole. We test a Schwarzschild-Tangherlini black hole in 5 dimensions with initial data constructed using isotropic coordinates, and a 5 dimensional singly spinning Myers-Perry black hole, with initial data in Kerr-Schild coordinates. We then use numerically constructed data, in the fashion of Bowen-York data, as given in [285, 271] and described in Chapter 6, to construct 2 black holes with initial orbital angular momentum, and so simulate a black hole inspiral in higher dimensions (here $6D$). In the first example we use the horizon mass as a diagnostic for the horizon finder, and in the latter two examples we use the horizon mass and spin to analyse the accuracy of our horizon finder.

7.3.1 Isotropic Schwarzschild-Tangherlini

In Schwarzschild coordinates the Schwarzschild-Tangherlini metric (7.14) is singular at the event horizon. These coordinates are therefore not suitable for a numerical computation of the horizon and we consequently change to isotropic coordinates (see e.g. [160]),

$$\tilde{r} = r \left(1 + \frac{\mu}{4r^{D-3}}\right)^{2/(D-3)} , \tag{7.23}$$

which results in the line element

$$ds^2 = -\frac{4r^{D-3} - \mu}{4r^{D-3} + \mu} dt^2 + \left(1 + \frac{\mu}{4r^{D-3}}\right)^{4/(D-3)} \left(dx^2 + dy^2 + dz^2 + \sum_a dw_a^2\right) . \tag{7.24}$$

Here $r^2 = \sum_I (x^I)^2$ is the isotropic radius, there is now no coordinate singularity at the horizon, and the coordinate singularity at $r = 0$ is dealt with through use of the moving puncture gauge [139, 140, 166], as detailed in Section 2.5. We next perform the ADM spacetime decomposition, picking the isotropic time coordinate as the time coordinate of our foliation, from which we can read off our initial data,

$$\alpha = \left(\frac{4r^{D-3}+\mu}{4r^{D-3}-\mu}\right)^{1/2} , \qquad\qquad \beta^I = 0 , \tag{7.25}$$

$$\gamma_{IJ} = \delta_{IJ} \left(1 + \frac{\mu}{4r^{D-3}}\right)^{4/(D-3)} , \quad K_{IJ} = 0. \tag{7.26}$$

Note that in our simulations we will not evolve these data in time, so the values of lapse and shift are merely included here for completeness but not used in the numerical computation. We note that the construction of this initial data is analogous to the construction of the higher dimensional Brill-Lindquist data in Section 2.4.

We use our horizon finder to calculate the BH mass for a single isotropic Schwarzschild-Tangherlini BH with mass parameter $\mu = 1$, for a grid configuration with 7 nested grids with radii $\{(128, 64, 32, 16, 8, 4, 1) \times (), h\}$, using the notation of Sec. II F in [192], in units of the horizon radius $R_h = \mu^{1/(D-3)}$. We shall quote the simulation resolution, h as the grid spacing on the finest refinement level. In this setup, the apparent horizon is computed on the 6th refinement level $\{x, y, z\} < 4$ and we find, for 3 simulations of differing resolution, the results of Table 7.1. To investigate numerical convergence we calculate Q_M given by

$$Q_M = \frac{M_{1/48} - M_{1/64}}{M_{1/64} - M_{1/96}} = 2.5924, \tag{7.27}$$

R_h/h	48	64	96
M_{hor}/M_{ADM}	1.000041	0.999981	0.999958
Q	$Q_4 = 2.69$	$Q_M = 2.59$	

Table 7.1 Measured horizon mass of Schwarzschild-Tangherlini BH at different resolutions. The bottom row gives the expected convergence factor for 4th order convergence, Q_4, and the measured convergence factor for the mass, Q_M.

where M_h is the value of the horizon mass calculated for a given resolution. The empirical convergence factor is very close to the value expected for fourth-order convergence, $Q_4 = 2.6923$, consistent with the fourth-order differencing employed in the code.

7.3.2 $5D$ **Myers-Perry in Kerr-Schild coordinates**

As in the case of the Schwarzschild black hole, the numerical calculation of the apparent horizon of a spinning Myers-Perry BH requires coordinates that are not singular at the BH horizon. One such set of coordinates are Kerr-Schild coordinates, in which the metric is written in the form

$$ds^2 = (\eta_{AB} + H l_A l_B) dx^A dx^B, \tag{7.28}$$

for an appropriate function H, and null vector l_A. Let us specifically consider a $D = 5$ singly spinning Myers-Perry black hole, in Cartesian coordinates (t, x, y, z, w). The spin parameter is a and the spin lies purely in the $x - y$ plane. Following [15] we can write this metric in Kerr-Schild form, with the functions in Eq. (7.28) given by

$$H = \frac{\mu r^2}{\Pi F}, \qquad \Pi = r^2(r^2 + a^2), \qquad F = 1 - \frac{a^2(x^2 + y^2)}{(r^2 + a^2)^2}, \tag{7.29}$$

and

$$l_A = \left(1, \ \frac{rx + ay}{r^2 + a^2}, \frac{ry - ax}{r^2 + a^2}, \ \frac{z}{r}, \ \frac{w}{r}\right), \tag{7.30}$$

where r is given by the solution to the equation $l_A l^A = 0$, i.e. $r^4 - r^2(\rho^2 - a^2) - a^2(z^2 + w^2) = 0$, where $\rho^2 = x^2 + y^2 + z^2 + w^2$. Again we foliate the spacetime with slices of constant Kerr-Schild time, t, and read off the initial lapse, shift and induced metric from the line element, and calculate the initial extrinsic curvature with Eq. (2.12), which for brevity we do not reproduce here.

$a/\sqrt{\mu}$	0.1			0.9		
$\sqrt{\mu}/h$	16	32	64	32	48	64
M_{hor}/M	1.0005025	1.0001200	1.0000287	1.0012295	1.0003776	1.0000498
$a_{\text{hor}}/\sqrt{\mu}$	0.1007076	0.1001868	0.1000571	0.8979883	0.8991569	0.8995459
Q	$Q_2 = 4$	$Q_M = 4.02$	$Q_a = 4.19$	$Q_2 = 2.86$	$Q_M = 2.60$	$Q_a = 3.00$

Table 7.2 Horizon mass M_{hor} and spin a_{hor} in units of the analytic values M, $\sqrt{\mu}$ as obtained for a Myers-Perry BH in Kerr-Schild coordinates (7.28) in $D = 5$ for spin parameters $a/\sqrt{\mu} = 0.1$ and 0.9. The bottom row lists the expected convergence factor Q_2 for second-order convergence and the measured convergence factors $Q_f = (f_{h_1} - f_{h_2})/(f_{h_2} - f_{h_3})$ for mass ($f = M$) and spin ($f = a$). For the large spin $a/\sqrt{\mu} = 0.9$, we require higher grid resolution to find the apparent horizon; hence the different range of resolutions used in the convergence analysis.

In Table 7.2 we present the calculated angular momentum and mass for the Myers-Perry BH for different resolution simulations for different spin values. The grid set up is the same as for Section 7.3.1, and all results are extracted on refinement level 6.

7.3.3   Numerically constructed Bowen-York like data for a BH inspiral in $6D$

For the third test, we consider the dynamic formation of a rotating BH through the coalescence of a BH binary with non-vanishing initial orbital angular momentum or, equivalently, with non-zero impact parameter b. Before we quantitatively analyse such configurations, however, we emphasize a few important points about orbiting binaries in $D > 4$ dimensions.

In general, we expect this type of BH collisions to yield similar regimes of scattering and merging configurations in $D > 4$ as known in $D = 4$ [48]; below a scattering threshold, $b < b_{\text{scat}}$, the binary results in a merger while for $b > b_{\text{scat}}$, the constituents will scatter off to infinity. Even without numerical simulations, however, we immediately notice two major differences between inspirals or grazing collisions in $D = 4$ as compared with their $D > 4$ counterparts. (i) Unlike in $D = 4$, there exist no stable circular orbits around a Myers-Perry black hole in $D > 4$ [300], ruling out, for instance, stable planetary orbits in a $D > 4$ solar system. Viable gravity theories based on higher-dimensional GR therefore require some kind of screening mechanism limiting the impact of extra dimensions to very large or small scales. (ii) The second difference is of quantitative nature and concerns the relatively weaker gravitational binding force

in binary systems in $D > 4$. For any black hole binary whose orbit begins close to an unstable circular orbit, this implies correspondingly weaker centrifugal forces and, thus, that the orbital velocity in the inspiral will be much slower than in $D = 4$. This is, of course, a special manifestation of the well-known result that in the large D limit, there is no gravitational force outside the horizon; cf. [16]. In practice, both features manifest themselves in the dependence of the binary dynamics on the initial momentum parameters: (i) we need relatively small initial momenta lest the binary scatters rather than merges and (ii) without careful fine-tuning of the initial momentum, we find it hard to obtain inspirals completing more than about one orbit prior to a rapid plunge phase.

We note that in [112], grazing black hole collisions have been studied in $5D$. In this work it was noted that no "zoom-whirl" orbits were found in $5D$. These orbits have been identified in numerical studies in $4D$, where inspiralling black holes whirl around each other for a number of orbits before either merging or scattering to infinity [301–303, 48]. Though we cannot make a statement on the existence of such orbits generically in higher dimensions without fully exploring the parameter space of initial momenta and impact parameters, and in particular investigating high energy grazing collisions, we note that the sharp transition between scattering orbits and mergers that only involve a single orbit supports the hypothesis that such zoom-whirl orbits cannot be formed in higher dimensions.

Bearing in mind these considerations, we numerically model orbiting binaries and compute the apparent horizon of post-merger remnant BHs. We construct our initial data following the procedure outlined in Section 6.2. This determines $\bar{A}_{IJ}$, the trace free conformally rescaled extrinsic curvature, and gives us an elliptic PDE for ψ, the conformal factor, Eqs (6.27), (6.28), which we solve by means of an elliptic PDE solver provided by the CACTUS thorn TWOPUNCTURES [156]. In these simulations we set the parameter $P_x = 0$ and vary the transverse momentum P_y.

We now consider the specific configuration of two equal-mass, non-spinning BHs starting from positions $x_0/R_h = \pm 3.185$ with transverse initial linear momentum $P_y/M_{\mathrm{ADM}} = \pm 0.0286$. We have evolved this configuration using a grid setup given by $\{(160, 120, 72, 24, 12, 6) \times (1.25, 0.625), h_i\}$ in the notation of Sec. II F in [192]. In order to study the convergence of the radiated energy and the spin of the merger remnant, we have used three values for the grid resolution on the innermost refinement level, $h_1 = R_h/64$, $h_2 = R_h/96$ and $h_3 = R_h/128$. For illustration, we show in Fig. 7.1 the puncture trajectory of the two BHs. We find that, for resolutions lower than these
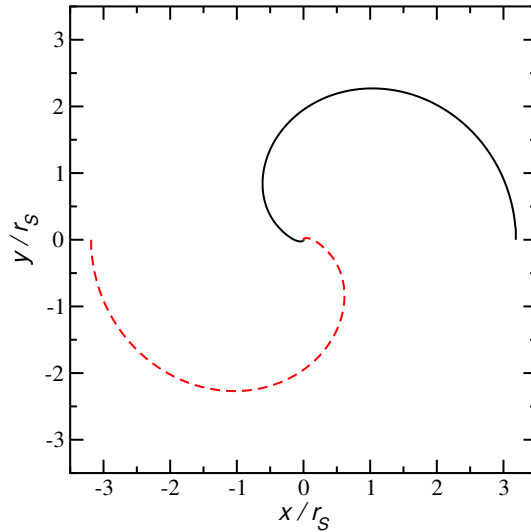
Fig. 7.1 Puncture trajectories of the grazing collision of two equal-mass, non-spinning BHs in $D = 6$ dimensions starting from positions $x/R_h = \pm 3.185$ with transverse linear momentum $P_y/M_{\mathrm{ADM}} = 0.0286$.

our results become very untrustworthy, especially for simulations with P_y near the critical value separating scattering and merging orbits. In this critical region altering the resolution can change a scattering orbit into a merging orbit. Also, at lower resolutions than reported here we find that the coordinate time until merger varies non-monotonically with resolution. At the various values of higher resolution reported here we see none of these issues, so we consider ourselves to be using sufficiently high resolutions for this problem in the simulations presented in this chapter. Following the wave extraction procedure described in Chapter 4, we have calculated the energy emitted in gravitational waves in this collision and for the post-merger phase (starting at about $t/R_h = 150$), we extract the spin of the merger remnant as detailed in Sec. 7.2.3 above. The results obtained for the different resolutions are shown in Fig. 7.2 together with an analysis of the respective convergence properties. We find the radiated energy to converge at 4th order and the spin between 3rd and 4th order. These findings are consistent with our code setup which employs 4th-order differencing in space and time and 2nd order discretisation techniques at the outer boundary and prolongation in space. Comparison with the corresponding Richardson extrapolated values gives us an uncertainty estimate of $1.8\,\%$ ($0.5\,\%$, $0.22\,\%$) for the dimensionless spin at low (medium, high) resolution and a discretisation error well below $1\,\%$ for the energy extracted at any of the resolutions. Note that the radiated energy in this particular grazing collision is $E_{\mathrm{rad}}/M_{\mathrm{ADM}} = 0.199\,\%$, more than twice as large as the head-on
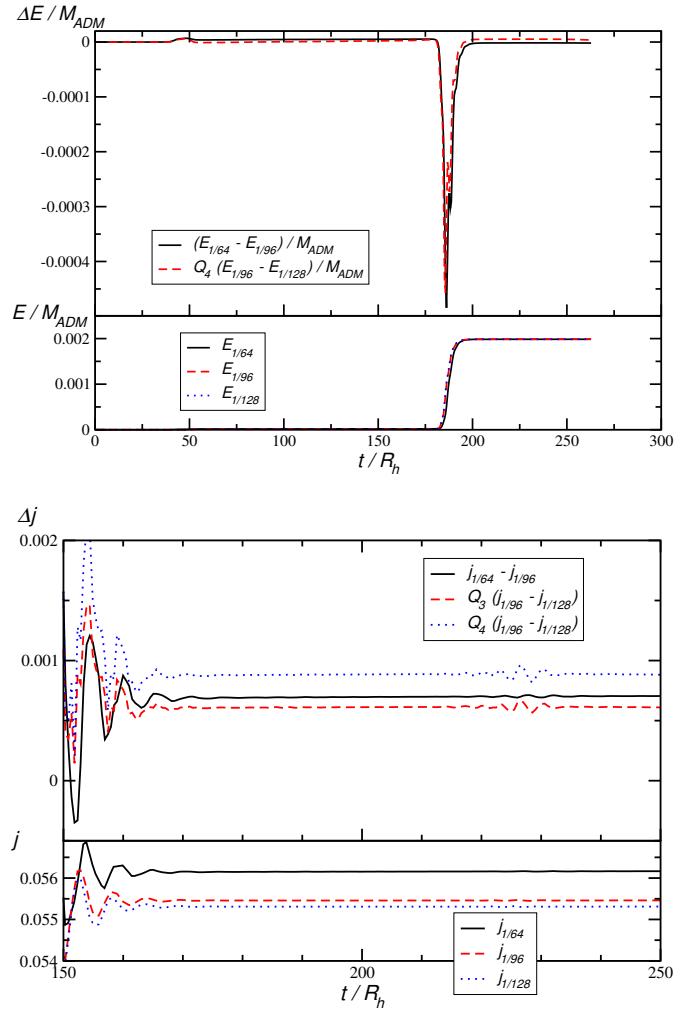
Fig. 7.2 Analysis of the energy radiated in gravitational waves (top) and the merger remnant's dimensionless spin (bottom). For either quantity, we show results obtained for the three grid resolutions in the lower panel and compare in the upper panel the differences low-medium vs. medium-high resolution, rescaling the latter by a factor $Q_4 = 5.94$ or $Q_3 = 4.11$ expected for 4th or 3rd order convergence.

value $E_{\mathrm{rad,headon}}/M_{\mathrm{ADM}} = 0.0819\,\%$, as reported in Chapter 5. Note that in Fig. 7.2 we report the dimensionless spin parameter defined in [232] as

$$j = c_J^{1/(D-3)} \frac{J}{M^{1/(D-3)}\,M}\,, \qquad c_J = \frac{\mathcal{A}_{D-3}}{2^{D+1}} \frac{(D-2)^{D-2}}{(D-3)^{(D-3)/2}}\,, \qquad J = \frac{2}{D-2}Ma\,. \quad (7.31)$$

7.4 Conclusions

In this chapter we have demonstrated the accuracy of an apparent horizon finder, using a minimisation algorithm, in higher dimensional numerical relativity, and its application to various types of initial black hole data. In particular the success of the finder in tracking black holes through merger, and outputting diagnostic quantities for the final post-merger black hole should provide a valuable tool in the analysis of black hole inspirals in higher dimensional numerical relativity. We have also performed the first simulation of a BH inspiral in more than $4D$ using Bowen-York like data. With this code in place there is now scope for a much more extensive exploration of inspiralling black holes in higher dimensions. We can now investigate how the radiated energy in gravitational waves varies as a function of the angular momentum of the initial data, as well as the number of dimensions D. It is also of interest to investigate how high a spin a black hole can be formed with, as the product of binary black hole coalescence. It is known that above $5D$ there is no theoretical extremality bound on the spin of a black hole, however the sharp drop off in the gravitational field indicates it may be difficult for inspirals in higher dimensions to produce highly spinning remnants. It would be of further interest to use the spinning initial data of Section 6.3 to investigate how initially spinning black holes would affect such results, as well as potential generalisations of known effects in $4D$ that are a result of the interaction between black hole spins and orbital angular momentum, such as the "hang-up" effect [304] and black hole superkicks [305–308].

Chapter 8

Angular Momentum Wave Extraction

The work in this chapter is unpublished. It was performed by the author alone.

8.1 Introduction

In order to fully analyse black hole inspirals of the type presented in Chapter 7 we must implement one more diagnostic quantity. Using our apparent horizon finder we can calculate the post merger spin of a black hole, and with Eq. (6.43) we can calculate the total angular momentum in a spatial slice of the spacetime. The difference between these measures is the Bondi angular momentum, the angular momentum radiated away in gravitational waves. In this chapter we will implement a formula for the Bondi angular momentum in the Weyl scalar wave extraction formalism of Chapter 4, using the modified Cartoon dimensional reduction scheme. As we have seen in Section 2.6.4, the calculation of the angular momentum in a spacetime proceeds differently to that for mass and linear momentum, due to the so called supertranslation ambiguity in $4D$ of defining angular momentum. For the ADM integrals defined at spatial infinity, the angular momentum, Eq. (2.95), is not preserved under the symmetry group of spatial infinity, which contains supertranslations, and so stronger conditions than asymptotic flatness must be imposed upon the spacetime, given in Eqs (2.96), (2.97). This problem also arises when defining the ADM integrals in higher dimensions, as we have seen in Chapter 6. In $4D$ the asymptotic symmetry group of null infinity is the BMS group [309, 180], which also contains supertranslations, and so the same problem arises when considering the angular momentum in gravitational waves in $4D$, a problem that has

been widely studied in e.g. [310–313]. In higher dimensions however, it has been shown that the symmetry group of null infinity is the Poincaré group [270], which does not contain supertranslations. This means that in $D > 4$ we have a well defined Bondi angular momentum, which has been shown in [314] to obey the equation

$$\frac{d}{du}J_{(p)}^{Bondi} = \frac{1}{16\pi}\int_{S^{D-2}}\varphi_{(p)}^{\alpha}\left(2\dot{h}_{\alpha\beta}^{(1)}\mathcal{D}_{\gamma}h^{\beta\gamma(1)} - \mathcal{D}_{\gamma}h_{\alpha\beta}^{(1)}\dot{h}^{\beta\gamma(1)} + \frac{1}{2}\dot{h}^{(1)\beta\gamma}\mathcal{D}_{\alpha}h_{\beta\gamma}^{(1)}\right)d\Omega. \quad (8.1)$$

Here $\varphi_{(p)}^{\alpha}$ is the Killing vector associated to the rotational symmetry of our angular momentum, labelled by (p), $h_{\alpha\beta}^{(1)}$ is the Bondi news function, and $\mathcal{D}_{\alpha}$ is the covariant derivative associated with the round metric on the $D - 2$ sphere, which we denote with $\omega_{\alpha\beta}$. An overdot $\dot{h}$ here denotes a derivative with respect to the retarded Bondi time. The remainder of this chapter is structured as follows. In Section 8.2 we briefly recap the derivation of Eq. (8.1), as given in [314]. In Section 8.3 we will describe how to recast Eq. (8.1) in a form suitable for our numerical code, which takes as inputs the Weyl scalar data calculated from our simulations as described in Chapter 4, and outputs the flux of angular momentum. Much of the detail of this calculation can be found in Appendix C.

8.2 Background theory

In Section 4.2 we saw that an asymptotically flat metric can be written in Bondi coordinates in the form

$$ds^2 = g_{AB}dx^A dx^B = -\mathcal{A}e^{\mathcal{B}}du^2 - 2e^{\mathcal{B}}dud\mathbf{r} + \mathbf{r}^2 h_{\alpha\beta}(d\phi^{\alpha} + \mathcal{C}^{\alpha}du)(d\phi^{\beta} + \mathcal{C}^{\beta}du), \quad (8.2)$$

where u is a retarded time coordinate, $\mathbf{r}$ a radial coordinate and ϕ^{α} angular coordinates. We also saw that the Bondi news function $h_{\alpha\beta}^{(1)}$ arises from this metric in an expansion of the function $h_{\alpha\beta}$, c.f. Eq. (4.2).

In [314], Tanabe et al. expand g_{uu} and $g_{u\alpha}$ as a power series in $\mathbf{r}$, with g_{uu} depending on a free function of integration $m(u, \phi^{\alpha})$ and $g_{u\alpha}$ depending on the free function $j^{\alpha}(u, \phi^{\beta})$. m corresponds to the Bondi mass, and linear momentum of the system as shown in [270],

$$M_{Bondi} \quad = \quad \frac{D-2}{16\pi} \int_{S^{D-2}} m d\Omega, \tag{8.3}$$

$$P_{Bondi}^{(I)} \quad = \quad \frac{D-2}{16\pi} \int_{S^{D-2}} m \hat{x}^{(I)} d\Omega, \tag{8.4}$$

where $\hat{x}^{(I)}$ is the Ith Cartesian unit vector. Similarly the Bondi angular momentum is defined to be

$$J_{Bondi,(p)} \quad = \quad -\frac{D-1}{16\pi} \int_{S^{D-2}} \varphi_{(p)}^{\alpha} j_{\alpha} d\Omega, \tag{8.5}$$

where $\varphi_{(p)}^{\alpha}$ is the pth Killing vector of the $D-2$ sphere. Both functions m and j_α can be freely specified on an initial time slice $u = u_0$. By now considering the evolution equations of the metric, it is shown in [314] how j_α evolves in time, i.e. how it changes as gravitational waves are emitted to future null infinity. This provides the radiation formula for angular momentum in higher dimensions, given above in Eq. (8.1).

8.3   Modified Cartoon implementation

The primary concern of this chapter will be writing Eq. (8.1) in a form compatible with our implementation of the modified Cartoon formalism. A key difficulty in generalising results on angular momentum radiation in the literature on $3 + 1$ numerical relativity, e.g. [194], to higher dimensions, is that in $4D$ the spin weighted spherical harmonic formalism of Newman and Penrose [178] is widely used, which is absent in higher dimensions. In order to rewrite Eq. (8.1), we must evaluate three objects in our $SO(D-3)$ symmetry. The Killing vector φ^α, the Bondi news function $h_{\alpha\beta}$, and the covariant derivative $\mathcal{D}_\alpha$. Note, here we have dropped the superscript label on the Bondi news and shall henceforth only refer to it as $h_{\alpha\beta}$, as we will not refer to the other function $h_{\alpha\beta}$ defined in Eq. (8.2) again in this chapter or in Appendix C.

8.3.1   The Killing vector

In this chapter we shall only consider the case of angular momentum in the $x - y$ plane, which is the only plane that our $SO(D-3)$ symmetry assumption will allow us

to perform a BH inspiral in. We remind ourselves of the angular coordinates that we have already defined in Section 2.1,

$$(w^1 \equiv) \quad x^1 = r \cos \phi^2 \,,$$

$$(w^2 \equiv) \quad x^2 = r \sin \phi^2 \, \cos \phi^3 \,,$$

$$\vdots$$

$$(w^{d-1} \equiv) \quad x^{d-1} = r \sin \phi^2 \, \dots \, \sin \phi^{d-1} \, \cos \phi^d \,,$$

$$(w^d \equiv) \quad z = r \sin \phi^2 \, \dots \, \sin \phi^{d-1} \, \sin \phi^d \, \cos \phi^{d+1} \,,$$

$$w^{d+1} = r \sin \phi^2 \, \dots \, \sin \phi^{d-1} \, \sin \phi^d \, \sin \phi^{d+1} \, \cos \phi^{d+2} \,,$$

$$\vdots$$

$$w^{D-3} = r \sin \phi^2 \, \dots \, \sin \phi^{D-3} \, \cos \phi^{D-2} \,,$$

$$w^{D-2} = r \sin \phi^2 \, \dots \, \sin \phi^{D-3} \, \sin \phi^{D-2} \, \cos \phi^{D-1} \,,$$

$$w^{D-1} = r \sin \phi^2 \, \dots \, \sin \phi^{D-3} \, \sin \phi^{D-2} \, \sin \phi^{D-1} \,. \tag{8.6}$$

This coordinate system is not naturally suited to give us the Killing vector associated to the $x - y$ plane, since the 2 angles that are not fixed in our computational domain, ϕ_2, ϕ_3, are colatitudinal angles measuring the angle down from the x and y axis respectively. Instead we require an azimuthal angle in the $x - y$ plane. We shall therefore switch to a coordinate system in which there is an azimuthal angle in the $x - y$ plane, calculate the Killing vector in this coordinate system, and then change coordinates back to the spherical coordinates in Eq. (8.6). What follows is effectively the same problem as constructing the rotation vector around the x or y axis in a standard $3D$ spherical coordinate system that uses the z axis as its reference axis.

Let us define a new angular coordinate system (ψ^α), where the coordinates are defined in the opposite way to that in which they were defined before,

$$w^{D-1} = r \cos \psi^2 \,,$$

$$w^{D-2} = r \sin \psi^2 \cos \psi^3 \,,$$

$$\vdots$$

$$z \equiv w^3 = r \sin \psi^2 \ldots \sin \psi^{D-3} \cos \psi^{D-2} \,,$$

$$y \equiv w^2 = r \sin \psi^2 \ldots \sin \psi^{D-3} \sin \psi^{D-2} \cos \psi^{D-1} \,,$$

$$x \equiv w^1 = r \sin \psi^2 \ldots \sin \psi^{D-3} \sin \psi^{D-2} \sin \psi^{D-1} \,. \tag{8.7}$$

Now the azimuthal angle ψ^{D-1} lies in the $x - y$ plane, and parametrises the entire $2D$ plane, as it runs from $[0, 2\pi]$. We now need to express the relevant Killing vector,

$$\varphi^\alpha = (\partial/\partial \psi^{D-1})^\alpha \tag{8.8}$$

in terms of our old angular coordinate system, (ϕ^α). We perform this calculation in Appendix C.1, which gives the Killing vector

$$\varphi^\alpha = (-\cos \phi_3, \cot \phi_2 \sin \phi_3, 0, \ldots, 0). \tag{8.9}$$

8.3.2   The Bondi news

From [265], as referenced in Chapter 4, we know that the Bondi news function can be extracted from the spacetime in terms of a particular projection of the Weyl tensor, that we refer to as $\Omega'_{(\alpha)(\beta)}$. In Eq. (37) of Godazgar and Reall [265] we are told that

$$\Omega'_{(\alpha)(\beta)} = -\frac{1}{2} \frac{\hat{e}^\alpha_{(\alpha)} \hat{e}^\beta_{(\beta)} \ddot{h}_{\alpha\beta}}{r^{D/2-1}}. \tag{8.10}$$

Here $\hat{e}_{\alpha(\alpha)}$ is a basis for the round metric on the sphere, $\omega_{\alpha\beta}$, meaning

$$\omega_{\alpha\beta} = \delta_{(\alpha)(\beta)} \hat{e}_{\alpha(\alpha)} \hat{e}_{\beta(\beta)}. \tag{8.11}$$

Explicitly in terms of our ϕ^α coordinate system,

$$\omega_{\alpha\beta} = \begin{pmatrix} 1 & 0 & 0 & \cdots & 0 \\ 0 & \sin^2\phi_2 & 0 & \cdots & 0 \\ 0 & 0 & \sin^2\phi_2\sin^2\phi_3 & \cdots & 0 \\ \vdots & \vdots & \vdots & \ddots & \vdots \\ 0 & 0 & 0 & \cdots & \sin^2\phi_2\sin^2\phi_3\cdots\sin^2\phi_{D-2} \end{pmatrix}, \qquad (8.12)$$

giving the basis elements

$$\hat{e}_{\alpha(\alpha)} = \delta_{\alpha(\alpha)}\prod_{\beta=2}^{\alpha-1}\sin\phi_\beta. \qquad (8.13)$$

Raising the α index with the inverse metric $\omega^{\alpha\beta}$ gives,

$$\hat{e}^{\alpha}_{(\alpha)} = \delta^{\alpha}_{(\alpha)}\prod_{\beta=2}^{\alpha-1}\csc\phi_\beta. \qquad (8.14)$$

In the computational domain $\sin\phi_a = 0$, so, due to the presence of these $\csc\phi$ terms, we cannot immediately restrict our discussion to the computational domain, we must first ensure that these terms cancel off.

Using Eq. (8.11) we can construct an expression for $h_{\alpha\beta}$ in terms of the Weyl scalars, by rearranging Eq. (8.10). We remind ourselves at this point that in our $SO(D-3)$ symmetry assumption each component of $\Omega'_{(\alpha)(\beta)}$ is a scalar, that only depends on the 2 angles ϕ_2, ϕ_3, and that there are only 4 non zero components of $\Omega'_{(\alpha)(\beta)}$: $\left(\Omega'_{(2)(2)}, \Omega'_{(2)(3)}, \Omega'_{(3)(3)}, \Omega'_{(w)(w)}\right)$. As $\Omega'_{(\alpha)(\beta)}$ is trace free, in fact only 3 of these are independent components. We multiply both sides of Eq. (8.10) by $\hat{e}^{\gamma}_{(\gamma)}\hat{e}^{\delta}_{(\delta)}\delta_{(\alpha)(\gamma)}\delta_{(\beta)(\delta)}$, to obtain the Bondi news and its first time derivative,

$$
\begin{aligned}
-2r^{D/2-1}\Omega'_{(\alpha)(\beta)}\hat{e}^\gamma_{(\gamma)}\hat{e}^\delta_{(\delta)}\delta_{(\alpha)(\gamma)}\delta_{(\beta)(\delta)} &= \hat{e}^\gamma_{(\gamma)}\hat{e}^\delta_{(\delta)}\delta_{(\alpha)(\gamma)}\delta_{(\beta)(\delta)}\hat{e}^\alpha_{(\alpha)}\hat{e}^\beta_{(\beta)}\ddot{h}_{\alpha\beta} \\
-2r^{D/2-1}\Omega'_{(\alpha)(\beta)}\hat{e}^\gamma_{(\alpha)}\hat{e}^\delta_{(\beta)} &= \omega^{\alpha\gamma}\omega^{\beta\delta}\ddot{h}_{\alpha\beta} \\
-2r^{D/2-1}\Omega'_{(\alpha)(\beta)}\hat{e}^\gamma_{(\alpha)}\hat{e}^\delta_{(\beta)} &= \ddot{h}^{\gamma\beta} \\
\int_{-\infty}^{u} -2r^{D/2-1}\Omega'_{(\alpha)(\beta)}\hat{e}^\gamma_{(\alpha)}\hat{e}^\delta_{(\beta)}d\tilde{u} &= \dot{h}^{\gamma\beta} \\
\int_{-\infty}^{u}\int_{-\infty}^{\hat{u}} -2r^{D/2-1}\Omega'_{(\alpha)(\beta)}\hat{e}^\gamma_{(\alpha)}\hat{e}^\delta_{(\beta)}d\tilde{u}d\hat{u} &= h^{\gamma\beta}.
\end{aligned}
\tag{8.15}
$$

Lowering the indices we find

$$
h_{\alpha\beta} = \int_{-\infty}^{u}\int_{-\infty}^{\hat{u}} -2r^{D/2-1}\Omega'_{(\alpha)(\beta)}\hat{e}_{\alpha(\alpha)}\hat{e}_{\beta(\beta)}d\tilde{u}d\hat{u}.
\tag{8.16}
$$

8.3.3 Covariant derivatives on S^{D-2}

When evaluating the covariant derivatives of the Bondi news, we will need to calculate terms involving the Christoffel symbols, and partial derivatives of the Bondi news. We first note that the Christoffel symbols given by the metric $\omega_{\alpha\beta}$ are

$$
\Gamma^\beta_{\beta\alpha} = \begin{cases} \cot\phi_\alpha & \text{if } \beta > \alpha, \\ 0 & \text{if } \beta \le \alpha, \end{cases}
\tag{8.17}
$$

$$
\Gamma^\alpha_{\beta\beta} = \begin{cases} -\cos\phi_\alpha\sin\phi_\alpha\sin^2\phi_{\alpha+1}\sin^2\phi_{\alpha+2}\cdots\sin^2\phi_{\beta-1} & \text{if } \beta > \alpha, \\ 0 & \text{if } \beta \le \alpha. \end{cases}
\tag{8.18}
$$

Let us now consider the partial derivatives of the Bondi news. When we take the partial angular derivative $\partial/\partial\phi^\alpha$ of the Bondi news as given in Eq. (8.16) we only act on the term $\Omega'_{(\beta)(\gamma)}\hat{e}_{\beta(\beta)}\hat{e}_{\gamma(\gamma)}$, so we will at this point ignore the integrals over $\tilde{u}$ and $\hat{u}$ and the factor of r. Taking the partial derivative of the remaining term, we obtain

$$
\partial_\alpha\left(\Omega'_{(\beta)(\gamma)}\hat{e}_{\beta(\beta)}\hat{e}_{\gamma(\gamma)}\right) = \partial_\alpha(\hat{e}_{\beta(\beta)})\hat{e}_{\gamma(\gamma)}\Omega'_{(\beta)(\gamma)} + \hat{e}_{\beta(\beta)}\partial_\alpha(\hat{e}_{\gamma(\gamma)})\Omega'_{(\beta)(\gamma)} + \hat{e}_{\beta(\beta)}\hat{e}_{\gamma(\gamma)}\partial_\alpha\Omega'_{(\beta)(\gamma)}.
\tag{8.19}
$$

As discussed above $\Omega'_{(\beta)(\gamma)}$ is a scalar on the computational domain, only depending on ϕ_2, ϕ_3, so the final term on the right hand side of Eq. (8.19) will be found by

differentiating the data we calculate for $\Omega'_{(\beta)(\gamma)}$, using finite difference methods on a $2D$ spherical grid. To calculate the first two terms, we must consider the derivative of the basis vector,

$$
\begin{aligned}
\partial_\alpha \hat{e}_{\beta(\beta)} &= \partial_\alpha \delta_{\beta(\beta)} \prod_{\gamma=2}^{\beta-1} \sin \phi_\gamma, \\
&= \begin{cases} \delta_{\beta(\beta)} \cos \phi_\alpha \prod_{\gamma=2, \gamma \neq \alpha}^{\beta-1} \sin \phi_\gamma & \text{if } \alpha \leq \beta - 1, \\ 0 & \text{o/w.} \end{cases}
\end{aligned} \tag{8.20}
$$

8.3.4 Evaluating the angular momentum

We now have all the information required to calculate the angular momentum. Since the Killing vector lies in the computational domain we can set the indices that are contracted with the Killing vector (i.e. α) to be indices that lie in the computational domain. We calculate the three terms inside the integral on the right hand side of Eq. (8.1) in Appendix C.2, and confirm our calculation using the DIFFGEO package in MATHEMATICA. For the sake of brevity we do not reproduce the lengthy expression here, but it can be found in Eq. (C.34) in Appendix C.2.

8.4 Conclusions

In this chapter we have obtained an expression for calculating the angular momentum radiated in gravitational waves, based on the work of [314]. In the form that we have calculated, we can now take the data that we have calculated for wave extraction in Chapter 4, namely the Weyl scalars $\left(\Omega'_{(2)(2)}, \Omega'_{(2)(3)}, \Omega'_{(3)(3)}, \Omega'_{(w)(w)} \right)$, and their angular derivatives, computed using finite differencing methods, and calculate the flux in angular momentum. Combined with the spin measurement of the apparent horizon introduced in Chapter 7, and the ADM integral for angular momentum on the spatial slice in Chapter 6, we can now independently account for the individual contributions to the angular momentum content of a black hole spacetime.

Chapter 9

Conclusions and Outlook

9.1 Conclusions

In this thesis we have attempted to extend the reach of numerical relativity in higher dimensions by developing new diagnostic tools and initial data for studying black hole mergers in higher dimensions. Firstly we have demonstrated the application of the modified Cartoon formalism of dimensional reduction to the BSSN equations, and used this to simulate the merger of black holes in over 6 dimensions for the first time. This formalism has allowed us to perform simulations in higher dimensions efficiently, by exploiting the symmetry of the spacetimes we consider, without falling victim to the curse of dimensionality. In addition, this method has shown numerical stability in higher dimensions than the previously employed method of dimensional reduction by isometry. By following analytic work on the peeling of the Weyl tensor in higher dimensions, we have developed a new method for performing wave extraction in higher dimensional numerical relativity. This is analogous to the Newman-Penrose Ψ_4 wave extraction formalism in $4D$, and can be used as a complementary tool to the already implemented Kodama-Ishibashi wave extraction, with which our Weyl scalar formalism gives good agreement. Using the Weyl scalar method we obtain all of the radiated energy in gravitational waves at once, avoiding the truncation error introduced in the Kodama-Ishibashi method, which requires summing a finite number of l modes. The disadvantage of this method however is the lack of a mode decomposition, making the Weyl scalar method less suitable for the analysis of, for example, quasinormal modes. The Weyl scalar method and the Kodama-Ishibashi method should therefore act as complementary diagnostic tools in the analysis of gravitational waves.

Using the Weyl scalar method, we have investigated the gravitational waves emitted when black holes merge, head-on, from rest, in up to 10 spacetime dimensions, and investigated the dependence of the radiated energy and momentum on the number of dimensions and the mass ratio. We have found for the equal mass case that the dependence of radiated energy on D closely resembles that of the surface area of the sphere in its qualitative form, but clearly differs in the values of the parameters in the fit. When considering the unequal mass case, we learned that the dependence of radiated energy on mass ratio is strongly dimension dependent, which allows us to make contact with results calculated in the point particle limit, which were seemingly in tension with the numerical results found for the equal mass case. By analysing the quasinormal modes of the final black holes, found using the Kodama-Ishibashi wave extraction method, we have matched our numerical data to results from higher dimensional black hole perturbation theory, and results calculated in the large D limit. We find that in the unequal mass case "non-decoupling" modes are the dominant modes excited, as opposed to the equal mass case in which both non-decoupling and decoupling modes were found. By investigating the emission of linear momentum in these collisions, we have also obtained a fitting formula for the velocity of the post-merger black hole.

Taking the Bowen-York procedure for calculating extrinsic curvature for an initial timeslice containing boosted or spinning black holes, we have implemented such initial data in the modified Cartoon method and evolved higher dimensional black hole inspirals. By developing an apparent horizon finder for use in higher dimensions we have have been able to analyse these inspirals to find the spin and mass of the final black hole, allowing us to, for the first time, analyse a dynamically formed Myers-Perry black hole. We have also introduced ADM integrals for mass and momentum in higher dimensions, and an integral for the angular momentum of a spatial slice. Finally, we have recast a formula for calculating the angular momentum radiated in gravitational waves in a form compatible with the modified Cartoon implementation of our numerical code. With these diagnostics in place, we have constructed a toolbox that should allow us to analyse the behaviour of many more types of black hole-black hole interactions in higher dimensional general relativity.

9.2   Outlook

There is much work still to be done in the numerical study of higher dimensional black hole spacetimes, and we hope that the tools constructed in this thesis will provide

a valuable starting point to investigate outstanding problems. For the first time we have presented the inspiral of black holes in higher dimensions using Bowen-York like data, inspirals which, as in the $4D$ case, will emit angular momentum through gravitational waves during the inspiral and merger. Now, with the ability to extract angular momentum from gravitational waves we can fully analyse this. It would be interesting to see how the value of the parameter D affects the radiated angular momentum for higher dimensional mergers, especially given that the end product of the inspiral, the Myers-Perry black hole, does not have an upper limit on its spin in greater than 5 dimensions. This could lead to qualitatively different behaviour in 6 dimensions and greater, when compared to known results in $4D$. Our early results presented in Chapter 7 suggest that the spins produced in inspirals are low, but a full investigation of grazing collisions will be required to fully explore both this issue and the potential existence of zoom-whirl orbits in $D > 4$. One phenomenon in $4D$ that can now be tested in higher dimensions is the hang-up effect [304], where the alignment of black hole spins with the orbital plane can cause longer or shorter black hole orbits, as the individual angular momenta of the black holes interact with the orbital angular momentum. This can be interpreted as an attempt by the black holes to shed their angular momentum before merger to prevent the formation of a super-extremal Kerr black hole, so the generalisation of this process to higher dimensions where there is no upper limit on spin, is not obvious. Beyond this, other spin effects such as black hole superkicks [305–308], where particular spin configurations cause large emissions of linear momentum in gravitational waves at the point of merger, can now be investigated in higher dimensions. In [112] evidence was found for a violation of the weak cosmic censorship conjecture in black hole inspirals in higher dimensions, with a point identified outside of any black hole horizon which had super-Planckian curvature. Our code now has the capability of investigating these results and their extension to $D > 5$.

In the analysis of non-head on collisions, it will be useful to have the ability to decompose wave signals into their fundamental modes. Currently we are unaware of a method for projecting the higher dimensional Weyl scalars onto a higher dimensional family of spin weighted spherical harmonics as can be done in $4D$ for Ψ_4, and, at present, the Kodama-Ishibashi formalism has only been implemented for scalar perturbations. Either constructing the appropriate basis functions for higher dimensional spin weighted quantities, or implementing the vector and tensor sectors of the Kodama-Ishibashi wave extraction would allow us to fully investigate the nature of the quasinormal modes of the final merged black holes after a boosted grazing collision, inspiral, or collision of spinning

black holes. We note the existence of some work in this direction generalising the spin weighted spherical harmonics to spheroidal harmonics and generalising spherical harmonics to higher dimensions in [315].

In order to fully mirror the collisions at the Large Hadron Collider that might, in TeV gravity scenarios, lead to black hole production, we must investigate the behaviour of highly boosted black hole collisions. The Bowen-York data presented in this thesis should give a valuable tool to calculate initial data for such simulations, to investigate such questions as the maximum energy that can be radiated in black hole collisions, the scattering cross section of black hole collisions, and whether universality behaviour seen in $4D$ generalises to higher dimensions. We will also have the opportunity to compare numerical data to fitting formulae found in [37, 40], generalised from the $4D$ work of D'Eath and Payne, [95–98], for the energy radiated when Aichelberg-Sexl shockwaves collide. Such simulations would also allow us to address the question posed in Chapter 5, as to whether universality from high boosts, or structure that becomes apparent in the large D limit, dominates for highly boosted collisions at higher values of D.

In Chapter 7 we have presented a horizon finder that utilises a straightforward minimisation algorithm to minimise Eq. (7.10). A commonly used apparent horizon finder provided as part of the CACTUS computational toolkit, AHFINDERDIRECT [316], uses more efficient spectral methods to find the horizon. For more extreme black hole mergers, such as those with large boosts, it may become necessary to implement a more efficient horizon finder, with an adaptation of AHFINDERDIRECT to higher dimensions being a natural candidate for this problem. Recent papers have also studied the use of algebraic conditions on spacetimes as a means of locating BH horizons [317–321]. These methods can be applied in $4D$ and higher dimensions, and, as they require the calculation of fewer derivatives than apparent horizon finding methods, it has been suggested that they could be more efficient within numerical codes. Investigating the relative merits of these methods could prove a valuable insight into how horizon finding should be performed in numerical relativity.

References

[1] Albert Einstein. The Field Equations of Gravitation. *Sitzungsber. Preuss. Akad. Wiss. Berlin (Math. Phys.)*, 1915:844–847, 1915.

[2] Albert Einstein. The Foundation of the General Theory of Relativity. *Annalen Phys.*, 49(7):769–822, 1916. [,65(1916)].

[3] A. Einstein. Approximative Integration of the Field Equations of Gravitation. *Sitzungsber.Preuss.Akad.Wiss.Berlin (Math.Phys.)*, 1916:688–696, 1916.

[4] C. M. Will. The Confrontation between General Relativity and Experiment. *Living Reviews in Relativity*, 17(1):4, Jun 2014.

[5] B. P Abbott et al. Observation of Gravitational Waves from a Binary Black Hole Merger. *Phys. Rev. Lett.*, 116(6):061102, 2016. arXiv:1602.03837 [gr-qc].

[6] B. P. Abbott et al. Astrophysical Implications of the Binary Black-Hole Merger GW150914. *Astrophys. J.*, 818(2):L22, 2016. arXiv:1602.03846 [astro-ph].

[7] B. P. Abbott et al. Tests of general relativity with GW150914. *Phys. Rev. Lett.*, 116(22):221101, 2016. arXiv:1602.03841 [gr-qc].

[8] Emanuele Berti et al. Testing General Relativity with Present and Future Astrophysical Observations. *Class. Quant. Grav.*, 32:243001, 2015. arXiv:1501.07274 [gr-qc].

[9] Theodor Kaluza. Zum Unitätsproblem der Physik. *Sitzungsber. Preuss. Akad. Wiss. Berlin (Math. Phys.)*, 1921:966–972, 1921.

[10] Oskar Klein. Quantum Theory and Five-Dimensional Theory of Relativity. (In German and English). *Z. Phys.*, 37:895–906, 1926. [,76(1926)].

[11] Petr Horava and Edward Witten. Heterotic and type I string dynamics from eleven-dimensions. *Nucl. Phys.*, B460:506–524, 1996. [,397(1995)].

[12] Ming-liang Cai and Gregory J. Galloway. On the Topology and area of higher dimensional black holes. *Class. Quant. Grav.*, 18:2707–2718, 2001.

[13] R. Emparan and H. S. Reall. A Rotating black ring solution in five-dimensions. *Phys. Rev. Lett.*, 88:101101, 2002. hep-th/0110260.

[14] H. Elvang and P. Figueras. Black Saturn. *JHEP*, 0705:050, 2007. hep-th/0701035.

[15] R. C. Myers and M. J. Perry. Black Holes in Higher Dimensional Space-Times. *Annals Phys.*, 172:304, 1986.

[16] R. Emparan, R. Suzuki, and K. Tanabe. The large D limit of General Relativity. *JHEP*, 06:009, 2013. arXiv:1302.6382 [hep-th].

[17] R. Emparan, T. Shiromizu, R. Suzuki, K. Tanabe, and T. Tanaka. Effective theory of Black Holes in the 1/D expansion. *JHEP*, 06:159, 2015. arXiv:1504.06489 [hep-th].

[18] Roberto Emparan, Ryotaku Suzuki, and Kentaro Tanabe. Evolution and End Point of the Black String Instability: Large D Solution. *Phys. Rev. Lett.*, 115(9):091102, 2015.

[19] Roberto Emparan and Kentaro Tanabe. Universal quasinormal modes of large D black holes. *Phys. Rev.*, D89(6):064028, 2014.

[20] M. Cavaglià. Black hole and brane production in TeV gravity: A Review. *Int. J. Mod. Phys.*, A18:1843–1882, 2003. hep-ph/0210296.

[21] P. Kanti. Black holes in theories with large extra dimensions: A review. *Int. J. Mod. Phys. A*, 19:4899–4951, 2004. hep-ph/0402168.

[22] V. Cardoso, L. Gualtieri, C. Herdeiro, and U. Sperhake. Exploring New Physics Frontiers Through Numerical Relativity. *Living Rev. Relativity*, 18:1, 2015. arXiv:1409.0014 [gr-qc].

[23] N. Arkani-Hamed, S. Dimopoulos, and G. R. Dvali. The hierarchy problem and new dimensions at a millimeter. *Phys. Lett. B*, 429:263–272, 1998. hep-ph/9803315.

[24] Nima Arkani-Hamed, Savas Dimopoulos, and G. R. Dvali. Phenomenology, astrophysics and cosmology of theories with submillimeter dimensions and TeV scale quantum gravity. *Phys. Rev.*, D59:086004, 1999.

[25] I. Antoniadis, N. Arkani-Hamed, S. Dimopoulos, and G. R. Dvali. New dimensions at a millimeter to a Fermi and superstrings at a TeV. *Phys. Lett. B*, 436:257–263, 1998. hep-ph/9804398.

[26] Ignatios Antoniadis. A Possible new dimension at a few TeV. *Phys. Lett. B*, 246:377–384, 1990.

[27] Gary Shiu and S. H. Henry Tye. TeV scale superstring and extra dimensions. *Phys. Rev.*, D58:106007, 1998.

[28] Karim Benakli and Yaron Oz. Small instantons and weak scale string theory. *Phys. Lett.*, B472:83–88, 2000.

[29] Ignatios Antoniadis, Savas Dimopoulos, and Amit Giveon. Little string theory at a TeV. *JHEP*, 05:055, 2001.

[30] Ignatios Antoniadis and B. Pioline. Large dimensions and string physics at a TeV. In *Beyond the desert: Accelerator, non-accelerator and space approaches into the next millennium. Proceedings, 2nd International Conference on particle physics beyond the standard model, Ringberg Castle, Tegernsee, Germany, June 6-12, 1999*, pages 373–384, 1999. [,373(1999)].

[31] L. Randall and R. Sundrum. A large mass hierarchy from a small extra dimension. *Phys. Rev. Lett.*, 83:3370–3373, 1999. hep-ph/9905221.

[32] L. Randall and R. Sundrum. An alternative to compactification. *Phys. Rev. Lett.*, 83:4690–4693, 1999. hep-th/9906064.

[33] Eugene A. Mirabelli, Maxim Perelstein, and Michael E. Peskin. Collider signatures of new large space dimensions. *Phys. Rev. Lett.*, 82:2236–2239, 1999.

[34] T. Banks and W. Fischler. A Model for High Energy Scattering in Quantum Gravity. 1999. hep-th/9906038.

[35] P. C. Argyres, S. Dimopoulos, and J. March-Russell. Black holes and submillimeter dimensions. *Phys. Lett. B*, 441:96–104, 1998. hep-th/9808138.

[36] P. C. Aichelburg and R. U. Sexl. On the Gravitational field of a massless particle. *Gen. Rel. Grav.*, 2:303–312, 1971.

[37] C. Herdeiro, M. O. P. Sampaio, and C. Rebelo. Radiation from a D-dimensional collision of shock waves: First order perturbation theory. *JHEP*, 1107:121, 2011. arXiv:1105.2298 [hep-th].

[38] Flavio S. Coelho, Carlos Herdeiro, Carmen Rebelo, and Marco Sampaio. Radiation from a D-dimensional collision of shock waves: Higher-order setup and perturbation theory validity. *Phys. Rev.*, D87:084034, 2013.

[39] Flávio S. Coelho, Carlos Herdeiro, Carmen Rebelo, and Marco O. P. Sampaio. Radiation from a D-Dimensional Collision of Shock Waves: Numerics and a Charged Case. *Springer Proc. Math. Stat.*, 60:193–197, 2014.

[40] Flavio S. Coelho, Carlos Herdeiro, and Marco O. P. Sampaio. Radiation from a D-dimensional collision of shock waves: a remarkably simple fit formula. *Phys. Rev. Lett.*, 108:181102, 2012.

[41] S. B. Giddings and S. Thomas. High energy colliders as black hole factories: The end of short distance physics. *Phys. Rev. D*, 65:056010, 2002. hep-ph/0106219.

[42] S. Dimopoulos and G. Landsberg. Black Holes at the LHC. *Phys. Rev. Lett.*, 87:161602, 2001. hep-th/0106295.

[43] King-man Cheung. Black hole production and large extra dimensions. *Phys. Rev. Lett.*, 88:221602, 2002.

[44] Yosuke Uehara. New potential of black holes: Quest for TeV scale physics by measuring top quark sector using black holes hep-ph/0205199. 2002.

[45] Luis Anchordoqui and Haim Goldberg. Black hole chromosphere at the CERN LHC. *Phys. Rev.*, D67:064010, 2003.

[46] U. Sperhake, V. Cardoso, F. Pretorius, E. Berti, and J. A. González. The high-energy collision of two black holes. *Phys. Rev. Lett.*, 101:161101, 2008. arXiv:0806.1738 [gr-qc].

[47] M. Shibata, H. Okawa, and T. Yamamoto. High-velocity collisions of two black holes. *Phys. Rev. D*, 78:101501(R), 2008. arXiv:0810.4735 [gr-qc].

[48] U. Sperhake, V. Cardoso, F. Pretorius, E. Berti, T. Hinderer, and N. Yunes. Cross section, final spin and zoom-whirl behavior in high-energy black hole collisions. *Phys. Rev. Lett.*, 103:131102, 2009. arXiv:0907.1252 [gr-qc].

[49] U. Sperhake, E. Berti, V. Cardoso, and F. Pretorius. Universality, maximum radiation and absorption in high-energy collisions of black holes with spin. *Phys. Rev. Lett.*, 111:041101, 2013. arXiv:1211.6114 [gr-qc].

[50] Matthew W. Choptuik and Frans Pretorius. Ultra Relativistic Particle Collisions. *Phys. Rev. Lett.*, 104:111101, 2010. arXiv:0908.1780 [gr-qc].

[51] W. E. East and F. Pretorius. Ultrarelativistic black hole formation. *Phys. Rev. Lett.*, 110:101101, 2013. arXiv:1210.0443 [gr-qc].

[52] L. Rezzolla and K. Takami. Black-hole production from ultrarelativistic collisions. *Class. Quant. Grav.*, 30:012001, 2013. arXiv:1209.6138 [gr-qc].

[53] James Healy, Ian Ruchlin, Carlos O. Lousto, and Yosef Zlochower. High Energy Collisions of Black Holes Numerically Revisited. *Phys. Rev.*, D94(10):104020, 2016.

[54] U. Sperhake, E. Berti, V. Cardoso, and F. Pretorius. Gravity-dominated unequal-mass black hole collisions. *Phys. Rev. D*, 93:044012, 2016. arXiv:1511.08209 [gr-qc].

[55] D. J. Kapner, T. S. Cook, E. G. Adelberger, J. H. Gundlach, Blayne R. Heckel, C. D. Hoyle, and H. E. Swanson. Tests of the gravitational inverse-square law below the dark-energy length scale. *Phys. Rev. Lett.*, 98:021101, 2007.

[56] S. J. Smullin, A. A. Geraci, D. M. Weld, J. Chiaverini, Susan P. Holmes, and A. Kapitulnik. New constraints on Yukawa-type deviations from Newtonian gravity at 20 microns. *Phys. Rev.*, D72:122001, 2005. [Erratum: Phys. Rev.D72,129901(2005)].

[57] Oleg Y. Gnedin, Thomas J. Maccarone, Dimitrios Psaltis, and Stephen E. Zepf. Shrinking the Braneworld: Black Hole in a Globular Cluster. *Astrophys. J.*, 705:L168–L171, 2009.

[58] Dimitrios Psaltis. Constraints on Braneworld Gravity Models from a Kinematic Limit on the Age of the Black Hole XTE J1118+480. *Phys. Rev. Lett.*, 98:181101, 2007.

[59] Tim Johannsen. Constraints on the Size of Extra Dimensions from the Orbital Evolution of the Black-Hole X-Ray Binary XTE J1118+480. *Astron. Astrophys.*, 507:617, 2009.

[60] Tim Johannsen, Dimitrios Psaltis, and Jeffrey E. McClintock. Constraints on the Size of Extra Dimensions from the Orbital Evolution of Black-Hole X-Ray Binaries. *Astrophys. J.*, 691:997–1004, 2009.

[61] F. Dahia and A. S. Lemos. Constraints on extra dimensions from atomic spectroscopy. *Phys. Rev.*, D94(8):084033, 2016.

[62] Morad Aaboud et al. Search for new phenomena in dijet events using 37 fb^{-1} of pp collision data collected at $\sqrt{s} =$13 TeV with the ATLAS detector. 2017. arXiv:1703.09127 [hep-ex].

[63] Albert M Sirunyan et al. Search for black holes in high-multiplicity final states in proton-proton collisions at sqrt(s) = 13 TeV. 2017. arXiv:1705.01403 [hep-ex].

[64] J. M. Maldacena. The large N limit of superconformal field theories and supergravity. *Adv. Theor. Math. Phys.*, 2:231, 1997. hep-th/9711200.

[65] S. S. Gubser, Igor R. Klebanov, and Alexander M. Polyakov. Gauge theory correlators from non-critical string theory. *Phys. Lett. B*, 428:105–114, 1998. hep-th/9802109.

[66] E. Witten. Anti-de Sitter space and holography. *Adv. Theor. Math. Phys.*, 2:253–291, 1998. hep-th/9802150.

[67] P. M. Chesler and L. G. Yaffe. Horizon formation and far-from-equilibrium isotropization in supersymmetric Yang-Mills plasma. *Phys. Rev. Lett.*, 102:211601, 2009. arXiv:0812.2053 [hep-th].

[68] H. Bantilan, F. Pretorius, and S. S. Gubser. Simulation of Asymptotically AdS5 Spacetimes with a Generalized Harmonic Evolution Scheme. *Phys. Rev. D*, 85:084038, 2012. arXiv:1201.2132 [hep-th].

[69] P. M. Chesler and L. G. Yaffe. Numerical solution of gravitational dynamics in asymptotically anti-de Sitter spacetimes. *JHEP*, 1407:086, 2014. arXiv:1309.1439 [hep-th].

[70] S. S. Gubser and W. van der Schee. Complexified boost invariance and holographic heavy ion collisions. *JHEP*, 01:028, 2015. arXiv:1410.7408 [hep-th].

[71] A. Buchel, M. P. Heller, and R. C. Myers. Equilibration rates in a strongly coupled nonconformal quark-gluon plasma. *Phys. Rev. Lett.*, 114(25):251601, 2015. arXiv:1503.07114 [hep-th].

[72] Maximilian Attems, Jorge Casalderrey-Solana, David Mateos, Daniel Santos-Oliván, Carlos F. Sopuerta, Miquel Triana, and Miguel Zilhão. Holographic Collisions in Non-conformal Theories. *JHEP*, 01:026, 2017.

[73] Hans Bantilan, Pau Figueras, Markus Kunesch, and Paul Romatschke. Non-spherically Symmetric Collapse in Asymptotically AdS Spacetimes. *Phys. Rev. Lett.*, 119(19):191103, 2017.

[74] LIGO website: http://www.ligo.org.

[75] B. P. Abbott et al. LIGO: The Laser interferometer gravitational-wave observatory. *Rept. Prog. Phys.*, 72:076901, 2009. arXiv:0711.3041 [gr-qc].

[76] Gregory M. Harry. Advanced LIGO: The next generation of gravitational wave detectors. *Class. Quant. Grav.*, 27:084006, 2010.

[77] Advanced VIRGO website: http://wwwcascina.virgo.infn.it/advirgo/.

[78] T. Accadia et al. Virgo: a laser interferometer to detect gravitational waves. *JINST*, 7:P03012, 2012.

[79] F. Acernese et al. Advanced Virgo: a second-generation interferometric gravitational wave detector. *Class. Quant. Grav.*, 32(2):024001, 2015.

[80] B. P. Abbott et al. GW170814: A Three-Detector Observation of Gravitational Waves from a Binary Black Hole Coalescence. *Phys. Rev. Lett.*, 119(14):141101, 2017.

[81] B. P. Abbott et al. GW151226: Observation of Gravitational Waves from a 22-Solar-Mass Binary Black Hole Coalescence. *Phys. Rev. Lett.*, 116(24):241103, 2016. arXiv:1606.04855 [gr-qc].

[82] Benjamin P. Abbott et al. GW170104: Observation of a 50-Solar-Mass Binary Black Hole Coalescence at Redshift 0.2. *Phys. Rev. Lett.*, 118(22):221101, 2017.

[83] B.. P.. Abbott et al. GW170608: Observation of a 19-solar-mass Binary Black Hole Coalescence. *Astrophys. J.*, 851(2):L35, 2017.

[84] B. P. Abbott et al. GW170817: Observation of Gravitational Waves from a Binary Neutron Star Inspiral. *Phys. Rev. Lett.*, 119(16):161101, 2017.

[85] A. Buonanno and T. Damour. Effective one-body aproach to general relativistic two-body dynamics. *Phys. Rev. D*, 59:084006, 1999. gr-qc/9811091.

[86] L. Blanchet. Gravitational Radiation from Post-Newtonian Sources and Inspiralling Compact Binaries. *Living Reviews in Relativity*, 9(4), 2006. http://www.livingreviews.org/lrr-2006-4.

[87] K. Kokkotas and B. G. Schmidt. Quasi-Normal Modes of Stars and Black Holes. *Living Reviews in Relativity*, 2(2), 1999. http://www.livingreviews.org/lrr-1999-2.

[88] E. Berti, V. Cardoso, and A. O. Starinets. Quasinormal modes of black holes and black branes. *Class. Quantum Grav.*, 26:163001, 2009. arXiv:0905.2975 [gr-qc].

[89] F. Pretorius. Evolution of Binary Black-Hole Spacetimes. *Phys. Rev. Lett.*, 95:121101, 2005. gr-qc/0507014.

[90] P. Anninos, D. Hobill, E. Seidel, L. Smarr, and W.-M. Suen. Collision of Two Black Holes. *Phys. Rev. Lett.*, 71:2851–2854, 1993. gr-qc/9309016.

[91] P. Anninos, D. Hobill, E. Seidel, L. Smarr, and W.-M. Suen. Head-on collision of two equal mass black holes. *Phys. Rev. D*, 52:2044–2058, 1995.

[92] S. W. Hawking. Gravitational radiation from colliding black holes. *Phys. Rev. Lett.*, 26:1344–1346, 1971.

[93] R. Penrose, 1974. presented at the Cambridge University Seminar, Cambridge, England (unpublished).

[94] D. M. Eardley and S. B. Giddings. Classical black hole production in high-energy collisions. *Phys. Rev. D*, 66:044011, 2002. gr-qc/0201034.

[95] P. D. D'Eath. High Speed Black Hole Encounters And Gravitational Radiation. *Phys. Rev. D*, 18:990, 1978.

[96] P. D. D'Eath and P. N. Payne. Gravitational radiation in black-hole collisions at the speed of light. 1. Perturbation treatment of the axisymmetric collision. *Phys. Rev. D*, 46:658–674, 1992.

[97] P. D. D'Eath and P. N. Payne. Gravitational radiation in black-hole collisions at the speed of light. 2. Reduction to two independent variables and calculation of the second-order news function. *Phys. Rev. D*, 46:675–693, 1992.

[98] P. D. D'Eath and P. N. Payne. Gravitational radiation in black-hole collisions at the speed of light/ 3. Results and conclusions. *Phys. Rev. D*, 46:694–701, 1992.

[99] K.S. Thorne. Nonspherical gravitational collapse: A short review. In J. Klauder, editor, *Magic Without Magic*, page 231. Freeman, San Francisco, 1972.

[100] M. Shibata and H. Yoshino. Bar-mode instability of rapidly spinning black hole in higher dimensions: Numerical simulation in general relativity. *Phys. Rev. D*, 81:104035, 2010. arXiv:1004.4970 [gr-qc].

[101] M. Shibata and H. Yoshino. Nonaxisymmetric instability of rapidly rotating black hole in five dimensions. *Phys. Rev. D*, 81:021501, 2010. arXiv:0912.3606 [gr-qc].

[102] O. J. C. Dias, G. S. Hartnett, and J. E. Santos. Quasinormal modes of asymptotically flat rotating black holes. *Class. Quant. Grav.*, 31(24):245011, 2014. arXiv:1402.7047 [hep-th].

[103] M. Shibata and H. Yoshino. Revisiting stabilities of 5D Myers-Perry black holes in numerical relativity, 2014. Presented at conference *New frontiers in dynamical gravity*, Cambridge, UK.

[104] R. Gregory and R. Laflamme. Black strings and p-branes are unstable. *Phys. Rev. Lett.*, 70:2837–2840, 1993. hep-th/9301052.

[105] L. Lehner and F. Pretorius. Black Strings, Low Viscosity Fluids, and Violation of Cosmic Censorship. *Phys. Rev. Lett.*, 105:101102, 2010. arXiv:1006.5960 [hep-th].

[106] L. Lehner and F. Pretorius. Final State of Gregory-Laflamme Instability. In G. Horowitz, editor, *Black Holes in Higher Dimensions*. Cambridge University Press, Cambridge, 2012. arXiv:1106.5184 [gr-qc].

[107] P. Figueras, M. Kunesch, and S. Tunyasuvunakool. End Point of Black Ring Instabilities and the Weak Cosmic Censorship Conjecture. *Phys. Rev. Lett.*, 116(7):071102, 2016. arXiv:1512.04532 [hep-th].

[108] Jorge E. Santos and Benson Way. Neutral Black Rings in Five Dimensions are Unstable. *Phys. Rev. Lett.*, 114:221101, 2015. arXiv:1503.00721 [hep-th].

[109] Pau Figueras, Markus Kunesch, Luis Lehner, and Saran Tunyasuvunakool. End Point of the Ultraspinning Instability and Violation of Cosmic Censorship. *Phys. Rev. Lett.*, 118(15):151103, 2017.

[110] H. Witek, M. Zilhão, L. Gualtieri, V. Cardoso, C. Herdeiro, A. Nerozzi, and U. Sperhake. Numerical relativity for D dimensional space-times: head-on collisions of black holes and gravitational wave extraction. *Phys. Rev. D*, 82:104014, 2010. arXiv:1006.3081 [gr-qc].

[111] H. Witek, V. Cardoso, L. Gualtieri, C. Herdeiro, U. Sperhake, and M. Zilhão. Head-on collisions of unequal mass black holes in $D = 5$ dimensions. *Phys. Rev. D*, 83:044017, 2011. arXiv:1011.0742 [gr-qc].

[112] H. Okawa, K.-i. Nakao, and M. Shibata. Is super-Planckian physics visible? Scattering of black holes in 5 dimensions. *Phys. Rev. D*, 83:121501, 2011. arXiv:1105.3331 [gr-qc].

[113] H. Witek, H. Okawa, V. Cardoso, L. Gualtieri, C. Herdeiro, M. Shibata, U. Sperhake, and M. Zilhão. Higher dimensional Numerical Relativity: code comparison. *Phys. Rev. D*, 90(8):084014, 2014. arXiv:1406.2703 [gr-qc].

[114] William G. Cook, Pau Figueras, Markus Kunesch, Ulrich Sperhake, and Saran Tunyasuvunakool. Dimensional reduction in numerical relativity: Modified cartoon formalism and regularization. In *3rd Amazonian Symposium on Physics and 5th NRHEP Network Meeting: Celebrating 100 Years of General Relativity Belem, Brazil, September 28-October 2, 2015*, volume 25, page 1641013, 2016. arXiv:1603.00362 [gr-qc].

[115] William G. Cook and Ulrich Sperhake. Extraction of gravitational-wave energy in higher dimensional numerical relativity using the Weyl tensor. *Class. Quant. Grav.*, 34(3):035010, 2017. arXiv:1609.01292 [gr-qc].

[116] William G. Cook, Ulrich Sperhake, Emanuele Berti, and Vitor Cardoso. Black-hole head-on collisions in higher dimensions. *Phys. Rev.*, D96(12):124006, 2017.

[117] C. W. Misner, K. S. Thorne, and J. A. Wheeler. *Gravitation*. W. H. Freeman, New York, 1973.

[118] R. Arnowitt, S. Deser, and C. W. Misner. The dynamics of general relativity. In L. Witten, editor, *Gravitation an introduction to current research*, pages 227–265. John Wiley, New York, 1962. gr-qc/0405109.

[119] Jr. J. W. York. Kinematics and dynamics of general relativity. In L. Smarr, editor, *Sources of Gravitational Radiation*, pages 83–126. Cambridge University Press, Cambridge, 1979.

[120] Jr. J. W. York. The initial value problem and dynamics. In N. & Piran T. Deruelle, editor, *Gravitational radiation*, pages 175–201. North-Holland Publishing Company, 1983.

[121] M. Alcubierre. *Introduction to 3+1 Numerical Relativity*. Oxford University Press, Oxford, 2008.

[122] E. Gourgoulhon. 3+1 Formalism and Bases of Numerical Relativity. 2007. gr-qc/0703035.

[123] C. Gundlach, G. Calabrese, I. Hinder, and J. M. Martín-García. Constraint damping in the Z4 formulation and harmonic gauge. *Class. Quantum Grav.*, 22:3767–3773, 2005.

[124] H.-J. Yo, T. W. Baumgarte, and S. L. Shapiro. Improved numerical stability of stationary black hole evolution calculations. *Phys. Rev. D*, 66:084026, 2002. gr-qc/0209066.

[125] O. Sarbach and M. Tiglio. Continuum and Discrete Initial-Boundary-Value Problems and Einstein's Field Equations. *Living Reviews in Relativity*, 15:9, 2012. arXiv:1203.6443 [gr-qc].

[126] M. E. Taylor. *Pseudodifferential operators*. Princetone University Press, Princeton, 1981.

[127] M. E. Taylor. *Pseudodifferential Operators and Nonlinear PDE (Progress in Mathematics 100)*. Birkhäuser, boston-Basel-Berlin, 1991.

[128] David Hilditch. An Introduction to Well-posedness and Free-evolution. *Int. J. Mod. Phys. A*, 28:1340015, 2013. arXiv:1309.2012 [gr-qc].

[129] G. Nagy, O. E. Ortiz, and O. A. Reula. Strongly hyperbolic second order Einstein's evolution equations. *Phys. Rev. D*, 70:044012, 2004. gr-qc/0402123.

[130] Y. Fourés-Bruhat. Théoreme d'existence pour certains système d'équations aux dérivées partielles non linéaires. *Acta Math.*, 88:141–225, 1952.

[131] D. Garfinkle. Harmonic coordinate method for simulating generic singularities. *Phys. Rev. D*, 65:044029, 2002. gr-qc/0110013.

[132] L. Lindblom, M. A. Scheel, L. E. Kidder, R. Owen, and O. Rinne. A New Generalized Harmonic Evolution System. *Class. Quant. Grav.*, 23:S447–S462, 2006. gr-qc/0512093.

[133] F. Pretorius. Numerical relativity using a generalized harmonic decomposition. *Class. Quantum Grav.*, 22:425–452, 2005. gr-qc/0407110.

[134] H. Friedrich. On the Hyperbolicity of Einstein's and Other Gauge Field Equations. *Comm. Math. Phys.*, 100:525, 1985.

[135] H. Friedrich. Hyperbolic reductions for Einstein's equations. *Class. Quantum Grav.*, 13:1451–1469, 1996.

[136] T. W. Baumgarte and S. L. Shapiro. On the Numerical integration of Einstein's field equations. *Phys. Rev. D*, 59:024007, 1998. gr-qc/9810065.

[137] M. Shibata and T. Nakamura. Evolution of three-dimensional gravitational waves: Harmonic slicing case. *Phys. Rev. D*, 52:5428–5444, 1995.

[138] C. Gundlach and J. M. Martín-García. Well-posedness of formulations of the Einstein equations with dynamical lapse and shift conditions. *Phys. Rev. D*, 74:024016, 2006. gr-qc/0604035.

[139] J. G. Baker, J. Centrella, D.-I. Choi, M. Koppitz, and J. van Meter. Gravitational-Wave Extraction from an inspiraling Configuration of Merging Black Holes. *Phys. Rev. Lett.*, 96:111102, 2006. gr-qc/0511103.

[140] M. Campanelli, C. O. Lousto, P. Marronetti, and Y. Zlochower. Accurate Evolutions of Orbiting Black-Hole Binaries without Excision. *Phys. Rev. Lett.*, 96:111101, 2006. gr-qc/0511048.

[141] C. Bona, T. Ledvinka, C. Palenzuela, and M. Žáček. A symmetry-breaking mechanism for the Z4 general-covariant evolution system. *Phys. Rev. D*, 69:064036, 2003. gr-qc/0307067.

[142] C. Bona, T. Ledvinka, C. Palenzuela, and M. Žáček. General-covariant evolution formalism for numerical relativity. *Phys. Rev. D*, 67:104005, 2003. gr-qc/0302083.

[143] C. Bona, T. Ledvinka, C. Palenzuela-Luque, and M. Žáček. Constraint-preserving boundary conditions in the Z4 numerical relativity formalism. *Class. Quant. Grav.*, 22:2615–2634, 2005. gr-qc/0411110.

[144] D. Alic, C. Bona-Casas, C. Bona, L. Rezzolla, and C. Palenzuela. Conformal and covariant formulation of the Z4 system with constraint-violation damping. *Phys. Rev. D*, 85:064040, 2012. arXiv:1106.2254 [gr-qc].

[145] Z. Cao and D. Hilditch. Numerical stability of the Z4c formulation of general relativity. *Phys. Rev. D*, 85:124032, 2012. arXiv:1111.2177 [gr-qc].

[146] A. Weyhausen, S. Bernuzzi, and D. Hilditch. Constraint damping for the Z4c formulation of general relativity. *Phys. Rev. D*, 85:024038, 2012. arXiv:1107.5539 [gr-qc].

[147] D. Hilditch, S. Bernuzzi, M. Thierfelder, Z. Cao, W. Tichy, and B. Brügmann. Compact binary evolutions with the Z4c formulation. *Phys. Rev. D*, 88:084057, 2013. arXiv:1212.2901 [gr-qc].

[148] G. B. Cook. Initial Data for Numerical Relativity. *Living Reviews in Relativity*, 3(5), 2000. gr-qc/0007085.

[149] A. Lichnerowicz. L'integration des équations de la gravitation relativiste et le problème des *n* corps. *J. Math. Pures et Appl.*, 23:37–63, 1944.

[150] Jr. J. W. York. Gravitational degrees of freedom and the initial-value problem. *Phys. Rev. Lett.*, 26:1656–1658, 1971.

[151] Jr. J. W. York. Role of conformal three-geometry in the dynamics of gravitation. *Phys. Rev. Lett.*, 28:1082–1085, 1972.

[152] Jr. J. W. York. Conformally invariant orthogonal decomposition of symmetric tensors on Riemannian manifolds and the initial-value problem of general relativity. *J. Math. Phys.*, 14:456–464, 1973.

[153] Jr. J. W. York. Covariant decompositions of symmetric tensors in the theory of gravitation. *Ann. Inst. Henri Poincaré A*, 21:319–332, 1974.

[154] D. R. Brill and R. W. Lindquist. Interaction Energy in Geometrostatics. *Phys. Rev.*, 131:471–476, 1963.

[155] J. M. Bowen and Jr. J. W. York. Time-asymmetric initial data for black holes and black-hole collisions. *Phys. Rev. D*, 21:2047–2056, 1980.

[156] M. Ansorg, B. Brügmann, and W. Tichy. A single-domain spectral method for black hole puncture data. *Phys. Rev. D*, 70:064011, 2004. gr-qc/0404056.

[157] Vasileios Paschalidis, Zachariah B. Etienne, Roman Gold, and Stuart L. Shapiro. An efficient spectral interpolation routine for the TwoPunctures code. 2013.

[158] H. Yoshino, T. Shiromizu, and M. Shibata. The close limit analysis for head-on collision of two black holes in higher dimensions: Brill-Lindquist initial data. *Phys. Rev. D*, 72:084020, 2005. gr-qc/0508063.

[159] F.R. Tangherlini. Schwarzschild field in n dimensions and the dimensionality of space problem. *Nuovo Cim.*, 27:636–651, 1963.

[160] K. A. Dennison, J. P. Wendell, T. W. Baumgarte, and J. D. Brown. Trumpet slices of the Schwarzschild-Tangherlini spacetime. *Phys. Rev. D*, 82:124057, 2010. arXiv:1010.5723 [gr-qc].

[161] L. Smarr and Jr. J. W. York. Kinematical conditions in the construction of spacetime. *Phys. Rev. D*, 17:2529–2551, 1978.

[162] F. Estabrook, H. Wahlquist, S. Christensen, B. DeWitt, L. Smarr, et al. Maximally slicing a black hole. *Phys. Rev. D*, 7:2814–2817, 1973.

[163] C. Bona, J. Massó, E. Seidel, and J. Stela. A New Formalism for Numerical Relativity. *Phys. Rev. Lett.*, 75:600–603, 1995. gr-qc/9412071.

[164] M. Alcubierre. Hyperbolic slicings of spacetime: singularity avoidance and gauge shocks. *Class. Quantum Grav.*, 20:607–624, 2003. gr-qc/0210050.

[165] M. Alcubierre, B. Brügmann, P. Diener, M. Koppitz, D. Pollney, E. Seidel, and R. Takahashi. Gauge conditions for long-term numerical black hole evolutions without excision. *Phys. Rev. D*, 67:084023, 2003. gr-qc/0206072.

[166] J. R. van Meter, J. G. Baker, M. Koppitz, and D.-I. Choi. How to move a black hole without excision: gauge conditions for the numerical evolution of a moving puncture. *Phys. Rev. D*, 73:124011, 2006. gr-qc/0605030.

[167] L. D. Landau and E. M. Lifshitz. *The Classical Theory of Fields*, volume 2 of *Course of Theoretical Physics*. Butterworth-Heinemann, Oxford, 4th edition, 1980.

[168] H. Yoshino and M. Shibata. Higher-dimensional numerical relativity: Formulation and code tests. *Phys. Rev. D*, 80:084025, 2009. arXiv:0907.2760 [gr-qc].

[169] C. Reisswig, N. T. Bishop, D. Pollney, and B. Szilagyi. Characteristic extraction in numerical relativity: binary black hole merger waveforms at null infinity. *Class. Quantum Grav.*, 27:075014, 2010. arXiv:0912.1285 [gr-qc].

[170] C. Reisswig, N. T. Bishop, D. Pollney, and B. Szilagyi. Unambiguous determination of gravitational waveforms from binary black hole mergers. *Phys. Rev. Lett.*, 103:221101, 2009. arXiv:0907.2637 [gr-qc].

[171] M.C. Babiuc, B. Szilagyi, J. Winicour, and Y. Zlochower. A Characteristic Extraction Tool for Gravitational Waveforms. *Phys. Rev. D*, 84:044057, 2011. arXiv:1011.4223 [gr-qc].

[172] N. T. Bishop and L. Rezzolla. Extraction of gravitational waves in numerical relativity. *Living Reviews in Relativity*, 20(1):1, 2016. arXiv:1606.02532 [gr-qc].

[173] T. Regge and J. A. Wheeler. Stability of a Schwarzschild Singularity. *Phys. Rev.*, 108:1063–1069, 1957.

[174] F. J. Zerilli. Gravitational field of a particle falling in a schwarzschild geometry analyzed in tensor harmonics. *Phys. Rev. D*, 2:2141–2160, 1970.

[175] V. Moncrief. Gravitational Perturbations of Spherically Symmetric Systems. I. The Exterior Problem. *Ann. Phys.*, 88:323–343, 1974.

[176] E. T. Newman and R. Penrose. An Approach to Gravitational Radiation by a Method of Spin Coefficients. *J. Math. Phys.*, 3:566–578, 1962.

[177] J. N. Goldberg, A. J. MacFarlane, E. T. Newman, F. Rohrlich, and E. C. G. Sudarshan. Spin s spherical harmonics and edth. *J. Math. Phys.*, 8:2155, 1967.

[178] E. T. Newman and R. Penrose. Note on the Bondi-Metzner-Sachs group. *J. Math. Phys.*, 7:863–870, 1966.

[179] C. Reisswig, C. D. Ott, U. Sperhake, and E. Schnetter. Gravitational Wave Extraction in Simulations of Rotating Stellar Core Collapse. *Phys. Rev. D*, 83:064008, 2011. arXiv:1012.0595 [gr-qc].

[180] H. Bondi, M. G. J. van der Burg, and A. W. K. Metzner. Gravitational waves in general relativity VII. Waves from axi-symmetric isolated systems. *Proc. Roy. Soc. A*, 269:21–52, 1962.

[181] R.K. Sachs. Gravitational waves in general relativity. 8. Waves in asymptotically flat space-times. *Proc. Roy. Soc. A*, 270:103–126, 1962.

[182] R. Penrose. Asymptotic properties of fields and spacetimes. *Phys. Rev. Lett.*, 10:66–68, 1963.

[183] R.K. Sachs. Gravitational waves in general relativity. 6. The outgoing radiation condition. *Proc. Roy. Soc. Lond. A*, 264:309–338, 1961.

[184] W. Kinnersley. Type D Vacuum Metrics. *J. Math. Phys.*, 10:1195–1203, 1969.

[185] S. A. Teukolsky. Perturbations of a Rotating Black Hole. I. Fundamental Equations for Gravitational, Electromagnetic, and Neutrino-Field Perturbations. *Astrophys. J.*, 185:635–648, 1973.

[186] L. Lehner and O. M. Moreschi. Dealing with delicate issues in waveform calculations. *Phys. Rev. D*, 76:124040, 2007. arXiv:0706.1319 [gr-qc].

[187] C. Beetle, M. Bruni, L. M. Burko, and A. Nerozzi. Towards a novel wave-extraction method for numerical relativity. I. Foundations and initial-value formulation. *Phys. Rev. D*, 72:024013, 2005. gr-qc/0407012.

[188] A. Nerozzi, C. Beetle, M. Bruni, L. M. Burko, and D. Pollney. Towards wave extraction in numerical relativity: the quasi-Kinnersley frame. *Phys. Rev. D*, 72:024014, 2005. gr-qc/0407013.

[189] A. Nerozzi and O. Elbracht. Using curvature invariants for wave extraction in numerical relativity. 2008. arXiv:0811.1600 [gr-qc].

[190] A. Nerozzi, M. Bruni, V. Re, and L. M. Burko. Towards a wave-extraction method for numerical relativity: IV. Testing the quasi-Kinnersley method in the Bondi-Sachs framework. *Phys. Rev. D*, 73:044020, 2006.

[191] A. Nerozzi. A new approach to the Newman-Penrose formalism. 2011. arXiv:1109.4400 [gr-qc].

[192] U. Sperhake. Binary black-hole evolutions of excision and puncture data. *Phys. Rev. D*, 76:104015, 2007. gr-qc/0606079.

[193] T. W. Baumgarte and S. L. Shapiro. *Numerical Relativity*. Cambridge University Press, 2010.

[194] M. Ruiz, R. Takahashi, M. Alcubierre, and D. Nuñez. Multipole expansions for energy and momenta carried by gravitational waves. *Gen. Rel. Grav.*, 40:1705–1729, 2008. arXiv:0707.4654 [gr-qc].

[195] A. Nagar and L. Rezzolla. Gauge-invariant non-spherical metric perturbations of Schwarzschild black-hole spacetimes. *Class. Quant. Grav.*, 22:R167, 2005. gr-qc/0502064.

[196] U. Sperhake, B. Kelly, P. Laguna, K. L. Smith, and E. Schnetter. Black-hole head-on collisions and gravitational waves with fixed mesh-refinement and dynamic singularity excision. *Phys. Rev. D*, 71:124042, 2005. gr-qc/0503071.

[197] F. J. Zerilli. Effective potential for even-parity Regge-Wheeler gravitational perturbations. *Phys. Rev. Lett.*, 24:737–738, 1970.

[198] H. Kodama and A. Ishibashi. A master equation for gravitational perturbations of maximally symmetric black holes in higher dimensions. *Prog. Theor. Phys.*, 110:701–722, 2003. hep-th/0305147.

[199] Hideo Kodama, Akihiro Ishibashi, and Osamu Seto. Brane world cosmology: Gauge invariant formalism for perturbation. *Phys. Rev.*, D62:064022, 2000.

[200] H. Kodama and A. Ishibashi. Master equations for perturbations of generalized static black holes with charge in higher dimensions. *Prog. Theor. Phys.*, 111:29–73, 2004. hep-th/0308128.

[201] E. Berti, M. Cavaglia, and L. Gualtieri. Gravitational energy loss in high energy particle collisions: ultrarelativistic plunge into a multidimensional black hole. *Phys. Rev. D*, 69:124011, 2004. hep-th/0309203.

[202] Milton Abramowitz and Irene A Stegun. *Handbook of mathematical functions: with formulas, graphs, and mathematical tables*, volume 55. Courier Corporation, 1964.

[203] J. L. Jaramillo and E. Gourgoulhon. Mass and Angular Momentum in General Relativity. *Fundam. Theor. Phys.*, 162:87–124, 2011. [,87(2010)].

[204] Eric Poisson. *A Relativist's Toolkit: The Mathematics of Black-Hole Mechanics*. Cambridge University Press, 2004.

[205] Abhay Ashtekar and Anne Magnon. From i° to the 3+1 description of spatial infinity. *Journal of Mathematical Physics*, 25(9):2682–2690, 1984.

[206] Abhay Ashtekar and R. O. Hansen. A unified treatment of null and spatial infinity in general relativity. I. Universal structure, asymptotic symmetries, and conserved quantities at spatial infinity. *Journal of Mathematical Physics*, 19(7):1542–1566, 1978.

[207] A. Ashtekar. Asymptotic Structure of the Gravitational Field at Spatial Infinity. In A. Held, editor, *General Relativity and Gravitation II*, volume 2, page 37, 1980.

[208] Alexander B. Atanasov and Erik Schnetter. Sparse Grid Discretizations based on a Discontinuous Galerkin Method. *CoRR*, abs/1710.09356, 2017.

[209] R. Geroch. A method for generating solutions of Einstein's equations. *J. Math. Phys.*, 12:918–924, 1970.

[210] Y.M. Cho. Dimensional Reduction by Isometry. *Phys. Lett. B*, 186:38, 1987.

[211] Y.M. Cho and D.S. Kim. Higher Dimensional Unification by Isometry. *J.Math.Phys.*, 30:1570–1578, 1989.

[212] M. Zilhão, H. Witek, U. Sperhake, V. Cardoso, L. Gualtieri, C. Herdeiro, and A. Nerozzi. Numerical relativity for D dimensional axially symmetric space-times: formalism and code tests. *Phys. Rev. D*, 81:084052, 2010. arXiv:1001.2302 [gr-qc].

[213] M. Zilhao, H. Witek, U. Sperhake, V. Cardoso, L. Gualtieri, C. Herdeiro, and A. Nerozzi. Numerical relativity in higher dimensions. *J. Phys. Conf. Ser.*, 229:012074, 2010.

[214] M. Zilhão. *New frontiers in Numerical Relativity*. PhD thesis, University of Porto, 2012. arXiv:1301.1509 [gr-qc].

[215] Helvi Witek. *Black hole dynamics in generic spacetimes*. PhD thesis, IST/CENTRA Lisbon, 2012. arXiv:1307.1145 [gr-qc].

[216] H. Witek. Numerical Relativity in higher dimensional spacetimes. *Int. J. Mod. Phys. A*, 28:1340017, 2013. arXiv:1308.1686 [gr-qc].

[217] M. W. Choptuik. Universality and Scaling in Graviational Collapse of a Massless Scalar Field. *Phys. Rev. Lett.*, 70:9–12, 1993.

[218] E. Schnetter, S. H. Hawley, and I. Hawke. Evolutions in 3-D numerical relativity using fixed mesh refinement. *Class. Quant. Grav.*, 21:1465–1488, 2004. gr-qc/0310042.

[219] Carpet Code homepage: `http://www.carpetcode.org/`.

[220] Cactus Computational Toolkit homepage: `http://www.cactuscode.org/`.

[221] M. J. Berger and J. Oliger. Adaptive Mesh Refinement for Hyperbolic Partial Differential Equations. *J. Comput. Phys.*, 53:484–512, 1984.

[222] O. Rinne, L. Lindblom, and M. A. Scheel. Testing outer boundary treatments for the Einstein equations. *Class. Quant. Grav.*, 24:4053–4078, 2007. arXiv:0704.0782 [gr-qc].

[223] M. Alcubierre, S. Brandt, B. Brügmann, D. Holz, E. Seidel, R. Takahashi, and J. Thornburg. Symmetry without Symmetry: Numerical Simulation of Axisymmetric Systems using Cartesian Grids. *Int. J. Mod. Phys. D*, 10:273–290, 2001. gr-qc/9908012.

[224] H. Yoshino and M. Shibata. Higher-Dimensional Numerical Relativity: Current Status. *Prog.Theor.Phys.Suppl.*, 189:269–310, 2011.

[225] H. Yoshino and M. Shibata. Exploring Higher-Dimensional Black Holes in Numerical Relativity. *Prog.Theor.Phys.Suppl.*, 190:282–303, 2011.

[226] P. Marronetti, W. Tichy, B. Brügmann, J. A. González, and U. Sperhake. High-spinning binary black hole mergers. *Phys. Rev. D*, 77:064010, 2008. arXiv:0709.2160 [gr-qc].

[227] U. Sperhake, E. Berti, V. Cardoso, J. A. González, B. Brügmann, and M. Ansorg. Eccentric binary black-hole mergers: The transition from inspiral to plunge in general relativity. *Phys. Rev. D*, 78:064069, 2008. arXiv:0710.3823 [gr-qc].

[228] Allen, G. and Goodale, T. and Massó, J. and Seidel, E. The Cactus Computational Toolkit and Using Distributed Computing to Collide Neutron Stars. In *Proceedings of Eighth IEEE International Symposium on High Performance Distributed Computing, HPDC-8, Redondo Beach, 1999*, , 1999. IEEE Press.

[229] B. P. Abbott et al. Properties of the binary black hole merger GW150914. *Phys. Rev. Lett.*, 116(24):241102, 2016. arXiv:1602.03840 [gr-qc].

[230] B. P. Abbott et al. Directly comparing GW150914 with numerical solutions of Einstein's equations for binary black hole coalescence. *Phys. Rev. D*, 94:064035, 2016. arXiv:1606.01262 [gr-qc].

[231] S. Adrian-Martinez et al. High-energy Neutrino follow-up search of Gravitational Wave Event GW150914 with ANTARES and IceCube. *Phys. Rev. D*, 93(12):122010, 2016. arXiv:1602.05411 [astro-ph].

[232] R. Emparan and H. S. Reall. Black Holes in Higher Dimensions. *Living Reviews in Relativity*, 11(6), 2008. http://www.livingreviews.org/lrr-2008-6.

[233] M. Zilhão, V. Cardoso, C. Herdeiro, L. Lehner, and U. Sperhake. Testing the nonlinear stability of Kerr-Newman black holes. *Phys. Rev. D*, 90(12):124088, 2014. arXiv:1410.0694 [gr-qc].

[234] M. Dafermos and I. Rodnianski. The black hole stability problem for linear scalar perturbations. In *On recent developments in theoretical and experimental general relativity, astrophysics and relativistic field theories. Proceedings, 12th Marcel Grossmann Meeting on General Relativity, Paris, France, July 12-18, 2009. Vol. 1-3*, pages 132–189, 2010. arXiv:1010.5137 [gr-qc].

[235] P. Kanti. Black Holes at the LHC. *Lect.Notes Phys.*, 769:387–423, 2009. arXiv:0802.2218 [hep-th].

[236] Matthew W. Choptuik, Luis Lehner, and Frans Pretorius. Probing Strong Field Gravity Through Numerical Simulations. 2015. arXiv:1502.06853 [gr-qc].

[237] H. Bondi, F. A. E. Pirani, and I. Robinson. Gravitational waves in general relativity. 3. Exact plane waves. *Proc. Roy. Soc. Lond.*, A251:519–533, 1959.

[238] F. A. E. Pirani. Invariant formulation of gravitational radiation theory. *Phys. Rev.*, 105:1089–1099, 1957.

[239] H. Bondi. Plane gravitational waves in general relativity. *Nature*, 179:1072–1073, 1957.

[240] H. Bondi. Gravitational Waves in General Relativity. *Nature*, 186(4724):535–535, 1960.

[241] P. R. Saulson. Josh Goldberg and the physical reality of gravitational waves. *Gen. Rel. Grav.*, 43:3289–3299, 2011.

[242] P. C. Peters. Gravitational Radiation and the Motion of Two Point Masses. *Phys. Rev.*, 136:B1224–B1232, 1964.

[243] C. T. Cunningham, R. H. Price, and V. Moncrief. Radiation from collapsing relativistic stars. I. Linearized odd-parity radiation. *Astrophys. J.*, 224:643–667, 1978.

[244] C.T. Cunningham, R.H. Price, and V. Moncrief. Radiation from collapsing relativistic stars. II. Linearized even parity radiation. *Astrophys. J.*, 230:870–892, 1979.

[245] Luc Blanchet, Thibault Damour, and Gerhard Schaefer. Postnewtonian hydrodynamics and postnewtonian gravitational wave generation for numerical relativity. *Mon. Not. Roy. Astron. Soc.*, 242:289–305, 1990.

[246] L. Blanchet, T. Damour, B. R. Iyer, C. M. Will, and A. G. Wiseman. Gravitational-Radiation Damping of Compact Binary Systems to Second Post-Newtonian Order. *Phys. Rev. Lett.*, 74:3515–3518, 1995.

[247] J. M. Centrella, J. G. Baker, B. J. Kelly, and J. R. van Meter. Black-hole binaries, gravitational waves, and numerical relativity. *Rev. Mod. Phys.*, 82:3069, 2010. arXiv:1010.5260 [gr-qc].

[248] I. Hinder et al. Error-analysis and comparison to analytical models of numerical waveforms produced by the NRAR Collaboration. *Class. Quant. Grav.*, 31:025012, 2014. arXiv:1307.5307 [gr-qc].

[249] J. S. Read et al. Matter effects on binary neutron star waveforms. *Phys. Rev. D*, 88:044042, 2013. arXiv:1306.4065 [gr-qc].

[250] A. H. Mroué et al. A catalog of 171 high-quality binary black-hole simulations for gravitational-wave astronomy. *Phys. Rev. Lett.*, 111:241104, 2013. arXiv:1304.6077 [gr-qc].

[251] A. Taracchini *et al.* Effective-one-body model for black-hole binaries with generic mass ratios and spins. *Phys. Rev. D*, 89(6):061502, 2014. arXiv:1311.2544 [gr-qc].

[252] M. Pürrer. Frequency domain reduced order models for gravitational waves from aligned-spin compact binaries. *Class. Quant. Grav.*, 31(19):195010, 2014. aRxiv:1402.4146 [gr-qc].

[253] S. Khan et al. Frequency-domain gravitational waves from non-precessing black-hole binaries. II. A phenomenological model for the advanced detector era. *Phys. Rev. D*, 93:044007, 2016. arXiv:1508.07253 [gr-qc].

[254] M. Hannam *et al.* A simple model of complete precessing black-hole-binary gravitational waveforms. *Phys.Rev.Lett.*, 113:151101, 2014. arXiv:1308.3271 [gr-qc].

[255] K. S. Thorne. Multipole expansions of gravitational radiation. *Rev. Mod. Phys.*, 52:299–339, 1980.

[256] C. D. Ott, H. Dimmelmeier, A. Marek, H.-T. Janka, I. Hawke, B. Zink, and E. Schnetter. 3D Collapse of Rotating Stellar Iron Cores in General Relativity with Microphysics. *Phys. Rev. Lett.*, 98:261101, 2007. astro-ph/0609819.

[257] M. Shibata and Y.-i. Sekiguchi. Three-dimensional simulations of stellar core collapse in full general relativity: Nonaxisymmetric dynamical instabilities. *Phys. Rev. D*, 71:024014, 2005. astro-ph/0412243.

[258] G. Lovelace, Y. Chen, M. Cohen, J. Kaplan, D. Keppel, K. D. Matthews, D. A. Nichols, M. A. Scheel, and U. Sperhake. Momentum flow in black-hole binaries: II. Numerical simulations of equal-mass, head-on mergers with antiparallel spins. *Phys. Rev. D*, 82:064031, 2010. arXiv:0907.0869 [gr-qc].

[259] F. Herrmann, I. Hinder, D. Shoemaker, P. Laguna, and R. A. Matzner. Gravitational recoil from spinning binary black hole mergers. *Astrophys. J.*, 661:430–436, 2007. gr-qc/0701143.

[260] B. Brügmann, J. A. González, M. D. Hannam, S. Husa, U. Sperhake, and W. Tichy. Calibration of Moving Puncture Simulations. *Phys. Rev. D*, 77:024027, 2008. gr-qc/0610128.

[261] M. Boyle, D. A. Brown, L. E. Kidder, A. H. Mroué, H. P. Pfeiffer, M. A. Scheel, G. B. Cook, and S. A. Teukolsky. High-accuracy comparison of numerical relativity simulations with post-Newtonian expansions. *Phys. Rev. D*, 76:124038, 2007. arXiv:0710.0158 [gr-qc].

[262] V. Cardoso, O. J. C. Dias, and J. P. S. Lemos. Gravitational radiation in D-dimensional space-times. *Phys. Rev. D*, 67:064026, 2003. hep-th/0212168.

[263] A. Ishibashi and H. Kodama. Perturbations and Stability of Static Black Holes in Higher Dimensions. *Prog. Theor. Phys. Suppl.*, 189:165–209, 2011. arXiv:1103.6148 [hep-th].

[264] H. Witek, V. Cardoso, L. Gualtieri, C. Herdeiro, U. Sperhake, and M. Zilhão. Numerical Relativity in *D* dimensional space-times: Collisions of unequal mass black holes. *J. Phys. Conf. Ser.*, 314:012104, 2011.

[265] M. Godazgar and H. S. Reall. Peeling of the Weyl tensor and gravitational radiation in higher dimensions. *Phys. Rev. D*, 85:084021, 2012. arXiv:1201.4373 [gr-qc].

[266] M. Ortaggio, V. Pravda, A. Pravdova, and H. S. Reall. On a five-dimensional version of the Goldberg-Sachs theorem. *Class. Quant. Grav.*, 29:205002, 2012. arXiv:1205.1119 [gr-qc].

[267] S. A. Teukolsky. Rotating black holes - separable wave equations for gravitational and electromagnetic perturbations. *Phys. Rev. Lett.*, 29:1114–1118, 1972.

[268] Mark Durkee and Harvey S. Reall. Perturbations of higher-dimensional spacetimes. *Class. Quant. Grav.*, 28:035011, 2011.

[269] Mark Durkee, Vojt Pravda, Alena Pravdova, and Harvey S. Reall. Generalization of the Geroch-Held-Penrose formalism to higher dimensions. *Class. Quant. Grav.*, 27:215010, 2010.

[270] Kentaro Tanabe, Shunichiro Kinoshita, and Tetsuya Shiromizu. Asymptotic flatness at null infinity in arbitrary dimensions. *Phys. Rev.*, D84:044055, 2011.

[271] M. Zilhão, M. Ansorg, V. Cardoso, L. Gualtieri, C. Herdeiro, U. Sperhake, and H. Witek. Higher-dimensional puncture initial data. *Phys. Rev. D*, 84:084039, 2011. arXiv:1109.2149 [gr-qc].

[272] Roberto Emparan, Ryotaku Suzuki, and Kentaro Tanabe. Decoupling and non-decoupling dynamics of large D black holes. *JHEP*, 07:113, 2014.

[273] Roberto Emparan, Ryotaku Suzuki, and Kentaro Tanabe. Quasinormal modes of (Anti-)de Sitter black holes in the 1/D expansion. *JHEP*, 04:085, 2015.

[274] M. Davis, R. Ruffini, W. H. Press, and R. H. Price. Gravitational radiation from a particle falling radially into a schwarzschild black hole. *Phys. Rev. Lett.*, 27:1466–1469, 1971.

[275] E. Berti, V. Cardoso, and B. Kipapa. Up to eleven: radiation from particles with arbitrary energy falling into higher-dimensional black holes. *Phys. Rev. D*, 83:084018, 2011.

[276] Madalena Lemos. Approximation Methods in the Study of Gravitational-Wave Generation: From the Quadrupole to the ZFL. Master's thesis, 2010.

[277] E. Berti, V. Cardoso, J. A. González, U. Sperhake, M. D. Hannam, S. Husa, and B. Brügmann. Inspiral, merger and ringdown of unequal mass black hole binaries: a multipolar analysis. *Phys. Rev. D*, 76:064034, 2007. gr-qc/0703053.

[278] Alexandre Le Tiec, Abdul H. Mroue, Leor Barack, Alessandra Buonanno, Harald P. Pfeiffer, Norichika Sago, and Andrea Taracchini. Periastron Advance in Black Hole Binaries. *Phys. Rev. Lett.*, 107:141101, 2011.

[279] A. Le Tiec. The Overlap of Numerical Relativity, Perturbation Theory and Post-Newtonian Theory in the Binary Black Hole Problem. *Int. J. Mod. Phys. D*, 23(10):1430022, 2014. arXiv:1408.5505 [gr-qc].

[280] T. Nakamura and M. P. Haugan. Gravitational radiation from particles falling along the symmetry axis into a Kerr black hole: The momentum radiated. *Astrophys. J.*, 269:292–296, 1983.

[281] E. Berti, V. Cardoso, T. Hinderer, M. Lemos, F. Pretorius, U. Sperhake, and N. Yunes. Semianalytical estimates of scattering thresholds and gravitational radiation in ultrarelativistic black hole encounters. *Phys. Rev. D*, 81:104048, 2010. arXiv:1003.0812 [gr-qc].

[282] U. Sperhake, V. Cardoso, C. D. Ott, E. Schnetter, and H. Witek. Extreme black hole simulations: collisions of unequal mass black holes and the point particle limit. *Phys. Rev. D*, 84:084038, 2011. arXiv:1105.5391 [gr-qc].

[283] M. J. Fitchett and S. Detweiler. Linear momentum and gravitational waves - Circular orbits around a Schwarzschild black hole. *MNRAS*, 211:933–942, 1984.

[284] M. Favata, S. A. Hughes, and D. E. Holz. How black holes get their kicks: Gravitational radiation recoil revisited. *Astrophys. J.*, 607:L5–L8, 2004. astro-ph/0402056.

[285] H. Yoshino, T. Shiromizu, and M. Shibata. Close-slow analysis for head-on collision of two black holes in higher dimensions: Bowen-York initial data. *Phys. Rev. D*, 74:124022, 2006. gr-qc/0610110.

[286] M. Shibata. *Numerical Relativity*, volume 1 of *100 Years of General Relativity*. World Scientific, 2015.

[287] Robert C. Myers. Myers-Perry black holes, arXiv:1111.1903. 2011.

[288] Kentaro Tanabe, Norihiro Tanahashi, and Tetsuya Shiromizu. Asymptotic flatness at spatial infinity in higher dimensions. *J. Math. Phys.*, 50:072502, 2009.

[289] Peter Diener. A New general purpose event horizon finder for 3-D numerical space-times. *Class. Quant. Grav.*, 20:4901–4918, 2003. gr-qc/0305039.

[290] M. I. Cohen, H. P. Pfeiffer, and M. A. Scheel. Revisiting Event Horizon Finders. *Class. Quant. Grav.*, 26:035005, 2009. arXiv:0809.2628 [gr-qc].

[291] M. Alcubierre, S. Brandt, Bernd Brügmann, C. Gundlach, J. Masso, E. Seidel, and P. Walker. Test beds and applications for apparent horizon finders in numerical relativity. *Class. Quant. Grav.*, 17:2159–2190, 2000. gr-qc/9809004.

[292] C. Gundlach. Pseudospectral apparent horizon finders: An Efficient new algorithm. *Phys. Rev. D*, 57:863–875, 1998. gr-qc/9707050.

[293] J. Thornburg. A Fast apparent horizon finder for three-dimensional Cartesian grids in numerical relativity. *Class. Quant. Grav.*, 21:743–766, 2004. gr-qc/0306056.

[294] J. Thornburg. Finding apparent horizons in numerical relativity. *Phys. Rev. D*, 54:4899–4918, 1996. gr-qc/9508014.

[295] J. Thornburg. Event and Apparent Horizon Finders in 3+1 Numerical Relativity. *Living Reviews in Relativity*, 10(3), 2007. gr-qc/0512169.

[296] T. W. Baumgarte, G. B. Cook, M. A. Scheel, S. L. Shapiro, and S. A. Teukolsky. Implementing an apparent-horizon finder in three dimensions. *Phys. Rev. D*, 54:4849, 1996. gr-qc/9606010.

[297] W. H. Press, B. P. Flannery, S. A. Teukolsky, and W. T. Vetterling. *Numerical Recipes.* Cambridge University Press, Cambridge, 1989.

[298] S. W. Hawking and G. F. R. Ellis. *The Large Scale Structure of Space-Time.* Cambridge University Press, 1973.

[299] Gregory J. Galloway. Constraints on the topology of higher dimensional black holes. 2011. arXiv:1111.5356 [gr-qc].

[300] V. Cardoso, A. S. Miranda, E. Berti, H. Witek, and V. T. Zanchin. Geodesic stability, Lyapunov exponents and quasinormal modes. *Phys. Rev. D*, 79:064016, 2009. arXiv:0812.1806 [hep-th].

[301] F. Pretorius and D. Khurana. Black Hole Mergers and Unstable Circular Orbits. *Class. Quantum Grav.*, 24:S83–S108, 2007. gr-qc/0702084.

[302] J. Healy, J. Levin, and D. Shoemaker. Zoom-Whirl Orbits in Black Hole Binaries. *Phys. Rev. Lett.*, 103:131101, 2009. arXiv:0907.0671 [gr-qc].

[303] R. Gold and B. Brügmann. Radiation from low-momentum zoom-whirl orbits. *Class. Quant. Grav.*, 27:084035, 2010. arXiv:0911.3862 [gr-qc].

[304] M. Campanelli, C. O. Lousto, and Y. Zlochower. Spinning-black-hole binaries: The orbital hang up. *Phys. Rev. D*, 74:041501, 2006. gr-qc/0604012.

[305] J. A. González, U. Sperhake, B. Brügmann, M. D. Hannam, and S. Husa. The maximum kick from nonspinning black-hole binary inspiral. *Phys. Rev. Lett.*, 98:091101, 2007. gr-qc/0610154.

[306] B. Brügmann, J. A. González, M. D. Hannam, S. Husa, and U. Sperhake. Exploring black hole superkicks. *Phys. Rev. D*, 77:124047, 2008. arXiv:0707.0135 [gr-qc].

[307] J. A. González, M. D. Hannam, U. Sperhake, B. Brügmann, and S. Husa. Supermassive kicks for spinning black holes. *Phys. Rev. Lett.*, 98:231101, 2007. gr-qc/0702052.

[308] M. Campanelli, C. O. Lousto, Y. Zlochower, and D. Merritt. Maximum gravitational recoil. *Phys. Rev. Lett.*, 98:231102, 2007. gr-qc/0702133.

[309] R. Sachs. Asymptotic symmetries in gravitational theory. *Phys. Rev.*, 128:2851–2864, 1962.

[310] Louis A. Tamburino and Jeffrey H. Winicour. Gravitational Fields in Finite and Conformal Bondi Frames. *Phys. Rev.*, 150:1039–1053, 1966.

[311] C. R. Prior. Angular momentum in general relativity I. Definition and asymptotic behaviour. *Proceedings of the Royal Society of London A: Mathematical, Physical and Engineering Sciences*, 354(1679):379–405, 1977.

[312] A. Ashtekar and M. Streubel. Symplectic Geometry of Radiative Modes and Conserved Quantities at Null Infinity. *Proc. Roy. Soc. Lond.*, A376:585–607, 1981.

[313] T. Dray and M. Streubel. Angular momentum at null infinity. *Class. Quant. Grav.*, 1(1):15–26, 1984.

[314] K. Tanabe, T. Shiromizu, and S. Kinoshita. Angular momentum at null infinity in higher dimensions. *Phys. Rev. D*, 85:124058, 2012. arXiv:1203.0452 [gr-qc].

[315] Emanuele Berti, Vitor Cardoso, and Marc Casals. Eigenvalues and eigenfunctions of spin-weighted spheroidal harmonics in four and higher dimensions. *Phys. Rev.*, D73:024013, 2006. [Erratum: Phys. Rev.D73,109902(2006)].

[316] J. Thornburg. A Fast Apparent-Horizon Finder for 3-Dimensional Cartesian Grids in Numerical Relativity. *AIP Conference Proceedings*, 686:247–252, 2003.

[317] Majd Abdelqader and Kayll Lake. Invariant characterization of the Kerr spacetime: Locating the horizon and measuring the mass and spin of rotating black holes using curvature invariants. *Phys. Rev.*, D91(8):084017, 2015.

[318] Don N. Page and Andrey A. Shoom. Local Invariants Vanishing on Stationary Horizons: A Diagnostic for Locating Black Holes. *Phys. Rev. Lett.*, 114(14):141102, 2015.

[319] Alan Coley and David McNutt. Identification of black hole horizons using scalar curvature invariants. *Class. Quant. Grav.*, 35(2):025013, 2018.

[320] D. Brooks, M. A. H. MacCallum, D. Gregoris, A. Forget, A. A. Coley, P. C. Chavy-Waddy, and D. D. McNutt. Cartan Invariants and Event Horizon Detection, Extended Version. *Gen. Rel. Grav.*, 50(4):37, 2018.

[321] Alan A. Coley, David D. McNutt, and Andrey A. Shoom. Geometric horizons. *Phys. Lett.*, B771:131–135, 2017.

Appendix A

Dimensional Reduction with the Modified Cartoon Formalism - Appendix

A.1 Cartesian components in $SO(D - d)$ symmetry

We present here the list of all modified Cartoon expressions for the case of $SO(D - d)$ symmetry with $d < D - 2$. The index range for early Latin indices is $a, b, \ldots = d + 1, \ldots, D - 1$ and for middle Latin indices $i, j, \ldots = 1, \ldots d$. Furthermore, an index z denotes the coordinate z while the index w only appears in the tensor component T_{ww} which represents the additional function that needs to be evolved numerically in addition to the T_{ij}. For example, the spacetime metric is fully described by the components $g_{\alpha\beta}$, α, $\beta = 0, 1, \ldots d$, plus one additional field g_{ww}. For arbitrary scalar,

vector and tensor densities Ψ, V^A and T_{AB}, the expressions are

$$0 = \partial_a \Psi = \partial_i \partial_a \Psi , \tag{A.1}$$

$$\partial_a \partial_b \Psi = \delta_{ab} \frac{\partial_z \Psi}{z} , \tag{A.2}$$

$$0 = V^a = \partial_i V^a = \partial_a V^i = \partial_a \partial_b V^c , \tag{A.3}$$

$$\partial_a V^b = \delta_a{}^b \frac{V^z}{z} , \tag{A.4}$$

$$\partial_i \partial_a V^b = \delta^b{}_a \left(\frac{\partial_i V^z}{z} - \delta_{iz} \frac{V^z}{z^2} \right) , \tag{A.5}$$

$$\partial_a \partial_b V^i = \delta_{ab} \left(\frac{\partial_z V^i}{z} - \delta^i{}_z \frac{V^z}{z^2} \right) , \tag{A.6}$$

$$0 = T_{ia} = \partial_a T_{bc} = \partial_i \partial_a T_{bc} = \partial_a \partial_b T_{ic} = \partial_a T_{ij} = \partial_i \partial_a T_{jk} , \tag{A.7}$$

$$T_{ab} = \delta_{ab} T_{ww} , \tag{A.8}$$

$$\partial_a \partial_b T_{cd} = (\delta_{ac}\delta_{bd} + \delta_{ad}\delta_{bc}) \frac{T_{zz} - T_{ww}}{z^2} + \delta_{ab}\delta_{cd} \frac{\partial_z T_{ww}}{z} , \tag{A.9}$$

$$\partial_a T_{ib} = \delta_{ab} \frac{T_{iz} - \delta_{iz} T_{ww}}{z} , \tag{A.10}$$

$$\partial_i \partial_a T_{jb} = \delta_{ab} \left(\frac{\partial_i T_{jz} - \delta_{jz} \partial_i T_{ww}}{z} - \delta_{iz} \frac{T_{jz} - \delta_{jz} T_{ww}}{z^2} \right) , \tag{A.11}$$

$$\partial_a \partial_b T_{ij} = \delta_{ab} \left(\frac{\partial_z T_{ij}}{z} - \frac{\delta_{iz} T_{jz} + \delta_{jz} T_{iz} - 2\delta_{iz}\delta_{jz} T_{ww}}{z^2} \right) . \tag{A.12}$$

A.2 Regularization at $z = 0$ for $d < D - 2$

The presence of z in the denominator of several terms in the system of Eqs. (3.28)-(3.48) merely arises from the quasi-radial nature of the coordinate z and can be handled straightforwardly in analogy to the treatment of the origin in spherical or axisymmetry.

We will present the regularized terms needed in the generic $SO(D - d)$ symmetry; however, it should be noted that terms involving the inverse metric become much more complicated for a large d, and so we will also explicitly show these terms for the most common case, $d = 3$.

We first require that all components expressed in a fully Cartesian set of coordinates are regular. A well known consequence of this assumption is that tensor density components containing an odd (even) number of radial, i.e. z, indices contain only odd (even) powers of z in a series expansion around $z = 0$. The same holds for quantities derived from tensors and densities such as the BSSN variable $\tilde{\Gamma}^i$.

Next, we consider the inverse metric which we obtain through inversion of the matrix equation (3.27). By constructing the cofactor matrix and dividing by the determinant, we obtain, for $d = 3$

$$\tilde{\gamma}^{xx} = \tilde{\gamma}^\eta_{ww} \frac{\tilde{\gamma}_{yy}\tilde{\gamma}_{zz} - \tilde{\gamma}^2_{yz}}{\det \tilde{\gamma}_{IJ}}, \qquad \tilde{\gamma}^{xy} = \tilde{\gamma}^\eta_{ww} \frac{\tilde{\gamma}_{yz}\tilde{\gamma}_{xz} - \tilde{\gamma}_{xy}\tilde{\gamma}_{zz}}{\det \tilde{\gamma}_{IJ}}, \qquad \tilde{\gamma}^{xz} = \tilde{\gamma}^\eta_{ww} \frac{\tilde{\gamma}_{xy}\tilde{\gamma}_{yz} - \tilde{\gamma}_{xz}\tilde{\gamma}_{yy}}{\det \tilde{\gamma}_{IJ}},$$

$$\dots \qquad\qquad\qquad \tilde{\gamma}^{yy} = \tilde{\gamma}^\eta_{ww} \frac{\tilde{\gamma}_{xx}\tilde{\gamma}_{zz} - \tilde{\gamma}^2_{xz}}{\det \tilde{\gamma}_{IJ}}, \qquad \tilde{\gamma}^{yz} = \tilde{\gamma}^\eta_{ww} \frac{\tilde{\gamma}_{xy}\tilde{\gamma}_{xz} - \tilde{\gamma}_{xx}\tilde{\gamma}_{yz}}{\det \tilde{\gamma}_{IJ}}, \qquad \text{(A.13)}$$

$$\dots \qquad\qquad\qquad \dots \qquad\qquad\qquad \tilde{\gamma}^{zz} = \tilde{\gamma}^\eta_{ww} \frac{\tilde{\gamma}_{xx}\tilde{\gamma}_{yy} - \tilde{\gamma}^2_{xy}}{\det \tilde{\gamma}_{IJ}}.$$

Next, we recall that the BSSN metric has unit determinant, so that

$$
\begin{aligned}
1 = \det \tilde{\gamma}_{IJ} &= \tilde{\gamma}^\eta_{ww} (\tilde{\gamma}_{xx}\tilde{\gamma}_{yy}\tilde{\gamma}_{zz} + 2\tilde{\gamma}_{xy}\tilde{\gamma}_{xz}\tilde{\gamma}_{yz} - \tilde{\gamma}_{xx}\tilde{\gamma}^2_{yz} - \tilde{\gamma}_{yy}\tilde{\gamma}^2_{xz} - \tilde{\gamma}_{zz}\tilde{\gamma}^2_{xy}) \\
&\overset{*}{=} \tilde{\gamma}^\eta_{ww}\tilde{\gamma}_{zz} (\tilde{\gamma}_{xx}\tilde{\gamma}_{yy} - \tilde{\gamma}^2_{xy}),
\end{aligned}
\tag{A.14}
$$

where we introduced the symbol "$\overset{*}{=}$" to denote equality in the limit $z \to 0$. The components for the inverse BSSN metric in Eq. (A.13) simplify accordingly.

For a general d we know that the matrix takes the form given in Eq. (3.27). Then, denoting the cofactor matrix for a given element of $\tilde{\gamma}_{IJ}$ by C_{IJ}, the inverse BSSN metric components are (note that the metric is symmetric, so that $C_{IJ} = C_{JI}$)

$$\tilde{\gamma}^{x^1 x^1} = \frac{C_{x^1 x^1}}{\det \tilde{\gamma}_{IJ}}, \qquad \dots, \qquad \tilde{\gamma}^{x^1 x^{d-1}} = \frac{C_{x^1 x^{d-1}}}{\det \tilde{\gamma}_{IJ}}, \qquad \tilde{\gamma}^{x^1 z} = \frac{C_{x^1 z}}{\det \tilde{\gamma}_{IJ}},$$

$$\vdots \qquad\qquad \ddots \qquad\qquad \vdots \qquad\qquad\qquad \vdots$$

$$\tag{A.15}$$

$$\vdots \qquad\qquad \dots \qquad \tilde{\gamma}^{x^{d-1} x^{d-1}} = \frac{C_{x^{d-1} x^{d-1}}}{\det \tilde{\gamma}_{IJ}}, \qquad \tilde{\gamma}^{x^{d-1} z} = \frac{C_{x^{d-1} z}}{\det \tilde{\gamma}_{IJ}}$$

$$\dots \qquad\qquad \dots \qquad\qquad \dots \qquad\qquad \tilde{\gamma}^{zz} = \frac{C_{zz}}{\det \tilde{\gamma}_{IJ}}.$$

Again, in the BSSN case $\det \tilde{\gamma}_{IJ} = 1$, and the inverse metric element is simply the cofactor of that element. For simplicity, we will use indices $\hat{i}$ in place of $x^{\hat{i}}$ in the remainder of this section, so that, for example $C_{12} \equiv C_{x^1 x^2}$, $C_{1z} \equiv C_{x^1 z}$ etc. When used without a caret, the lower case Latin indices i, j, ... also include the z component.

If we denote the upper-left quadrant of the matrix in Eq. (3.27) as the matrix M_{ij}, then we can write the cofactor of an element in this upper-left quadrant as

$$C_{ij} = (-1)^{i+j} \tilde{\gamma}^\eta_{ww} \det(M_{kl\{k \neq j, l \neq i\}}). \tag{A.16}$$

Here, the notation $\det(M_{kl\{k\neq j, l\neq i\}})$ denotes the determinant of the matrix obtained by crossing out the jth row and i^{th} column. Likewise, we may add further inequalities inside the braces to denote matrices obtained by crossing out more than one row and column.

The next regularity condition we require our spacetime to satisfy is the absence of a conical singularity at $z = 0$. In polar coordinates (ρ, φ) constructed as in Sec. 3.2.2, this condition can be expressed as $\tilde{\gamma}_{\varphi\varphi} = \rho^2 \tilde{\gamma}_{\rho\rho}$ which translates into the conditions

$$\tilde{\gamma}_{zz} - \tilde{\gamma}_{ww} \stackrel{*}{=} \mathcal{O}(z^2), \qquad \tilde{\gamma}^{zz} - \tilde{\gamma}^{ww} \stackrel{*}{=} \mathcal{O}(z^2), \tag{A.17}$$

in Cartesian coordinates. By taking the time derivative of these relations and combining these with Eqs. (3.31), (3.32), we obtain an analogous relation for the traceless extrinsic curvature,

$$\tilde{A}_{zz} - \tilde{A}_{ww} \stackrel{*}{=} \mathcal{O}(z^2). \tag{A.18}$$

We thus arrive at the following list of regularized terms valid in the limit $z \to 0$.

(1) By expanding $\beta^z = b_1 z + b_3 z^3 + \ldots$, and likewise for $\tilde{\Gamma}^z$ and $\partial_z \tilde{\gamma}_{ww}$, we obtain

$$\frac{\beta^z}{z} \stackrel{*}{=} \partial_z \beta_z, \qquad \frac{\tilde{\Gamma}^z}{z} \stackrel{*}{=} \partial_z \tilde{\Gamma}^z, \qquad \frac{\partial_z \tilde{\gamma}_{ww}}{z} \stackrel{*}{=} \partial_z \partial_z \tilde{\gamma}_{ww}, \tag{A.19}$$

and likewise for α or χ in place of $\tilde{\gamma}_{ww}$ in the last expression.

(2) We express the inverse metric components through their cofactors, given for arbitrary d by Eq. (A.16), and then apply the same trading of divisions by z for derivatives as done for β^z/z, to obtain

$$\frac{\delta^i_{\ z} - \tilde{\gamma}^{zi}\tilde{\gamma}_{ww}}{z} \stackrel{*}{=} \begin{cases} \displaystyle\sum_{\hat{m}=1}^{d-1} (-1)^{\hat{m}+\hat{i}} \partial_z(\tilde{\gamma}_{\hat{m}z}) \tilde{\gamma}_{ww}^{\eta+1} \det(M_{jl\{j\neq z, j\neq \hat{m}, l\neq i, l\neq z\}}) & \text{if } i = \hat{i} \\ \\ 0 & \text{if } i = z \end{cases}. \tag{A.20}$$

Here, as well in items **(5)** and **(9)** below, we formally set $\det(M_{jl\{j\neq z, j\neq \hat{m}, l\neq i, l\neq z\}}) = 1$ for the case $d = 2$ where no entries would be left in the matrix after crossing out two rows and columns. For $d = 1$, the case $i = \hat{i}$ does not arise which obviates the need to evaluate the determinant. For the case $d = 3$, the expression (A.20)

becomes

$$
\frac{\delta^i{}_z - \tilde{\gamma}^{zi}\tilde{\gamma}_{ww}}{z} \stackrel{*}{=}
\begin{cases}
\tilde{\gamma}_{ww}^{\eta+1}(\tilde{\gamma}_{yy}\partial_z\tilde{\gamma}_{xz} - \tilde{\gamma}_{xy}\partial_z\tilde{\gamma}_{yz}) & \text{if } i = x \\[2mm]
\tilde{\gamma}_{ww}^{\eta+1}(\tilde{\gamma}_{xx}\partial_z\tilde{\gamma}_{yz} - \tilde{\gamma}_{xy}\partial_z\tilde{\gamma}_{xz}) & \text{if } i = y \\[2mm]
0 & \text{if } i = z
\end{cases}
\qquad\text{.}
\tag{A.21}
$$

(3) Expanding $\beta^{\hat{i}} = b_0 + b_2 z^2 + \ldots$ and $\beta^z = b_1 z + b_3 z^3 + \ldots$, we trade two divisions by z for a second derivative and obtain

$$
\frac{\partial_z\beta^i}{z} - \delta^i{}_z\frac{\beta^z}{z^2} =
\begin{cases}
\partial_z\partial_z\beta^{\hat{i}} & \text{if } i = \hat{i} \\[2mm]
0 & \text{if } i = z
\end{cases}
\qquad\text{.}
\tag{A.22}
$$

(4) We rewrite the term

$$
\tilde{\gamma}^{im}\frac{\partial_m\beta^z}{z} - \tilde{\gamma}^{iz}\frac{\beta^z}{z^2} = \tilde{\gamma}^{im}\left(\frac{\partial_m\beta^z}{z} - \delta^z{}_m\frac{\beta^z}{z^2}\right),
\tag{A.23}
$$

and expand $\beta^z = b_1 z + b_3 z^3 + \ldots$ which leads to

$$
\frac{\partial_m\beta^z}{z} - \delta^z{}_m\frac{\beta^z}{z^2} =
\begin{cases}
\partial_{\hat{m}}\partial_z\beta^z & \text{if } m = \hat{m} \\[2mm]
0 & \text{if } m = z
\end{cases}
\qquad\text{.}
\tag{A.24}
$$

(5) Similarly to Eq. (A.20), we find for general d that

$$
\begin{aligned}
\frac{\tilde{\gamma}^{zm}}{z}\partial_m\alpha \;=\; & \sum_{\hat{m}=1}^{d-1}\sum_{\hat{i}=1}^{d-1}(-1)^{\hat{m}+\hat{i}-1}\partial_z(\tilde{\gamma}_{\hat{m}z})\tilde{\gamma}_{ww}^{\eta}\det(M_{jl\{j\neq z,j\neq\hat{m},l\neq\hat{i},l\neq z\}})\partial_{\hat{i}}\alpha \\
& +\tilde{\gamma}^{zz}\partial_z\partial_z\alpha,
\end{aligned}
\tag{A.25}
$$

where again we formally set $\det(M_{jl\{j\neq z,j\neq\hat{m},l\neq i,l\neq z\}}) = 1$ for the case $d = 2$; c.f. item **(2)** above. For $d = 3$, we obtain

$$
\begin{aligned}
\frac{\tilde{\gamma}^{zm}}{z}\partial_m\alpha \;=\; & \tilde{\gamma}_{ww}^{\eta}\left[(\tilde{\gamma}_{xy}\partial_z\tilde{\gamma}_{yz} - \tilde{\gamma}_{yy}\partial_z\tilde{\gamma}_{xz})\,\partial_x\alpha + (\tilde{\gamma}_{xy}\partial_z\tilde{\gamma}_{xz} - \tilde{\gamma}_{xx}\partial_z\tilde{\gamma}_{yz})\,\partial_y\alpha\right] \\
& +\tilde{\gamma}^{zz}\partial_z\partial_z\alpha,
\end{aligned}
\tag{A.26}
$$

and likewise for χ in place of α.

(6) Using $\tilde{A}_{zz} - \tilde{A}_{ww} = \mathcal{O}(z^2)$, we obtain

$$\frac{\tilde{A}_{iz} - \delta_{iz}\tilde{A}_{ww}}{z} = \begin{cases} \partial_z \tilde{A}_{\hat{i}z} & \text{if } i = \hat{i} \\ 0 & \text{if } i = z \end{cases}. \tag{A.27}$$

(7) Using $\tilde{\gamma}_{zz} - \tilde{\gamma}_{ww} = \mathcal{O}(z^2)$ and trading a division by z for a z derivative, we find

$$-\frac{1}{2}\frac{\partial_z \tilde{\gamma}_{ij}}{z} + \frac{\delta_{z(i}\tilde{\gamma}_{j)z} - \delta_{iz}\delta_{jz}\tilde{\gamma}_{ww}}{z^2} = \begin{cases} -\frac{1}{2}\partial_z\partial_z\tilde{\gamma}_{\hat{i}\hat{j}} & \text{if } (i,j) = (\hat{i},\hat{j}) \\ 0 & \text{if } (i,j) = (\hat{i},z) \text{ or } (z,\hat{j}) \\ -\frac{1}{2}\partial_z\partial_z\tilde{\gamma}_{ww} & \text{if } (i,j) = (z,z) \end{cases}. \tag{A.28}$$

(8) Using $\tilde{\gamma}^{ww}\tilde{\gamma}_{zz} - 1 = \tilde{\gamma}^{ww}(\tilde{\gamma}_{zz} - \gamma_{ww}) = \tilde{\gamma}^{ww}\mathcal{O}(z^2)$ and $\tilde{\gamma}_{z\hat{i}}/z = \partial_z\tilde{\gamma}_{z\hat{i}}$, we can rewrite

$$\frac{\tilde{\gamma}^{ww}\tilde{\gamma}_{z(j} - \delta_{z(j}}{z}\partial_{i)}\tilde{\gamma}_{ww} = \begin{cases} \tilde{\gamma}^{ww}\partial_z\tilde{\gamma}_{z(\hat{j}}\partial_{\hat{i})}\tilde{\gamma}_{ww} & \text{if } (i,j) = (\hat{i},\hat{j}) \\ 0 & \text{if } (i,j) = (\hat{i},z) \text{ or } (z,\hat{j}) \\ 0 & \text{if } (i,j) = (z,z) \end{cases}. \tag{A.29}$$

(9) The term $(\tilde{\gamma}^{zz}\tilde{\gamma}_{ww} - 1)/z^2$ requires slightly more work and we describe its derivation here in a little more detail. We first rewrite this term in the form

$$\frac{\tilde{\gamma}^{zz}\tilde{\gamma}_{ww} - 1}{z^2} = -\tilde{\gamma}^{zz}\frac{\frac{1}{\tilde{\gamma}^{zz}} - \tilde{\gamma}_{ww}}{z^2}, \tag{A.30}$$

and express the inverse metric component $\tilde{\gamma}^{zz}$ in terms of the corresponding cofactor matrix component and the determinant as

$$\frac{1}{\tilde{\gamma}^{zz}} = \frac{\det\tilde{\gamma}_{IJ}}{C_{zz}} = \frac{\tilde{\gamma}_{zz}C_{zz}}{C_{zz}} + \frac{\sum_{\hat{i}=1}^{d-1}\tilde{\gamma}_{z\hat{i}}C_{zx_{\hat{i}}}}{C_{zz}}. \tag{A.31}$$

Note that these expressions are all valid for arbitrary values of z and we are not yet using the BSSN condition $\det\tilde{\gamma}_{IJ} = 1$. We can now plug this relation into Eq. (A.30). We then trade divisions by z for derivatives with respect to z, bearing

in mind that $\tilde{\gamma}_{zz} = \tilde{\gamma}_{ww} + \mathcal{O}(z^2)$ and find

$$\frac{\tilde{\gamma}^{zz}\tilde{\gamma}_{ww} - 1}{z^2} \overset{*}{=} \frac{\tilde{\gamma}^{zz}}{2}\left(\partial_z\partial_z\tilde{\gamma}_{ww} - \partial_z\partial_z\tilde{\gamma}_{zz}\right) \tag{A.32}$$
$$+ \tilde{\gamma}^{zz}\sum_{\hat{i}=1}^{d-1}\sum_{\hat{j}=1}^{d-1}(-1)^{\hat{i}+\hat{j}}\,\tilde{\gamma}_{ww}^{\eta}\frac{(\partial_z\tilde{\gamma}_{z\hat{i}})\,\partial_z\tilde{\gamma}_{\hat{j}z}}{C_{zz}}\det(M_{kl\{k\neq z, k\neq\hat{j}, l\neq\hat{i}, l\neq z\}})\,.$$

Again, we formally set $\det(M_{jl\{j\neq z, j\neq\hat{m}, l\neq i, l\neq z\}}) = 1$ for the case $d = 2$; c.f. item **(2)** above. Finally we use $1 = \det\tilde{\gamma}_{IJ} \Rightarrow C_{zz} = \tilde{\gamma}^{zz}$ to obtain

$$\frac{\tilde{\gamma}^{zz}\tilde{\gamma}_{ww} - 1}{z^2} \overset{*}{=} \frac{\tilde{\gamma}^{zz}}{2}\left(\partial_z\partial_z\tilde{\gamma}_{ww} - \partial_z\partial_z\tilde{\gamma}_{zz}\right) \tag{A.33}$$
$$+ \sum_{\hat{i}=1}^{d-1}\sum_{\hat{j}=1}^{d-1}(-1)^{\hat{i}+\hat{j}}\,\tilde{\gamma}_{ww}^{\eta}(\partial_z\tilde{\gamma}_{z\hat{i}})\,\partial_z\tilde{\gamma}_{z\hat{j}}\det(M_{kl\,\{k\neq z, k\neq\hat{j}, l\neq\hat{i}, l\neq z\}})\,.$$

For the case $d = 3$ this reduces to:

$$\frac{\tilde{\gamma}^{zz}\tilde{\gamma}_{ww} - 1}{z^2} \overset{*}{=} \frac{\tilde{\gamma}^{zz}}{2}\partial_z\partial_z(\tilde{\gamma}_{ww} - \tilde{\gamma}_{zz}) - \tilde{\gamma}_{ww}^{\eta}\left[2\tilde{\gamma}_{xy}(\partial_z\tilde{\gamma}_{xz})\partial_z\tilde{\gamma}_{yz} - \tilde{\gamma}_{xx}(\partial_z\tilde{\gamma}_{yz})^2\right.$$
$$\left. - \tilde{\gamma}_{yy}(\partial_z\tilde{\gamma}_{xz})^2\right]\,. \tag{A.34}$$

Finally, we list for completeness the regularization of Eqs. (A.2), (A.5), (A.6), (A.9), (A.10) and (A.11) expressed here in terms of generic vector and tensor fields rather than the BSSN variables,

$$\frac{\partial_z\psi}{z} \overset{*}{=} \partial_z\partial_z\psi\,, \tag{A.35}$$

$$\frac{V^z}{z} \overset{*}{=} \partial_z V^z\,, \tag{A.36}$$

$$\frac{\partial_i V^z}{z} - \delta^z_{\ i}\frac{V^z}{z^2} \overset{*}{=} \begin{cases} \partial_i\partial_z V^z & \text{if } i = \hat{i} \\ 0 & \text{if } i = z \end{cases}\,, \tag{A.37}$$

$$\frac{\partial_z V^i}{z} - \delta^i_{\ z}\frac{V^z}{z^2} \overset{*}{=} \begin{cases} \partial_z\partial_z V^i & \text{if } i = \hat{i} \\ 0 & \text{if } i = z \end{cases}\,, \tag{A.38}$$

$$\frac{T_{zz} - T_{ww}}{z^2} \overset{*}{=} \frac{1}{2}\partial_z\partial_z(T_{zz} - T_{ww})\,, \tag{A.39}$$

$$\frac{\partial_z T_{ww}}{z} \stackrel{*}{=} \partial_z \partial_z T_{ww}\,, \tag{A.40}$$

$$\frac{T_{iz} - \delta_{iz} T_{ww}}{z} \stackrel{*}{=} \begin{cases} \partial_z T_{iz} & \text{if } i = \hat{i} \\[2mm] 0 & \text{if } i = z \end{cases}\,, \tag{A.41}$$

$$\frac{\partial_i T_{jz} - \delta_{jz} \partial_i T_{ww}}{z} - \delta_{iz} \frac{T_{jz} - \delta_{jz} T_{ww}}{z^2} \stackrel{*}{=} \begin{cases} \partial_i \partial_z T_{jz} & \text{if } (i,j) = (\hat{i}, \hat{j}) \\[2mm] 0 & \text{if } (i,j) = (\hat{i}, z) \text{ or } (z, \hat{j}) \\[2mm] \frac{\partial_z \partial_z (T_{zz} - T_{ww})}{2} & \text{if } (i,j) = (z, z) \end{cases}\,, \tag{A.42}$$

$$\frac{\partial_z T_{ij}}{z} - \frac{\delta_{iz} T_{jz} + \delta_{jz} T_{iz} - 2\delta_{iz}\delta_{jz} T_{ww}}{z^2} \stackrel{*}{=} \begin{cases} \partial_z \partial_z T_{ij} & \text{if } (i,j) = (\hat{i}, \hat{j}) \\[2mm] 0 & \text{if } (i,j) = (\hat{i}, z) \text{ or } (z, \hat{j}) \\[2mm] \partial_z \partial_z T_{ww} & \text{if } (i,j) = (z, z) \end{cases}\,. \tag{A.43}$$

Appendix B

Higher Dimensional Gravitational Wave Extraction - Appendix

B.1   Regularisation of terms at $z = 0$

For the axisymmetric case $d = D - 2$, we only need to regularise terms appearing in the calculation of derivatives in the off-domain w direction. All these terms are given explicitly in Appendix C of [114], so that in the following we can focus exclusively on the additional terms appearing for $1 \leq d \leq D - 3$, i.e. for spacetimes admitting two or more rotational Killing vector fields.

The treatment of these terms proceeds in close analogy to that of the BSSN equations in the modified Cartoon approach as described in detail Appendix A.2. In contrast, here we will not be using the conformally rescaled metric of the BSSN equations, which satisfies the simplifying condition $\det \tilde{\gamma} = 1$, and so certain regularised terms involving the inversion of the metric will differ from the expressions obtained for the BSSN equations.

We start with a brief summary of the techniques and the main assumptions we will use to regularise expressions:

1. Regularity: We require all tensor components and their derivatives to be regular when expressed in Cartesian coordinates. Under transformation to spherical coordinates this implies that tensors containing an odd (even) number of radial indices, i.e. z indices in our notation, contain exclusively odd (even) powers of z in a series expansion around $z = 0$. Using such a series expansion enables us to trade divisions by z for derivatives

with respect to z. For example, for the z component of a vector field $\boldsymbol{V}$, we obtain

$$\frac{V^z}{z} = \frac{a_1 z + a_3 z^3 + \ldots}{z} = a_1 + a_3 z^2 + \ldots \overset{*}{=} a_1 \overset{*}{=} \partial_z V^z \,, \tag{B.1}$$

where again the symbol $\overset{*}{=}$ denotes equality in the limit $z \to 0$.

2. *Absence of conical singularities:* We require that the spacetime contain no conical singularity at the origin $z = 0$. For the implications of this condition, we consider the coordinate transformation from $(x^{\hat{i}}, z, w^{d+1}, \ldots, w^a \ldots, w^{D-1})$ to $(x^{\hat{i}}, \rho, w^{d+1}, \ldots, w^{a-1}, \varphi, w^{a+1}, \ldots, w^{D-1})$. As no other w^b, $b \neq a$, coordinates will enter into this discussion we shall refer to w^a as w. In these coordinates we have that

$$\gamma_{\rho\rho} = \frac{z^2}{\rho^2}\gamma_{zz} + 2\frac{zw}{\rho^2}\gamma_{zw} + \frac{w^2}{\rho^2}\gamma_{ww} \,, \tag{B.2}$$

$$\gamma_{\varphi\varphi} = w^2\gamma_{zz} - 2wz\gamma_{zw} + z^2\gamma_{ww} \,, \tag{B.3}$$

and the line element for vanishing $dx^{\hat{i}} = 0$ and $dw^b = 0$, $b \neq a$, is given by

$$ds^2 = \gamma_{\rho\rho}d\rho^2 + \rho^2\gamma_{\varphi\varphi}d\varphi^2 \,. \tag{B.4}$$

Requiring the circumference to be the radius times 2π, we have that $\gamma_{\varphi\varphi} = \rho^2\gamma_{\rho\rho}$. Substituting the above expressions and taking the limit $z \to 0$, we obtain

$$\gamma_{zz} - \gamma_{ww} \overset{*}{=} \mathcal{O}(z^2) \,. \tag{B.5}$$

Taking the time derivative of this relation and using the definition of the extrinsic curvature, we find that likewise

$$K_{zz} - K_{ww} \overset{*}{=} \mathcal{O}(z^2) \,. \tag{B.6}$$

3. *Inverse metric*: Various terms that we need to address contain factors of the inverse metric γ^{IJ}. In the practical regularisation procedure, these terms are conveniently handled by expressing γ^{IJ} in terms of the downstairs metric components γ_{ij} and γ_{ww} which are the fields we evolve numerically. We know the metric takes the

following form:

$$\gamma_{IJ} = \left(\begin{array}{cccc|cccc} \gamma_{x^1 x^1} & \cdots & \gamma_{x^1 x^{d-1}} & \gamma_{x^1 z} & 0 & 0 & \cdots & 0 \\ \vdots & \ddots & \vdots & \vdots & \vdots & \vdots & \cdots & \vdots \\ \gamma_{x^{d-1} x^1} & \cdots & \gamma_{x^{d-1} x^{d-1}} & \gamma_{x^{d-1} z} & 0 & 0 & \cdots & 0 \\ \gamma_{z x^1} & \cdots & \gamma_{z x^{d-1}} & \gamma_{zz} & 0 & 0 & \cdots & 0 \\ \hline 0 & \cdots & 0 & 0 & \gamma_{ww} & 0 & \cdots & 0 \\ 0 & \cdots & 0 & 0 & 0 & \gamma_{ww} & \cdots & 0 \\ \vdots & \cdots & \vdots & \vdots & \vdots & \vdots & \ddots & \vdots \\ 0 & \cdots & 0 & 0 & 0 & 0 & \cdots & \gamma_{ww} \end{array} \right) , \tag{B.7}$$

and we shall denote the upper left quadrant by the matrix M_{ij}. Again, we will use the index $\hat{i}$ to denote $x^{\hat{i}}$ in this section, so e.g. cofactors $C_{12} = C_{x^1 x^2}$ and $C_{1z} = C_{x^1 z}$. Similarly the indices i, j, ... will stand for the x^i, i.e. include the z component.

We can now write the cofactor of an element in the top left quadrant of γ_{IJ} as

$$C_{ij} = (-1)^{i+j} \gamma_{ww}^{\eta} \det(M_{kl\{k \neq j, l \neq i\}}), \tag{B.8}$$

where $\eta = D - d - 1$ and the notation $\det(M_{kl\{k \neq j, l \neq i\}})$ denotes the determinant of the matrix M_{kl} obtained by crossing out the jth row and i^{th} column. Likewise, we may add further inequalities inside the braces to denote matrices obtained by crossing out more than one row and column. Note that here, in contrast to Appendix A, C_{ij} denotes the cofactor of the element γ_{ij}, not $\tilde{\gamma}_{ij}$. We can then use this expression for C_{ij} and the determinant of the right hand side of Eq. (B.7),

$$\begin{aligned} \det \gamma_{IJ} &= \gamma_{ww}^{\eta} \det \gamma_{ij} \\ &\overset{*}{=} \gamma_{ww}^{\eta} \gamma_{zz} \det(M_{kl\{k \neq z, l \neq z\}}) \,, \end{aligned} \tag{B.9}$$

in order to obtain expressions for inverse metric components according to

$$\gamma^{ij} = \frac{C_{ij}}{\det \gamma_{IJ}} \,. \tag{B.10}$$

For $d = 3$, this procedure starts from the spatial metric

$$\gamma_{IJ} = \left(\begin{array}{ccc|cccc} \gamma_{xx} & \gamma_{xy} & \gamma_{xz} & 0 & \cdots & 0 \\ \gamma_{yx} & \gamma_{yy} & \gamma_{yz} & 0 & \cdots & 0 \\ \gamma_{zx} & \gamma_{zy} & \gamma_{zz} & 0 & \cdots & 0 \\ \hline 0 & 0 & 0 & \gamma_{ww} & \cdots & 0 \\ \vdots & \vdots & \vdots & \vdots & \ddots & \vdots \\ 0 & 0 & 0 & 0 & \cdots & \gamma_{ww} \end{array} \right). \tag{B.11}$$

The components C_{ij} of the cofactor matrix (which is symmetric) are given by

$$C_{xx} = \gamma_{ww}^{\eta}(\gamma_{yy}\gamma_{zz} - \gamma_{yz}^2), \quad C_{xy} = -\gamma_{ww}^{\eta}(\gamma_{yx}\gamma_{zz} - \gamma_{zx}\gamma_{yz}), \quad C_{xz} = \gamma_{ww}^{\eta}(\gamma_{yx}\gamma_{zy} - \gamma_{zx}\gamma_{yy}),$$

$$\cdots \qquad\qquad C_{yy} = \gamma_{ww}^{\eta}(\gamma_{xx}\gamma_{zz} - \gamma_{zx}^2), \qquad\qquad C_{yz} = -\gamma_{ww}^{\eta}(\gamma_{xx}\gamma_{zy} - \gamma_{zx}\gamma_{xy}),$$

$$\cdots \qquad\qquad \cdots \qquad\qquad C_{zz} = \gamma_{ww}^{\eta}(\gamma_{xx}\gamma_{yy} - \gamma_{xy}^2),$$

$$\tag{B.12}$$

the determinant becomes

$$\det \gamma_{IJ} = \gamma_{ww}^{\eta}\left(\gamma_{xx}\gamma_{yy}\gamma_{zz} + 2\gamma_{xy}\gamma_{xz}\gamma_{yz} - \gamma_{xx}\gamma_{yz}^2 - \gamma_{yy}\gamma_{xz}^2 - \gamma_{zz}\gamma_{xy}^2\right)$$

$$\stackrel{*}{=} \gamma_{ww}^{\eta}\gamma_{zz}\left(\gamma_{xx}\gamma_{yy} - \gamma_{xy}^2\right), \tag{B.13}$$

and the inverse metric follows by inserting these into Eq. (B.10).

Using these techniques, we can regularise all terms in Eqs. (4.15), (4.16), (4.19), (4.25) and (4.33) that contain divisions by z. It turns out to be convenient to combine the individual terms into the following six expressions.

(1)

$$\frac{\delta_z^i - \gamma^{zi}\gamma_{ww}}{z}$$

We express γ^{zi} in terms of the metric, and trade divisions by z for derivatives ∂_z

and obtain

$$\frac{\delta_z^i - \gamma^{zi}\gamma_{ww}}{z} \overset{*}{=} \begin{cases} \sum_{\hat{j}=1}^{d-1} (-1)^{\hat{i}+\hat{j}} \dfrac{\gamma_{ww}}{\det M_{mn}} \partial_z\gamma_{z\hat{j}} \det(M_{kl\{k\neq\hat{i},k\neq z,l\neq z,l\neq\hat{j}\}}) & \text{if } i = \hat{i} \\[12pt] 0 & \text{if } i = z \end{cases}$$

(B.14)

For the $d = 3$ case this reduces to

$$\frac{\delta_z^i - \gamma^{zi}\gamma_{ww}}{z} \overset{*}{=} \begin{cases} \dfrac{\gamma_{yy}\partial_z\gamma_{xz} - \gamma_{xy}\partial_z\gamma_{yz}}{\gamma_{xx}\gamma_{yy} - \gamma_{xy}^2} & \text{if } i = x \\[12pt] \dfrac{\gamma_{xx}\partial_z\gamma_{yz} - \gamma_{xy}\partial_z\gamma_{xz}}{\gamma_{xx}\gamma_{yy} - \gamma_{xy}^2} & \text{if } i = y \\[12pt] 0 & \text{if } i = z \end{cases} \quad .$$

(B.15)

(2)

$$\frac{\partial_i\gamma_{jz} - \delta_{jz}\partial_i\gamma_{ww}}{z} - \delta_{iz}\frac{\gamma_{jz} - \delta_{jz}\gamma_{ww}}{z^2} + \frac{\partial_j\gamma_{iz} - \delta_{iz}\partial_j\gamma_{ww}}{z} - \delta_{jz}\frac{\gamma_{iz} - \delta_{iz}\gamma_{ww}}{z^2}$$

Here we simply trade divisions by z for ∂_z and obtain

$$\frac{\partial_i\gamma_{jz} - \delta_{jz}\partial_i\gamma_{ww}}{z} - \delta_{iz}\frac{\gamma_{jz} - \delta_{jz}\gamma_{ww}}{z^2} + \frac{\partial_j\gamma_{iz} - \delta_{iz}\partial_j\gamma_{ww}}{z} - \delta_{jz}\frac{\gamma_{iz} - \delta_{iz}\gamma_{ww}}{z^2}$$

$$\overset{*}{=} \begin{cases} 2\partial_z\partial_{(\hat{i}}\gamma_{\hat{j})z} & \text{if } i = \hat{i},\ j = \hat{j} \\[10pt] 0 & \text{if } (i,j) = (\hat{i}, z) \text{ or } (z, \hat{j}) \\[10pt] \partial_z\partial_z(\gamma_{zz} - \gamma_{ww}) & \text{if } i = j = z \end{cases} \quad .$$

(B.16)

(3)

$$-\frac{1}{2}\frac{\partial_z\gamma_{ij}}{z} + \frac{\delta_{z(i}\gamma_{j)z} - \delta_{iz}\delta_{jz}\gamma_{ww}}{z^2}$$

We use $\gamma_{zz} - \gamma_{ww} \stackrel{*}{=} \mathcal{O}(z^2)$ and trade a division by z for a z derivative. The result is

$$-\frac{1}{2}\frac{\partial_z \gamma_{ij}}{z} + \frac{\delta_{z(i}\gamma_{j)z} - \delta_{iz}\delta_{jz}\gamma_{ww}}{z^2} \stackrel{*}{=} \begin{cases} -\frac{1}{2}\partial_z\partial_z\gamma_{\hat{i}\hat{j}} & \text{if } i = \hat{i}, \ j = \hat{j} \\ 0 & \text{if } (i,j) = (\hat{i}, z) \text{ or } (z, \hat{j}) \\ -\frac{1}{2}\partial_z\partial_z\gamma_{ww} & \text{if } i = j = z \end{cases}.$$

$$\text{(B.17)}$$

(4)

$$\frac{\gamma_{ww}\gamma^{zj}\partial_j\gamma_{ww}}{z}$$

Using Eqs. (B.7)-(B.10), we express the inverse metric components γ^{zj} in terms of the downstairs metric and trade the division by z for a z derivative. We thus obtain

$$\frac{\gamma_{ww}\gamma^{zj}\partial_j\gamma_{ww}}{z} \stackrel{*}{=} \sum_{\hat{j}=1}^{d-1}\sum_{\hat{m}=1}^{d-1}(-1)^{\hat{m}+\hat{j}-1}\frac{\gamma_{ww}}{\det(M_{pq})}\partial_{\hat{j}}\gamma_{ww}\partial_z\gamma_{z\hat{m}}\det(M_{kl\{k\neq\hat{j},k\neq z, l\neq z, l\neq\hat{m}\}})$$
$$+ \frac{\gamma_{ww}\det(M_{kl\{k\neq z, l\neq z\}})}{\det(M_{pq})}\partial_z\partial_z\gamma_{ww}. \tag{B.18}$$

which in the case $d = 3$ reduces to

$$\frac{\gamma_{ww}\gamma^{zj}\partial_j\gamma_{ww}}{z} \stackrel{*}{=} \frac{(\gamma_{yx}\partial_z\gamma_{zy} - \gamma_{yy}\partial_z\gamma_{zx})\partial_x\gamma_{ww} + (\gamma_{yx}\partial_z\gamma_{zx} - \gamma_{xx}\partial_z\gamma_{yz})\partial_y\gamma_{ww}}{\gamma_{xx}\gamma_{yy} - \gamma_{xy}^2}$$
$$+ \partial_z\partial_z\gamma_{ww}. \tag{B.19}$$

(5)

$$\frac{\gamma^{zz}\gamma_{ww}^2 - \gamma_{ww}}{z^2}$$

The regularisation of this term proceeds in analogy to that of term (9) in Appendix A.2, except we do not set $\det\gamma = 1$. By rewriting $1 = \gamma^{zz}/\gamma^{zz} = \gamma^{zz}\det\gamma_{IJ}/C_{zz}$,

trading divisions by z for z derivatives and using $\gamma_{zz} \overset{*}{=} \gamma_{ww} + \mathcal{O}(z^2)$, we obtain

$$
\frac{\gamma^{zz}\gamma_{ww}^2 - \gamma_{ww}}{z^2} \overset{*}{=} \frac{1}{2}\partial_z\partial_z(\gamma_{ww} - \gamma_{zz})
$$
$$
- \frac{\sum_{\hat{i}=1}^{d-1}\sum_{\hat{m}=1}^{d-1}(-1)^{\hat{i}+\hat{m}-1}\partial_z\gamma_{z\hat{i}}\partial_z\gamma_{z\hat{m}}\det(M_{kl\{k\neq\hat{i},k\neq z,l\neq z,l\neq\hat{m}\}})}{\det(M_{kl\{k\neq z,l\neq z\}})} ,
$$
$$\tag{B.20}$$

which in the case $d = 3$ reduces to

$$
\frac{\gamma^{zz}\gamma_{ww}^2 - \gamma_{ww}}{z^2} \overset{*}{=} \frac{1}{2}\partial_z\partial_z(\gamma_{ww} - \gamma_{zz})
$$
$$
+ \frac{-2\gamma_{xy}\partial_z\gamma_{xz}\partial_z\gamma_{yz} + \gamma_{xx}(\partial_z\gamma_{yz})^2 + \gamma_{yy}(\partial_z\gamma_{xz})^2}{\gamma_{xx}\gamma_{yy} - \gamma_{xy}^2} .
$$
$$\tag{B.21}$$

(6)

$$
\frac{K_{iz} - \delta_{iz}K_{ww}}{z}
$$

The division by z is again traded for a derivative if $i \neq z$ and for $i = z$, we use $K_{zz} = K_{ww} + \mathcal{O}(z^2)$, so that

$$
\frac{K_{iz} - \delta_{iz}K_{ww}}{z} \overset{*}{=}
\begin{cases}
\partial_z K_{\hat{i}z} & \text{if } i = \hat{i} \\
\\
0 & \text{if } i = z
\end{cases} .
$$
$$\tag{B.22}$$

B.2 Normalisation of the spatial normal frame vectors

In this section, we discuss how the set of spatial normal frame vectors, Eq. (4.42), can be recast in a form suitable for applying Gram-Schmidt orthonormalisation. It turns out to be convenient to first rescale the $\tilde{m}_{(\alpha)}$ such that they would acquire unit length in a flat spacetime with spatial metric δ_{IJ}. Denoting these rescaled vectors with a caret,

we have

$$
\hat{m}_{(\alpha)} = \frac{1}{\sqrt{\left(\sum\limits_{s=\alpha}^{D-1} w_s^2\right)\left(\sum\limits_{s=\alpha-1}^{D-1} w_s^2\right)}}
\begin{pmatrix}
\left.\begin{matrix} 0 \\ \vdots \\ 0 \end{matrix}\right\} (\alpha-2)\times \\
-\sum_{s=\alpha}^{D-1}(w^s)^2 \\
\left.\begin{matrix} w^{\alpha-1}w^\alpha \\ \vdots \\ w^{\alpha-1}w^{D-2} \\ w^{\alpha-1}w^{D-1} \end{matrix}\right\} (D-\alpha)\times
\end{pmatrix}
, \quad \alpha = 2, \ldots, D-1 .
$$

(B.23)

Recall that we formally set $w^1 \equiv x^1, \ldots, w^{d-1} \equiv x^{d-1}, w^d \equiv z$. As a convenient shorthand, we define

$$
\rho_I^2 \equiv \sum_{s=I}^{D-1}(w^s)^2 ,
$$

(B.24)

so that, for instance, $\rho_1^2 = r^2$, $\rho_4^2 = (w^4)^2 + \ldots + (w^{D-1})^2$, $\rho_{D-1} = w^{D-1}$. This definition allows us to write

$$
\hat{m}_{(\alpha)}^I = \frac{1}{\rho_\alpha \, \rho_{\alpha-1}}
\begin{pmatrix}
\left.\begin{matrix} 0 \\ \vdots \\ 0 \end{matrix}\right\} (\alpha-2)\times \\
-\rho_\alpha^2 \\
\left.\begin{matrix} w^{\alpha-1}w^\alpha \\ \vdots \\ w^{\alpha-1}w^{D-2} \\ w^{\alpha-1}w^{D-1} \end{matrix}\right\} (D-\alpha)\times
\end{pmatrix} .
$$

(B.25)

We can now express the angles ϕ^α in terms of the radial variables ρ_I,

$$
\sin \phi^\alpha = \frac{\rho_\alpha}{\rho_{\alpha-1}} , \qquad \cos \phi^\alpha = \frac{w^{\alpha-1}}{\rho_{\alpha-1}} .
$$

(B.26)

Using these relations in (B.25), we obtain

$$
\hat{m}^I_{(\alpha)} =
\begin{pmatrix}
\left.\begin{matrix} 0 \\ \vdots \\ 0 \end{matrix}\right\}(\alpha-2)\times \\
-\sin\phi^\alpha \\
\cos\phi^\alpha\,\cos\phi^{\alpha+1} \\
\cos\phi^\alpha\,\sin\phi^{\alpha+1}\,\cos\phi^{\alpha+2} \\
\vdots \\
\cos\phi^\alpha\,\sin\phi^{\alpha+1}\,\ldots\,\sin\phi^{D-2}\,\cos\phi^{D-1} \\
\cos\phi^\alpha\,\sin\phi^{\alpha+1}\,\ldots\,\sin\phi^{D-2}\,\sin\phi^{D-1}
\end{pmatrix}
=
\begin{pmatrix}
\left.\begin{matrix} 0 \\ \vdots \\ 0 \end{matrix}\right\}(\alpha-2)\times \\
-\sin\phi^\alpha \\
\vdots \\
\cos\phi^\alpha\left(\displaystyle\prod_{s=\alpha+1}^{\alpha+n-1}\sin\phi^s\right)\cos\phi^{\alpha+n} \\
\vdots
\end{pmatrix},
\tag{B.27}
$$

where $n = 1, \ldots, D - \alpha$, and we formally set $\cos\phi^{D-1} \equiv 1$ and $\prod_{s=\alpha+1}^{\alpha}\sin\phi^\alpha \equiv 1$.

Now, in our computational domain $\rho^2_{d+1} = 0$, which, from the definition of our coordinate system in Eq. (2.4) gives

$$
r^2 \sin^2\phi^2 \ldots \sin^2\phi^{d+1} = 0
\tag{B.28}
$$

Since $\phi^2, \ldots, \phi^d$ are arbitrary in our computational domain, we must have either $\phi^{d+1} = 0$ or π. Without loss of generality, we choose $\phi^{d+1} = 0$, which fixes the $d - 1$ vectors

$$
\hat{m}_{(2)} = (-\sin\phi^2,\ \cos\phi^2\,\cos\phi^3,\ \ldots,\ \cos\phi^2\prod_{s=3}^{d}\sin(\phi^s),\ \underbrace{0,\ \ldots,\ 0}_{(D-d-1)\times}).
\tag{B.29}
$$

$$
\vdots
$$

$$
\hat{m}_{(\hat\alpha)} = (\underbrace{0,\ \ldots,\ 0}_{(\hat\alpha-2)\times},\ -\sin\phi^{\hat\alpha},\ \cos\phi^{\hat\alpha}\,\cos\phi^{\hat\alpha+1},\ \ldots,\ \cos\phi^{\hat\alpha}\prod_{s=\hat\alpha+1}^{d}(\sin\phi^s),\ \underbrace{0,\ \ldots,\ 0}_{(D-d-1)\times})
\tag{B.30}
$$

$$
\vdots
$$

$$
\hat{m}_{(d)} = (\underbrace{0,\ \ldots,\ 0}_{(d-2)\times},\ -\sin\phi^d,\ \cos\phi^d,\ \underbrace{0,\ \ldots,\ 0}_{(D-d-1)\times}),
\tag{B.31}
$$

which, up to rescaling by $\rho_{\hat\alpha}\rho_{\hat\alpha-1}$, are equal to the vectors in Eqs. (4.44)-(4.46). For the remaining vectors, we can use the rotational freedom in the angles $\phi^{d+2}, \ldots, \phi^{D-1}$.

Any choice for these values will satisfy $w^{d+1} = \ldots = w^{D-1} = 0$ as required on our computational domain and we merely need to ensure that we choose these angles such that the resulting set of vectors is orthogonal. This is most conveniently achieved by setting

$$\phi^{d+2} = \ldots = \phi^{D-1} = 0\,, \tag{B.32}$$

which, inserted into Eq. (B.27), implies

$$\hat{m}^I_{(a)} = \delta^I_a, \qquad a = d+1, \ldots, D-1. \tag{B.33}$$

Combined with Eqs. (B.29)-(B.31) and restoring the tilde in place of the caret on the $\tilde{m}_{(a)}$, we have recovered Eqs. (4.47)-(4.48) in Section 4.3.2 for the angular vectors. For the case $d = 3$ we have just two non-trivial vectors:

$$\hat{m}_{(2)} = (-\sin\phi^2,\ \cos\phi^2\cos\phi^3,\ \cos\phi^2\sin\phi^3,\ \underbrace{0,\ \ldots,\ 0}_{(D-4)\times})\,, \tag{B.34}$$

$$\hat{m}_{(3)} = (0,\ -\sin\phi^3,\ \cos\phi^3,\ \underbrace{0,\ \ldots,\ 0}_{(D-4)\times})\,, \tag{B.35}$$

recovering Eqs. (4.50)-(4.54).

Appendix C

Angular Momentum Wave Extraction - Appendix

C.1 Calculation of the Killing vector φ

We present here the calculation to put the Killing vector φ^α, defined in Eq. (8.8), into spherical coordinates ϕ^α, given in Eq. (2.4), from its definition in terms of the new spherical coordinates ψ^α, defined in Eq. (8.7). By the chain rule,

$$\frac{\partial}{\partial \psi^{D-1}} = \frac{\partial \phi^\alpha}{\partial \psi^{D-1}} \frac{\partial}{\partial \phi^\alpha}, \tag{C.1}$$

so we must calculate all of the terms $\partial \phi^\alpha / \partial \psi^{D-1}$. We will deal with the case for ϕ_2 and ϕ_3 first, and then all of the other terms at once.

ϕ_2

We differentiate the expression for x with respect to ψ^{D-1} in both (ϕ and ψ) coordinate systems and set these equal to each other,

$$
\begin{aligned}
-\sin(\phi_2)\frac{\partial \phi_2}{\partial \psi_{D-1}} &= \sin\psi_2 \sin\psi_3 \ldots \sin\psi_{D-2} \cos\psi_{D-1}, \\
\implies \frac{\partial \phi_2}{\partial \psi_{D-1}} &= -\frac{y}{r\sin\phi_2} \\
&= -\cos\phi_3.
\end{aligned}
\tag{C.2}
$$

ϕ_3

We differentiate the 2 expressions for y with respect to ψ^{D-1} and set these equal to each other,

$$
\begin{aligned}
-\sin\phi_2 \sin\phi_3 \frac{\partial\phi_3}{\partial\psi_{D-1}} + \cos\phi_2 \cos\phi_3 \frac{\partial\phi_2}{\partial\psi_{D-1}} &= -\sin\psi_2 \ldots \sin\psi_{D-2} \sin\psi_{D-1} \\
&= -\frac{x}{r}, \\
\implies \frac{\partial\phi_3}{\partial\psi_{D-1}} &= \cot\phi_2 \sin\phi_3. \quad\quad (C.3)
\end{aligned}
$$

ϕ_a

To calculate $\frac{\partial\phi_a}{\partial\psi_{D-1}}$ we differentiate the two expressions for w^{a-1} and set them equal to each other. Note that for all values of a the expression for w^{a-1} in terms of the ψ coordinate system does not depend on ψ_{D-1}, and so this derivative is 0.

$$
\begin{aligned}
0 &= \frac{\partial}{\partial\psi_{D-1}}(w^{a-1}(\phi^\alpha)) \\
&= -\frac{\partial\phi_a}{\partial\psi_{D-1}} \prod_{\beta=2}^{a} \sin\phi_\beta + \cos\phi_a \sum_{\gamma=2}^{a-1} \frac{\partial\phi_\gamma}{\partial\psi_{D-1}} \cos\phi_\gamma \prod_{\beta=2,\beta\neq\gamma}^{a-1} \sin\phi_\beta, \\
\implies \frac{\partial\phi_a}{\partial\psi_{D-1}} &= \cos\phi_a \sum_{\gamma=2}^{a-1} \frac{\partial\phi_\gamma}{\partial\psi_{D-1}} \cot\phi_\gamma. \quad\quad (C.4)
\end{aligned}
$$

Here we see that each of these partial derivatives depends on all of the previously calculated derivatives. Let us use this formula to calculate the first, $a = 4$, term.

$$
\begin{aligned}
\frac{\partial\phi_4}{\partial\psi_{D-1}} &= \cos\phi_4 \sum_{\gamma=2}^{3} \frac{\partial\phi_\gamma}{\partial\psi_{D-1}} \cot\phi_\gamma \\
&= \cos\phi_4(-\cot\phi_2 \cos\phi_3 + \cot\phi_3 \cot\phi_2 \sin\phi_3) = 0. \quad\quad (C.5)
\end{aligned}
$$

As this term is 0, so are all further terms for $a > 4$. So the Killing vector is, in spherical, ϕ, coordinates,

$$
\varphi^\alpha = (-\cos\phi_3, \cot\phi_2 \sin\phi_3, 0, \ldots, 0). \quad\quad (C.6)
$$

C.2   Calculation of Bondi angular momentum

We present here the explicit calculation of the Bondi angular momentum in higher dimensions, given in Eq. (8.1). Let us first introduce the following notation. $H(\alpha)$ is the Heaviside step function defined such that $H(\alpha) = 1$ if $\alpha \geq 0$, and 0 otherwise. We also define the notation $\bar{\Omega}_{\alpha\beta} := \int \Omega'_{\alpha\beta} du$, and $\bar{\bar{\Omega}}_{\alpha\beta} := \int \int \Omega'_{\alpha\beta} d\hat{u} du$. For brevity we will denote specific components of $\Omega'_{(\alpha)(\beta)}$, e.g. $\Omega'_{(2)(3)}$, as Ω'_{23}. Finally, let us formally set

$$\prod_{\alpha=2}^{1} f_\alpha = 1, \tag{C.7}$$

for any function f. We will calculate the three terms in Eq. (8.1) separately, dividing each into terms involving partial derivatives, and terms involving Christoffel symbols. As mentioned in the main text, we will set the index α to 2 or 3 only, due to the contraction with the Killing vector φ^α given by Eq. (8.9).

C.2.1   Term 1: $\dot{h}_{\alpha\beta} \mathcal{D}_\gamma h^{\beta\gamma}$

Since we can take a factor of the round metric, $\omega_{\alpha\beta}$, out of the covariant derivative, since it is metric compatible, we can take it out of the partial derivative too, as long as we also take it out of the Christoffel symbols.

A brief calculation, using the results for the derivatives of the Bondi news in Eq. (8.20) gives the partial derivative terms,

$$\omega^{\gamma\sigma} \omega^{\beta\rho} \dot{h}_{\alpha\beta} \partial_\gamma h_{\rho\sigma} = 4r^{D-2} \prod_{\mu=2}^{\sigma-1} (\csc \phi_\mu) \bar{\Omega}_{\alpha\rho} \prod_{\zeta=2}^{\alpha-1} (\sin \phi_\zeta) \left(\cot \phi_\sigma \bar{\bar{\Omega}}_{\rho\sigma} H(\rho - \sigma - 1) + \partial_\sigma \bar{\bar{\Omega}}_{\rho\sigma} \right).$$

$$\tag{C.8}$$

For $\alpha = 2$,

$$\begin{aligned}
\omega^{\gamma\sigma} \omega^{\beta\rho} \dot{h}_{2\beta} \partial_\gamma h_{\rho\sigma} = {} & 4r^{D-2} (\bar{\Omega}_{22} \partial_2 \bar{\bar{\Omega}}_{22} + \csc \phi_2 \bar{\Omega}_{22} \partial_3 \bar{\bar{\Omega}}_{23} + \bar{\Omega}_{23} \cot \phi_2 \bar{\bar{\Omega}}_{23} + \bar{\Omega}_{23} \partial_2 \bar{\bar{\Omega}}_{23} \\
& + \csc \phi_2 \bar{\Omega}_{23} \partial_3 \bar{\bar{\Omega}}_{33}).
\end{aligned}$$

$$\tag{C.9}$$

For $\alpha = 3$,

$$
\begin{aligned}
\omega^{\gamma\sigma}\omega^{\beta\rho}\dot{h}_{3\beta}\partial_\gamma h_{\rho\sigma} &= 4r^{D-2}(\bar{\Omega}_{23}\sin\phi_2\partial_2\bar{\bar{\Omega}}_{22} + \bar{\Omega}_{23}\partial_3\bar{\bar{\Omega}}_{23} \\
&\quad + \bar{\Omega}_{33}\sin\phi_2(\cot\phi_2\bar{\bar{\Omega}}_{23} + \partial_2\bar{\bar{\Omega}}_{23}) + \bar{\Omega}_{33}\partial_3\bar{\bar{\Omega}}_{33}).
\end{aligned} \tag{C.10}
$$

We now calculate the Christoffel symbol terms, noting that, for brevity, terms such as $\Gamma^\lambda_{\sigma\rho}\delta^{\sigma\rho}$ have been written as $\Gamma^\lambda_{\sigma\sigma}$.

$$
\begin{aligned}
-\dot{h}_{\alpha\beta}\omega^{\gamma\sigma}\omega^{\beta\rho}\left(\Gamma^\lambda_{\gamma\rho}h_{\lambda\sigma} + \Gamma^\lambda_{\gamma\sigma}h_{\rho\lambda}\right) &= -4r^{D-2}\prod_{\mu=2}^{\sigma-1}(\csc^2\phi_\mu)\prod_{\nu=2}^{\rho-1}(\csc\phi_\nu)\bar{\Omega}_{\alpha\rho}\prod_{\zeta=2}^{\alpha-1}(\sin\phi_\zeta) \\
&\quad \left(\Gamma^\lambda_{\sigma\rho}\bar{\bar{\Omega}}_{\lambda\sigma}\prod_{\epsilon=2}^{\lambda-1}(\sin\phi_\epsilon)\prod_{\eta=2}^{\sigma-1}(\sin\phi_\eta) \right. \\
&\quad \left. + \Gamma^\lambda_{\sigma\sigma}\bar{\bar{\Omega}}_{\rho\lambda}\prod_{\epsilon=2}^{\rho-1}(\sin\phi_\epsilon)\prod_{\eta=2}^{\lambda-1}(\sin\phi_\eta)\right).
\end{aligned} \tag{C.11}
$$

We now take the two terms in parentheses separately. Take the first term and set $\alpha = 2$, then

$$
\begin{aligned}
-\dot{h}_{2\beta}\omega^{\gamma\sigma}\omega^{\beta\rho}\left(\Gamma^\lambda_{\gamma\rho}h_{\lambda\sigma}\right) &= -4r^{D-2}\prod_{\mu=2}^{\sigma-1}(\csc\phi_\mu)\prod_{\nu=2}^{\rho-1}(\csc\phi_\nu)\bar{\Omega}_{2\rho}\Gamma^\lambda_{\sigma\rho}\bar{\bar{\Omega}}_{\lambda\sigma}\prod_{\epsilon=2}^{\lambda-1}(\sin\phi_\epsilon) \\
&= -4r^{D-2}\left(\bar{\Omega}_{22}\cot\phi_2(\bar{\bar{\Omega}}_{33} + (D-4)\bar{\bar{\Omega}}_{ww}) \right. \\
&\quad \left. + (D-4)\bar{\Omega}_{23}\csc\phi_2\cot\phi_3\bar{\bar{\Omega}}_{ww}\right).
\end{aligned} \tag{C.12}
$$

For $\alpha = 3$ the expression is very similar, simply multiply by $\sin\phi_2$ and exchange the first index on every $\bar{\Omega}_{2\beta}$ for a 3. So for $\alpha = 3$, we have

$$
\begin{aligned}
-\dot{h}_{3\beta}\omega^{\gamma\sigma}\omega^{\beta\rho}\left(\Gamma^\lambda_{\gamma\rho}h_{\lambda\sigma}\right) &= -4r^{D-2}\left(\bar{\Omega}_{23}\cos\phi_2(\bar{\bar{\Omega}}_{33} + (D-4)\bar{\bar{\Omega}}_{ww}) \right. \\
&\quad \left. + (D-4)\bar{\Omega}_{33}\cot\phi_3\bar{\bar{\Omega}}_{ww}\right).
\end{aligned} \tag{C.13}
$$

We now calculate the second term in parentheses in Eq. (C.11) for $\alpha = 2$,

$$-\dot{h}_{2\beta}\omega^{\gamma\sigma}\omega^{\beta\rho}\left(\Gamma^\lambda_{\gamma\sigma}h_{\rho\lambda}\right) \quad = \quad -4r^{D-2}\prod_{\mu=2}^{\sigma-1}(\csc^2\phi_\mu)\bar{\Omega}_{2\rho}\Gamma^\lambda_{\sigma\sigma}\bar{\bar{\Omega}}_{\rho\lambda}\prod_{\eta=2}^{\lambda-1}(\sin\phi_\eta). \quad (C.14)$$

We note here that, following a brief calculation,

$$\Gamma^2_{\sigma\sigma}\prod_{\mu=2}^{\sigma-1}(\csc^2\phi_\mu) = -(D-3)\cot\phi_2,$$

$$\Gamma^3_{\sigma\sigma}\prod_{\mu=2}^{\sigma-1}(\csc^2\phi_\mu) = -(D-4)\cot\phi_3\csc^2\phi_2, \quad\quad (C.15)$$

hence,

$$-\dot{h}_{2\beta}\omega^{\gamma\sigma}\omega^{\beta\rho}\left(\Gamma^\lambda_{\gamma\sigma}h_{\rho\lambda}\right) \quad = \quad 4r^{D-2}\bigg((\bar{\Omega}_{22}\bar{\bar{\Omega}}_{22}+\bar{\Omega}_{23}\bar{\bar{\Omega}}_{23})\cot\phi_2(D-3)$$

$$+(\bar{\Omega}_{22}\bar{\bar{\Omega}}_{23}+\bar{\Omega}_{23}\bar{\bar{\Omega}}_{33})\csc\phi_2\cot\phi_3(D-4)\bigg). \quad (C.16)$$

For this term the same transformation as above can be used to get to $\alpha=3$, that is multiply by $\sin\phi_2$ and send $\bar{\Omega}_{2\beta}\to\bar{\Omega}_{3\beta}$. So for $\alpha=3$

$$-\dot{h}_{3\beta}\omega^{\gamma\sigma}\omega^{\beta\rho}\left(\Gamma^\lambda_{\gamma\sigma}h_{\rho\lambda}\right) \quad = \quad 4r^{D-2}\bigg((\bar{\Omega}_{23}\bar{\bar{\Omega}}_{22}+\bar{\Omega}_{33}\bar{\bar{\Omega}}_{23})\cos\phi_2(D-3)$$

$$+(\bar{\Omega}_{23}\bar{\bar{\Omega}}_{23}+\bar{\Omega}_{33}\bar{\bar{\Omega}}_{33})\cot\phi_3(D-4)\bigg). \quad\quad (C.17)$$

C.2.2   Term 2: $\mathcal{D}_\gamma h_{\alpha\beta}\dot{h}^{\beta\gamma}$

Let's first calculate the partial derivative terms,

$$\partial_\gamma h_{\alpha\beta}\dot{h}^{\beta\gamma} \quad = \quad 4r^{D-2}\prod_{\mu=2}^{\gamma-1}(\csc\phi_\mu)\delta_{\beta(\rho)}\delta_{\gamma(\sigma)}\bar{\Omega}_{(\rho)(\sigma)}\delta_{\alpha(\alpha)}\delta_{\beta(\beta)}\prod_{\zeta=2}^{\alpha-1}(\sin\phi_\zeta)$$

$$\bigg(\cot\phi_\gamma H(\alpha-\gamma-1)\bar{\bar{\Omega}}_{(\alpha)(\beta)}+\cot\phi_\gamma H(\beta-\gamma-1)\bar{\bar{\Omega}}_{(\alpha)(\beta)}$$

$$+\partial_\gamma\bar{\bar{\Omega}}_{(\alpha)(\beta)}\bigg). \quad\quad (C.18)$$

Now let us set $\alpha=2$,

$$
\begin{aligned}
\partial_\gamma h_{2\beta}\dot{h}^{\beta\gamma} &= 4r^{D-2}\prod_{\mu=2}^{\gamma-1}(\csc\phi_\mu)\bar{\Omega}_{\beta\gamma}\Bigg(\cot\phi_\gamma H(1-\gamma)\bar{\bar{\Omega}}_{2\beta} \\
&\quad + \cot\phi_\gamma H(\beta-\gamma-1)\bar{\bar{\Omega}}_{2\beta} + \partial_\gamma\bar{\bar{\Omega}}_{2\beta}\Bigg) \\
&= 4r^{D-2}\Big(\bar{\Omega}_{22}(\partial_2\bar{\bar{\Omega}}_{22}) + \csc\phi_2\bar{\Omega}_{23}\partial_3\bar{\bar{\Omega}}_{22} + \bar{\Omega}_{23}(\cot\phi_2\bar{\bar{\Omega}}_{23} + \partial_2\bar{\bar{\Omega}}_{23}) \\
&\quad + \csc\phi_2\bar{\Omega}_{33}\partial_3\bar{\bar{\Omega}}_{23}\Big).
\end{aligned}
\tag{C.19}
$$

If we set $\alpha = 3$ instead we find

$$
\begin{aligned}
\partial_\gamma h_{3\beta}\dot{h}^{\beta\gamma} &= 4r^{D-2}\Big(\cos\phi_2\left(\bar{\Omega}_{22}\bar{\bar{\Omega}}_{23} + 2\bar{\Omega}_{23}\bar{\bar{\Omega}}_{33}\right) + \bar{\Omega}_{22}\sin\phi_2\partial_2\bar{\bar{\Omega}}_{23} + \bar{\Omega}_{23}\partial_3\bar{\bar{\Omega}}_{23} \\
&\quad + \bar{\Omega}_{23}\sin\phi_2\partial_2\bar{\bar{\Omega}}_{33} + \bar{\Omega}_{33}\partial_3\bar{\bar{\Omega}}_{33}\Big).
\end{aligned}
\tag{C.20}
$$

We now calculate the terms involving Christoffel symbols.

$$
\begin{aligned}
-\dot{h}^{\beta\gamma}\left(\Gamma^\delta_{\gamma\alpha}h_{\delta\beta} + \Gamma^\delta_{\gamma\beta}h_{\alpha\delta}\right) &= -4r^{D-2}\delta^{\beta\rho}\delta^{\gamma\sigma}\prod_{\nu=2}^{\beta-1}(\csc^2\phi_\nu)\prod_{\mu=2}^{\gamma-1}(\csc^2\phi_\mu)\delta_{\rho(\alpha)}\delta_{\sigma(\beta)} \\
&\quad \prod_{\zeta=2}^{\rho-1}(\sin\phi_\zeta)\prod_{\xi=2}^{\sigma-1}(\sin\phi_\xi)\bar{\Omega}_{(\alpha)(\beta)} \\
&\quad \Bigg(\Gamma^\delta_{\gamma\alpha}\delta_{\delta(\gamma)}\delta_{\beta(\delta)}\prod_{\epsilon=2}^{\delta-1}(\sin\phi_\epsilon)\prod_{\eta=2}^{\beta-1}(\sin\phi_\eta)\bar{\Omega}_{(\gamma)(\delta)} \\
&\quad + \Gamma^\delta_{\gamma\beta}\delta_{\alpha(\rho)}\delta_{\delta(\sigma)}\prod_{\chi=2}^{\alpha-1}(\sin\phi_\chi)\prod_{\kappa=2}^{\delta-1}(\sin\phi_\kappa)\bar{\bar{\Omega}}_{(\rho)(\sigma)}\Bigg).
\end{aligned}
\tag{C.21}
$$

Now set $\alpha = 2$ again, and take the two terms summed in parentheses separately. The first term gives

$$
\begin{aligned}
-\dot{h}^{\beta\gamma}\left(\Gamma^\delta_{\gamma 2}h_{\delta\beta}\right) &= -4r^{D-2}\delta^{\beta\rho}\delta^{\gamma\sigma}\prod_{\nu=2}^{\beta-1}(\csc^2\phi_\nu)\prod_{\mu=2}^{\gamma-1}(\csc^2\phi_\mu)\delta_{\rho(\alpha)}\delta_{\sigma(\beta)}\prod_{\zeta=2}^{\rho-1}(\sin\phi_\zeta) \\
&\qquad \prod_{\xi=2}^{\sigma-1}(\sin\phi_\xi)\bar{\Omega}_{(\alpha)(\beta)}\left(\Gamma^\delta_{\gamma 2}\delta_{\delta(\gamma)}\delta_{\beta(\delta)}\prod_{\epsilon=2}^{\delta-1}(\sin\phi_\epsilon)\prod_{\eta=2}^{\beta-1}(\sin\phi_\eta)\bar{\bar{\Omega}}_{(\gamma)(\delta)}\right) \\
&= -4r^{D-2}\prod_{\mu=2}^{(\beta)-1}(\csc\phi_\mu)\bar{\Omega}_{(\alpha)(\beta)}\left(\Gamma^{(\gamma)}_{(\beta)2}\prod_{\epsilon=2}^{(\gamma)-1}(\sin\phi_\epsilon)\bar{\bar{\Omega}}_{(\gamma)(\alpha)}\right) \\
&= \begin{cases} -4r^{D-2}\prod_{\mu=2}^{(\beta)-1}(\csc\phi_\mu)\bar{\Omega}_{(\alpha)(\beta)}\left(\cot\phi_2\delta^{(\gamma)}_{(\beta)}\prod_{\epsilon=2}^{(\gamma)-1}(\sin\phi_\epsilon)\bar{\bar{\Omega}}_{(\gamma)(\alpha)}\right) & \text{if } (\gamma) > 2 \\ 0 \text{ if } (\gamma) = 2. \end{cases}
\end{aligned}
$$

$$(C.22)$$

Summing over (γ), we obtain

$$
\begin{aligned}
-\dot{h}^{\beta\gamma}\left(\Gamma^\delta_{\gamma 2}h_{\delta\beta}\right) &= -4r^{D-2}\cot\phi_2\bar{\Omega}_{(\alpha)(\gamma)}\bar{\bar{\Omega}}_{(\gamma)(\alpha)} \\
&= -4r^{D-2}\cot\phi_2(\bar{\Omega}_{23}\bar{\bar{\Omega}}_{23}+\bar{\Omega}_{33}\bar{\bar{\Omega}}_{33}+(D-4)\bar{\Omega}_{ww}\bar{\bar{\Omega}}_{ww}).
\end{aligned}
$$

$$(C.23)$$

The second term in parentheses in Eq. (C.21) (with $\alpha = 2$) gives

$$
\begin{aligned}
-\dot{h}^{\beta\gamma}\left(\Gamma^\delta_{\gamma\beta}h_{2\delta}\right) &= -4r^{D-2}\prod_{\nu=2}^{(\alpha)-1}(\csc\phi_\nu)\prod_{\mu=2}^{(\beta)-1}(\csc\phi_\mu)\bar{\Omega}_{(\alpha)(\beta)}\left(\Gamma^2_{(\beta)(\alpha)}\bar{\bar{\Omega}}_{22}+\Gamma^3_{(\beta)(\alpha)}\sin\phi_2\bar{\bar{\Omega}}_{23}\right) \\
&= -4r^{D-2}\left(2\cot\phi_2\bar{\Omega}_{23}\bar{\bar{\Omega}}_{23}-\cot\phi_2\bar{\Omega}_{33}\bar{\bar{\Omega}}_{22}-\cot\phi_2\bar{\bar{\Omega}}_{22}(D-4)\bar{\Omega}_{ww}\right. \\
&\qquad \left.-\csc\phi_2\cot\phi_3\bar{\bar{\Omega}}_{23}(D-4)\bar{\Omega}_{ww}\right).
\end{aligned}
$$

$$(C.24)$$

Let us now take these 2 terms again for $\alpha = 3$. The first term in parentheses from Eq. (C.21) is

$$
\begin{aligned}
-\dot{h}^{\beta\gamma}\left(\Gamma^{\delta}_{\gamma 3}h_{\delta\beta}\right) &= -4r^{D-2}\delta^{\beta\rho}\delta^{\gamma\sigma}\prod_{\nu=2}^{\beta-1}(\csc^2\phi_\nu)\prod_{\mu=2}^{\gamma-1}(\csc^2\phi_\mu)\delta_{\rho(\alpha)}\delta_{\sigma(\beta)}\prod_{\zeta=2}^{\rho-1}(\sin\phi_\zeta) \\
&\qquad \prod_{\xi=2}^{\sigma-1}(\sin\phi_\xi)\bar{\Omega}_{(\alpha)(\beta)}\left(\Gamma^{\delta}_{\gamma 3}\delta_{\delta(\gamma)}\delta_{\beta(\delta)}\prod_{\epsilon=2}^{\delta-1}(\sin\phi_\epsilon)\prod_{\eta=2}^{\beta-1}(\sin\phi_\eta)\bar{\bar{\Omega}}_{(\gamma)(\delta)}\right) \\
&= -4r^{D-2}\left(\cos\phi_2(\bar{\Omega}_{22}\bar{\bar{\Omega}}_{23} + \bar{\Omega}_{23}\bar{\bar{\Omega}}_{33} - \bar{\Omega}_{23}\bar{\bar{\Omega}}_{22} - \bar{\Omega}_{33}\bar{\bar{\Omega}}_{23}) \right. \\
&\qquad \left. + \cot\phi_3(D-4)\bar{\Omega}_{ww}\bar{\bar{\Omega}}_{ww}\right),
\end{aligned}
$$
$$(\text{C.25})$$

and the second term is

$$
\begin{aligned}
-\dot{h}^{\beta\gamma}\left(\Gamma^{\delta}_{\gamma\beta}h_{3\delta}\right) &= -4r^{D-2}\prod_{\nu=2}^{(\alpha)-1}(\csc\phi_\nu)\prod_{\mu=2}^{(\beta)-1}(\csc\phi_\mu)\bar{\Omega}_{(\alpha)(\beta)}\left(\Gamma^{\delta}_{(\beta)(\alpha)}\sin\phi_2\prod_{\kappa=2}^{\delta-1}(\sin\phi_\kappa)\bar{\bar{\Omega}}_{3\delta}\right) \\
&= -4r^{D-2}\left(\cos\phi_2(2\bar{\Omega}_{23}\bar{\bar{\Omega}}_{33} - \bar{\Omega}_{33}\bar{\bar{\Omega}}_{32}) \right. \\
&\qquad \left. -(D-4)\bar{\Omega}_{ww}(\cos\phi_2\bar{\bar{\Omega}}_{23} + \cot\phi_3\bar{\bar{\Omega}}_{33})\right).
\end{aligned}
$$
$$(\text{C.26})$$

C.2.3   Term 3: $\dot{h}^{\beta\gamma}\mathcal{D}_\alpha h_{\beta\gamma}$

Again, let us first calculate the partial derivatives.

$$
\omega^{\rho\beta}\omega^{\sigma\gamma}\dot{h}_{\rho\sigma}\partial_\alpha h_{\beta\gamma} = 4r^{D-2}\left(\bar{\Omega}_{\beta\gamma}\left(\cot\phi_\alpha\bar{\bar{\Omega}}_{\beta\gamma}(H(\beta-\alpha-1) + H(\gamma-\alpha-1)) + \partial_\alpha\bar{\bar{\Omega}}_{\beta\gamma}\right)\right).
$$
$$(\text{C.27})$$

For $\alpha = 2$ this becomes

$$
\begin{aligned}
\omega^{\rho\beta}\omega^{\sigma\gamma}\dot{h}_{\rho\sigma}\partial_2 h_{\beta\gamma} &= 4r^{D-2}\left(2\cot\phi_2(\bar{\Omega}_{23}\bar{\bar{\Omega}}_{23} + \bar{\Omega}_{33}\bar{\bar{\Omega}}_{33} + (D-4)\bar{\Omega}_{ww}\bar{\bar{\Omega}}_{ww}) \right. \\
&\qquad \left. +\bar{\Omega}_{22}\partial_2\bar{\bar{\Omega}}_{22} + 2\bar{\Omega}_{23}\partial_2\bar{\bar{\Omega}}_{23} + \bar{\Omega}_{33}\partial_2\bar{\bar{\Omega}}_{33} + (D-4)\bar{\Omega}_{ww}\partial_2\bar{\bar{\Omega}}_{ww}\right),
\end{aligned}
$$
$$(\text{C.28})$$

and for $\alpha = 3$

$$\omega^{\rho\beta}\omega^{\sigma\gamma}\dot{h}_{\rho\sigma}\partial_3 h_{\beta\gamma} = 4r^{D-2}\Big(2(D-4)\cot\phi_3\bar{\Omega}_{ww}\bar{\bar{\Omega}}_{ww} + \bar{\Omega}_{22}\partial_3\bar{\bar{\Omega}}_{22} + 2\bar{\Omega}_{23}\partial_3\bar{\bar{\Omega}}_{23}$$
$$+\bar{\Omega}_{33}\partial_3\bar{\bar{\Omega}}_{33} + (D-4)\bar{\Omega}_{ww}\partial_3\bar{\bar{\Omega}}_{ww}\Big). \tag{C.29}$$

Finally we calculate the Christoffel terms,

$$-\omega^{\rho\beta}\omega^{\sigma\gamma}\dot{h}_{\rho\sigma}(\Gamma^\lambda_{\alpha\beta}h_{\lambda\gamma} + \Gamma^\lambda_{\alpha\gamma}h_{\beta\lambda}). \tag{C.30}$$

We first notice by symmetry of interchanging indices, the two terms in parentheses are identical, so we calculate

$$-\omega^{\rho\beta}\omega^{\sigma\gamma}\dot{h}_{\rho\sigma}(2\Gamma^\lambda_{\alpha\beta}h_{\lambda\gamma}) = -8r^{D-2}\prod_{\mu=2}^{\beta-1}(\csc\phi_\mu)\prod_{\nu=2}^{\gamma-1}(\csc\phi_\nu)\bar{\Omega}_{\beta\gamma}\Gamma^\lambda_{\alpha\beta}\bar{\bar{\Omega}}_{\lambda\gamma}\prod_{\epsilon=2}^{\lambda-1}(\sin\phi_\epsilon)\prod_{\eta=2}^{\gamma-1}(\sin\phi_\eta)$$
$$= -8r^{D-2}\prod_{\mu=2}^{\beta-1}(\csc\phi_\mu)\bar{\Omega}_{\beta\gamma}\Gamma^\lambda_{\alpha\beta}\bar{\bar{\Omega}}_{\lambda\gamma}\prod_{\epsilon=2}^{\lambda-1}(\sin\phi_\epsilon). \tag{C.31}$$

Now let $\alpha = 2$

$$-\omega^{\rho\beta}\omega^{\sigma\gamma}\dot{h}_{\rho\sigma}(2\Gamma^\lambda_{2\beta}h_{\lambda\gamma}) = -8r^{D-2}\cot\phi_2(\bar{\Omega}_{23}\bar{\bar{\Omega}}_{23} + \bar{\Omega}_{33}\bar{\bar{\Omega}}_{33} + (D-4)\bar{\Omega}_{ww}\bar{\bar{\Omega}}_{ww}), \tag{C.32}$$

and for $\alpha = 3$,

$$-\omega^{\rho\beta}\omega^{\sigma\gamma}\dot{h}_{\rho\sigma}(2\Gamma^\lambda_{3\beta}h_{\lambda\gamma}) = -8r^{D-2}(\cos\phi_2(\bar{\Omega}_{22}\bar{\bar{\Omega}}_{23} + \bar{\Omega}_{23}\bar{\bar{\Omega}}_{33} - \bar{\Omega}_{23}\bar{\bar{\Omega}}_{22} - \bar{\Omega}_{33}\bar{\bar{\Omega}}_{23}) +$$
$$\cot\phi_3(D-4)\bar{\Omega}_{ww}\bar{\bar{\Omega}}_{ww}). \tag{C.33}$$

We now have the full $\alpha = 2$ and $\alpha = 3$ components, which we can then contract with the Killing vector. Thus the full expression for the rate of change of Bondi angular momentum is

$$
\begin{aligned}
\frac{d}{du} J^{Bondi}_{(p)} = \quad & \frac{r^{D-2}}{4\pi} \int_{S^{D-2}} d\Omega (-\cos\phi_3) \Big(2\bar{\Omega}_{22}\partial_2\bar{\bar{\Omega}}_{22} + 2\csc\phi_2\bar{\Omega}_{22}\partial_3\bar{\bar{\Omega}}_{23} + 2\bar{\Omega}_{23}\cot\phi_2\bar{\bar{\Omega}}_{23} \\
& +2\bar{\Omega}_{23}\partial_2\bar{\bar{\Omega}}_{23} + 2\csc\phi_2\bar{\Omega}_{23}\partial_3\bar{\bar{\Omega}}_{33} - \\
& 2\Big(\bar{\Omega}_{22}\cot\phi_2(\bar{\bar{\Omega}}_{33} + (D-4)\bar{\bar{\Omega}}_{ww}) + (D-4)\bar{\Omega}_{23}\csc\phi_2\cot\phi_3\bar{\bar{\Omega}}_{ww} \Big) + \\
& 2\Big((\bar{\Omega}_{22}\bar{\bar{\Omega}}_{22} + \bar{\Omega}_{23}\bar{\bar{\Omega}}_{23})\cot\phi_2(D-3) + (\bar{\Omega}_{22}\bar{\bar{\Omega}}_{23} + \bar{\Omega}_{23}\bar{\bar{\Omega}}_{33})\csc\phi_2\cot\phi_3(D-4) \Big) \\
& -\Big(\bar{\Omega}_{22}(\partial_2\bar{\bar{\Omega}}_{22}) + \csc\phi_2\bar{\Omega}_{23}\partial_3\bar{\bar{\Omega}}_{22} + \bar{\Omega}_{23}(\cot\phi_2\bar{\bar{\Omega}}_{23} + \partial_2\bar{\bar{\Omega}}_{23}) + \csc\phi_2\bar{\Omega}_{33}\partial_3\bar{\bar{\Omega}}_{23} \Big) \\
& + \cot\phi_2\Big(\bar{\Omega}_{23}\bar{\bar{\Omega}}_{23} + \bar{\Omega}_{33}\bar{\bar{\Omega}}_{33} + (D-4)\bar{\Omega}_{ww}\bar{\bar{\Omega}}_{ww} \Big) \\
& + \Big(2\cot\phi_2\bar{\Omega}_{23}\bar{\bar{\Omega}}_{23} - \cot\phi_2\bar{\Omega}_{33}\bar{\bar{\Omega}}_{22} - \cot\phi_2\bar{\bar{\Omega}}_{22}(D-4)\bar{\Omega}_{ww} - \\
& \csc\phi_2\cot\phi_3\bar{\bar{\Omega}}_{23}(D-4)\bar{\Omega}_{ww} \Big) \\
& +0.5\Big(2\cot\phi_2(\bar{\Omega}_{23}\bar{\bar{\Omega}}_{23} + \bar{\Omega}_{33}\bar{\bar{\Omega}}_{33} + (D-4)\bar{\Omega}_{ww}\bar{\bar{\Omega}}_{ww}) + \\
& \bar{\Omega}_{22}\partial_2\bar{\bar{\Omega}}_{22} + 2\bar{\Omega}_{23}\partial_2\bar{\bar{\Omega}}_{23} + \bar{\Omega}_{33}\partial_2\bar{\bar{\Omega}}_{33} + (D-4)\bar{\Omega}_{ww}\partial_2\bar{\bar{\Omega}}_{ww} \Big) \Big) \\
& +(\cot\phi_2\sin\phi_3)\Big(2\Big(\bar{\Omega}_{23}\sin\phi_2\partial_2\bar{\bar{\Omega}}_{22} + \bar{\Omega}_{23}\partial_3\bar{\bar{\Omega}}_{23} + \bar{\Omega}_{33}\sin\phi_2(\cot\phi_2\bar{\bar{\Omega}}_{23} + \partial_2\bar{\bar{\Omega}}_{23}) \\
& +\bar{\Omega}_{33}\partial_3\bar{\bar{\Omega}}_{33} \Big) - 2\Big(\bar{\Omega}_{23}\cos\phi_2(\bar{\bar{\Omega}}_{33} + (D-4)\bar{\bar{\Omega}}_{ww}) + (D-4)\bar{\Omega}_{33}\cot\phi_3\bar{\bar{\Omega}}_{ww} \Big) \\
& +2\Big((\bar{\Omega}_{23}\bar{\bar{\Omega}}_{22} + \bar{\Omega}_{33}\bar{\bar{\Omega}}_{23})\cos\phi_2(D-3) + (\bar{\Omega}_{23}\bar{\bar{\Omega}}_{23} + \bar{\Omega}_{33}\bar{\bar{\Omega}}_{33})\cot\phi_3(D-4) \Big) \\
& -\Big(\cos\phi_2\Big(\bar{\Omega}_{22}\bar{\bar{\Omega}}_{23} + 2\bar{\Omega}_{23}\bar{\bar{\Omega}}_{33} \Big) + \bar{\Omega}_{22}\sin\phi_2\partial_2\bar{\bar{\Omega}}_{23} + \bar{\Omega}_{23}\partial_3\bar{\bar{\Omega}}_{23} + \bar{\Omega}_{23}\sin\phi_2\partial_2\bar{\bar{\Omega}}_{33} \\
& +\bar{\Omega}_{33}\partial_3\bar{\bar{\Omega}}_{33} \Big) \\
& +\Big(\cos\phi_2(\bar{\Omega}_{22}\bar{\bar{\Omega}}_{23} + \bar{\Omega}_{23}\bar{\bar{\Omega}}_{33} - \bar{\Omega}_{23}\bar{\bar{\Omega}}_{22} - \bar{\Omega}_{33}\bar{\bar{\Omega}}_{23}) + \cot\phi_3(D-4)\bar{\Omega}_{ww}\bar{\bar{\Omega}}_{ww} \Big) \\
& +\Big(\cos\phi_2(2\bar{\Omega}_{23}\bar{\bar{\Omega}}_{33} - \bar{\Omega}_{33}\bar{\bar{\Omega}}_{32}) - (D-4)\bar{\Omega}_{ww}(\cos\phi_2\bar{\bar{\Omega}}_{23} + \cot\phi_3\bar{\bar{\Omega}}_{33}) \Big) \\
& +0.5\Big(2(D-4)\cot\phi_3\bar{\Omega}_{ww}\bar{\bar{\Omega}}_{ww} + \bar{\Omega}_{22}\partial_3\bar{\bar{\Omega}}_{22} + 2\bar{\Omega}_{23}\partial_3\bar{\bar{\Omega}}_{23} + \bar{\Omega}_{33}\partial_3\bar{\bar{\Omega}}_{33} \\
& +(D-4)\bar{\Omega}_{ww}\partial_3\bar{\bar{\Omega}}_{ww} \Big) \\
& -\Big(\cos\phi_2(\bar{\Omega}_{22}\bar{\bar{\Omega}}_{23} + \bar{\Omega}_{23}\bar{\bar{\Omega}}_{33} - \bar{\Omega}_{23}\bar{\bar{\Omega}}_{22} - \bar{\Omega}_{33}\bar{\bar{\Omega}}_{23}) + \cot\phi_3(D-4)\bar{\Omega}_{ww}\bar{\bar{\Omega}}_{ww} \Big) \Big).
\end{aligned}
$$

$$\text{(C.34)}$$